

TERA

DYNAMIC SIMULATION OF LMFBR SYSTEMS\*

ASHOK K. AGRAWAL  
and  
MOHSEN KHATIB-RAHBAR

DEPARTMENT OF NUCLEAR ENERGY  
BROOKHAVEN NATIONAL LABORATORY  
UPTON, NEW YORK 11973 USA

JULY 1979

To be published in the Journal of Atomic Energy Review, Vienna, Austria

\*The views expressed herein are those of the authors and do not necessarily represent those of the USNRC, the USDOE or Brookhaven National Laboratory.

629 011

7908140005

TABLE OF CONTENTS

	<u>Page</u>
1. INTRODUCTION . . . . .	1
2. SIMULATION APPROACHES . . . . .	6
3. IN-REACTOR MODELS . . . . .	10
3.1 Core Design . . . . .	10
3.2 Core Physics . . . . .	15
3.2.1 Spatial Power Distribution . . . . .	15
3.2.2 Temporal Power Distribution . . . . .	18
3.2.3 Decay Heat . . . . .	24
3.2.4 Reactivity Coefficients . . . . .	27
3.2.5 Reactor Control and Stability . . . . .	40
3.3 Coolant Dynamics . . . . .	45
3.3.1 Overall Flow Distribution . . . . .	45
3.3.2 Pressure-Drop Calculations . . . . .	48
3.3.3 Flow Redistribution . . . . .	54
3.3.4 Intra-Assembly Flow Distribution . . . . .	58
3.3.5 Mixing of Coolant in Plena . . . . .	59
3.4 Heat Transfer . . . . .	63
3.4.1 Correlations . . . . .	63
3.4.2 Heat Transfer Models . . . . .	66
3.4.2.1 Core Model . . . . .	66
3.4.2.2 Rod Bundle . . . . .	68
3.4.2.3 Heat Conduction in a Rod . . . . .	71
3.4.2.4 Structural Materials . . . . .	76
3.4.2.5 Time-Dependent Conservation Equations for Coolant . . . . .	77
3.4.2.6 Cover Gas . . . . .	79

TABLE OF CONTENTS (cont.)

	<u>Page</u>
4. INTERMEDIATE HEAT EXCHANGER . . . . .	81
4.1 Description . . . . .	81
4.1.1 Design for the Loop Concept . . . . .	81
4.1.2 Design for the Pool Concept . . . . .	82
4.2 Dynamical Model . . . . .	83
4.3 Lumped-Parameter Model . . . . .	86
4.3.1 Heat Transfer Coefficients . . . . .	93
4.3.2 Pressure Drop Model . . . . .	96
4.4 Thermal Buoyancy Effects . . . . .	97
5. HEAT TRANSPORT SYSTEMS . . . . .	98
5.1 Description . . . . .	98
5.2 Thermal Transport Model . . . . .	99
5.3 Coolant Dynamics Model . . . . .	102
5.3.1 Pumps . . . . .	104
5.3.1.1 Electromagnetic Pumps . . . . .	104
5.3.1.2 Mechanical Pumps . . . . .	105
5.3.1.3 Dynamic Simulation . . . . .	106
5.4 Pipe Break Model . . . . .	108
5.5 Valves . . . . .	111
5.6 Thermal Stratification and Multidimensional Effects . . . . .	113
6. STEAM GENERATING SYSTEM . . . . .	116
6.1 Description . . . . .	116
6.2 Designs . . . . .	116
6.3 Thermodynamic Models . . . . .	118
6.4 Empirical Consideration for Two-Phase Flows . . . . .	124

TABLE OF CONTENTS (cont.)

	<u>Page</u>
6.4.1 Heat Transfer Correlations . . . . .	125
6.4.2 Critical Heat Flux . . . . .	130
6.4.3 Two-Phase Flow Pressure Drop . . . . .	133
7. NUMERICAL CONSIDERATIONS AND METHODS . . . . .	138
7.1 Background and Requirements . . . . .	138
7.2 Steady-State Solution Methods . . . . .	142
7.3 Transient Solution Method . . . . .	145
7.3.1 Parabolic Equation . . . . .	145
7.3.2 Hyperbolic Equation . . . . .	147
7.3.3 Ordinary Differential Equation . . . . .	150
7.3.4 System Integration Method . . . . .	151
8. SAFETY AND TRANSIENT ANALYSIS . . . . .	155
8.1 Design Approach to Safety . . . . .	155
8.2 Event Classification . . . . .	157
8.3 Plant Protection System . . . . .	158
8.4 Example of Transients . . . . .	160
8.4.1 Normal Reactor Scram . . . . .	161
8.4.2 Control Assembly Withdrawal at Full Power . . . . .	162
8.4.3 Protected Loss-of-Flow Transient . . . . .	163
8.4.4 "Calculated" Loss-of-Piping Integrity . . . . .	177
9. CODE VERIFICATION . . . . .	180
10. SUMMARY AND FUTURE AREAS OF INTEREST . . . . .	183
REFERENCES . . . . .	186
APPENDIX A - TABLES	
APPENDIX B - FIGURES	

629 014

#### ACKNOWLEDGEMENT

We would like to thank all those who have generously provided us with their unpublished results. The authors would also like to acknowledge support from a number of colleagues both at Brookhaven and elsewhere, and to extend appreciations to Dr. Walter Y. Kato for his continuous encouragement in this often taxing endeavor. A special note of thanks to Miss Deborah J. Clay for her skillful typing of the manuscript.

This work was partially performed under the auspices of the United States Nuclear Regulatory Commission.

## ABSTRACT

This review article focuses on the dynamic analysis of liquid-metal-cooled fast breeder reactor systems in the context of protected transients. Following a brief discussion on various design and simulation approaches, a critical review of various models for in-reactor components, intermediate heat exchangers, heat transport systems and the steam generating system is presented. A brief discussion on choice of fuels as well as core and blanket system designs is also included. Numerical considerations for obtaining system-wide steady state and transient solutions are discussed, and examples of various system transients are presented. Another area of major interest is verification of phenomenological models. Various steps involved in the code and model verification are briefly outlined. The review concludes by posing some further areas of interest in fast reactor dynamics and safety.

629 016

## 1. INTRODUCTION

The first nuclear reactor ever to generate electrical energy was a liquid metal fast breeder reactor (LMFBR) - the Experimental Breeder Reactor-I (EBR-I) - when it lit a bulb on December 20, 1951. Since then, LMFBR development programs in several countries have reached a stage where prototype and even commercial size power plants have been either built or are being built. A further indication of the maturity of technology is indicated by a number of international conferences [1-5] that have been held in this decade. The role of fast power reactors in power production was discussed by Kazachkovsky and Lytkin [6] and also in a Commemorative Issue of the Atomic Energy Review [7]. The design and safety aspects in large fast power reactors were reviewed by Okrent [8] and Wilson [9]. Design of heat exchangers was reviewed by Muller and Schnauder [10]. In this paper, we discuss dynamic simulation of the entire LMFBR system.

The history of liquid-metal cooled fast breeder reactors goes back to the construction (in 1946) of an experimental-size fast reactor, Clementine, cooled by liquid mercury. This facility was constructed and operated soon after the Second World War, to demonstrate the feasibility of operating with plutonium fuel and fast neutrons. The next major milestone was the EBR-I (1951). Highly enriched uranium ( $U^{235}$ ) fuel was surrounded by a blanket of  $U^{238}$  and cooled by sodium-potassium alloy (NaK). The EBR-I reactor was the first one to demonstrate the feasibility of breeding and establish the engineering feasibility of liquid-metal coolants. Subsequently, a number of LMFBR projects have been undertaken throughout the world as summarized in Table 1.1. In this table, the type of facility is identified as "Experimental,"

"Demonstration," or "Commercial." Although there is a clear distinction between projects that are clearly experimental in nature and other projects, the latter two classifications are somewhat arbitrary. We have classified plants that are intended for 500 MWe, or larger, as commercial.

There are a number of design differences between various LMFBR projects. But, from the system design viewpoint, there are two major variations in use: a loop-type or spread-out design, and a pool-type or integrated design. Schematic layouts of the heat transfer system for both loop and pool concepts are shown in Figures 1.1 and 1.2, respectively. In loop concepts, the reactor vessel contains fuel, blanket, control and shielding assemblies. Heat generated in the core is removed through a heat transport system. This system, consisting of pipings, intermediate heat exchanger (IHX), pump and valves, resides outside the reactor vessel but inside the containment building. The intermediate heat transport loop transfers reactor heat to the steam generating system, which, in turn, provides steam for generation of electrical power. In pool concepts, on the other hand, the entire radioactive primary cooling system, including the reactor is located in a single large tank. The tank is essentially filled with sodium. Penetrations to this tank are provided for intermediate sodium pipes.

In general, loop-type designs employ thin and long reactor vessels. For example, the height and diameter of the reactor vessel for the Clinch River Breeder Reactor Plant (a loop-type LMFBR) are approximately 14.5 m and 6.1 m, respectively. The pool-type reactors, on the other hand, have chubby and short vessel tanks to accommodate pumps and IHXs. The height and diameter of the primary vessel for PHENIX (a pool-type plant) are approximately 12.0 m and 11.8 m, respectively. In larger and more contemporary designs, however,



reactor vessels for loop designs are getting less thin and less tall, and, for pool designs the vessel tank is beginning to resemble reactor vessels for loop designs. Perhaps this trend is reflective of evolution of both designs. It is interesting to note, at this time, that the countries that have had the most design and operating experience with loop concepts are now leaning toward pool designs and vice versa (although there seems to be a slight preference toward pool designs). The choice between the two design concepts has to be made by detailed evaluation of advantages and/or disadvantages. It appears to authors that this choice is a matter of individual preference, as either concept can be designed and developed to meet the requirements that may be required of them.

The dynamic simulation of the entire LMFBR system is required in design evolution, in establishing operating specifications, as well as in safety analysis of the plant. The degree of interdependence of a component on other components can be assessed only after developing a tool (analytical, empirical or semi-empirical) which encompasses all essential components. The degree of modeling sophistication for the components, however, is dependent upon the nature of problems under investigation. As an example, for safety-related transients (such as natural circulation as a mode of decay heat removal, or the consequence of a major rupture in sodium carrying pipe) the heat producing portions need to be modeled in sufficient details. The balance-of-plant need not be represented in great detail. On the other hand, for operational transients such as turbine trip the reactor core could very well be represented in less detail. More sophistication in modeling of the balance-of-plant, however, may be required.

629 019

The dynamic simulation of the entire system is also required for licensing needs. The impact of a routine, day-to-day operational transients, as well as "unlikely" and "extremely unlikely" events need to be assessed individually to ascertain that the pressures and temperatures anywhere in the entire system remain within pre-determined conditions. A cumulative impact must also be determined in that while single events may not pose serious threat to plant safety, their accumulated consequence must also be within the safety limits. For example, important structural components, such as reactor vessel, has to be evaluated for a cumulative damage from all transients over a period of its design life.

The whole spectrum of conceivable accident chains for LMFBRs can conveniently be divided into two broad categories: local fault events and whole core accidents (WCA). In the former case one considers the consequences of faults within a single fuel or blanket assembly, such as a partial blockage. The single assembly events usually are associated with only minor power changes. In whole core accidents, one considers events that influence the whole core, for example, loss of electrical power supply. This category of events often involve power changes. Major emphasis in WCA events is focused on hypothetical core disruptive accidents (CDA) where the plant protection system is assumed inoperative, after an undercooling or overpower initiating event. As a result, core overheats and may undergo a prompt critical excursion. For these types of CDA events, the whole plant simulation is not necessary since disassembly would occur faster than the time required for sodium to complete one pass through the heat transport circuit. On the other hand, there are other WCA initiators for which the whole plant simulation is required. Some examples of these initiators are: after-heat removal under

529 020

natural circulation, turbine trip, a pump seizure, the control rod withdrawal, load-changing, etc.

The scope of this paper is to focus on dynamic simulation of the entire LMFBR system. The emphasis is given to those areas where significant differences between LMFBRs and other power plants occur. After a brief discussion on various simulation approaches, critical review of various models for in-reactor components, heat transport systems, heat exchangers and steam generative systems will be made. A brief discussion on the choice of fuels as well as core and blanket system designs is also included. Numerical considerations in solving conservative equations will also be discussed. Some examples of various transients will then be presented. Another area of major interest is verification of phenomenological models. Various steps involved in verification will be briefly outlined. Finally, further areas of interest will be discussed.

629 021

## 2. SIMULATION APPROACHES

Dynamic simulation of a system, which consists of many components, involves solution of a set of conservation equations. In general, these conservation equations are partial differential equations in three spatial and one time coordinates. For single-phase systems, there are three such equations per cell: continuity, momentum and energy. The number of equations for a two-phase system (such as water/steam in the steam generator) are twice that for the single phase system. The complexity of the problem at hand can be envisioned by multiplying the number of equations per cell with the total number of cells that may be required to model the system.

There are two aspects of system simulation: modeling and computational (see Figure 2.1). A physical process or a component may be simulated in multi-dimensional space coordinates. Alternately, one or more integrations over space coordinates may be performed analytically. In that case, space-dependent variables are replaced by space-averaged quantities. In most cases, at least one or two spatial coordinates can be eliminated. Consequently, significant simplification results. In this section, a brief overview of computational methods is noted.

Regardless of the modeling details, the system may be simulated on an analog, digital or hybrid computer. Historically, the field of analog and digital computation gained their popularity to electronic developments during and immediately after World War II. The actual usage of these machines was guided primarily by users' familiarity and machine's availability. Digital computers gradually became the cornerstone of all computational needs.

There are a number of well-defined advantages and disadvantages of both analog and digital computers, depending on the specific application. Bekey and Karplus [11] have discussed these in detail in their book on hybrid computation. The major attributes of the two computational techniques are noted in Table 2.1. Perhaps the key distinction between analog and digital computers lies in the accuracy offered by them. In analog machines, the accuracy is limited by the quality of computer components and is rarely better than 0.01% of full-scale. The accuracy of data in digital computers is controlled by the number of bits in memory registers and numerical technique employed.

Hybrid computer techniques, as the name implies, represent an effort to combine in one system some of the characteristics associated with analog systems with those of digital systems. Thus, in principle, a hybrid computer can be utilized as purely analog or purely digital. In actual usage, however, hybridization involves the actual interconnecting of analog and digital portions within the system. The spectrum of hybrid computing techniques is discussed by Bekey and Karplus [11].

Hybrid simulation techniques are typically utilized in early (preliminary) phase of design development of the entire plant. In this stage, emphasis is placed on determining the overall global response of the system. A very precise representation for a component or a subcomponent is deferred to digital computers. In one such application [12] to the Fast Flux Test Facility (FFTF), a hybrid computer simulation was used to demonstrate the adequacy of the control system, design and to determine typical plant operations for a variety of disturbances. In this study, the reactor core was represented as a deviation model. The heat transfer partial differential equations were discretized in

627 023

spatial coordinates. The propagation of disturbances through pipings was represented by using a time-delay model. Brukx [13] has also applied the hybrid technique to simulate the SNR-300 reactor dynamics.

Hybrid techniques are particularly suited for determining sensitive parameters in a system that can be represented by, relatively speaking, smaller numbers of equations. As the number of equations increases, it becomes increasingly more difficult to work with hybrid computers. In that case, digital simulation is used where many equations can be programmed within a "do" loop.

Analog computers are particularly useful in solving initial value problems in one independent variable. Partial differential equations involving two or more independent variables can be solved by permitting no more than one variable to vary in continuous form; the remaining variables will then have to be discretized by the application of finite difference approximations. Out of the range of basic analog approaches, the most widely used approach to the analog simulation of transient field problems involves the approximation of all derivatives with respect to space variables by finite-difference approximations. A major difficulty arises in the utilization of this method when it is necessary to simulate time-varying or nonlinear problems. Under these conditions, it is necessary to adjust continuously the magnitudes of a multitude of circuit elements in the course of a computer run, or to provide a separate non-linear function generator at each node point. This is always difficult and usually economically impossible. Therefore, this analog approach is essentially limited to linear, constant-parameter fields.

Digital computers are capable only of solving algebraic expressions. Therefore, all independent variables must be discretized. There are a number of numerical techniques that are developed for, and particularly suited to,

digital computers. These will be briefly reviewed in a later section. It should, however, be added that the digital techniques are by far the most popular ones in use.

629 025

### 3. IN-REACTOR MODELS

#### 3.1 Core Design

The heart of a nuclear power plant is the reactor core where heat is generated from nuclear fission of both fissile and fertile materials. The reactor core itself occupies a rather small space of the entire plant. Yet, a controlled production of power and its dissipation is of utmost concern to reactor physicists and engineers alike.

Like water cooled thermal reactors (LWRs) the core of an LMFBR plant consists of fuel, control and shielding assemblies. In addition, the fast breeder core also has blanket assemblies where much of the breeding takes place. All of these assemblies are hexagonal in shape. The fuel assemblies are made up of closely packed fuel rods in a triangular pitch. All LMFBR projects that are currently in operation, construction, or design use ceramic fuels although the very early test reactors, such as Clementine at the Los Alamos Scientific Laboratory, EBR-I and EBR-II at the Argonne National Laboratory and BR-1 in the USSR, have used metal fuel [14]. It should be noted that Clementine was the first fast reactor and the first to use  $\text{Pu}^{239}$  as fuel. It demonstrated the feasibility of plutonium as a fast reactor fuel.

Some of the key design parameters for more contemporary plants are noted in Table 3.1. The CRBRP (Clinch River Breeder Reactor Plant) data [15] are referred as typical of prototype or demonstration plants. For commercial size reactor, data for the SUPERPHENIX [16] are noted where available. The fuel used in either of these two plants is  $(\text{U-Pu})\text{O}_2$  with depleted  $\text{UO}_2$  as blanket material. The core configuration is of homogeneous or 'conventional' type, fueled with two-zone enrichments with inner zone having slightly less enriched



(U-Pu) $O_2$  than the outer zone. Figures 3.1 and 3.2 show the nominal configuration of these reactor cores.

Fuel, blanket and control assemblies are hexagonal in cross section and are typically four to five meters in length. Figure 3.3 is a schematic sketch of the CRBRP fuel assembly. Major sections of these assemblies include (a) discrimination post which fits in the lower core support structure, (b) inlet nozzle through which sodium flows inside the assembly, (c) lower shielding and orifice blocks through which designed coolant flow is controlled, (d) the lower axial blanket region, (e) the active core region where most of the power is generated, (f) the upper axial blanket, and (g) the fission gas plenum. The radial blanket and control assemblies have similar design. The number of rods per assembly, diameters and lengths of various regions do, however, differ from those of fuel assemblies and from each other. All of these assemblies are separated from each other through thicker load pads. A small, essentially stagnant sodium gap inbetween assemblies exist. Figure 3.4 is a sketch of the SUPERPHENIX fuel assembly.

Typically, fuel rods are from 3.0 m to 4.0 m long, of which roughly one meter is filled with enriched fuel pellets to form the active core. Figure 3.5 is a schematic representation of fuel rods for CRBRP and SUPERPHENIX. In non-vented LMFBR fuel designs, such as these reactors, a gas plenum is provided for in each of these rods. The fission gases that are released during fuel burnup are collected in this space. The gas pressure can reach as high as 70 to 80 atmospheres towards the end-of-life-fuel rods. The fission gas plenum is located either above the upper axial blanket, as in CRBRP, or below the lower axial blanket, as in Great Britain's Prototype Fast Reactor (PFR), or at both ends, as in SUPERPHENIX. An advantage of locating the gas plenum above

629 027

the upper blanket is that the fission gases, when accidentally released by cladding rupture, can escape without inducing significant reactivity effect on the core. In this case, the possibility of accidental cladding rupture, however, is higher because of the higher temperature seen by the cladding. In the case of a bottom location of the gas plenum, on the other hand, the accidental release of fission gas will have to sweep through the active position of the core. In the process, induced voiding will result in a positive sodium void reactivity effect. The likelihood of an accidental rupture is remote since the plenum is at the core inlet temperature.

An interesting variation in the design of fuel assembly is in use in the PHENIX reactor. In here, the fuel assembly consists of two separated rods: lower region of 217-pin bundle and the upper region of 61-pin bundle. The lower region includes the fission gas plenum, lower axial blanket, active core, and a small plenum to house spring retainer. The upper region is made of depleted  $UO_2$  and it acts like a reflector. This two-region design of rod bundle apparently was used for ease in fabrication. From the modeling point of view, one must account for hydraulic diameter to vary with axial height.

Radial blanket assemblies are generally made of thicker rods. These are filled with depleted  $UO_2$  or  $ThO_2$  pellets. The rod bundle is made of 61 rods in the case of CRBRP and 91 rods for SUPERPHENIX. A fission gas plenum is also provided for. Control assemblies are made of rod bundles and filled with neutron absorber such as boron carbide. A gas plenum is provided for accumulation of the helium gas that is produced from  $(n,\alpha)$  reaction with  $B^{10}$ .

Fuel, radial blanket, and control assemblies are thus made of rod bundles arranged in a hexagonal geometry. Individual rods are separated either via spacer wire, as in the case of CRBRP or SUPERPHENIX, or via a grid structure.

629 028

The radial shielding assemblies are either similar in design to fuel assemblies (i.e., a group of stainless steel rods in a triangular pitch) or these can be solid hexagonal steel blocks with holes drilled through them to provide for cooling.

The coolant flow through these assemblies are orificed to give a flatter temperature distribution across the reactor core. This is done by zoning orifice patterns at the bottom of these assemblies. In CRBRP, for example, the lower shield/orifice blocks have five zones of orificing for fuel assemblies and four zones of orificing for the blanket assemblies.

In addition to the core design used in the above mentioned reactors, there exist a variety of other design schemes that can be employed. Various parameters that can be varied are (1) actual arrangement of fuel and blanket assemblies, i.e., homogeneous or heterogeneous; (2) form of fuel such as oxide, carbide or nitride and (3) the fuel cycle i.e., U-Pu or Th-U.

The homogeneous design is characterized by having a cylindrical core surrounded by radial blanket assemblies and the upper and lower axial blankets. Examples of this design are the CRBRP and the SUPERPHENIX (see Figure 3.1 and 3.2). The heterogeneous design, also referred to as parfait design, employs alternating rows of fuel and internal blanket assemblies. The resulting cylindrical core is then surrounded by radial and axial blankets. A typical design [17] for a 1200 MWe plant is shown in Figure 3.6. The actual number of rows of either the fuel or blanket assemblies can also be varied as it was done in some other studies [18, 19]. Neutronically, the inter-dispersion of fuel and blanket assemblies enhances neutron leakage from the fuel zones into the internal blanket zones. This results in a low sodium void reactivity which is a safety consideration. On the other hand, higher fissile enrichments

are needed for the heterogeneous core than the homogeneous core. The higher enrichments lead to a reduced Doppler coefficient and an increased fuel compaction reactivity [20]. From hydraulics point of view, the average core outlet temperature, for the same mixed-mean average outlet temperature at the beginning-of-life core will have to be higher in a heterogeneous design than the homogeneous design. The choice between homogeneous and heterogeneous designs, therefore, should be made by weighing these opposing consequences.

The fast reactor fuel in power plants can be in either oxide, carbide or nitride forms. Table 3.2 shows a comparison of some of the major material properties of these fuels. The actual choice between them is made on the basis of nuclear and economic performance characteristics and operating fuels experience. As mentioned earlier, the most popular form of fuel has been  $(U-Pu)O_2$ . Interest in carbide and nitride fuels stem from their improved breeding ratio. In a comparative study [21] of these fuels (see Table 3.3), it was found that significant economic and doubling time advantages exist for carbide fuel over both oxide and nitride fuels. For example, the breeding gain (breeding ratio-1) of the carbide is more than twice that of the oxide. This is due to increased heavy metal atom density as well as difference in neutron cross sections between the carbon and oxygen dilutents.

From the designer's point of view, there is a lack of sufficient irradiation experience with the carbide and nitride fuels. Safety implications of utilizing these fuels in other accident scenarios which may lead to a core disruptive accident will also have to be assessed. Finally, because of the higher thermal conductivity of these fuels than that for oxide, fuel-cladding gap will have to be filled with sodium or NaK alloy. This, perhaps, poses some fabrication concern. Nevertheless, the economic incentives offered by carbide fuel may just mandate detailed characterization of these fuels.

A number of thorium-based fuel cycles have also been studied. These include (1) (U-Pu) $O_2$  as core and  $ThO_2$  as blanket materials, as it is being used in India's experimental Fast Breeder Test Reactor (FBTR), (2) (U $^{233}$ -Th) oxide or carbide, (3) (Pu-Th) $O_2$  and (4) Th-U-Pu or Th-U $^{233}$  metal alloy. Interest in the thorium-based fuel cycle stems from a factor of three times more abundance of thorium than uranium. In addition, certain combinations of the thorium fuel offer a negative sodium void coefficient [22,23] which is a definite plus from safety considerations. Table 3.4 shows a comparison [17] of essential nuclear characteristics for (Pu-U) and (U $^{233}$ -Th) oxide fuels for both homogeneous and heterogeneous designs.

### 3.2 Core Physics:

#### 3.2.1 Spatial Power Distribution

A precise calculation of the heat generation rate throughout the reactor core is required at all times of reactor operation. The heat generation rate per unit volume due to nuclear fission,  $P_f(\vec{r},t)$ , at a point in space denoted by coordinate  $\vec{r}$  and time  $t$  is given by

$$P_f(\vec{r},t) = P_0 \cdot \frac{\int \Sigma_f(\vec{r},E,t) \phi(\vec{r},E,t) dE}{dE}, \quad (3.1)$$

$P_0$  is the recoverable heat generation per fission, where  $\Sigma_f(\vec{r},E,t)$  is the macroscopic fission cross section,  $\phi(\vec{r},E,t)$  is the neutron flux and  $E$  denotes neutron energy. An explicit dependence on the space and time coordinates in the macroscopic cross section is included since the number density of the fissionable material depends upon the burnup and the enrichment.

Another contribution to the heat generation rate results from the decay of fission products by emission of radioactive rays ( $\beta$ - and  $\gamma$ -rays). The total heat generation per unit volume then is given as:

$$P(\vec{r},t) = P_f(\vec{r},t) + P_d(\vec{r},t) \quad (3.2)$$

where  $P_d(\vec{r},t)$  is the decay heat generation rate per unit volume. The reactor power at any time,  $P(t)$ , can be obtained by integrating  $P(\vec{r},t)$  as

$$P(t) = \int P(\vec{r},t) d\vec{r} \quad (3.3)$$

In this section, only time-independent or static power distribution is considered. The following section will deal with the dynamics.

The static distribution of the neutron flux is obtained rigorously by solving the space and energy dependent neutron transport equation. The numerical solution can be obtained either in diffusion theory approximation, the discrete ordinates approximation or the Monte Carlo method. Of these three, the last method is computationally the most expensive. In actual reactor computations, the neutron flux is obtained by using computer codes that are based either on the diffusion or the discrete ordinate approximations. Excellent reviews of the state-of-the-art for these methods have been made by Adams [24] and Lewis [25], respectively.

Power distribution calculations are performed first by selecting a point-wise cross section data such as the Evaluated Nuclear Data File (ENDF), then multigroup (usually less than thirty) and composition dependent cross section files are prepared by employing appropriate spectrum collapse techniques.

629 032

Finally, diffusion calculations are performed to determine the radial and power distribution for a variety of reactor configurations. As an example, the power fraction values for the first and equilibrium cycle cores of CRBRP [15] are noted in Figure 3.7. All of the values are normalized to a total power generation equal to unity. The remainder of power fraction is produced in control and shielding assemblies and plena etc. Note that at the end of equilibrium cycle, power generation in blanket assemblies is about three times that for the beginning of cycle.

The radial power distribution across the reactor core can also be obtained for each fuel or blanket assembly. Because there exist a profile or distribution of power within an assembly, power distribution is often quoted as the normalized values of the power in an average and the peak rods of an assembly. Figure 3.8 shows [15] assembly radial power factor and peak rod radial power factor, with respect to the average rod in the whole core or blanket, at the beginning of the equilibrium cycle in CRBRP. As an example, the average pin power in a fuel assembly in row 2 is 1.335 times the average power per pin in the whole core.

The axial power distribution in the driver and blanket regions differ more than its variation from one assembly to another within the same region. Figure 3.9 shows a typical axial power shape in the CRBRP core region. The power shapes in the lower and upper axial blanket regions are shown in Figure 3.10. The axial power shape for a radial blanket assembly is shown in Figure 3.11 for a particular location and the beginning of the first cycle. All of these power shapes are normalized to unity in the region.

### 3.2.2 Temporal Power Distribution

While the spatial power distribution in a reactor core is of interest in the steady-state operation of the plant, the temporal power distribution is of utmost importance in day-to-day plant operation, reactor stability studies, and safety. It is seen from Equation (3.2) that the time-dependence of both fission heating (prompt and delayed fissions) and decay heating is required. A rigorous solution of the space, energy and time dependent neutron transport equation is not practical [26]. In fact, the solution of the neutron balance equation even in a multi energy-group diffusion theory is by no means a trivial problem, as attested by a number of articles [27-29] and books [30,31] that have appeared in the past ten years. In the following, a short overview of these methods is given, prior to going into details of a much simplified, conventional approach.

Any reactor when subjected to a spatially non-uniform perturbation, which is always the case, will experience both spatially and spectrally (energy dependent) non-uniform change in time-dependent neutron density. This change in the neutron density, in multi energy-group diffusion theory approximation, can be calculated by employing either direct or indirect methods. In direct method, the governing equations are expressed in finite difference form in both space and time coordinates. Computer programs to solve these equations now exist [27] for one-, two- or three-spatial dimension geometries. Although the finite difference methods require large memory space and computing time, their outstanding virtue, with respect to indirect methods (see below), is the existence of rigorous error bounds.

The indirect methods can be further classified as 'modal' and 'nodal' methods. The modal methods are further subdivided into 'quasi-static,'

629 034



'time-synthesis' and 'space-time synthesis' categories. These methods are discussed in detail by Stacey [32]. Instead of going into the details for the last two methods, it is pointed out that the space-time synthesis techniques are generally preferable to time synthesis techniques for multidimensional problems. Although the synthesis techniques are in extensive usage for thermal reactors at the naval reactor laboratories [28], these are not popular with LMFBRs due to the lack of an error bound. The quasi-static method, on the other hand, is much in use for LMFBRs.

The quasi-static method was first proposed by Ott [33] and improved by Ott and Meneley [34]. In this method, the space, energy and time dependent neutron density is expressed as a product of two quantities:

$$P_f(\vec{r}, E, t) = \psi(\vec{r}, E, t) \cdot A(t) , \quad (3.4)$$

where  $\psi(\vec{r}, E, t)$  is called the shape function and  $A(t)$  is the amplitude function. The quasi-static and improved quasi-static approximations then deal with the degree of time dependence used in the shape function. Computer codes, QX-1 for one dimensional geometry [35], FX-2 [36] and KINTIC-1 [37] for two-dimensional geometry, based on the improved quasi-static approximation are available. Convergence of the quasi-static solution to the solution obtained by direct numerical integration for both fast [38] and thermal [39] reactor problems has been demonstrated.

There is yet another approximation, known as the adiabatic approximation, that has been used for severe excursions in LMFBRs. This method formed the basis of the AX-1 code [40] that has existed for almost twenty years. All of these sophisticated techniques are used in hydrodynamic disassembly calcula-

tions where the importance of small reactivity errors in the range near and beyond prompt critical is much greater. For a class of transients, such as the entire system simulation, where the reactivity additions are relatively small a much simplified reactor kinetics formulation is utilized.

When the time dependence of the shape function in Equation (3.4) is completely ignored, i.e., the power generation is assumed to be separable in space and time variables, a multi energy-group space-dependent formalism is obtained. The more common form of kinetics equations is obtained when only one energy group is considered. This approximation is known as the point kinetics (or one energy group, spaced averaged) approximation. Recently, Dorning and Spiga [41] have shown that the point kinetics equations correspond to the leading term of an asymptotic expansion of the solution to the space- and energy-dependent reactor kinetics equation for large reactors. The correction due to the higher-order terms can be explicitly calculated.

The general equations relating to the time-dependent fission power behavior, under the above mentioned point-kinetics approximation without the source term, are:

$$\frac{dN}{dt} = \frac{\rho(t) - \beta}{\Lambda} N(t) + \sum_i^m \lambda_i C_i \quad (3.5)$$

and,

$$\frac{dC_i}{dt} = \frac{\beta_i}{\Lambda} N(t) - \lambda_i C_i \quad (3.6)$$

where  $N(t)$  is the neutron density,  $\rho(t)$  is the total reactivity in  $\Delta k/k$ ,  $\beta_i$  is the fraction of delayed neutron in  $i$ -th group ( $i$  ranges from 1 to  $m$ ),

629 036

$\beta = \beta_1 + \beta_2 + \dots$ ,  $\Lambda$  is the prompt neutron generation,  $\lambda_i$  is the decay constant for  $i$ -th group of precursors and  $C_i$  is the concentration of  $i$ -th group of precursors. The number of precursor group is usually taken as six. A set of values [42] for  $\lambda_i$  and  $\beta_i$  for fast fission of  $U^{235}$  and  $Pu^{239}$  is noted in Table 3.5. Also included in this table are the values for CRBRP fueled with the light-water grade plutonium. For other isotopes these values may be obtained from Reference 42. It should be noted that for a particular isotopic composition of a reactor, a single set of these values are obtained and utilized in the kinetics equations.

It is convenient to rewrite Equations (3.5) and (3.6) in a normalized form by defining the normalized neutron density,  $n(t)$ , and the concentration of  $i$ -th group precursor,  $c_i(t)$ , as

$$\begin{aligned} n(t) &= \frac{N(t)}{N(0)} , \\ c_i(t) &= \frac{C_i(t)}{C_i(0)} , \end{aligned} \tag{3.7}$$

where,

$$c_i(t) = \frac{\beta_i}{\Lambda \lambda_i} N(0) . \tag{3.8}$$

Thus, Equations (3.5) and (3.6) become, respectively,

$$\frac{dn}{dt} = \frac{\rho - \beta}{\Lambda} n(t) + \frac{1}{\Lambda} \sum \lambda_i C_i , \tag{3.9}$$

and,

$$\frac{dc_i}{dt} = \lambda_i [n(t) - c_i(t)] . \tag{3.10}$$

The direct integration of these equations requires very small timestep sizes due to the small value of  $\Lambda$  ( $\sim 6 \times 10^{-7}$  s for large ceramic reactors). To assure numerical stability and accuracy, step sizes of approximately 100 to 1000 times  $\Lambda$ , i.e., 0.0006 to 0.00060 s, will be required. Various methods, therefore, have been developed.

The most useful method is termed the prompt jump approximation. In this approximation,  $\Lambda \frac{dn}{dt}$  in Equation (3.9) is neglected. In that case,

$$n(t) = \frac{1}{\beta - \rho} \sum \lambda_i C_i(t) \quad (3.11)$$

In other words, any disturbance in the reactivity results in an instantaneous jump in the neutron density (hence the name prompt jump). This approximation is found to be in excellent agreement (to within less than 0.1%) with the exact solution for values of  $\rho$  less than  $0.5\beta$ . The agreement between this method and the exact solution diminishes as  $\rho$  approaches  $\beta$ . In fact, when  $\rho = \beta$  this method breaks down. For most transients of interest in LMFBR simulation, however, this method is a good one since a reactivity addition will be less than  $+50\beta$  (i.e.,  $0.5\beta$ ) as the reactor will be scrammed or shutdown well before reactivity approaches this value.

A number of methods for exact solution of Equations (3.9) and (3.10) have also been developed. A polynomial method developed by Kaganove [43] is quite good for all values of  $\rho$ . In this method, it is assumed that over an integration step ( $\Delta t$ ),  $n(t)$  and total reactivity  $\rho(t)$  may be represented by second order polynomials. Thus,

$$n(t) = n_0 + n_1 t + n_2 t^2 \quad 0 \leq t \leq \Delta t \quad (3.12)$$

and,

$$\rho(t) = \rho_0 + \rho_1 t + \rho_2 t^2 \quad 0 \leq t \leq \Delta t \quad (3.13)$$

where  $n_0$  and  $\rho_0$ , respectively, are the values of  $n$  and  $\rho$  at the beginning of this time interval, and  $n_1$ ,  $n_2$ ,  $\rho_1$ , and  $\rho_2$  are constants to be evaluated. When Equations (3.12) and (3.13) are substituted in Equations (3.9) and (3.10) and solved for, an analytic equation, which relates  $n_1$  and  $n_2$  with  $\rho_1$  and  $\rho_2$ , is obtained. The boundary conditions are now imposed at the midpoint and end of the step (i.e., at  $t = \Delta t/2$  and  $\Delta t$ ). Thus, two equations in the unknowns  $n_1$  and  $n_2$  are obtained in terms of  $\rho_1$  and  $\rho_2$ . An additional assumption that the power and reactivity are functions of time only is made, i.e., during the time interval  $\Delta t$ ,  $\rho(t)$  is assumed to be independent of  $n(t)$ . The solution, therefore, for  $n(t)$  is now complete. It should be added that higher order polynomials for  $n(t)$  and  $\rho(t)$  could also be used. In that case, the boundary conditions will have to be applied for as many intermediate points as the order of the polynomials. Any potential benefit in computing effort is questionable, particularly when it is remembered that the solution of the thermohydraulics equations takes most of the total computing time.

Depending upon the transient, the prompt jump approximation, when applicable, has been found to be more than twenty times faster than the Kaganove method. In any event, the solution of neutron kinetics equations, under point kinetics approximation, requires a small fraction of the total computational effort needed to solve the thermohydraulic equations. More on the numerical methods will be discussed later.

### 3.2.3 Decay Heat

When a nuclear fission takes place, a number of fission products are formed. In addition to the fission fragments, neutrons,  $\alpha$ -,  $\beta$ -, and  $\gamma$  rays are emitted. Most of the heat generated is felt instantaneously and is either absorbed in fuel or some of it escapes and gets absorbed in the coolant and structural material. There is another source of heat from the fission fragments. The fission fragment nuclei are, in general, unstable (i.e., have an excess of neutrons) and they undergo several transitions by  $\beta$ -emission before they reach stability. Each such process is often accompanied by release of one or more  $\beta$ - and  $\gamma$ -rays. The energy deposition due to these  $\beta$ - and  $\gamma$ -rays is termed fission product heat. Depending upon the history, i.e., duration of power productions, the level of power and isotopic composition of fuel, it can be as much as 6 to 8 percent of the total heat production. The actual magnitude of the fission-product heat is computed by integrating balance equation for every radionuclide. Most parent radionuclide attain their equilibrium concentration in a few days of operation, hence, contribution from fission products is essentially constant after a few days of reactor operation.

When the reactor is scrammed or shutdown, the concentration of radionuclides starts tapering off. The fission-product heat, now termed as decay heat or 'after heat,' continues to be produced even after fission reaction has stopped. A nuclear reactor, therefore, needs to be cooled long after the shutdown.

The energy emitted per second per fission at time  $t$  after a fission is obtained by integrating the energy available from each disintegrating nuclei.

A quantitative estimate was first given by Way and Wigner [44]. Accordingly, the power generation due to beta and gamma rays,  $P_d(\tau, t)$ , is:

$$P_d(\tau, t) = 0.0622 P_0 \left[ t^{-0.2} - (\tau+t)^{-0.2} \right] \quad (3.14)$$

where  $P_0$  is the reactor power before shutdown,  $\tau$  is time, in seconds of power operation before shutdown and  $t$  is time, in seconds, elapsed since shutdown. The total disintegration energy per fission turns out to be approximately  $22 \pm 3$  MeV.

The above empirical relation is correct to within a factor of two between 10 seconds and 100 days. A more accurate result, now a days, is obtained by following the decay of individual nuclides in detail with modern computers. The total decay heat is given by summing contributions from each disintegration. This method is also referred to as the 'summation rule'. The decay heat is given by

$$P_d(\tau, t) = \sum \epsilon_i \lambda_i n_i(\tau, t) \quad (3.15)$$

where  $\epsilon_i$ ,  $\lambda_i$  and  $n_i(\tau, t)$  denote the average decay energy, decay constant, and inventory, respectively, for the  $i$ -th nuclide. A number of computer programs, namely RIBD at the Hanford Engineering Development Laboratory [45], CINDER at the Los Alamos Scientific Laboratory [46], and ORIGEN at the Oak Ridge National Laboratory [47], now are available which can be used to calculate the decay heat values.

A major problem in getting precise values for the decay heat is the lack of data for the short-lived nuclides. Nuclear models are being used to

629 041

substantiate data or provide a reasonable value in cases where direct measurements are not available. This data set is now part of the Evaluated Nuclear Data File (ENDF/B-IV) available from, and maintained by, the National Nuclear Data Center at Brookhaven National Laboratory [48].

A typical value [45] of decay heat at goal exposure in FFTF is shown in Figure 3.12 for time from one second to three years after shutdown. Also shown in this figure is the decay heat value at zero decay time as approximately 6.8 percent of the operating power. It should be emphasized that the results shown here are representative of a certain fuel isotopic composition and operating mode. Similar values should be obtained for the plant under evaluation.

The uncertainty in decay heat values results from uncertainties in all of the three contributors of Equation (3.15), namely decay energy, decay constant and yield values. The uncertainties due to these factors have been evaluated by Schmittroth and Schenter [49] for the thermal fission of  $U^{235}$  the fast fission by  $U^{238}$ , and the fast fission of  $Pu^{239}$  for a typical reactor exposure period  $\tau$  of  $10^7$  s (116 days) and a burst exposure. They report that the total uncertainty for a typical reactor exposure is smaller by a factor of three to four than that for a burst exposure. For the case of reactor exposure, which is what we are interested in here, most (>90%) of the uncertainties in uranium fission result from uncertainty in decay energies for up to 100 seconds after shutdown. Beyond this time, the uncertainties in yield and decay constants account for roughly half of the total uncertainties. In the case of plutonium fission, the uncertainty in fission product yields is significant.

The computed decay heat values have been compared with some integral (calorimetric) measurements (see [49]). Reasonable agreement in decay heat



values for  $U^{235}$  fission were obtained for cooling time of up to 1000 seconds. Additional measurements of both point data and calorimetric data will narrow down the uncertainties that are currently associated with the decay heat values.

The reactor power calculation scheme is illustrated in Figure 3.13. Various contributors to the reactivity feedback are discussed in the following section.

### 3.2.4 Reactivity Coefficients

In going from a 'cold' (just critical) to 'hot' (power operation) condition the temperature of the core rises, which causes change in the atom densities as well as microscopic reaction cross sections for various elements in the core. The atom densities also change during plant operation due to burnup. The effect of these changes in criticality is expressed as reactivity coefficients. Starting from the conventional definition of reactivity

$$\rho = \frac{k-1}{k} \quad (3.16)$$

where  $k$  is the effective multiplication factor, the change in reactivity can be expressed as

$$d\rho = \frac{dk}{k^2} \quad (3.17)$$

Since  $k$  differs from one by small fractions only, the above equation can be rewritten as

$$d\rho \approx \frac{dk}{k} \quad (3.18)$$

The form of this equation suggests the unit of reactivity as  $\Delta k/k$ , which is often used. Another unit of reactivity is in 'dollars' and 'cents.' One dollar of reactivity is defined to be equal to a change in  $\Delta k/k$  by  $\beta$ , the total delayed neutron fraction. The temperature coefficient of reactivity,  $d\rho/dT$ , is then equal to  $(1/k) dk/dT$  but it is also approximated as  $dk/dT$  since  $k$  is so close to unity.

A change in reactivity can either be relatively prompt-acting or be long-term. The prompt component is associated with the change in temperature of the system. There are five temperature coefficients of reactivity of major importance in LMFBRs: (1) the Doppler coefficient, (2) the sodium temperature coefficient, (3) the fuel expansion temperature coefficient, (4) the fuel-element bowing coefficient, and (5) the power coefficient. The long-term reactivity effects are due to (1) the fuel burnup and blanket buildup, (2) the buildup of fission products, and (3) fuel growth under irradiation. These effects have been discussed by McCarthy and Okrent [50] and by Hummel and Okrent [51]. A brief review is given here.

### Doppler Effect

In large, fast breeder reactors, the Doppler reactivity effect results from broadening of fission and capture resonances in fissile ( $\text{Pu}^{239}$ ,  $\text{U}^{233}$ ) and fertile ( $\text{U}^{238}$ ,  $\text{Th}^{232}$ ) materials. This broadening of cross sections causes a difference in fission-source neutrons produced per neutron absorbed. Depending upon the fuel composition, i.e., fissile-to-fertile ratio, the Doppler reactivity effect can be either positive or negative. In highly enriched core, the effect of temperature rise in fuel could lead to a positive value for the Doppler effect. In fact, in EBR-I reactor with the Mark I and

Mark II fuel loadings, the positive power coefficient of reactivity was initially thought to arise from a positive Doppler effect. Later experiments demonstrated that the positive coefficient arose due to bowing of the fuel rods. Further calculations and experiment indicated that the Doppler effect was almost negligible. In large, fast ceramic-fueled reactors the Doppler effect is negative due to the relatively large ratio of fertile-to-fissile atoms, and sufficient neutron flux at low energies.

The Doppler reactivity effect plays an important role in plant operation and safety analysis. Since the associated reactivity coefficient is negative and it is felt almost instantaneously, it offers an inherent mechanism to overcome positive reactivity from other sources. For this reason, there has been a significant amount of work done in developing calculational methods and also to measure this in critical experiments. The calculational techniques are based either on perturbation theory or direct eigenvalue calculation [51,52]. Theoretical studies have shown that the Doppler coefficient of reactivity can be approximated as

$$\begin{aligned} \left(\frac{d\rho}{dT}\right)_{DOP} &\equiv \frac{1}{k} \frac{dk}{dT} \\ &\approx \alpha_{DOP} T^{-1} \end{aligned} \quad (3.19)$$

Because of the  $T^{-1}$  dependence, the Doppler coefficient of reactivity is often quoted as  $T \frac{dk}{dT}$ . The change in reactivity due to change in fuel temperature from  $T_1$  to  $T_2$  is obtained by integrating this equation. One gets,

$$(\Delta\rho)_{DOP} = \alpha_{DOP} \ln (T_2/T_1) \quad (3.20)$$

Some representative values [21] for the Doppler coefficient of reactivity are shown in Table 3.6 for various (U-Pu) fuels for a 500 MWe plant. The variation in the Doppler coefficient between oxide, carbide or nitride fuels is largely due to the variation in the fertile-to-fissile atom ratios. The effects associated with slight change in the neutrons spectrum (because of variation in moderating power) and fuel pin design are small. The magnitude of the Doppler effect for a uniform rise in fuel temperature from 1100 K to 1500 K results in the reactivity decrease of approximately 63¢ (for  $\beta = 0.0035$ ).

The Doppler coefficient of reactivity for (Th-U<sup>233</sup>) fuel cycles is considerably higher than that for the (U-Pu) fuels. In one such comparison, Lu, et al., [17] have reported a considerably larger value for (Th-U<sup>233</sup>)O<sub>2</sub> fuel than that for (U-Pu)O<sub>1.98</sub> fuel (see Table 3.4). Since a large but negative reactivity feedback value is desirable from the operating and safety considerations this is just another factor in favor of employing (Th-U) fuel cycle.

The uncertainties in evaluating the Doppler effect arise due to (1) uncertainties in the point-wise reaction cross section data and (2) the calculational techniques. Recently, an international comparison of various physics data was made [53] for a large 1200-MWe LMFBR design. For this particular benchmark problem, the Doppler effect,  $(k_{2200} - k_{1100})/k_{1100}$ , in raising fuel temperature from 1100 K to 2200 K was found to be  $-0.00743 \pm 0.00096$ . Most of the uncertainty is associated with the neutron cross section data set.

The Doppler effect depends considerably on the neutron spectrum. If the coolant were to be voided, the neutron spectrum will shift towards higher neutron energy, thereby reducing the Doppler effect. For the above mentioned benchmark problem, this results in  $(k_{2200} - k_{1100})/k_{1100}$  of  $-0.00439 \pm 0.00085$ .

The Doppler coefficient of reactivity for a voided core, however, is not of much interest in LMFBR system simulation since the core is either submerged with liquid sodium for all transients of interest, or the reactor is in shut-down condition. The computed values [15] of the Doppler coefficient of reactivity for the CRBRP reactor are shown in Table 3.7 for the beginning-of-equilibrium-cycle (BOEC) and the end-of-equilibrium-cycle (EOEC) conditions. These values are noted for different regions of the reactor core for both sodium 'in' and 'out' conditions.

A number of experiments for the Doppler effect have been performed (see, for example, [51,52]). It appears that the calculated values are in reasonable agreement with the measured ones. Hummel and Okrent [51] conclude that overall Doppler effects can be calculated with a precision adequate for most design purposes.

#### Sodium Temperature Coefficient

The reactivity effect associated with the change in sodium temperature is the composite of changes due to neutron capture, leakage, and spectral shift. The effect of neutron capture is positive but is usually small. Hence, it may be neglected. An increase in the sodium temperature gives rise to increase in neutron leakage, i.e., the leakage term is negative. The magnitude of this effect decreases as reactor size is increased. The spectral shift component is positive due to spectrum hardening. Both the leakage and the spectral shift components, depending upon the actual design, can be comparable, and yet of opposite signs, to each other. A small error in either of these two contributions can cause the total reactivity to vary over a wide range of values. Great care, therefore, must be exercised in calculating these contributions.

For normal start-up and operational transients, where the entire system simulation is required, the rise in sodium temperature, hence, change in sodium density is small. The associated reactivity effect is small compared with the accompanying Doppler reactivity effect. In other accident situations, such as a pipe rupture followed by reactor scram, there can be at least partial voiding of the core. Although the accompanying reactivity effect can be substantial, it is still not important due to the large negative reactivity worth of control rods. The calculated values of the sodium temperature coefficient of reactivity for CRBRP are noted in Table 3.8 for different reactor regions.

An order of magnitude estimate for the relative importance of the reactivity insertions due to the Doppler and the sodium temperature effects was made for the CRBRP. For the case of a programmed reactivity insertion of  $2\text{¢}/\text{s}$  over the nominal operating conditions of CRBRP with reactor scram from the secondary shutdown system, the core-wide-average fuel temperature rises from  $\sim 1350\text{ K}$  to  $1500\text{ K}$ . The resulting Doppler contribution to reactivity is approximately  $-5.3 \times 10^{-4} \Delta k/k$  (i.e., about  $-15\text{¢}$ ). Even for the core-wide average increase in the sodium temperature of about  $25\text{ K}$ , the reactivity effect is estimated to be  $0.4 \times 10^{-4} \Delta k/k$  (i.e., about  $1\text{¢}$ ). In other words, the Doppler effect dominates the effect of increase in sodium temperature by an order of magnitude.

The reactivity effect associated with sodium void is not of much interest in the overall system simulation. Nevertheless, this effect for certain (U-Pu) oxide core can be positive and large enough to override the negative Doppler effect. An accurate estimation of the sodium void worth is essential for transients such as the hypothetical core disassembly accidents. There,

however, are a number of possible design options which can give low or negative sodium void effects. One such option is to enhance the leakage term by reducing the height-to-diameter ratio of the core. Other options include heterogeneous cores, or thorium-based internal blanket materials. Hummel and Okrent [51] discuss various methods of evaluating the sodium void effect.

#### Fuel Expansion Temperature Coefficient

The temperature changes in the reactor core contributes to the reactivity feedback by the thermal expansion of fuel and blanket, in addition to the Doppler and sodium density effects. The temperature increase causes the fuel and blanket rods to expand radially and axially. The radial expansion results in compression and then ejection of sodium from the core and blanket. The effect of axial expansion is to elongate the effective fuel column length. A quantitative estimation of these effects on reactivity is neither simple nor exact. In general, the reactivity contribution from a single source under study is obtained by ignoring all other contributors.

The reactivity effects due to the thermal expansion usually decreases with the increase in reactor core size. Table 3.9 shows the isothermal temperature coefficients of reactivity [50] for EBR-II and FERMI reactors. If the temperature of the entire reactor were changed by 1 K, the resulting reactivity change due to the effect of each component would be by the number given in this table. It is observed that the axial fuel expansion causes a significant change in reactivity. The radial fuel expansion effect is almost one-fourth of that due to axial expansion.

The effect associated with the axial expansion of fuel is, relatively speaking, larger for metal fueled core than that for the ceramic fuels. This

is primarily due to the fact that the fuel pellets move freely within the clad tubes only for fresh fuel. With some irradiation, the pellets tend to stick to the clad as observed in the RAPSODIE reactor [54].

#### Bowing Effect

In addition to reactivity changes associated with the expansion of core assemblies, additional reactivity contributions occur as a result of bowing of core assemblies during reactor startup and shutdown. Bowing of assemblies can occur if there exists a temperature gradient in the radial direction. The reactivity effect associated with bowing was first observed in the EBR-I reactor. Interestingly enough, the accompanying positive reactivity was at first associated with the Doppler effect (which can be positive for highly enriched fuel) but later was confirmed to be due to in-ward thermal bowing of the fuel assemblies.

If the core structure is held firmly at the top and bottom of the core the radial temperature gradient causes a differential expansion between the inside and outside of the structure. This differential expansion results in forces tending to bow them toward the center of the reactor. If clearances exist, movement of fuel assemblies will occur. The resulting net fuel movement toward the core center increases the reactivity. Both because of the magnitude of the reactivity contribution, due to bowing and resulting load on the load points of fuel assemblies, computer programs have been employed to calculate the extent of bowing. Figure 3.14 shows one such calculation made by Cha and McLenan [55] for a typical LMFBR core at 400 full power days with five support points. It is seen that almost all fuel assemblies bow in towards the reactor center while blanket assemblies bow away from the reactor



core. For the case where fuel assemblies are supported from just one end, as for example, in the gas-cooled fast breeder reactor, the differential thermal expansion tends to 'flower out' the assemblies.

The reactivity effects associated with bowing depends upon the magnitude and direction of bowing as well as the material worths. The magnitude and direction of bowing is strongly dependent upon the reactor power-to-flow ratio and inter-assembly gap size. The material worths depends upon the control rod position and fuel history. The calculated reactivity effect due to bowing is shown in Figure 3.15 for the CRBRP. Results [56] are shown for the beginning-of-cycle 1 (BOC 1), and the end-of-cycle 1 (EOC 1). It is seen that maximum bowing results when interassembly gap is at its nominal value (3 mm). When the gap size is reduced to 2.5 mm, the reactivity effect of bowing is considerably reduced. For normal operating conditions (i.e., power-to-flow ratio of one), bowing can lead to a positive reactivity effect of from 4¢ to 54¢.

#### Power Coefficient

The incremental change in reactivity for an increment increase in power is called the power coefficient. When the reactor power is at least a few percent of its rated power, it is no longer at isothermal conditions. The isothermal temperature coefficients discussed earlier will, therefore, have to be appropriately weighted in accordance to the temperature distribution in the core. From the reactor operator's point of view, this is the most important reactivity effect that has to be accounted for when plant is started from standby to full power conditions. Since this reactivity effect has a negative sign that must be overcome, the magnitude of this value is often termed the power reactivity defect (PRD).

629 051

The non-isothermal conditions that develop in a reactor from zero, or essentially zero power to full power depends upon the plant design. The power coefficient for each reactor should be computed and it can vary significantly from one design to another. Great care should be exercised not only in its computation but also in its usage. Generally, the power coefficient of reactivity is calculated for the normal operation of the plant. The reactor power is raised slowly compared to the time required to reach thermal equilibrium. The reactivity coefficient thus obtained would not be proper during rapid power transients where such equilibrium may not be established.

For EBR-II, the power coefficient of reactivity is  $-3.2 \times 10^{-5} \Delta k/k/MW$  in going from zero power to 22.5 MW and  $-6.0 \times 10^{-5} \Delta k/k/MW$  from 22.5 MW to 62.5 MW [14]. The total reactivity change from standby to its full power of 62.5 MW is  $-0.00312 \Delta k/k$ . Recently, Shields and Armstrong [57] have reported the PRD values versus EBR-II run number. As noted earlier, the PRD is the reactivity decrement required to raise the reactor from zero power (hot standby) to a given power level (in this case, 62.5 MW). Their results are shown in Figure 3.16. With the stainless steel reflector that is now in EBR-II, the value of  $\beta$  is 0.0068. Anomalies in reactivity parameters have been the subject of extensive investigation in the past. Although no clear explanation has yet been given, one possible explanation for part of the observed long-term increase in PRD could be increased neutron leakage in the stainless steel reflector region, brought about by bowing of reflector assemblies. Note that there is a substantial decrease in PRD due to rotation of reflector assemblies in Rows 9 and 10.

For FERMI, the power coefficient of reactivity is  $-1.61 \times 10^{-5} \Delta k/k/MW$  and the change in reactivity from zero power to 200 MW is  $-0.00312 \Delta k/k$  [14].

The reactivity effects for CRBRP due to hot, full power operation from an initial standby condition at 478 K (400F) and 589 K (600 F) are noted in Table 3.10. Also shown in this table are the individual contributors. These numbers are for the first cycle of full load. Note that the reactivity contribution due to bowing was estimated to be +50¢. The power coefficient of reactivity, including the bowing effect, is  $-9.7 \times 10^{-6} \Delta k/k/MW$  at an initial isothermal temperature of 478 K.

#### Long-Term Reactivity Effects

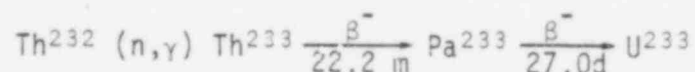
The reactivity effect due to the burnup and buildup of the fissile and fertile materials needs to be considered in the long-term operation of the plant. For homogeneous reactors, this effect is generally negative since (1) the inner core tends to burn fuel up faster than it is bred, and (2) the buildup of fissile material in blanket regions is in less reactive zone. For example, in a homogeneous oxide reactor with an internal breeding ratio of 0.4, the reactivity loss of 0.15  $\Delta k/k$  is reported [50]. The buildup of plutonium in the blanket zone was estimated to add only 0.025  $\Delta k/k$  in the same period.

A variety of fission products are generated during fissioning. Since all of the fission products have finite capture cross section, their buildup results in a negative reactivity feedback term. In oxide reactors where the neutron spectrum is considerably softer than that for the carbide or metal fuels, the loss in reactivity due to buildup of fission products is greatest. An estimate of the combined reactivity effects of fission products, blanket buildup and core burnup was made by McCarthy and Okrent [50] and is shown in Table 3.11. For large oxide and carbide fueled reactors, the long-term reactivity

losses are very large, primarily as a consequence of their lower internal breeding ratio. This implies that frequent reloading will be required. The internal breeding ratio can be raised by introducing more fertile material into the core. This, unfortunately, leads to a more positive sodium void coefficient.

The reactivity effect of fuel growth under irradiation comes largely from the axial expansion and it is negative. In the case of sodium-bonded fuel rods the radial growth of the fuel within the cladding tube has small effect due to small displacement. This effect can be estimated in a manner analogous to that used in the reactivity feedback due to the thermal expansion of fuel.

Another important contributor to the long-term reactivity effect is due to the buildup of Pa<sup>233</sup> in thorium-fed reactors. Protactinium is formed in the core by the following chain:



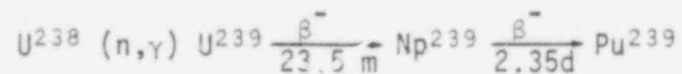
The reactivity of a shutdown core containing Pa<sup>233</sup> may be expressed as:

$$\Delta k = \Delta k_0 (1 - e^{-\lambda t}) \quad (3.21)$$

where  $\Delta k_0$  is the potential worth of all U<sup>233</sup> formed from Pa<sup>233</sup>,  $\lambda$  the decay constant (0.693/27.0 d<sup>-1</sup>) and  $t$  is the time after shutdown. In an example studied by Goldman [58], a decrease in reactivity of 1.76%  $\Delta k/k$  due to U<sup>233</sup> burnup inbetween refuelings would be compensated by Pa<sup>233</sup> decay in 22 days after the shutdown. The upper limit of reactivity insertion,  $\Delta k_0$ , in this case was 4.1%  $\Delta k/k$ .

An additional effect due to the delay time in formation of bred  $U^{233}$  in core is the increase in net burnup reactivity change during a cycle. If the  $Pa^{233}$  had zero decay time, for example, the reactivity decrease with burnup in the reference reactor core would be 1.1%  $\Delta k/k$  as compared to an actual decrease of 1.76%. This is due to the fact that only 40% of the  $Pa^{233}$  formed by radiative capture of  $Th^{232}$  actually decays to  $U^{233}$  while in-pile.

A similar situation occurs in  $Pu^{239}$  breeders. The breeding cycle in this system is:



The half-life of  $Np^{239}$  is about 1/12 that of  $Pa^{233}$ . Assuming equal power densities in  $U^{233}$  and  $Pu^{239}$  breeders, the equilibrium concentration of  $Np^{239}$  would be roughly 1/12 that of  $Pa^{233}$ . Because of the small half-life of neptunium compared to the fuel in-pile residence time, the actual concentration would be close to the equilibrium value. This is not the case in the reference  $U^{233}$  breeder, where the average  $Pa^{233}$  concentration is about one-half its equilibrium value. The average  $Np^{239}$  concentration in a  $Pu^{239}$  breeder should, therefore, be about 1/5 that of  $Pa^{233}$  in the  $U^{233}$  breeder. Assuming that  $U^{233}$  and  $Pu^{239}$  have the same reactivity worth, Goldman estimates that the total reactivity associated with  $Np^{239}$  is about 0.67%  $\Delta k/k$  for a reactor of similar design and operating method. Upon reactor shutdown, the reactivity associated with the  $Np^{239}$  would be essentially all released in about 11 days. Of course, a similar amount of reactivity would be lost in starting up the reactor and building up this equilibrium, quantity of neptunium.

### Reactivity Feedback

A generalized representation of the reactivity feedback on reactor power is shown in Figure 3.17. Any deviation in reactor power causes deviation in the fuel and blanket temperatures, and the coolant temperature. The reactivity effects associated with the change in fuel temperature are predominantly the Doppler and, to some extent, due to its thermal expansion. A deviation in the sodium temperature gives rise to a reactivity contribution due to the routine change in sodium density. Furthermore, a change in the coolant temperature also results in a change in the duct wall (hexagon can) temperature, thereby resulting in a reactivity contribution due to bowing of fuel and blanket assemblies. The sum of all these individual contributions with the applied reactivity,  $\rho_a$ , is the total reactivity,  $\rho(t)$ , i.e.,

$$\rho(t) = \rho_a(t) + \rho_{FB}(t) \quad (3.22)$$

where  $\rho_{FB}(t)$  represents the total feedback reactivity. The neutron kinetics equations, such as the point-kinetics equations (see Equation (3.9)), may now be solved to get a new value for the reactor power.

#### 3.2.5 Reactor Control and Stability

A reactor plant contains many systems that require control, but there are two in particular that are of most concern from the safety viewpoint: the reactor system and the containment system [59].

The reactor control system maintains the neutron flux and its rate of change at a level that meets the requirements imposed upon the reactor plant. To carry out the control two distinct aspects are usually evident, both of

which are included in the term "reactor control": a regulating or operational requirement and a safety requirement.

The regulating system maintains the neutron flux against disturbances in reactivity resulting from poison changes, fuel burnup, temperature and pressure effects, etc. Further, the regulating system maintains the flux at a value demanded by the power production requirements.

The safety system returns the neutron flux and its rate of change to a safe state whenever the regulating function is not properly carried out, or whenever lack of integrity in some part of the reactor system requires a speed of response beyond the capabilities of the regulating system. The safety system must be able to exercise its high speed control properties only in a direction that forces the system to a safer state.

The containment control system is in some respects a backup to the reactor safety system. Control must be exercised over all gaseous and liquid effluents, and over the action of plant personnel, so that radioactivity above preset levels is not permitted to reach the public domain.

The reactor control system must bring the reactor and its auxiliaries safely from a shutdown state to a power-producing state taking into account maximum allowable stresses in all plant components and the demands imposed by the external load.

The control system must also prevent excursions in any parameter that would permit a reactor component to go beyond its rating in the face of any credible disturbances. Included in such disturbances would be loss of load due to turbo-generator or transmission line faults or any reactivity to be inserted, or an absorber to be withdrawn, at its maximum rate (the maximum rate in general being determined by some fundamental means, such as the synchronous speed of control rod drive motors).

629 057

These requirements produce a conflict between regulating and safety system design. For example, the maximum rate of withdrawal of reactivity that can be effected by the regulating system, together with the total amount of reactivity available for withdrawal, can be used to set minimum requirements for the safety system. In general, it is required that the speed of response of any controller be limited by some fundamental means in order to produce sufficient time for the safety system to detect any controller failure and to override the fault.

There are also credible failures that cannot be forestalled by the control systems. Loss of integrity of a containment or a coolant system because of undetected flaws can allow rupture to occur at normal operating levels. In such cases the control system is required to actuate dousing systems and emergency cooling systems, to close containment vessels after initial surges have passed, to divert cooling water to delay storage tanks, and to reroute ventilating and cooling air.

In the particular case of fuel cladding failures, the control system must provide evidence of the failure soon enough to permit removal of the element or elements before a more serious failure occurs and the removal becomes potentially a difficult operation.

In loss of integrity incidents the main function of the control system is to prevent the spread of radioactive contamination. It must also warn of excessive radiation levels in a manner that provides personnel with the maximum opportunity to evacuate the affected area.

Finally, in considering control requirements, it is important to be precise in stating in detail what is expected of the control system under various fault conditions.



A reactor is said to be stable if, for any small disturbance, such as a change in coolant flow or movement of the control rods, and at powers up to and slightly above its design power level, the reactor response will tend to hold the power at a constant value that differs from the initial power by only a small amount [60]. This implies also a definition of an unstable reactor. In the latter, a slight change in coolant flow or control-rod setting could cause a power excursion or an oscillation of increasing amplitude. Either type of behavior could result in core damage if it were not terminated quickly by the control system.

Every reactor should be designed to be stable. Two kinds of instability namely, autocatalytic and oscillating instability, should be considered by the designer. A mechanism for autocatalytic instability exists if the net temperature coefficient in a reactor is positive. Thus an increase in reactor power leads to an increase in reactivity, which causes further rise in power and thereby results in a power excursion.

When the power in a reactor is increased slowly, with respect to the time constant of the system, only the total temperature coefficient is important. Thus, a reactor with a temperature coefficient that is not negative even though it has positive components will be safe under these conditions. However, if the power in a reactor is increased rapidly, owing to a sudden increase in reactivity, the fuel will be heated more quickly than will be the coolant and the structure. Consequently, if the fuel has a positive temperature coefficient, the reactor could be autocatalytic even if the coolant and structure temperature coefficients were large and negative. The long time constants of the coolant and structure would prohibit their negative temperature coefficients from responding quickly enough to counteract the prompt positive temperature coefficient of the fuel.

In large LMFBRs, most of the reactivity feedback mechanisms give rise to a negative value for the power coefficient. An exception being the reactivity effect due to fuel assembly bowing. In the case of CRBRP, this effect was estimated to be of the order of +50¢. If this were the only effect due to increase in reactor power, additional positive reactivity from bowing will make the system unstable. Fortunately, there are a number of other reactivity contributors which in general overcome the bowing effect and a net negative reactivity feedback results. In any case, the designer must take the necessary precautions to ascertain that the net temperature coefficient of reactivity is negative.

The second type of reactor instability to be considered is oscillating instability. Even if the prompt and delayed temperature coefficients are both negative, an instability of the oscillating type can occur in principle although the possibility is quite remote. In this type of instability, small power oscillations at a particular frequency increase in amplitude, and the peak power can increase by several orders of magnitude above the initial power. The mechanism can be explained as follows: if the reactivity is made to oscillate with the same frequency. The temperature acts back on the reactivity via the temperature coefficient. The temperature changes in the various reactor components will take place later than the power and reactivity changes because it takes time for the heat to be transported throughout the system. Thus, the feedback reactivity is not in phase with the driving reactivity oscillation. If the temperature coefficient is negative and the feedback reactivity is just out of phase with the driving function, then a resonant condition will exist, and the amplitude of the oscillation will become larger and larger. If the oscillations are permitted to continue, excessive heat may be generated, and the core may be damaged.

Reactor stability studies are usually based on linearity assumptions. Stability predictions based on linearity assumptions are valid for small variations about operating points for a reactor model which includes non-linear reactivity feedback effects. Stability of the system for large variation about the operating point may be inferred if the linear analysis demonstrated that the system is stable at operating points throughout the operating range. A dynamic model to examine stability of non-linear system has been developed [61] and applied to the SSC-L code [62]. Because of the non-linearity of the system, the stability is examined in time-domain and not frequency-domain.

### 3.3 Coolant Dynamics

#### 3.3.1 Overall Flow Distribution

The characterization of flow behavior of coolant in core and reactor internals is an integral part of the plant design. It is through this characterization and heat generation rates that the temperature response of the system is evaluated. This temperature response is then utilized in structural analysis to assure that the component under study fulfills its expected design objectives. This section is concerned with the hydraulics characterization; the following section deals with the heat transfer aspect.

In loop-type LMFBR designs, coolant enters the reactor vessel through several inlet nozzles which are, in general, equally spaced in a horizontal plane. From the nozzles, the coolant enters a large inlet or lower plenum where it gets thoroughly mixed to mitigate transients and thus reduce thermal load on surrounding structures. The coolant then enters a flow redistribution system which may differ from one design to another. This coolant is then allowed to pass through fuel, blanket, control and shielding assemblies after going

through a series of holes or slots. These slots coupled with the orifice blocks, if any, in assemblies, establish the fraction of coolant flow through a given assembly. There is an additional flow passage designed to minimize thermal load on some key structural components such as the reactor vessel. Coolant exiting from various assemblies mixes in a large, outlet plenum region before exiting through the evenly spaced outlet nozzles.

Figure 3.18 is a schematic of reactor coolant flow for the CRBRP [63]. Liquid sodium is seen to flow upward through all assemblies so that the direction of flow is the same as natural circulation. This is true in all LMFBR designs except in the Dounreay Fast Reactor where coolant flowed in the downward direction. Because of a considerable number of problems the downflow method has been abandoned in present systems. Typical flow distribution among various flow passages in CRBRP is shown in Table 3.12. The control of coolant flow through different core assemblies is accomplished by slot sizes in the inlet module. Each one of the modules feeds seven assemblies. In addition, there is lower shielding and orifice blocks within each assembly. In this design, the common pressure point is the lower plenum region of the reactor vessel. It should be pointed out that there are a total of nine different orifice zones in the fuel and radial blanket assemblies to equalize the maximum sodium heating.

In pool-type LMFBRs, like PHENIX or SUPERPHENIX, the design for coolant flow distribution appears to be simpler. Sodium coolant enters the core assemblies from the plenum between the core support grid (diagrid) via lateral slots in the assembly foot, and flows upward around the fuel pins. A schematic of flow fields is shown in Figure 3.19 for SUPERPHENIX.

In PHENIX reactor, the entire core is divided into 16 zones to equalize the maximum sodium heating in the hottest channels of each flow zone while

629 062

complying with the various criteria prescribed for each type of element. There are six zones in the inner fuel region, four in the outer fuel region, three in the radial blanket, one for the control assemblies, one for the fuel assemblies in storage positions, and one for the radial shielding assemblies. With an overall pressure drop of 500 kPa, the flow rates range from 25 kg/s in a central fuel assembly to 0.2 kg/s in a radial shielding assembly.

The support grid, or plenum, on which the assemblies are installed acts as a virtually constant pressure feed tank. Sodium inflow to the assemblies is radial. From the constant-pressure plenum, the sodium flows through passages machined in sleeves of the support grid, then through passages drilled in the lower angles of the assemblies, and then upward through the element bundles. Flow rates desired for the different flow zones are obtained by adjusting the hydraulic resistance between the plenum and the element bundle. A number of passages are drilled at different levels in each assembly nozzle, as schematically shown in Figure 3.20. Each grid sleeve also has the same number of slots sized to mate with a particular number of passages in the assembly, depending on the position of the assembly in the core. Additional hydraulic resistance into the nozzles of low-flow assemblies was incorporated to avoid cavitation. Coolant exits at the top of assemblies into a large pool of sodium. The mixing of coolant, in this region, is enhanced by the presence of structural and instrumentation components. The SUPERPHENIX reactor appears to have very similar flow distribution design as utilized in the PHENIX plant.

The design of the lower portion, i.e., the inlet to assemblies, is made sophisticated for the sole purpose of avoiding complete inlet blockage of any assembly. This is accomplished by a combination of a number of radial and vertical slots or holes. Perhaps the most important cause for this sophis-

tication resulted from an inlet-blockage accident in the FERMI reactor [14]. In here, due to the 'open' region between the reactor vessel and the primary tank an inlet-blockage of a core assembly occurred when a structural component (vibration reducer) became loose. This structural piece caused partial melt-down of the core. Subsequent designs of LMFBRs now provide for a variety of sieves in such a way that a complete flow starvation through an assembly is almost impossible to achieve.

### 3.3.2 Pressure-Drop Calculations

The overall pressure loss from the vessel inlet to the outlet can be written as a sum of individual contributors:

$$\Delta p = \Delta p_{\ell} + \Delta p_c + \Delta p_b + \Delta p_e + \Delta p_u \quad , \quad (3.23)$$

where the subscripts  $\ell$ ,  $b$  and  $u$  denote, respectively, the lower plenum, the rod bundle and the upper plenum and  $c$  and  $e$  denote the contraction and expansion form losses, respectively.

The most significant contributor in  $\Delta p_{\ell}$  and  $\Delta p_u$  is the static head term. For lower plenum, the coolant temperature is generally uniform, hence,

$$\Delta p_{\ell} = \rho g h_{\ell} \quad (3.24)$$

Because of the possibility of stratification in the upper plenum, an average density of sodium should be used in calculating  $\Delta p_u$ .

The pressure loss due to abrupt change in area can be expressed as [63]:

$$\Delta p = \frac{K}{2\rho} \left( \frac{W}{A_0} \right)^2 \quad (3.25)$$

where,

$$K_e = (1 - A_0/A_1)^2$$
$$K_c = \xi (1 - A_0/A_1)$$

The pressure loss in the rod bundle can be expressed as a sum of the frictional losses and the static head:

$$\Delta p_b = \Delta p_{bf} + \Delta p_{bs} \quad (3.26)$$

The pressure loss due to static head in the bundle is given by

$$\Delta p_{bs} = \int \rho(z) g dz, \quad (3.27)$$

where the integration over the bundle length must be carried out since there is an appreciable change in coolant density. Once the density profile, i.e., the temperature profile, along the core length becomes known, the static pressure loss can be expressed as [64]

$$\Delta p_{bs} = g L [c_3 \rho_0 + (1 - c_3) \rho_1], \quad (3.28)$$

where  $\rho_0$  and  $\rho_1$ , respectively, are the inlet and outlet coolant densities and the coefficient  $c_3$  depends on the temperature profile. For the case of uniform heat flux, it is 0.50. For reactor applications where the heat flux has chopped-cosine profile, it is estimated to be 0.54.

The frictional pressure loss in a rod bundle can be written as:

$$\Delta p_{bf} = f_b \cdot \frac{1}{2} \cdot \frac{L}{D_e} \cdot \frac{W^2}{\rho A^2}, \quad (3.29)$$

where  $W$  is the mass flow rate,  $A$  is the flow cross-sectional area,  $f_b$  is the friction factor, and  $D_e$  is the hydraulic diameter ( $= 4 \times$  flow area/wetted perimeter). This form of equation is analogous to the one used for flow in pipings.

Historically, the friction factor correlation for flow in pipings has also been used to approximate  $f_b$  for the wire-wrapped rod bundles. The familiar friction factor chart is shown [65] in Figure 3.21 for a number of values for relative roughness ( $\epsilon/D_e$ ). For turbulent flows,  $f$  is given by the following transcendental equation [66]:

$$\frac{1}{\sqrt{f}} = - 2.0 \log_{10} \left( \frac{\epsilon/D_e}{3.7} + \frac{2.51}{Re\sqrt{f}} \right) \quad (3.30)$$

Alternately, Equation (3.30) has been approximated to within five percent as:

$$f = 0.0055 \left\{ 1 + \left[ 20000 \frac{\epsilon}{D_e} + \frac{10^6}{Re} \right]^{1/3} \right\} \quad (3.31)$$

For laminar flows, i.e., for  $Re < 2000$ ,

$$f = 64/Re \quad (3.32)$$

An interpolation of  $f$  between the turbulent and laminar correlations may be used for the flow transition region ( $2000 \leq Re \leq 3000$ ).

Somewhat recently, Novendstern [67] has expressed the wire-wrapped bundle pressure loss in terms of an equivalent friction factor that depends upon the rod geometry. Accordingly, the friction factor is expressed as:

$$f_b = \left[ \frac{1.034}{(P/D)^{0.124}} + \frac{29.7 (P/D)^{6.94} Re^{0.0886}}{(H/D)^{2.239}} \right]^{0.885} \cdot 0.316 Re^{-0.25} \quad (3.33)$$

629 066



$P/D$  denotes the pitch-to-diameter ratio and  $h$  is the spiral wire lead. This equation is valid in turbulent flow regime only.

For laminar flow in rod bundles, Axford [68] gave the following expression:

$$f_b = \frac{2\pi}{3} \frac{1}{M} \frac{1}{(P/D)^4} \left[ \frac{2\sqrt{3}}{\pi} \left(\frac{P}{D}\right)^2 - 1 \right]^3 \cdot \frac{1}{Re} \quad (3.34)$$

where  $M$  is a function of  $(P/D)$ . From the computed values of  $M$  for  $P/D$  in the range 1.05 to 1.5, Yang [69] has developed a simple correlation:

$$M = f_0 + f_1(P/D) + f_2(P/D)^2 + f_3(P/D)^3, \quad (3.35)$$

where  $f_0 = 0.0618456$ ,  $f_1 = -0.137837$ ,  $f_2 = 0.0898949$ , and  $f_3 = -0.013786$ .

Recently, Rehme [70] has carried out systematic measurements of the pressure loss in wire-wrapped rod bundles over a range of Reynolds number from 1000 to highly turbulent region. The range of test conditions included the pitch-to-diameter ratio from 1.125 to 1.417, and the lead of the wire wraps between 100 to 600 mm. The number of rods in bundle was varied from 7 to 61 rods. He has correlated his data as

$$f_b = F \left( \frac{S_b}{S_t} \right) f', \quad (3.36)$$

where  $S_b$  and  $S_t$  are, respectively, the wetted perimeter of rods and wires, and total (including the subchannel walls) and  $F$  is given by:

$$F = \left(\frac{P}{D}\right)^{0.5} + \left\{ 7.6 \frac{dw}{H} \left(\frac{P}{D}\right)^2 \right\}^{2.16}. \quad (3.37)$$

The quantity  $f'$  is shown in Figure 3.22 as a function of the modified Reynolds number. The measured data has also been correlated as:

$$f' = \frac{64}{Re'} + \frac{0.0816}{Re'^{0.133}} \quad (3.38)$$

where  $Re' = \sqrt{F} Re$ .

Chiu, Todreas, and Rohsenow [71] have also reported their measurement of friction factor for the 61-rod bundle assembly. For blanket assembly ( $P/D = 1.067$ ) their results can be expressed by the following correlations:

for  $H/D = 8$

$$f_b = 0.48 Re^{-0.25} \quad Re \geq 7000 \quad (3.39)$$

$$f_b = \frac{90}{Re} \quad Re \leq 500$$

and,

for  $H/D = 4$

$$f_b = 0.90 Re^{-0.25} \quad Re \geq 7000 \quad (3.40)$$

$$f_b = \frac{160}{Re} \quad Re \leq 500$$

For  $5000 \leq Re \leq 7000$ , an interpolation between the two correlations may be used. These correlations fall between the Rehme's and Novendstern's results for high Reynolds number region.

In early 1979, Engel, Markley, and Bishop [72] reported a new correlation for the friction factor for rod-bundle-averaged conditions. Their correlation is based on pressure drop data obtained from a 61-rod bundle (4 inches wire wrap spacer lead) with isothermal sodium and water tests. The sodium tests covered the Reynolds number from 300 to 25,000. The water

629 068

test Reynolds number range was 50 to 4000. Their correlation for Re greater than 400 is:

$$f = \frac{110}{Re} (1-\psi)^{\frac{1}{2}} + \frac{0.55}{Re^{0.25}} \sqrt{\psi} \quad (3.41)$$

where the intermittency factor  $\psi$  is defined as:

$$\psi = \frac{Re - 400}{4600} ; \quad \text{for } 400 \leq Re \leq 5000 . \quad (3.42)$$

This result is also shown in Figure 3.23. Also included in this figure are the data obtained by Rehme [70], Chiu et. al. [71], and Hofmann [73] and the Novendstern's correlation [67]. It should be added that the test data for side and inboard interchannels were corrected for the bundle-averaged conditions by employing the appropriate subchannel velocities and hydraulic diameters.

In laminar flow region, it is well known that the product of the friction factor and Reynolds number is constant. However, this constant assumes a different numerical value for each specified geometry. Engel, Markley, and Bishop [72] have correlated this product as:

$$f Re = \frac{320}{\sqrt{H}} (P/D)^{1.5} \quad (3.43)$$

for a range of P/D and H values. Note that the wire-wrap lead, H, is in centimeters.

In the turbulent region ( $5000 \leq Re \leq 40,000$ ), the friction factor can be expressed as

$$f = 0.55 Re^{-0.25} \quad (3.44)$$

629 069

This expression differs by less than 14% from the Novendstern's prediction for the geometry and flow range tested. This result is in good agreement with the results of Chiu et al.

It is important to note that all of these experimental results confirm a smooth transition from laminar to turbulent regime for wire wrapped rod bundles, which is in contrast to the more conventional friction factor for the round tubes; where a discontinuity exists in the critical range ( $2000 \leq Re \leq 3000$ ) as it can be seen in Figure 3.21.

For grid-type rod bundles, Rehme [70] has measured the pressure drop due to frictional losses. He has noted that a single correlation, similar to that for the wire-wrapped rod bundles, is not readily discernable since the pressure loss is strongly dependent upon the type of grid spacers used.

### 3.3.3 Flow Redistribution

The coolant flow distribution in the reactor vessel through fuel, blanket, control and shielding assemblies is designed for the optimum characteristics at rated power operating conditions. The desired fractional flow rates through these assemblies are accomplished by a series of flow orifices and slots, as discussed in the beginning of this chapter. If the reactor is operated at conditions different than the designed flow conditions, as it is always the case in load changing operation or during transients, the fractional flow through any assembly will exhibit variation from the designed condition. This is due to the fact that the coolant flow through an assembly is coupled with the rest of assemblies and that the flow impedance offered by the assemblies exhibit flow-dependent characteristics. The importance of this effect was recognized from the early stage of development of the advanced SSC-L code [74].

The inter-dependence of coolant flow in one assembly and on the remaining assemblies can be seen schematically from Figure 3.24. Although this drawing is representative of the CRBRP design, it can be simplified by eliminating one or both inlet/outlet modules to include those designs where individual assemblies provide direct connection between the lower and upper plena of the reactor vessel. Alternately, one or more than one intermediate levels of common pressure points, indicated by the rectangular boxes, may be added. An electrical analog of this flow circuit is shown in Figure 3.25. Each assembly is represented by a number of flow impedances connected in series. These flow impedances represent pressure losses in various regions such as orifice plates, rod bundles, etc.

Calculations of flow redistribution in the reactor vessel can be performed by writing down the conservation equations and integrating them. A considerable insight into the effect of flow redistribution was obtained by Meyer [64] by computing this effect for a range of steady-state operating conditions. Due to the simplicity of this model, it is discussed here in detail. All of the assemblies are represented by a number of parallel, one-dimensional channels. Conservation of energy and momentum equations can be written as:

$$\Delta H_k = q_k / W_k \quad (3.45)$$

and,

$$\Delta P_k = c_{1k} W_k^2 + c_2 \left[ c_{3k} \rho_0 + (1 - c_{3k}) \rho_{1k} \right] \quad (3.46)$$

where  $q_k$  is power in the  $k$ -th channel,  $c_{1k}$ ,  $c_2$  and  $c_{3k}$  are constants,  $\rho_0$  is the inlet sodium density,  $\rho_{1k}$  is the core outlet sodium density for the  $k$ -th channel, and subscript  $k$  denotes the channel. The first term on the right hand side of Equation (3.46) represents frictional loss and the second term is due to static head. The coolant density can also be related with its enthalpy as

$$\rho = c_0 - c_1 H \quad (3.47)$$

The change in coolant enthalpy is expressed as

$$\Delta H_k = H_{1k} - H_0 \quad (3.48)$$

The overall flow in the vessel and power can be obtained by summing up individual flow and power values. Thus,

$$W_c = \sum W_k \quad (3.49)$$

$$Q_c = \sum q_k \quad (3.50)$$

Further,

$$H_c = Q_c / W_c \quad (3.51)$$

and,

$$\Delta p_c = \Delta p_1 = \Delta p_2 = \dots = \Delta p_k \quad (3.52)$$

The last equation is obtained by neglecting any radial variation in pressure for the inlet and outlet plena. These coupled algebraic equations can now be solved. Results of one such computation [64] for a two-channel representation

of channels in the CRBRP are shown in Figures 3.26-3.28. These calculations were made for five power levels (0, 0.1, 1.0, 10, and 100% of full power value of 975 MW). Channels 1 and 2 denote average of all fuel and blanket assemblies, respectively. For the normal operating case, i.e., for 100% flow and 100% power case, sodium flow rates in fuel and blanket channels were taken to be 4178 kg/s and 627 kg/s, respectively. The fraction of power generation was 0.9138 and 0.0779. Figure 3.26 shows the pressure drop as a function of total core flow for different power levels. Figure 3.27 shows the ratio of flow in fuel channel to the total and the ratio of enthalpy rise in channel 1 to the total as a function of the total flow rate. Similar quantities are shown for the blanket channel in Figure 3.28. The effect of flow redistribution is then seen to be significant for low flow conditions, even at steady state. For example, for the case of 1% of nominal power and 1% of nominal flow rate, sodium flow through average fuel channel increases by 5% while coolant flow through average blanket channel decreases by 37%. Another important observation that can be added is that the coolant exit temperature in either channel is almost identical for low flow and low power condition. In other words, radial temperature profile across the reactor core flattens out considerably.

The importance of flow redistribution during transients cannot be discussed easily. Yang and Agrawal [75] have modeled this effect in the SSC-L code by solving the conservation equations in one spatial dimension (the flow direction). Guppy and Agrawal [76] and Agrawal et. al. [77] have applied this model to study the flow coastdown transients to natural circulation in CRBRP. The magnitude of this effect can readily be seen by computing the ratio of the normalized coolant flow fractions,  $f_i(t)/f_i(0)$ , where  $f_i(t)$  is the fraction of total in-vessel flow in the  $i$ -th channel at time  $t$ . Figure 3.29 shows the

normalized flow fractions for a number of channels. It is noted that this effect begins to be pronounced around 60 to 70 seconds after scram. The hot channels are seen to draw coolant from other colder channels. Similar effects have also been calculated by other in-vessel codes such as FLODISC [78].

Another interesting point to note is that for very long times, the relative amount of sodium flow in different channels will approach a new quasi-steady value but different from the steady-state values for normal operating mode. If the flow redistribution were not included in the analysis, which is unrealistic, the normalized flow fractions would be identical to one at all times for all channels. The effect of flow redistribution is to lower the maximum hot channel temperature, as it can be seen in Figure 3.30 for a hot channel. The radial temperature profile across the reactor core will, therefore, be flatter than that obtained by ignoring this effect. This effect is, at least, one of the two factors that may account for the observed temperature flattening in some natural circulation simulation tests in EBR-II [79]. The other factor that has similar effect is the radial heat conduction from one assembly to another.

#### 3.3.4 Intra-Assembly Flow Distribution

The LMFBR core assembly is composed of a parallel array of fuel rods separated from each other by spacer wires (as it is in CRBRP, PHENIX, SUPER-PHENIX) or the grid structure (as it is in PFR). Even with the complete mixing of coolant in all subchannels, there is a substantial temperature and velocity distribution within the assembly. The mechanism of interchannel mixing has an important effect on the thermal design of LMFBR assemblies



because transfer of energy between subchannels results in (1) reducing local cladding hot-spot temperatures, (2) reducing cross-duct temperature difference, (3) reducing temperature differences between coolant channels and, hence, across fuel rods, and (4) alleviating subchannel flow blockage effects.

A number of computer programs are now available to predict velocity and temperature distributions within rod bundles. These include COBRA [80], THI-3D [81], ENERGY [82], COTEC [83], HAMBO [84], and THINC [85]. A brief description of these codes is noted by Tang et al [63]. Experiments with simulant fluid have been conducted to 'tune' these codes. Tests have also been conducted with electrically heated rods in sodium. It appears that the experimental data are predictable for turbulent flow conditions. For the case of laminar flows, there still exist some discrepancy between the predicted and measured values. Further discussions on this problem are included in Section 3.4.2.2.

### 3.3.5 Mixing of Coolant in Plena

For most transients of interest, the direction of coolant flow through assemblies is upward. Sodium enters the lower plenum from pipes and gets mixed with the resident sodium. Since sodium temperature does not change abruptly and the flow direction is upward, sodium in the inlet plenum may be characterized by a complete mixing model. If some or all of the assemblies were to undergo flow reversal, which is a possibility for some very severe incidences such as a massive pipe rupture in the primary sodium circuit, an adequate mixing model for the inlet plenum would also be required. Even in this case, the impact of detailed mixing treatment on system performance is not clearly established.

Mixing of the core outlet sodium in the outlet or upper plenum, on the other hand, should be treated adequately since a possibility for flow stratification exists. Detailed knowledge of sodium flow and temperature distributions is important for component designs as well as in assessing the adequacy of the natural circulation for decay heat removal. In certain designs, like CRBRP, the flow drops exponentially to approximately 10% of full flow in about twenty to thirty seconds after scram. The reactor heat generation drops almost abruptly. Therefore, the coolant entering the plenum is at a lower temperature than the bulk temperature of sodium in the plenum. This difference in sodium temperatures will lead to flow stratification when the coolant momentum is insufficient to overcome the negative buoyancy force. Figure 3.31 shows the general flow pattern for steady state and stratified conditions. Design fixes, such as chimney in the CRBRP, are provided in order to attenuate this effect.

Lorenz [86] has written a computer code, called MIX, by writing the two-dimensional continuity, momentum, and energy conservation equations in dimensionless forms and then transforming them in terms of vorticity and stream function variables. The solution of the resulting equations generally begins with a stagnant isothermal plenum. Specified inlet conditions are then imposed to generate a steady-state solution which is used in subsequent transient calculations. The computation was carried out for a 1/15-scale model test done with water. The temporal shape of the computed temperatures was found to be in reasonable agreement with the measured values [86].

Another approach, developed at Los Alamos Scientific Laboratory for the VARR-II Computer Code [87], was the numerical solution of the time-dependent turbulent, incompressible flow using the simplified marker-and-cell (SMAC) technique.

629 076

This code has been used to determine steady-state and transient thermal-hydraulic conditions in the outlet plenum for both FFTF and CRBRP designs. Agreement with experimental data is found to be similar to that found between MIX computer code predictions and measurements.

Recently, Domanus et. al. [88] have applied the COMMIX code to predict the three-dimensional temperature and velocity distributions for a 1/15-scale FFTF outlet plenum test simulation. In this test, liquid sodium was assumed to be at a uniform temperature of 754.1 K. A time-invariant liquid sodium flow of 0.3 m/s was assumed. The transient was initiated by injecting cooler sodium, hence, heavier fluid into the mixing region. The inlet sodium temperature used in the analytical studies was matched with the experimental measurements. The temperature was dropped by 57 K in about ten seconds and held at this temperature thereafter. The results of the COMMIX prediction compared with the data within  $\pm 5$  K, or  $\pm 10\%$  of the perturbation. The computing time required by this code is very high. For example, the steady state simulation alone for this problem took about two hours of computing time on an IBM 370/195 machine. It seems that the usefulness of COMMIX to this type of problem needs further examination particularly due to the large differences between the measurement and predictions.

A simplified treatment for flow stratification is essential in the overall simulation of transients in LMFBR systems. Yang [89] has developed a simplified, one-dimensional model for the SSC code. He divides the outlet plenum into two zones. The zone separation line is determined by computing the maximum jet penetration height. Within each of the two zones, a thermal equilibrium between coolant and structural material is assumed. The flow of heat through the zone boundary is also considered. The jet penetration height

is expressed in terms of Froude number,  $Fr_0$ , as:

$$z_j = 1.0484 Fr_0^{0.785} \cdot r_0, \quad (3.53)$$

where

$$Fr_0 = \frac{V^2}{g r_0 (\Delta\rho/\rho_0)}, \quad (3.54)$$

$V$  is the jet velocity,  $r_0$  is the characteristic dimension of the nozzle, and  $\Delta\rho/\rho_0$  is the fractional change in sodium density. The jet penetration height is thus seen to be dependent on the inlet flow conditions. At steady state, the jet was calculated to penetrate the entire sodium height, hence only one zone is used. During transients, the jet penetration height is computed using Equation (3.53). The formation of two zones is possible during transients. Yang [90] has applied his two-zone mixing model to predict the effective mixing volume for a number of test conditions which simulated mixing in the outlet plenum for either FFTF or CRBRP. Test results for the effective mixing volume are compared with the SSC-L model in Figure 3.32. Yang reports a good agreement between the initial jet penetration height and ANL's experimental data.

Lorenz and Howard [91] have argued that Yang's correlation be used only for the initial jet penetration height. The interface position at any time should be calculated using a modified correlation for the rise rate of interface,  $\epsilon(\equiv dz/dt)$ . The correlation for the case of a cylindrical plenum is written as:

$$\frac{\epsilon}{V} \left( \frac{R}{r_0} \right)^2 = 0.8 (Fr_0)^{1.6}, \quad (3.55)$$

where  $R$  is the plenum diameter.

Yang has applied his upper plenum mixing model to calculate sodium temperature at the outlet nozzle of the reactor vessel. He has compared his model with a two-dimensional mixing mode, MIX. In general, the two agree with each other within  $\pm 10\%$ , if not better, of the temperature perturbation, for both the constant flow rate and rapidly decreasing flow rates (typical of a reactor scram) condition. The computational time required in one-dimensional models is negligible, too. A model similar to Yang's is also in use by Jones [92]. Simplified models appear to be acceptable as long as they are checked and adjusted with experimental measurements over a wide range of conditions.

### 3.4 Heat Transfer

An accurate determination of temperature distribution in in-core assemblies such as fuel and radial blanket assemblies, is needed since they usually limit the power generated in the reactor. The temperature distribution in these assemblies as well as control and radial shielding assemblies then provide the boundary conditions for thermal analysis of reactor structural components including core support structure, upper internal structure and thermal baffles. From a detailed temperature profile, the structural analysis is conducted to determine the structural adequacy of major components. This section deals with the determination of steady-state and transient heat transfers in the LMFBR.

#### 3.4.1 Correlations

Heat transfer correlations for steady turbulent flow in channels or rod bundles are usually expressed in the following form:

$$Nu = c_1 + c_2 (\psi Pe)^{c_3} \quad (3.56)$$

629 079

where  $N_u$  ( $= hDe/k$ ) is the Nusselt number,  $c_1$ ,  $c_2$  and  $c_3$  are empirical constants,  $\bar{\psi}$  is the average effective value of the ratio of the eddy diffusivity of heat to that of momentum, and the Peclet number,  $Pe$ , is the product of the Reynolds and Prandtl numbers. The values for constants are given by Dwyer [93] for a range of conditions.

For liquid sodium flow parallel to rod bundles, Kazimi and Carelli [94] have compiled available experimental data and recommended the following correlations:

$$Nu = 4.0 + 0.33 (P/D)^{3.8} (Pe/100)^{0.86} + 0.16 (P/D)^{5.0} \quad (3.57)$$

for  $1.15 \leq P/D \leq 1.3$ ;  $10 \leq Pe \leq 5000$  ,

$$Nu = -16.15 + 24.96 (P/D) - 8.55 (P/D)^2 Pe^{0.3} \quad (3.58)$$

for  $1.05 \leq P/D \leq 1.15$ ;  $150 \leq Pe \leq 1000$  ,

$$Nu = 4.496 - 16.15 + 24.96 (P/D) - 8.55 (P/D) \quad (3.59)$$

for  $1.05 \leq P/D \leq 1.15$ ;  $Pe \leq 150$  .

Values for the Nusselt number were computed from these correlations for two values of  $P/D$  at an average sodium temperature of 700 K. Results are shown in Figure 3.33. The values of  $P/D$  were chosen to correspond to CRBRP fuel ( $P/D = 1.24$ ) and blanket ( $P/D = 1.072$ ) assemblies. It might be of interest to note that for normal operating (100% of full flow and 100% of full power) condition in CRBRP, the Peclet number for fuel assemblies range from 250 to 450, and that for blanket assemblies range from 60 to 240.

Relatively little heat transfer information is available on the in-line flow of liquid metals through square-arrayed rod bundles, presumably because

of the poorer heat transfer capabilities and less compactness of the bundle. A correlation based on heat transfer for flow of mercury and NaK is noted by Tang et. al. [63].

$$(Nu)_t = 0.48 + 0.0133 (Pe)^{0.70} \quad (3.60)$$

Free-convection heat transfer can occur when a solid surface is exposed to a volume of quiescent or slowly moving fluid, and the temperature of the surface is different from the bulk temperature of the liquid. Examples of this steady-state mode of heat transfer can be found in the fuel transfer machine and heat transport system during reactor shutdown or standby conditions. A comprehensive review of steady-state pure free convection is reported by Dwyer [93]. Recommended correlations are reproduced from Tang [63] in Table 3.13.

There are three distinct modes of free convection: creeping, laminar, and turbulent. These modes are marked by significantly different expressions for heat transfer and occur successively as the Rayleigh number - a product of Grashof and Prandtl numbers,  $\left(\frac{g\beta D^3 \Delta T}{\nu}\right)\left(\frac{C_p}{k}\right)$  - increases:

Creeping regime	$1700 \leq Ra < 3500$
Laminar regime	$3500 \leq Ra < 10^5$
Turbulent regime	$Ra \geq 10^5$

Thus, different correlations apply to various ranges of Rayleigh numbers as shown in the table.

In reactor applications, the coolant flow varies from turbulent to stagnant. Consequently, the mode of heat transfer changes from forced to free

convection. However, there are occasions in the forced-convection range when the buoyancy force due to heat addition is appreciable and its effect is superimposed on the forced-convection flow. Thus, the heat transfer mechanism becomes a combination of free and forced convections, or mixed convection, as the Grashof number increases. Heat transfer in radial blanket assemblies or in-vessel storages are examples of mixed convection in LMFBRs.

### 3.4.2 Heat Transfer Models

#### 3.4.2.1 Core Model

Almost all of the heat generated in the reactor is produced in fuel, radial blanket, control, and radial shielding assemblies. Of these, the fuel and blanket assemblies account for more than 99% of the total power. An adequate consideration of fuel and blanket assemblies, therefore, is desirable. The control and shielding assemblies, on the other hand, are not crucial in the overall heat generation and removal. Detailed temperature distribution within the control assemblies are still required in the design of control elements.

The simplest representation of in-core components is through a 'point core' model. In this model, all heat generation is approximated by a single lump or a point. Obviously, no detailed temperature distribution inside the core is possible. This model may still be helpful in overall simulation of the plant where emphasis is placed on the performance of the balance-of-plant. This approach has been used by Hetrick [95] in the BRENDA code.

The next degree of sophistication is to represent the entire core by a suitably averaged channel. In this method, axial temperature distributions in fuel, cladding, and coolant are computed for a mathematically defined average



channel. Temperature profiles in other assemblies are obtained by the use of appropriate weighting factors. For example, the 'hot' channel temperature is obtained by weighting the average channel temperature with a separately estimated hot channel factor. This method is clearly an improvement over the point core model, in that more accurate treatment for the reactivity feedback calculation is possible. IANUS [96] and DEMO [97] codes, among others, utilize this degree of sophistication. This is strictly a one-dimensional treatment.

Further sophistication in in-core treatment may be obtained by representing each and every assembly through an assembly-averaged channel. This scheme, therefore, allows for explicit treatment of 'hot', 'peak', 'average', or 'cold' assemblies. Agrawal et. al. [62,98], have used this detailed representation in their SSC code. All of the channels are hydraulically coupled through the lower and upper common pressure points (plena). The transient flow redistribution in in-vessel can also be computed. This method then allows a pseudo two-dimensional treatment.

A detailed three-dimensional treatment for flow and temperature fields across the reactor core has been attempted recently [99,100]. A key concern is to predict reliably the hexcan (duct) wall temperatures for the purpose of evaluating core restraint design. Other quantities of interest include fuel rod cladding maximum temperature and mixed-mean assembly coolant temperature. Analyses must include effects of the interassembly heat transfer as well as the intra-assembly effects. Carelli and Bach [99] have developed a computer code that is based on a cluster of seven adjacent assemblies. The hydraulic field within wire-wrapped assemblies is solved using a streamlined version of a subchannel analysis code. Once the hydraulics of each of the seven

629 083

assemblies is established, energy equations are solved simultaneously for the entire cluster. The whole core is then analyzed by scanning and changing sequentially the central, pivot assembly of the cluster. Wei [100] has also attempted to model the whole core. Although the mechanics of detailed calculations are somewhat different, his results agree favorably with those obtained by Carelli and Bach.

#### 3.4.2.2 Rod Bundle

It was noted earlier that LMFBR assemblies consist of closely-packed rod bundles. Analytical studies of heat transfer in rod bundles have been pursued along two separate paths - distributed parameters and lumped parameter methods [63]. In lumped parameter methods, often referred to as subchannel analyses, the rod bundle is divided into a number of subchannels whose boundaries are defined arbitrarily by surfaces of fuel elements and imaginary lines between elements and/or duct walls. Average subchannel parameters are evaluated by solving equations of continuity, momentum, and energy for each subchannel increment. Equations for each subchannel are coupled with those of its neighbors by interchannel transport of mass, momentum and energy which is treated in terms of integral transport coefficients. Distributed parameter methods solve time averaged Reynolds equations of momentum and energy transport for velocity and temperature distributions. These methods provide detailed information about thermal characteristics of an idealized array of fuel elements cooled by parallel flow, but have fallen short of providing overall power distribution and thermal behavior of entire fuel assemblies with spacers. Because of numerical and computer complications, as well as the lack of knowledge of local Reynolds shear stresses and turbulent heat fluxes in various

directions, application of distributed parameter methods has been rather restricted. Results of the distributed parameter method can be used to evaluate integral parameters to feed into lumped parameter analysis.

There now exist a number of computer codes which perform the steady-state subchannel analysis for wire-wrapped bundles. Tang et. al. [63], have compared them and their compilation is shown in Table 3.14. Of interest are comparisons of results obtained from several of these codes. By using a typical, identical configuration and steady-state conditions, fairly good agreement is obtained between predictions of fuel assembly temperatures. For a typical fuel assembly peak subchannel coolant temperature of 872 K, a difference of less than 6 K is found. Peripheral subchannel coolant temperatures in the range of 755 to 811 K differ by less than 17 K. On the other hand, comparisons for radial blanket prediction show rather poor agreement among these codes. Peak subchannel coolant temperature (867 K) predictions differ by as much as 33 K; peripheral coolant temperatures differ by as much as 94 K. To reduce large uncertainties in these code predictions, experiments have been performed to simulate the steady-state temperature distributions in blanket assemblies for a number of power factors and flow rates. Markley and Engel [108] have reported their measurements for a 61-rod bundle with dimensions typical of CRBRP blanket assemblies. The data were obtained over a wide range of operating conditions which include a power skew ranging from flat to about 3 to 1 between extreme pins and a Reynolds number ranging from 490 to 7300. The 1.14-m long heater zone and axial cosine power distribution was representative of the active blanket rod length. Coffield et. al. [109] have used COBRA IV, COTEC and ENERGY computer codes to analyze these data. Their results are shown in Figures 3.34-3.36. The radial power distributions are

also indicated on these figures. The test data and the results of calculations are shown for several axial locations. A comparison of the data clearly indicates that although the power skew and the power-to-flow ratios for these runs are nearly equal, a relative flattening of the radial temperature distribution occurs at lower Reynolds number. This flattening of temperature traverses is predominantly due to energy redistribution by thermal conduction and buoyancy induced flow redistribution.

Coffield et. al. [109] have also compared the results obtained from analysis of the low flow 217-pin Hanford Engineering Development Laboratory data and ORNL 19-pin data. The two runs compared have nearly identical power skew and operating conditions. It was found that at the low flow conditions ( $Re \sim 1000$ ), there is almost a complete flattening of the temperature profile across the assembly even though a steep (1.7:1 for maximum to average) radial power skew exists across the assembly.

The steady state analyses for rod-bundles have also been performed for a safety-related event in which a planar blockage in the heated region was postulated. Han [110] has recently reviewed both the experimental and analytical aspects of partial blockage in a fuel assembly. Recently, Sha et. al. [111] have applied their COMMIX code to analyze a blockage condition in a 19-pin bundle. It appears that the existing analytical tools for blockage studies are adequate.

Most of the computer programs noted in Table 3.14 provide for transient thermohydraulic analysis in multichannel geometry. Perhaps the most widely used program is the COBRA series of code. Many of these codes have been applied to a number of rod-bundle tests, with a varied degree of success. The agreement with measurements is, in general, good (adequate) for fully-developed

629 086

turbulent flows. The comparison begins to be less than adequate as the flow rate is dropped to very low Reynolds number. The flow field changes from turbulent to transition to laminar flow regimes. Such a change is experienced in the blanket assemblies much before the fuel assemblies.

Lately, the research emphasis has been changed from further refinement of subchannel analysis for a single assembly to modeling of a cluster of assemblies. The concern here is to calculate the effect of interassembly heat transfer at both steady state and transient conditions.

### 3.4.2.3 Heat Conduction in a Rod

The heat conduction equation, in cylindrical coordinates, can be written as

$$\rho c \frac{\partial T}{\partial t} = \frac{1}{r} \frac{\partial}{\partial r} \left( kr \frac{\partial T}{\partial r} \right) + \frac{\partial}{\partial z} \left( k \frac{\partial T}{\partial z} \right) + q''' \quad (3.61)$$

where  $q'''$  is the volumetric heat generation rate, and azimuthal symmetry around the axis of the cylindrical rod is assumed. This assumption implies that eccentricity of fuel pellets is small and neglected. A further simplification results if the axial conduction term can be neglected. The following example will illustrate the validity of this simplification.

Consider a simplified steady-state model [63] in which there is uniform axial power generation, fuel thermal conductivity and gap conductance are constant. Under these conditions and neglecting axial conduction, the fuel temperature difference with axial position would only be due to coolant temperature rise. Thus, the ratio of heat flowing radially from fuel surface ( $Q_r$ ) to that occurring from axial conduction ( $Q_z$ ), if the latter were not

629 087

neglected, would be

$$\frac{Q_r}{Q_z} = \frac{T(0,z) - T(r_o,z)}{\Delta T_c} \left(\frac{2H}{r_o}\right)^2 \quad (3.62)$$

where  $T(0,z)$  and  $T(r_o,z)$  are fuel temperatures at the center and surface, respectively, and  $\Delta T_c$  is the temperature rise of the coolant over height  $H$  of the fuel element. The temperature drop between the center and surface of the fuel element, in the case of oxide fuel, is considerably greater than the temperature rise of coolant in the core. Also, the height of a fuel element is several hundred times greater than its radius. Thus, the radial heat conduction is greater than the axial conduction by several orders of magnitude. Hence, for oxide fuel, the axial conduction can be neglected. For metal or sodium-bonded carbide fuels, the axial conduction is not as negligible.

For a solid cylindrical fuel rod with uniform heat generation at steady state, Equation (3.61) can be integrated to yield

$$\int_{T_s}^{T_c} k(T) dT = \frac{q'}{4\pi} \quad (3.63)$$

where the axial heat conduction was neglected,  $T_s$  and  $T_c$  are fuel temperatures at the surface and center, respectively, and  $q'$  is the linear power generation rate (W/m). This equation demonstrates that for a constant linear heating rate and a constant pellet surface temperature, the centerline temperature is independent of rod diameter. Fenech and Rohsenow [112] have noted forms for this integral for slabs, hollow cylinder and for non-uniform heat generation cases.

In order to perform representative calculations for temperature distributions in fuel, cladding and coolant an equivalent channel is defined by

surrounding the fuel rod with an equivalent, concentration of flowing sodium. The fuel rod heat conduction equation is then coupled, via boundary condition, with the coolant heat transport equation. Once again, the axial heat conduction in sodium can be neglected as demonstrated by Meyer [64]. He calculated the ratio of heat convected to heat transfer by conduction for selected core subcomponents in CRBRP operating at its nominal condition. Results are shown in Figure 3.37. The axial conduction is considered negligible if the Peclet number is equal to or greater than 50. It is seen from this figure that the axial condition is negligible not only when CRBRP is operating at its nominal (100% power, 100% flow) conditions but even when the coolant velocity is reduced by three orders of magnitude. The magnitude of axial conduction effects for this reduced flow will still be less than 2%.

Sample calculations for axial temperature distribution in an average fuel channel can now be readily performed. Figure 3.38 shows a typical temperature distribution along an average fuel channel in CRBRP. The sharp discontinuities at the interfaces between active core and blanket regions result from discontinuity in the axial power shape. Although the neutron flux is continuous at the interfaces, this discontinuity in power distribution is due to sudden change in fuel isotopic compositions between the core and blanket materials. It should be added that if axial conduction were incorporated, the predicted discontinuity in temperature would not be seen. The temperature will, nevertheless, still show a large change at the interfaces.

The mixed-oxide fuel is known to undergo densification or restructuring when irradiated in the fast flux, such as in LMFBRs or GCFRs. Figure 3.39 shows a cross-sectional view of a fuel pellet (20%  $\text{PuO}_2$ , 80%  $\text{UO}_2$  by weight) that was subjected to a power level between 37 to 44 kW/m and a cumulative

629 087

burnup of about 11% [113]. There seems to be a number of regions formed: (1) central void, (2) a columnar grain growth zone where the fuel density is equal to 99% TD, and (4) an unrestructured or outer zone of essentially initial or as-fabricated density. A major impact of this densification is that the fuel thermal conductivity improves substantially. Figure 3.40 shows the thermal conductivity of mixed-oxide fuel for unrestructured, equiaxed and columnar grain growth regions. Zone interface temperatures of 2273 K and 1873 K between the columnar and equiaxed, and equiaxed and unrestructured zones, respectively, were used. This improvement in thermal conductivity due to restructuring allows the maximum linear power rating to be increased from those obtained for an assumed uniform fuel density. The maximum linear power attainable, without fuel restructuring, by requiring peak and outer surface fuel temperatures of 3000 K and 870 K, respectively, is 55.9 kW/m. This value increases to 62.9 kW/m when fuel restructuring is considered. An implication of the fuel restructuring is that it provides an added margin of safety. The gap conductance between the fuel pellet and the cladding plays a major role in establishing actual temperature levels in the fuel pellet at steady state. During transients, the gap conductance determines the heat flux into the coolant. The magnitude of the gap conductance depends upon the bonding or fill agents as well as its size. In oxide-fueled LMFBRs, the gap is filled with gases such as argon and fission product gases that get released during reactor operation. The gap width varies over a wide range from essentially as-fabricated to almost negligible near core midplace. Furthermore, during transients the gap may close or widen. The gap conductance, therefore, should be computed for two cases: finite gap size and the closed gap.

629 099



For the case of finite gap size, heat can be transported across the gap by (1) conduction through the mixture of fill and fission gases, (2) thermal radiation between the outside surface of fuel and the inside surface of cladding, and (3) free convection of the gases in the gap. The heat transfer via free convection is negligible and generally neglected. Thus,

$$h_{\text{gap}} = h_{\text{cond}} + h_{\text{rad}} \quad (3.64)$$

where,

$$h_{\text{cond}} = \frac{k_{\text{mix}}}{\Delta r_{\text{gap}}} \quad (3.65)$$

There are several correlations to calculate the thermal conductivity of a mixture of gases. A simple empirical equation is given by Brokaw [114]:

$$k_{\text{mix}} = 0.5 \sum_{i=1}^N x_i k_i + \frac{1}{\sum_{i=1}^N x_i / k_i} \quad (3.66)$$

where  $x_i$  is the mole fraction and  $k_i$  is the thermal conductivity of the  $i$ -th constituent.

Another prescription for calculating  $h_{\text{cond}}$  is given by Biancheria et al [115]:

$$\frac{1}{h_{\text{cond}}} = \frac{2-a}{a} \cdot \frac{1}{C_p + C_v} \cdot \frac{9C_p - 5C_v}{2} \cdot \frac{\lambda}{k_{\text{mix}}} + \frac{\Delta r_{\text{gap}}}{k_{\text{mix}}} \quad (3.67)$$

where  $\lambda$  is the mean-free path of the gas and  $a$  is the accommodation coefficient (typically 0.05).

The radiative heat transfer coefficient can be written as [62]:

$$h_{\text{rad}} = \bar{\epsilon} \sigma (T_f^3 + T_f^2 T_c + T_f T_c^2 + T_c^3) \quad (3.68)$$

629 091

where

$$\frac{1}{\bar{\epsilon}} = \frac{1}{\epsilon_f} + \frac{r_f}{r_c} \left( \frac{1}{\epsilon_c} - 1 \right) . \quad (3.69)$$

$\sigma$  is the Boltzmann constant,  $\epsilon$  is the emissivity, and subscripts c and f denote, respectively, the inside cladding and outer fuel surface.

When the fuel pellet expands sufficiently to be in direct contact with the cladding, an improved gap conductance, also termed as contact conductance, results. For all practical purposes, a contact is assumed when the idealized, axisymmetric gap size is reduced to 5 to 10  $\mu\text{m}$ . The magnitude of the contact conductance, understandably, is a function of surface roughness, hardness and contact pressure. Some experimental and theoretical studies have been made and reported by Jacobs and Todreas [116].

#### 3.4.2.4 Structural Materials

There exist a large body of masses of structural materials such as core support structure, reactor vessel, thermal baffles, pump housing, check valves etc., that are in contact with liquid sodium. Temperatures in these structural materials change due primarily to heat transfer from the coolant or, in cool-down transients, by loss of heat to the coolant. For those components that are closer to the reactor core, there could be substantial internal heating due to gamma-ray attenuation. Since most structural materials have complicated geometry, the temperature distribution within the structure has to be obtained by solving the general heat conduction equation:

$$\rho c \frac{dT}{dt} = \nabla \cdot (k \nabla T) + \dot{q}''' \quad (3.70)$$

629 092

for the particular geometry involved. In order to solve this equation, the boundary conditions on the surface of the body must be defined. This often entails analysis of the entire reactor system. For simple geometrics, such as for thermal baffles, Equation (3.70) may be solved in one spatial dimension. The boundary conditions may be imposed explicitly. For complex problems, a general purpose multi-dimensional (two or three) in spatial coordinates may have to be used to obtain temperatures. These temperature distributions can then be used in structural analysis.

#### 3.4.2.5 Time-Dependent Conservation Equations for Coolant

In transient flow calculations, coolant velocities vary with time and position. With the addition of time as an independent variable, the solution of fluid flow problems are much more difficult. The governing conservation equations of continuity, momentum and energy for single-phase fluid flow in one dimension in space coordinates along the direction of bulk flow are [117]:

$$\frac{\partial \rho}{\partial t} + \frac{1}{A} \frac{\partial W}{\partial x} = 0 , \quad (3.71)$$

$$\frac{1}{A} \frac{\partial}{\partial t} \left( \frac{W}{\rho} \right) + \frac{W}{\rho A^2} \frac{\partial}{\partial x} \left( \frac{W}{\rho} \right) + \frac{1}{\rho} \frac{\partial P}{\partial x} + g \frac{\partial z}{\partial x} + \frac{f}{D_e} \frac{W|W|}{2\rho^2 A^2} = 0 , \quad (3.72)$$

$$\frac{\partial}{\partial t} (\rho h - P) + \frac{1}{A} \frac{\partial}{\partial x} (Wh) = \frac{\partial q}{\partial y} \quad (3.73)$$

where  $W$  is the coolant mass flow rate (kg/s),  $h$  is the coolant enthalpy (J/kg),  $D_e$  is the equivalent diameter (m),  $A$  is the cross sectional area (m<sup>2</sup>),  $q$  is the heat transfer rate in the  $y$  direction (W), and other variables have

629 093

their standard meanings. These equations, when coupled with initial boundary conditions, yield the variation of the pressure  $P(x,t)$ , mass flow rate  $W(x,t)$ , and enthalpy  $h(x,t)$  at a position  $x$  and time  $t$ .

It should be noted that Equations (3.71) to (3.73) neglect the variation of fluid properties, velocity, and pressure in the direction normal to the bulk flow direction. In practical applications, such as the application to a multichannel nuclear reactor, the pressures at the inlet and exit common points (plena) are either specified or are desired as a function of time. These pressures can be related to the pressure just inside the channel inlet and the pressure just inside the channel exit by accounting for pressure losses due to friction, expansion or contraction, as the case may be, and the static head, if any. These factors have been discussed earlier in Section 3.3.2. For Two-phase flow systems, which is not likely to occur in any anticipated operating mode for LMFBRs, Equations (3.71) to (3.73) are valid if the mixture can be approximated as homogeneous. Readers are referred to more detailed treatises such as Wallis's book [118] for detailed discussions on two phase models.

In order to solve the governing conservation equations, various numerical and physical approximations are often necessary [66]. The degree of simplification introduced and the type of model used in the calculations depend on the type of transient under consideration. For very fast transients, a multi-node compressible model is employed to obtain a finite difference solution to the controlling equations. For fast transients, a momentum integral model and a channel integral model may be used. In these models, an integrated (over the spatial coordinates) form of the momentum equations is used. For intermediate or slow transients, further simplification may be made by neglecting the

629 092

variation of flow with  $x$ . In other words, a single mass velocity model is employed. This single mass velocity model can effectively be used to model flow of liquid sodium in the entire primary and intermediate heat transport systems. More detailed discussions regarding the model selection are given in Section 6.

#### 3.4.2.6 Cover Gas

In LMFBRs, an inert cover gas (usually argon) is used between free sodium surfaces and structural closures and seals. The most significant presence of the cover gas is in the reactor vessel itself. An accurate calculation of the cover gas temperature is essential in determining its pressure which is used as a reference point.

The temperature calculations for the cover gas in the reactor vessel is best accomplished through a unified model for liquid sodium, structure and the cover gas. The heat transfer between different metal surfaces as well as liquid sodium, must be allowed. Such a calculation may be done by writing down an energy conservation equation such as

$$(\rho Vc)_g \frac{dT_g}{dt} = U_{gl} A_{gl} (T_l - T_g) + U_{gm} A_{gm} (T_m - T_g) \quad (3.74)$$

If more than one metal piece is in contact with the gas, the second term on the right hand side of Equation (3.74) will include a summation for all such metals.

There may be different control features provided for the cover gas system. In mathematical terms there is either a constant pressure model or a constant volume model. In the first case, the cover gas pressure is maintained from external on-line system. The second case, on the other hand, assumes no connection with the external gas supply system.

629 095

The effect of heat transfer to cover gas is insignificant on transient sodium temperatures for all operational events. For a pipe rupture accident, the effect of heat transfer to cover gas can be significant primarily through the pressure level of the gas which affects the coolant discharge rate through the break.

629 096

## 4. INTERMEDIATE HEAT EXCHANGER

### 4.1 Description

The Intermediate Heat Exchanger (IHX) transfers the thermal energy of the reactor from the radioactive primary sodium to the nonradioactive secondary sodium. The IHX and the complete secondary system, serve as a physical barrier between the radioactive coolant and the tertiary fluid system (normally water-steam). A detailed review of the evaluation of heat-exchanger design has been made by Muller and Schnauder [10]. In this section, only a brief review is made with particular emphasis on the factors interrelating the IHX with the overall reactor heat removal system in both loop and pool reactor concepts. Dynamical models required for the simulation of transients in the IHX are also discussed.

#### 4.1.1 Design for the Loop Concept

In the loop concept the primary sodium is piped in a closed circuit between the reactor vessel and an external heat exchanger. The relative elevation (with respect to the reactor core), and coolant pressure drop inside the IHX and heat transport circuit influence the decay heat removal capabilities during natural circulation cooling.

The primary coolant can be routed through either the shell or tube side. In standard heat exchanger designs and applications, it is common practice to place the more viscous fluid, having lower Reynolds number on the shell side [119]. Since liquid metal viscosities at LMFBR operating temperatures are low, the differential pressure between the primary and the secondary loops is a more significant effect that must be considered. In order to minimize flow

induced vibrations the higher pressure fluid is used in the tube side of the IHX [120].

Figure 4.1 shows a typical shell and tube IHX [15] for a loop-type LMFBR. It is a vertically mounted straight tube design. The directions of the two sodium flows are arranged to take benefit of natural circulation effects. Thus, the primary sodium flows downward on the shell-side and the secondary sodium flows upward inside the tubes. The tube bundle is arranged in a triangular array inside an annular region. Flexible bellows allow free-thermal expansion in the axial direction. Primary sodium enters the IHX through one nozzle located approximately at the midpoint along the height, and exits through a bottom nozzle. A small fraction of the primary sodium bypasses the tube bundle and flows downward inside the IHX shell, but outside the outer shroud, to limit the thermal stresses in the shell. Secondary sodium enters and exits the IHX through nozzles located at the upper end.

#### 4.1.2 Design for the Pool Concept

In the pool or pot concept the IHX is either connected to the reactor vessel directly (hot pool concept)[4], as in the PHENIX reactor [10], or through a connecting pipe (cold pool concept) [121]. The low primary system pressure drop and pumping powers lead to better natural convection coolant circulation in pool designs (see Section 5.1).

Configuration of the intermediate heat exchangers for the pool-type LMFBRs predicates primary coolant flow through the shell side, while in some designs the primary sodium flows through the tubes of IHX (e.g., PFR) [10]. If the problem of tube vibrations induced by the higher pressure coolant on the shell side is somehow remedied, it will be desirable for more uniform flow distribution to use the higher pressure secondary coolant on the shell side.



Figure 4.2 shows an IHX for a pool type LMFBR [121]. The heat exchanger is a single-pass, shell and tube model. The primary sodium enters at the top of the tube bundle, flows down around the tubes, and discharges at the bottom into the pool. The secondary sodium from the steam generating system flows down through the downcomer and into an inlet plenum at the bottom of the exchangers, where it turns and flows back up inside the tubes. Thus, this configuration is similar to the loop-type design. However, since the cylindrical housing is immersed in the sodium; thermal stresses and cycling is minimized and this eliminates the need for the bypass sodium flow as is normally required in the loop-reactor concept. Table 4.1 lists some important thermal design characteristics for some of the existing loop and pool-type LMFBR heat exchanger designs. In all of these designs, the tube bundle is arranged in a triangular pitch with pitch-to-diameter ratio between 1.30 to 1.50. For reasons noted above the primary sodium, which is always at a pressure lower than the secondary coolant is allowed to flow in the shell side, except for the PFR.

#### 4.2 Dynamical Model

Transient thermohydraulic performance of the loop-and pool-type LMFBR intermediate heat exchangers can be predicted from (a) theoretical calculations, (b) experimental measurements, or (c) theoretical calculations supported by experimental data.

To date, the theoretical models have not been able to adequately predict the actual condition, simply because of the multidimensional processes which are caused by geometric complexities in the heat exchanger. Sodium flow maldistribution on the shell side of the IHX especially under low flow, natural convection, or extreme turbulent nature of the flow are phenomena that do not

629 099

lend themselves easily to simple hydrodynamic analysis; on the other hand, purely experimental analysis is not feasible, hence semi-empirical modeling has proven to be the most reliable approach.

A wealth of performance and post-operative information available for many existing LMFBR heat exchangers seems to support the above contention. For example, the SRE heat exchanger was designed to transfer 20 MW(t) at a flow rate of 61 kg/s. Approach to full-power operation of the reactor permitted a variety of tests to be performed and analyzed before full-power operation of the plant [124]. Experimental data indicated that, during early low-power tests on the SRE reactor the main IHX was not functioning according to design specifications, the steady-state, log-mean temperature difference was approximately 42% higher than the predicted value. In addition, during a scram in which the power and flow rate were reduced to below 5% of the pre-scram level, this same temperature difference was observed to increase by as much as 90%, and the secondary temperature gradient collapsed at a very rapid rate. Similar performance problems were observed with the Fermi IHXs [125]; and among some of the possible causes, shell side sodium flow maldistribution and fouling of the tubes with sodium impurities were proposed. Therefore, it is apparent that the best approach for treatment of thermohydraulic transients in the IHX during normal and off-normal conditions is the semi-empirical methods.

Thermal simulation of the intermediate heat exchangers has utilized two models: (1) a lumped parameter single-tube model, and (2) a detailed multi-channel model. The lumped parameter single-tube model, assumes that all heat transfer tubes in the heat exchanger behave similarly and are treated as an average tube, allowing the energy equation to be applied to a single tube in many axial locations in the coolant flow direction [62,95,96,97,126]. It

629-100

neglects the heat transfer effect of stagnant sodium between the shell and the outer shroud, and all material elements other than the heat transfer tubes. In contrast, the detailed model simulates all material elements and various fluid channels present in the heat exchanger, and provides a complete temperature map of various elements of the IHX during the transient [127,128]. Aburomia, et al., [127] concluded that the lumped parameter single tube model and the detailed model yield approximately the same transient fluid temperature distribution, except under very low flow rate conditions. Under these low flow conditions, it is believed that the total heat stored within the IHX elements attenuates the abrupt changes of the entering fluids, which the lumped parameter single tube model does not represent very well.

The single-tube model can be improved by formulating several parallel channels and applying appropriate flow maldistribution factors to account for sodium flow maldistribution during low flow conditions.

The effect of heat transfer due to molecular conduction, turbulent thermal diffusion, and forced fluid mixing caused by shell side flow baffles has been studied by Aburomia, et al., [129]. Figure 4.3 shows that the effect of molecular conduction and turbulent thermal diffusion among various flow channels on the temperature distribution is small, and it is only significant near the edges of the tube bundle; also shown is the effect of sodium flow maldistribution which tends to aggravate the radial thermal imbalance among the heat transfer tubes. Forced fluid mixing, on the other hand, is shown to be an effective mechanism in reducing this thermal maldistribution.

The radial flow and temperature maldistribution across the IHX tube bundle is not normally of great importance in large system studies; since the IHX average outlet temperatures have the greatest impact on the overall prediction.

629 101

### 4.3 Lumped-Parameter Model

The application of partial differential form of the energy equation to a single average IHX tube represents the lumped parameter approximation.

The differential equation describing the thermal state of the sodium flow in the heat exchanger can be written as:

$$\rho \frac{\partial h}{\partial t} + \rho u \frac{\partial h}{\partial x} = \frac{\partial q''}{\partial y} \quad (4.1)$$

where  $\rho$  is the sodium density,  $h$  the sodium enthalpy,  $u$  the sodium velocity and  $q''$  is the heat flux in the radial direction. In deriving Equation (4.1) it was assumed that sodium is incompressible, also axial conduction and viscous dissipation terms are negligible.

In order to achieve separation of variables, various approximations for coolant enthalpy distributions are made. They include:

Nodal Heat Balance - In this approximation, the tube and shell wall nodes are placed in the midplane between the corresponding coolant nodes, giving rise to a staggered nodal arrangement as shown in Figure 4.4.

The coolant energy equation (Equation 4.1) can be simplified by representing the convective term in a backward difference approximation, where:

$$\frac{\partial h}{\partial x} \approx \frac{h_J - h_{J-1}}{\Delta x} + O(\Delta x) \quad (4.2)$$

The spatial increment  $\Delta x$  must be taken sufficiently small to insure that the higher-order terms remain negligible.

62° 10'

Therefore, the integrated form of the partial differential equation reduces to the following ordinary differential equation:

$$\rho_J V_J \frac{dh_J}{dt} = W(h_{J-1} - h_J) + q_J, \quad (4.3)$$

where

$V_J$  = nodal volume, ( $m^3$ ),

$W$  = sodium mass flow rate, (kg/s),

$\rho u A$ , and

$q_J$  = the heat transfer rate, (W/s).

In deriving this expression it was further assumed that the rate of change of enthalpy,  $h$ , in the node is directly related to the rate of change of enthalpy at the outlet, that is:

$$\frac{dh}{dt} \approx \frac{dh_J}{dt} \quad (4.4)$$

Finite Differencing Techniques - In this approach, the coolant and solid-wall material nodes are placed in parallel. The convective term in the energy equation can be represented by the following approximations:

1. Two-point backward difference:

$$\frac{dh}{\Delta x} \approx \frac{h_J - h_{J-1}}{\Delta x} \quad (4.5)$$

2. Three-point backward difference:

$$\frac{\partial h}{\partial x} \approx \frac{3h_J - 4h_{J-1} + h_{J-2}}{2\Delta x} \quad (4.6)$$

629 103

3. Central difference:

$$\frac{\partial h}{\partial x} = \frac{h_{J+1} - h_{J-1}}{2\Delta x} \quad (4.7)$$

4. Mixed difference:

$$\frac{\partial h}{\partial x} = \frac{h_{J+1} - h_{J-1}}{2\Delta x} \quad \text{for even number of nodes,} \quad (4.8)$$

$$\frac{\partial h}{\partial x} = \frac{3h_J - 4h_{J-1} + h_{J-2}}{2\Delta x} \quad \text{for odd number of nodes.} \quad (4.9)$$

The mixed difference approximation can be applied only when an even number of axial nodes is being used.

Gunby [130] simulated an intermediate flow coastdown transient in the tube side. His results are shown in Figure 4.5. It is apparent that the nodal heat balance and mixed difference model behave almost identically, while a considerable deviation is observed by other methods. Therefore, it is recommended to use the nodal heat balance method, since it is least dependent on the differencing technique; and its results improve as the number of nodes is increased.

The following is a complete set of nodal heat balance equations for the simulation of an LMFBR heat exchanger:

Shell-Side Sodium

$$\left[ \rho_s V_s \frac{dh_s}{dt} \right]_J = W_s (h_{s_{J-1}} - h_{s_J}) - q_{1J} - q_{2J} \quad (4.10)$$

629 104

Tube Side Sodium

$$\rho_t V_t \frac{dh_t}{dt} = W_t (h_{t_{J-1}} - h_{t_J}) + q_{3J} \quad (4.11)$$

Vessel (Shell) Structure

$$\rho_v V_v C_v \frac{d\bar{T}_v}{dt} = q_{1J} \quad (4.12)$$

Tube-Wall Structure

$$\rho_w V_w C_w \frac{d\bar{T}_w}{dt} = q_{2J} - q_{3J} \quad (4.13)$$

where  $C_v$  and  $C_w$ , respectively, are the vessel and tube-wall structure heat capacities,  $\bar{T}_v$ , and  $\bar{T}_w$  are vessel and tube wall average temperatures, respectively, and  $q_{1J}$ ,  $q_{2J}$  and  $q_{3J}$  are the heat transfer rates. These can be calculated as follows:

$$q_{1J} = U'_1 (\bar{T}_s - \bar{T}_v)_J \quad (4.14)$$

$$q_{2J} = U'_2 (\bar{T}_s - \bar{T}_w)_J \quad (4.15)$$

$$q_{3J} = U'_3 (\bar{T}_w - \bar{T}_t)_J \quad (4.16)$$

where:

$$\bar{T}_{sJ} = \frac{T_{sJ} + T_{s_{J-1}}}{2},$$

$$\bar{T}_{tJ} = \frac{T_{tJ} + T_{t_{J-1}}}{2},$$

629-105

and the heat transmission coefficients (W/k) are given as,

$$U'_1 = \frac{A_v}{r_1 + r_2},$$

$$U'_2 = \frac{2\pi n \Delta X}{r_3 + r_4},$$

$$U'_3 = \frac{2\pi n \Delta X}{r_5 + r_6},$$

$A_v$  is the vessel structure heat transfer area,  $r_i$  is the thermal resistance of the  $i$ -th layer, and  $n$  is the number of tubes.

The thermal resistances are defined as follows:

$$r_1 = \frac{\delta_v}{2k_v} \tag{4.17a}$$

$$r_2 = \frac{1}{h_{f_1}} \tag{4.17b}$$

$$r_3 = \frac{2}{(D_i + 2\delta_w)h_{f_2}} \tag{4.17c}$$

$$r_4 = \frac{\ln \left[ \frac{D_i + 2\delta_w}{D_i + \delta_w} \right]}{k_w} \tag{4.17d}$$

$$r_5 = \frac{\ln \left[ \frac{D_i + \delta_w}{D_i} \right]}{k_w} \tag{4.17e}$$

$$r_6 = \frac{2}{D_i h_{f_2}}$$

629 106



where  $\delta_v$  is the half thickness of the vessel shell,  $k_v$  is the vessel wall thermal conductivity,  $h_{f_1}$ ,  $h_{f_2}$  are the surface heat transfer coefficients (see the following section),  $D_i$  the tube inside diameter,  $\delta_w$  the tube wall thickness, and  $k_w$  is the tube wall thermal conductivity.

It is important to note that the assumption of linear enthalpy and temperature distribution within a nodal volume may fail under very abrupt transient conditions, thus requiring extremely small nodal size, which can lead to excessive computer time requirements. There are two alternative solutions to this problem:

1. Logarithmic Mean Temperature Difference Alternative - In this approach, the effect of tube wall heat capacity is assumed to be small and is, therefore neglected, leading to the following approximation:

$$q_{2J} \approx q_{3J} = U_T^i \Delta T_{\ell m J} \quad (4.18)$$

where the logarithmic mean temperature difference is defined as [129]:

$$\Delta T_{\ell m J} = \frac{(T_s - T_t)_J - (T_s - T_t)_{J-1}}{\ln \left[ \frac{(T_s - T_t)_J}{(T_s - T_t)_{J-1}} \right]}, \quad (4.19)$$

and  $U_T^i$  is the overall transmission coefficient given by:

$$U_T^i = \frac{2\pi n \Delta X}{\sum_{i=3}^6 r_i} \quad (4.20)$$

In case of cross-flow and a combination of cross-flow and counter-current designs a correction must be introduced in the logarithmic mean temperature difference:

$$(\Delta T_{\ell m})_{\text{cross-flow}} = \epsilon (\Delta T_{\ell m})_{\text{counter-flow}} \quad (4.21)$$

629-107

where  $\epsilon$  is a "correction factor" and is a function of the terminal fluid temperatures and exchanger arrangement and can be found in the literature [131]. The log-mean temperature difference approximation remains valid so long as the time constant of the tube wall is much smaller than the transient time scale. This has been shown to yield satisfactory results with limited number of nodalization in the IHX [126].

2. Nonuniform Nodalization Alternatives - In this approach, the effective heat transfer length is divided according to the sodium temperature behavior in both shell and tube sides of the exchanger, that is, more nodes are placed where the highest temperature nonlinearity exists and a smaller number of nodes are placed where the temperature distribution is fairly linear.

Figure 4.6 shows the steady state temperature distribution for the CRBRP intermediate heat exchanger. It is seen that at steady state the temperature distributions are fairly linear and pose no difficulty. Also shown in Figure 4.6 is a distorted temperature distribution (dashed lines) for the intermediate side which can occur under certain transient conditions (secondary flow coastdown). It is seen that most of the heat is transferred at the bottom, where the highest temperature nonlinearity exists.

The thermal resistance of any material deposited on the surface of the tube caused by mass transport or the presence of impurities in the coolant can be easily incorporated into the overall heat transmission coefficients by additional resistances. Normally this effect can be neglected, but, with the trend toward higher reactor outlet coolant temperatures, the surface buildup rate caused by material removal from the hotter surfaces and deposition on the colder ones may become quite significant [126].

629 10R

#### 4.3.1 Heat Transfer Coefficients

The film heat transfer coefficient,  $h_f$ , is usually determined from the Nusselt number  $Nu$ :

$$h_f = \frac{k_f}{D} Nu \quad (4.22)$$

where  $k_f$  is the fluid thermal conductivity at average bulk temperature, and  $D$  is the tube inside diameter or thermal equivalent diameter for fluid flowing inside and outside of the tube, respectively.

Since turbulent and laminar flow in circular tubes arises in many types of heat exchange equipment, these types of transfer processes have been studied in detail. Many expressions have been presented in attempts to summarize, quantitatively, the various influences to which such processes are subject. The convection coefficient, combined into a Nusselt number (Equation 4.22), depends upon the flow Reynolds number, the tube-wall roughness, the fluid Prandtl number, any density variation due to pressure drop and temperature change, transport-property variations due to temperature differences, and the relative length of the tube ( $L/D$ ).

For fully developed turbulent flow, that is, in long tubes (or far from the tube inlet) a number of correlations have been suggested. Table 4.2 lists some of the widely used Nusselt number correlations for round tubes, with uniform heat flux at the wall.

For developed laminar flow through the tubes with uniform heat flux at the wall the following equation is suggested [136]:

$$Nu = 48/11 \approx 4.36 \quad (4.23)$$

629 109

For undeveloped laminar flow, Sieder and Tate [130] suggested the following relation:

$$\text{Nu}_m = 1.86 \left(\frac{D}{L}\right)^{1/3} \left(\frac{\mu_m}{\mu_w}\right)^{0.14} (\text{Re} \cdot \text{Pr})^{1/3} \quad (4.24)$$

where  $h_f$  is based upon average of the inlet and outlet temperature differences and the properties are evaluated at the average fluid temperature. This relation is in close agreement with Equation (4.23) for  $\text{Re} \cdot \text{Pr} \frac{L}{D} > 10$ . This last condition excludes extremely large nodal lengths, for which a logarithmic temperature difference must be used to define  $h_f$  [130].

Heat transfer for turbulent flow in noncircular passages has been studied for many tube geometries. In passages, where the flow geometry is not drastically different from circular tubes, the concept of equivalent diameter is applied. For such a passage the velocity and temperature distribution may be assumed to be developed if  $L/D > 30$  [130].

The most common types of tube arrangements are the equilateral triangular pattern, and the square array. Such arrangements are shown in Figure 4.7 where;  $r$  and  $r_m$  are the inner and maximum-velocity radii.

It is shown [93] that for a triangular arrangement:

$$\frac{r_m}{r} = \sqrt{\frac{2\sqrt{3}}{\pi}} (P/D)_{t.a.} \quad (4.25)$$

and for a square array:

$$\frac{r_m}{r} = \frac{2}{\sqrt{\pi}} (P/D)_{s.a.} \quad (4.26)$$

629 110

Further comparisons of these two equations at the same value of  $r_m/r$ , results in,

$$(P/D)_{t.a.} = 1.075 (P/D)_{s.a.} \quad (4.27)$$

Therefore,  $1.075 (P/D)_{s.a.}$  can be substituted for  $(P/D)$  in Nusselt number correlations shown in Table 4.3 to make them applicable to square arrays.

The effect of baffles can be considered by including the cross flow of liquid metal through the rod banks. The heat transfer coefficient for the oblique flow through the rod banks is a function of the approach angle  $\theta$ , which can vary between 0 and  $90^\circ$ . The approach angle is defined as:

$$\theta = \tan^{-1} \left( \frac{u_c}{u_a} \right) \quad (4.28)$$

where  $u_c$  and  $u_a$  are the cross and axial components of velocity, respectively.

The oblique flow heat transfer coefficient can be calculated [93] using the following correlation:

$$Nu = \left[ 5.24 + 0.225 (Re \cdot Pr)_{\max}^{0.653} \right] \sqrt{\frac{\phi_u}{D} \left( 1 - \frac{1}{P/D} \right)} \cdot \sqrt{\frac{\sin \theta + \sin^2 \theta}{1 + \sin^2 \theta}} \quad (4.29)$$

where,  $\phi_u$  is the unit hydrodynamic potential at the rear stagnation point of the tube listed tabularly in Reference [93], and are reproduced for several  $P/D$  of interest in Table 4.4. The subscript "max" refers to Reynolds number based on cross-flow velocity of coolant at minimum flow area.

For fully developed heat-transfer in longitudinal laminar flow between tube or rod bundles arranged in an equilateral triangular array Sparrow, et al., [140] calculated Nusselt numbers for a wide range of pitch-to-diameter

629-111

ratio which can be approximated by the following correlations:

$$Nu = 9.10 (P/D) - 2.63 \quad 1.3 \leq P/D \leq 4 \quad (4.30a)$$

$$Nu = 3.52 (P/D)^{3.65} \quad 1.1 \leq P/D \leq 1.3 \quad (4.30b)$$

The aforementioned discussion of experimental and calculated correlations is by no means an exhaustive consideration of the large amount of such information which has been accumulated for various flow conditions and geometries. For a more detailed guide to the literature the reader is referred to Dwyer [93] and Pearson and Moore [120].

#### 4.3.2 Pressure Drop Model

The rate of heat removal from the reactor depends strongly on the flow behavior in both shell and tube sides of the intermediate heat exchangers. The IHX designs are based on achieving minimum temperature imbalances during steady-state and transient conditions.

The pressure drop calculations on the tube and shell sides of the IHX follow the standard procedure of adding up acceleration, gravity, frictional, inlet and exit pressure losses associated with other flow obstructions as was described previously for flow through rod bundles in section (3.3.2).

Müller and Schnauder [10] have reviewed heat exchanger pressure drop calculational models for a variety of tube and flow arrangements.

The effect of sodium flow maldistribution in the shell side of the heat exchanger has been studied extensively. Aburomia et. al., [127] examined the effect of flow splits caused by flow baffles such as the ones in the CRBRP or FFTF IHX designs. Dawson and Wolowosiuk [141] have carried out extensive

629 112

flow measurement studies; and concluded that complex flow baffles act as an equivalent orifice with loss coefficient of 0.85.

#### 4.4 Thermal Buoyancy Effects

The influence of thermal buoyancy produced by forces resulting from sodium flow field density variations caused by temperature field variations on IHX performance are very small under normal design full flow conditions. However, under low flow natural circulation conditions, buoyancy will strongly influence the overall system behavior. Thermal buoyancy would exert its influence on system dynamic energy and coolant transport prediction through alteration of heat transfer and friction factors.

The effect of local stratification, due to thermal buoyancy on IHX thermal and hydraulic behavior needs considerable investigation, since no conclusive comprehensive study has been made yet to delineate the thermal buoyancy related phenomena. A recent report by Kasza et al., [142] has reviewed the existing models and understanding of the processes controlling the heat and momentum transfer in sodium-to-sodium heat exchangers. Through their preliminary studies they claim that at natural circulation conditions (~5% flow) the thermal buoyancy forces are of the same order of importance as inertial forces.

## 5. HEAT TRANSPORT SYSTEMS

### 5.1 Description

The plant Heat Transport System (HTS) includes the primary and intermediate sodium pumps, and the system components that transport the thermal energy generated in the reactor core to the steam generating system.

In the loop reactor concept, each heat transport loop is arranged in an "elevated loop" concept. This arrangement protects against loss of coolant in the unaffected loops in the event of a sodium pipe rupture accident in one of the heat transport loops. Figure 1.1 shows the hydraulic profile for a typical loop-type design. It can be seen that guard vessels are placed around the reactor vessel, primary pumps, intermediate heat exchangers and all piping below the lips of the guard vessel to assure that the reactor coolant level will not drop below the minimum safe level for emergency core cooling. The sodium piping and components arrangement must promote natural circulation; they must also be routed and supported to keep the thermal expansion, dead weight, and seismic stress within specified limits.

In the pool concept, the primary piping is replaced with a large tank of sodium, while the secondary circuit is essentially identical to that in the loop concept. Two different primary system concepts in the pool design exist, namely, the hot pool and the cold pool concepts as illustrated in Figure 5.1.

In the hot pool concept, there is no piping connection between the reactor vessel outlet and the IHX inlet. The coolant leaves the core and enters the upper outlet plenum, a region of the primary tank that at steady state operates close to the reactor mixed mean outlet temperature (hot pool). The sodium in this region is separated from the cooler, pump suction portion of the tank by an insulated thermal barrier. In general, two different liquid



levels exist in the hot and cold sodium pools, and the liquid level difference manifests the pressure losses through the IHX.

The cold pool concept utilizes an enclosed reactor outlet plenum which is similar to that in the loop concept except for the fact that there is no cover gas present in the former type. Hot sodium leaves the outlet plenum and flows to the IHX via a short insulated piping. The bulk of sodium is at the reactor inlet temperature with only one free liquid level at the cold pool. The elevated IHX arrangement is to promote natural convection in the absence of forced cooling.

## 5.2 Thermal Transport Model

The coolant transport in the primary and secondary heat transport system is one of the most important effects that must be accounted for since the longest time the coolant spends in its passage through the heat transport circuit is in the piping (loop and pool) and the cold tank (pool). Therefore, the long term transient performance characteristics of LMFBR systems are highly influenced by the energy transport in the heat transport circuits.

Consider a pipe section of Figure 5.2; the coolant transport time along a subsection J is defined by [143]:

$$\int_t^{t+\tau_J} \frac{W(t')}{\rho_J(t')} dt' = V_J \quad (5.1)$$

where  $W$  is the coolant mass flow rate (kg/s),  $\rho_J$  the coolant density (kg/m<sup>3</sup>),  $V_J$  the coolant volume (m<sup>3</sup>) and  $\tau_J$  is the coolant or enthalpy transport time (s).

629 115

For an idealized, adiabatic plug-flow in a pipe system, the transient temperature (enthalpy) at the outlet of a pipe section is equivalent to the transient temperature (enthalpy) at its inlet delayed by an enthalpy transport lag time  $\tau_J$ . In other words,

$$T_J^{\text{out}}(t) = T_J^{\text{in}}(t - \tau_J) \quad (5.2)$$

It should be noted, however, that the delay time  $\tau_J$  can, and it indeed does, vary during transients. In the limiting case of a steady state,  $\tau_J$  is identically equal to  $\rho_J V_J / W$ . This model for propagation of disturbance is known as a time-delay model. System codes, such as DEMO [97], have used this simplified method to calculate transient temperatures in the piping network.

The time-delay model is not a realistic one in that it does not account for turbulent mixing of the coolant within the pipe, as well as heat storage in the pipe walls. Both of these factors can have a major influence on the transient sodium temperature. Various model and finite difference approximation to the coolant energy equation are discussed in Section 4.3; it is shown that the nodal heat balance approximation yields the most satisfactory results and hence, should be used for transient simulation. This method has been employed in several LMFBR piping models and simulation codes [62,96,126,144].

The nodal heat balance equations (Equations 4.3 and 4.12) are rewritten for a pipe subsection J ( $J = 1, 2, 3, \dots, N$ ) of Figure 5.2 as follows:

Coolant Energy Equation

$$\rho_J V_J \frac{dh_J}{dt} = W(h_{J-1} - h_J) + q_J, \quad (5.3)$$

629 116

Pipe Wall Energy Equation

$$\left[ \rho_W V_W \frac{dT_W}{dt} \right]_J = q_J, \quad (5.4)$$

where the heat transfer rate is defined as:

$$q_J = U_J A_J (\bar{T}_J - T_W), \quad (5.5)$$

and,

$$U_J = \frac{1}{\frac{1}{h} + \frac{D_i}{2k} \ln(1 + \delta/D_i)} \quad (5.6)$$

where  $A_J$  is the heat transfer area ( $\pi D_i \Delta x$ ),  $D_i$  is the pipe inside diameter,  $\delta$  is the pipe wall half thickness,  $h$  is the convection heat transfer coefficient, and  $\bar{T}_J$  is the coolant average temperature defined by  $(T_{J-1} + T_J)/2$ . The convection heat transfer coefficient  $h$  is evaluated using the Nusselt number definition (Equation 4.22) and the correlations given in Table 4.2 for turbulent flow or Equations (4.23) and (4.24) for laminar flow.

During steady state operation the pipe wall and the coolant are at thermal equilibrium for a very well insulated pipe; thus, the sodium temperature along the pipe is equal to the temperature at the pipe inlet. During transient operation, the heat capacity of the piping influences the sodium temperature significantly. Figure 5.3 shows the transient results for a ramp increase in sodium temperature at a pipe inlet, during full flow as calculated by Pavlenco [145]. The effect of turbulent mixing and wall heat capacity are compared to a purely transport delay plug-flow approximation. It is seen that turbulent mixing and wall coolant heat transfer do indeed mitigate the transient temperature perturbations in the piping.

629 117

The influence of the piping thermal calculations during long term simulations is quite significant and the results are very sensitive to the degree of nodalization along the pipe runs. Madni [144] has studied the problem of false diffusion caused by improper nodalization in the LMFBR piping systems; it is shown that the numerical diffusion can be minimized by increasing the number of temperature nodes. He has also shown that the number of nodes,  $N$ , is indeed bounded.

### 5.3 Coolant Dynamics Model

The calculation of sodium flow rate in the heat transport system is an important prerequisite for overall system simulation studies. The dynamics of coolant flows in a pipe can be modeled quite adequately using the macroscopic form of the one-dimensional, fully developed, homogeneous, incompressible equation of motion. The derivation of this equation, as a special form of the more general Navier-Stokes and continuity equations, will be treated in Section 6.3. There, it will be shown that for near constant density fluid (incompressible) the partial differential equations simplify to an ordinary differential equation of the form:

$$\frac{1}{A} \frac{dW}{dt} + \frac{W^2}{A^2} \frac{d(1/\rho)}{dx} + \frac{dP}{dx} + g \bar{\rho} dz + \frac{f}{2\rho D_i} \frac{W|W|}{A^2} = 0, \quad (5.7)$$

which when integrated over a flow length  $\Delta x$  yields:

$$\left(\frac{\Delta x}{A}\right) \frac{dW}{dt} + \frac{W^2}{A^2} \left[ \frac{1}{\rho_2} - \frac{1}{\rho_1} \right] + (P_2 - P_1) + g \bar{\rho} (Z_2 - Z_1) + \frac{W|W|}{2\rho A^2} \left( f \frac{\Delta x}{D_i} + K \right) = 0. \quad (5.8)$$

629 118

Equation (5.8) is simply a hydraulic head-balance equation which shows that the pressure head ( $P_2 - P_1$ ) is used to accelerate the fluid, to increase its velocity and vertical elevation, and to overcome friction and form losses. This equation can be applied between different points in the heat transport system, at the ends of which the pressures are assumed to be known. When the partial pressure drops are added in series, all intermediate pressure terms cancel out, and the network inlet and outlet pressure plus the pressure rise across the coolant pumps (if any) will remain as the boundary condition to the equation.

The flow regime in the piping system may change during transients, then the effect of Reynolds number on friction factor discussed in Section 3.3.2 are also applicable to pipe flow (Equations 3.30 through 3.22 and also Figure 3.21). Table 5.1 sets forth values for the velocity head factor  $K$  for various fittings and flow obstruction.

It must be noted that Equation (5.8) holds valid if the pipe is of sufficient length to have fully developed flow and to be free of possible entrance and exit effects. Under turbulent flow conditions, the fully developed flow is normally assumed if  $(L/D_i) \geq 10$ , while under conditions of laminar flow, the fully developed parabolic velocity profile is formed at some distance  $L_e$  from the entrance given by Langhaar [146]:

$$(L_e/D_i) \approx 0.058 Re \quad Re \lesssim 2000. \quad (5.9)$$

For a typical LMFBR piping system,  $L = 200$  m,  $D_i \approx 1$  m, and the Reynolds number is about  $10^7$  during normal operation and about  $10^5$  at natural convection flow condition. Therefore, assumption of fully developed velocity profile is quite valid for all practical purposes except for extremely short pipe runs.

629 119

### 5.3.1 Pumps

One of the most important components of an LMFBR plant are the liquid-metal pumps circulating the primary and intermediate coolant. The pumps used in the primary and intermediate systems are either electromagnetic or mechanical. To date both concepts have been extensively studied, and developed.

The relatively high electrical conductivity of sodium and sodium-potassium make them most amenable to being pumped by electromagnetic means. However, recently demonstrated reliable operation of mechanical seals has resulted in the selection of centrifugal mechanical pumps for many of the sodium heat-transfer systems.

#### 5.3.1.1 Electromagnetic Pumps

The operation of electromagnetic pumps is based on the electromagnetic principle that a conductor carrying a current in a magnetic field experiences a force. There are various means of creating the current and magnetic field, and thus, the electromagnetic (EM) pumps are classified according to the way in which this is accomplished.

The design features, advantages and the disadvantages of the EM pumps are discussed in detail by Chase [147]. The key advantages can be summarized as: (1) no moving parts, (2) hermetically sealed, (3) absence of free liquid surface, and (4) fine control over a very wide range of flow. The disadvantages include: (1) the pump duct is a thin-walled member (about 0.50 mm to 2 mm thick), requiring extreme care in design and fabrication and possibly a hermetically secondary seal, (2) nonconventional fabrication, (3) low pump efficiency (below 45%), and (4) adverse problems caused by gas entrainment.

629 120

The nonconventional and low efficiency problems of the EM pumps has led to the development and more universal usage of mechanical pumps for LMFBR plants, although the use of EM pumps during off-normal, auxiliary heat removal conditions is widespread.

#### 5.3.1.2 Mechanical Pumps

The dynamics of mechanical pumps are of considerable interest to the reactor designers and safety analysts. The sodium pumps are generally free-surface, single-stage centrifugal units. The centrifugal design is preferred because of its mechanical simplicity and favorable fluid mechanical characteristics. The usual approach for designing centrifugal pumps is to be able to obtain maximum efficiency, throughout the operating regime, with the exception that the ring-wear clearances are increased 50 to 100% over those used for normal low-temperature designs. This technique reduces the pump efficiency slightly but ensures long-term operation at high temperatures by preventing contact of the wear-ring surfaces [147].

The recent design approaches have been required to meet the rigid and difficult requirements of sealing the liquid metal to prevent any contamination by air entrainment or leakage through the joints and shaft penetration. All types of rubbing force seals, when in contact with liquid metals, deteriorate rapidly, due to the high temperatures and the contaminants in the liquid metal. Chase [147] has discussed various types of seals that have been developed in recent years.

Mechanically, every pump consists of two principle parts: an impeller, which forces the liquid into a rotary motion by impelling action, and the pump casing, which directs the liquid to the impeller and leads it away under a

629 121

high pressure. The impeller is mounted on a shaft which is supported by bearings and driven through a flexible or rigid coupling by a driver [148]. A cutaway diagram of one of the primary sodium pumps in the CRBRP is shown in Figure 5.4. The design of this pump is based on the free-surface centrifugal pump concept. It is driven by a conventional squirrel-cage induction motor rated at 5000 Horsepower at 1116 rpm. The pump is rated at 2.1 m<sup>3</sup>/s, and 140 meter total dynamic head [15].

A pony motor, rated at 75 Horsepower, is coupled to each pump motor by a reduction gear and an overrunning clutch to drive the pump system at about 7.5% rated speed during standby operation, refueling, and decay heat removal periods. Each pump drive motor is powered by a motor-generator set with a fluid coupling [15].

### 5.3.1.3 Dynamic Simulation

The application of Newton's second law of motion to the rotating system yields the torque balance equation for the shaft and rotating assembly [62,96,97,126]. The angular momentum equation is:

$$\left(\frac{2\pi}{60}\right)\left(\frac{I\Omega_D}{\Gamma_D}\right) \frac{d\alpha}{dt} = \beta_{Mt} - \beta_{F\ell} - \beta_{Fr} \quad (5.10)$$

where  $I$  is the moment of inertia of coupled motor and pump rotor (kg/m<sup>2</sup>),  $\Omega_D$  is the design speed (revolutions per minute),  $\Gamma_D$  is the design torque (N-m),  $\alpha$  is the normalized pump speed,  $\beta_{Mt}$  is the normalized drive motor torque,  $\beta_{F\ell}$  is the normalized hydraulic torque of the fluid and  $\beta_{Fr}$  is the normalized frictional torque.

The drive motor torque goes to zero during main motor trip or to pony motor torque during trip to pony motor level. During normal operation the main

629 122



motor torque is adjusted due to the action of the plant flow-speed controllers [61]. The fluid load torque,  $\beta_{FL}$ , and the frictional torque,  $\beta_{Fr}$  are determined from the pump characteristics and the flow of fluid through the pump system.

Pump Characteristics - The head and torque characteristics of a pump as a function of sodium flow rate, and rotor speed determine the pump characteristics [149].

The complete characteristics of pumps is normally available based on homologous theory. In this theory the pump parameters are represented by their normalized values (with respect to their rated values). The nondimensional (homologous) characteristics ( $h$ ,  $\beta$ ,  $v$ ,  $\alpha$ ) obtained are independent of the fluid pumped; the shape of the characteristic curves depends only on  $\Omega_s$ , the rated specific speed [149, 150].

The homologous modeling relates normalized head, ( $h$ ), torque, ( $\beta$ ), to normalized flow, ( $v$ ), and speed ( $\alpha$ ), by tabulating:

$$(h/v^2), (\beta/v^2) \text{ vs } (\alpha/v) \quad 0 \leq |\alpha/v| \leq 1$$

$$(h/\alpha^2), (\beta/\alpha^2) \text{ vs } (v/\alpha) \quad 0 \leq |v/\alpha| \leq 1$$

Based on this theory the performance data from Streeter and Wylie [148] and Donsky [151] were fitted with polynomials of the following form by Madni, et al., [150]:

$$\left(\frac{h}{v^2}\right) \text{ or } \left(\frac{\beta}{v^2}\right) = \sum_{i=0}^n c_i (\alpha/v)^i \quad 0 \leq |\alpha/v| \leq 1 \quad (5.11)$$

$$\left(\frac{h}{\alpha^2}\right) \text{ or } \left(\frac{\beta}{\alpha^2}\right) = \sum_{i=0}^n c_i (v/\alpha)^i \quad 0 \leq |v/\alpha| \leq 1 \quad (5.12)$$

629 123

The coefficients  $c_i$ 's are listed in Table 5.2 and shown graphically in Figure 5.5 and 5.6. These characteristics are based on data for a single stage centrifugal pump with  $\Omega_s = 35$  (SI units) or 1800 (gpm units) which lies in the range of specific speeds for many other LMFBR pumps (e.g., CRBRP  $\Omega_s = 43$ , PHENIX,  $\Omega_s = 37$ ; SNR,  $\Omega_s = 41$ ). Therefore, the homologous theory suggests that the data of Table 5.2 can be used directly to characterize the sodium pumps in any of these plants [150].

The pump head so determined, is used as an input to the equation of motion (Equation 5.8), and the pump torque is used as an input to the angular momentum equation (Equation 5.10).

The frictional torque,  $\beta_{Fr}$  is of considerable importance for simulation of low speed, low flow transients, especially during transition to natural convection.  $\beta_{Fr}$  represents the torque due to motor windage, bearing and seal losses and the fluid friction on the pump shaft. Table 5.3 summarizes several relationships that are currently used in the existing simulation models. These correlations are essentially unverified, and since their influence upon system behavior has been shown to be significant a thorough experimental verification is certainly warranted.

#### 5.4 Pipe-Break Model

Owing to the excellent heat transfer properties of liquid sodium, particularly the high boiling point of 1155 K at atmospheric pressure, the primary system is normally operated at or near atmospheric pressure while retaining a wider margin between operating and coolant boiling temperatures. Operation near atmospheric pressure is desirable both in reducing the probability of the occurrence of catastrophic vessel or pipe rupture and in minimizing the consequences should such an accident occur. Due to low system pressure, if the

629 124

system envelope is breached, a rapid coolant blowdown that occurs in high-pressure light water reactor (LWR) systems will not take place. The accident will, rather, be more accurately characterized by a pouring of fluid from the rupture, driven only by the hydrostatic and/or pump head.

Although the low operating pressures are an attractive feature, liquid-metal-cooled fast reactors have a number of characteristics that are less desirable when the possibility of loss-of-system integrity is considered.

First, changes of power level often entail swings of several hundred degrees in the coolant temperatures. As a result, large thermal stresses may appear in the reactor vessel, coolant piping, or other components, and care must be taken to ensure that thermally induced shocks, creep, or fatigue do not reduce the integrity of the system. Second, should sodium escape and come into contact with either water or oxygen, a fire will result, thereby increasing the thermal and mechanical loading on the containment structures. The possibility of sodium contacting water or oxygen is minimized by placing the primary system in a vault with inert atmosphere such as nitrogen. Another major design feature to prevent a loss in the coolant inventory is provided by placing guard vessels around most of the major components.

The effect of a major rupture of primary or secondary piping system on the LMFBR system response is highly influenced by the size and location of the break. In the loop-type LMFBR, perhaps the most severe loss of piping integrity accident is a double-ended rupture in the cold leg piping near the reactor inlet nozzle. Unlike the LWR, the LMFBR does not have an inherent negative feedback associated with the loss of coolant inventory. On the contrary, an undercooling accident in the LMFBR can lead to a positive reactivity feedback as a result of the positive sodium void effect, which is terminated by the plant protection system.

629 125

Therefore, it is quite clear that the "calculated" loss-of-piping integrity in loop-type LMFBRs must be based on sound and accurate physical and numerical models. The response time of the plant protection system to the accident condition and the details of the transient flow of the coolant through the core during the first few seconds after the pipe break are also significant factors in determining the severity of the transient response.

Various models have been developed and incorporated into several computer codes [62,96,97,124,149]. In all of these models the flow in the vicinity of the break is treated quasistatically, neglecting the effect of gravity on the jet discharge.

IANUS [96], DEMO [97] and RELAP [152] codes consider two limiting types of breaks. One is the small leak for which an orifice discharge coefficient is used. Another is the double-ended quillotine rupture with large separation distance so that the flow interaction between the two sides of the break can be neglected. The medium size breaks are treated as either small leaks or quillotine ruptures. The CURL code [126] models the pipe break based on a user specified discharge coefficient which can vary from a small value (leak) to a very large value (large rupture) and, hence, modeling a whole range of ruptures. The influence of sleeve or guard pipe on flow confinement is not represented in the above mentioned models leading to a conservative prediction for the discharge rate. However, this may not necessarily result in a conservative impact on the reactor core since the most conservative discharge rate results in most optimistic reactor scram time. Thus, it is important to employ a realistic rather than a conservative approach to determine the discharge rate.

629 126

The SSC-L model [62,153] was developed to predict the pipe-break coolant discharge rate under both free jet and confined flow situations. When the break area is small compared to the spacing between the coolant and the outer pipes, the discharge fluid is assumed to behave as a free jet. When the break area is large, such that the discharge fluid is limited by gap space, confined flow model accounting for dissipation pressure losses is employed. Although it neglects the influence of gravity, it seems to model the pipe-break reasonably.

The influence of the guard vessel on the discharge rate is adequately modeled by the current codes based on simple conservation of mass and momentum as discussed in References [62] and [97].

### 5.5 Valves

The LMFBR heat transport systems may require valves for reasons such as: (1) to control the sodium flow rate in the primary or intermediate heat transport systems, (2) to isolate a heat transport loop on a particular component of a loop in order to improve the system reliability and serviceability for a multi-loop plant. The isolation valves can also provide a safety duty by reducing the consequence of an unlikely fault. For example, the intermediate loop isolation valves can stop the pressure wave propagation caused by a possible steam generator leak-induced sodium water reaction, and (3) to control the sodium flow direction, check valves are normally installed in the primary heat transport system to prevent thermal shock and pump reversal in transients where flow direction may change (single pump trip or loss of piping integrity in the loop concept). This can allow for continued heat removal or plant operation at partial load conditions in the absence of a single loop.

629 127

Both the steady-state and dynamic characteristics of the valves should be considered during design and operation of the plant. The steady-state behavior depends mainly on the size and shape of the valve and on the pressure drop across the valve. The actuator characteristics have very little influence on the steady state operation. The dynamic response of a valve depends strongly on the actuator characteristics as well as the mechanical design of the valver and the local hydrodynamic conditions.

The flow characteristic of a valve defines the flow behavior as the valve operates through rated stroke. To take on full meaning, the definition must be considered from two view points: (1) the inherent flow characteristics, and (2) the actual installed flow characteristics.

The inherent flow characteristic is based on near constant drop across the valve body throughout the stroke. It is generally idealized and applied to a whole family of valves. This must be taken into consideration in the analysis since the difference between actual and ideal curves may be fairly large.

The installed flow characteristic is the actual relationship between valve stroke and a specific flow system. Many factors, in addition to the inherent characteristic, influence the installed characteristic. The most common are a restriction such as line loss in series with a valve, a change in total pressure drop in the system as a function of flow as may be caused by a pump, or an open bypass around the valve. The effect is often substantial and must always be considered in a complete analysis of any control problem.

The control valve sizing and flow characteristics for various types of valves are discussed in detail by Wing [154,155] and the dynamics are also discussed in References [143] and [156]. The objective for the heat

629 128

transport design is to provide only those necessary to operate the plant economically and safely and to provide maintainability as discussed earlier.

In order to minimize the backflow in a shutdown primary heat transport system, check valves are normally installed. A cutaway diagram of one of the primary check valves in the CRBRP is shown in Figure 5.7. The swing disc is open during forward flow operation; and closes as the flow reverses direction. To avoid excessive fluid hammer caused by valve closure, a dashpot arrangement is added to reduce the check valve closure rate during flow reversal.

The mathematical model describing the dynamics of a tilting disc check valve has been developed by Pool et al., [157,158]. They consider moments acting on the valve disc which are caused by the pivot pin friction, disc weight, torsional springs and fluid pressure. Ball and Trellis [159] have performed extensive tests on a model cold-leg check valve to understand the closure rate under reverse flow conditions.

## 5.6 Thermal Stratification and Multidimensional Effects

Under low velocity conditions with nonuniform temperature gradients in a pipe, there is a possibility for stratification to occur. For example, cold sodium entering a warmer pipe tends to slide under the warm sodium rather than advance in the plug-like manner [165].

Thermal stratification studies at low velocities have been attempted by several investigators [160,161,162]. COMMIX code [111] was used to investigate the stratification possibility in a horizontal pipe with  $L = 17.7$  m,  $D_i = 0.43$  m,  $\delta = 6.35$  mm and liquid sodium initially flowing at  $W = 805$  kg/s at 632 K and  $Re \approx 4 \times 10^5$ . Kasza et al., [160] and Domanus et al., [161], reported considerable flow redistribution and internal recirculation in an adiabatic pipe for a limited range of flow coastdown to natural circulation.

629 129

The identical problem was also analyzed by Trent [162] using the TEMPEST code. Although considerable flow redistribution was observed, no flow recirculation was predicted to occur when a tight enough convergence criteria on the mass balance error was employed. More recently, Trent [163] has simulated thermal stratification effects for the LMFBR intermediate loop horizontal pipe run for both adiabatic and conducting pipe wall using the TEMPEST code for cylindrical coordinates. Figure 5.8 illustrates the temperature and flow transient [164] used for the pipe entrance boundary conditions, which typifies the sodium temperature at the outlet of the evaporators during a loss-of-electrical power transient (natural circulation) in CRBRP as calculated by the system code DEMO [97].

Axial velocity profiles are illustrated in Figure 5.9. Velocity profile distortion resulting from density gradient is evident, especially at the lower flow conditions. The comparison between the adiabatic and non-adiabatic case indicates that the amount of velocity profile distortion can be significantly mitigated by wall conduction. Velocity profiles, after approximately 120 s illustrate opposite distortions from upstream to further downstream. The downstream profiles exhibit behavior from an earlier part of the transient where colder (heavier) fluid entered, causing a density current and higher axial velocities in the bottom portion of the pipe. However, fluid entering the pipe after 100 seconds is warmer than the fluid currently occupying the pipe and, hence, rises, thereby causing larger axial velocities in the upper portion of the pipe. Another phenomena of interest is the tendency for very localized flow stratification near the top of the pipe during the ramp down portion of the thermal transient (40 to 80 seconds) with wall conduction. This localized velocity profile distortion is thought to be caused by the hot pipe

629 130



Figure 5.10 shows the temperature time history of the fluid at the top and bottom of the pipe. Generally, the thermal capacity of the pipe slows the rate of the temperature decrease at both the top and bottom of the pipe, and decreases the top to bottom temperature differences particularly at locations farther down the pipe away from the inlet. The non-adiabatic pipe wall also delays the time at which the maximum top to bottom temperature difference occurs. Both top and bottom temperatures are considerably higher for the non-adiabatic case, than for the adiabatic one. Also shown in Figure 5.10 are results of similar calculations using the 1-D model described in Section 5.2 [165]. It is seen that the results compare quite favorably, and the 1-D results remain within the bounds of the 3-D calculations. This finding means that flow redistribution and stratification effects are mitigated significantly by wall conduction, and the perturbation signal damps out considerably towards the outlet, hence, the multidimensional effects are minimized and can safely be neglected in overall system simulation studies.

629 131

## 6. STEAM GENERATING SYSTEM

### 6.1 Description

The function of a steam generating system is to remove the heat from the intermediate heat transport system generated during operation of the reactor. This thermal energy is used to boil water and generate steam that is fed to a steam turbine. The turbine converts the thermal energy of the steam to mechanical energy which in turn is converted to electrical energy by a generator. The low pressure, saturated steam from the turbine exhaust is condensed to water in a condenser and the condensate returned to the steam generator through a series of preheaters.

Figures 6.1 and 6.2 show the schematics of the CRBRP and SUPER PHENIX steam generating systems, respectively.

### 6.2 Designs

The LMFBR steam generator design requirements are based on two important factors: safety and low energy cost.

The steam generator system is important, not only because of its function as a means of transferring the thermal energy to an electrical generating device, but also as an essential safety related heat rejection system that forms the interface between two chemically reactive fluids. The chemical affinity between sodium and water dictates high structural integrity to prevent sodium water contact, and that it should also be capable of withstanding the consequence of the worst possible accidents. Recent experimental advances in the area of sodium-water reactions have demonstrated that such a reaction can be contained in a safe manner.

The low energy cost involves a balance between capital cost, operating cost, and system availability. This leads to compromise between the overall plant efficiency, system component costs, and the operating cost and availability.

The unique situation has led to several different approaches to liquid-metal-heated steam generator designs. These include natural circulation, forced circulation, and once-through integral and modular designs with sodium on the tube or on the shell side [63,166,167,168].

The integral once-through type design is a large heat exchanger incorporating several functional elements of a steam generator (evaporator, superheater, separator, etc.), examples of which are the Russian BN-350 reactor, the American Fermi reactor and the French SUPER PHENIX reactor (Figure 6.3).

The modular-type design consists of individual units to perform the heat transfer duty for different thermodynamic states of the water-steam cycle. The designs normally include evaporator, superheaters, and steam drums, examples of which are the U.S. Clinch River Breeder Reactor (Figures 6.1 and 6.4), and the Experimental Breeder Reactor No. II.

Figure 6.4 shows one of the Clinch River reactor steam generator modules. The evaporator and superheater modules are essentially identical and are of "hockey stick" design. The module is a 757-tube counter-flow heat exchanger with sodium flow on the shell side and steam/water flow on the tube side. Heat removed from the secondary sodium produces saturated steam in the evaporators and superheated steam in the superheater. The modules are designed to be interchangeable, except that inlet water orifice inserts are added to the evaporators for hydrodynamic stability [15].

The major characteristics of typical liquid-metal-cooled steam generators are given in Table 6.1.

629 133

### 6.3 Thermodynamic Models

An important part in the thermal-hydraulics analysis of a fast breeder reactor involves the determination of thermodynamic state of the steam-water cycle during steady state and transient modes of operation.

The type of thermodynamic model used to describe a steam generator system is dictated by the system geometry and the problem under consideration. Due to the complex nature of the two-phase and compressible flows in the steam generating system, a purely theoretical, general solution is not possible. Therefore, simplifications are usually made to reduce the computational requirement.

As it was stated earlier, analyses of any flow system involve the solution of mass, momentum, and energy equations. There are four unknowns in a single-phase flow, which were discussed as velocity, pressure, temperature, and density. The number of unknowns in a two-phase flow is eight. These are: void fraction, liquid and vapor phase velocities, liquid and vapor phase densities, pressure, and the temperatures of each phase.

It is apparent that the two-phase compressible flow analysis is vastly more complicated than its single-phase counterpart. Most current simulation models are descendents of the original RELAP [152] and/or FLASH [169] computer programs. Both of these models solve the conservation equations of mass, energy, and momentum for a staggered node-flow path representation of a thermal-hydraulic system. These conservation laws for a one-dimensional (no slip) flow can be rewritten as previously discussed in section 3.4.2.5 [117]:

Mass continuity:

$$\frac{\partial}{\partial t} (\rho A) + \frac{\partial}{\partial x} (\rho u A) = 0 \quad (6.1)$$

629-134

Momentum:

$$\frac{\partial u}{\partial t} + u \frac{\partial u}{\partial x} + \frac{1}{\rho} \frac{\partial P}{\partial x} + g \frac{\partial z}{\partial x} + \frac{f}{di} \frac{u|u|}{2} = 0 \quad (6.2)$$

Energy:

$$\rho \left( \frac{\partial e}{\partial t} + u \frac{\partial e}{\partial x} \right) = \frac{\partial q}{\partial y} - \rho \frac{\partial u}{\partial x} + \mu \phi + q''' \quad (6.3)$$

where  $\rho$  is the fluid density,  $u$  the velocity,  $A$  the flow cross sectional area,  $P$  the pressure,  $g$  the gravitational acceleration,  $f$  the friction factor,  $z$  the vertical elevation,  $di$  the inner diameter of the channel,  $e$  the specific internal energy,  $q'''$  the heat generation rate,  $q$  the heat transfer rate, and  $\phi$  the dissipation function.

Defining the average mass flow rate as,

$$W \equiv \rho u A \quad (6.4)$$

and neglecting the heat generation rate and the viscous dissipation (small as compared to the heat transfer rate), and also substituting the definition of fluid enthalpy ( $h = e + P/\rho$ ) into the above equations for a constant area duct, one gets

$$\frac{\partial \rho}{\partial t} + \frac{1}{A} \frac{\partial W}{\partial x} = 0, \quad (6.5)$$

$$\frac{1}{A} \frac{\partial}{\partial t} \left( \frac{W}{\rho} \right) + \frac{W}{\rho A^2} \frac{\partial}{\partial x} \left( \frac{W}{\rho} \right) + \frac{1}{\rho} \frac{\partial P}{\partial x} + g \frac{\partial z}{\partial x} + \frac{f}{di} \frac{W|W|}{2\rho^2 A^2} = 0, \quad (6.6)$$

$$\frac{\partial}{\partial t} (\rho h - P) + \frac{1}{A} \frac{\partial}{\partial x} (Wh) = \frac{\partial q}{\partial y} \quad (6.7)$$

629 135

These equations can be applied to determine mass flow rate, pressure, and enthalpy as a function of position and time:  $W(x,t)$ ,  $P(x,t)$ , and  $h(x,t)$ , using equations of state which relate the thermodynamic variables. It is assumed that the initial distribution of these variables are known from steady state calculations. Also needed are the boundary conditions for  $W$ ,  $P$ ,  $h$  and the surface heat transfer rate  $q$  as a function of position and time.

There are basically three different approaches to obtain a numerical solution for Equations (6.5) through (6.7) that were mentioned in section 3.4.2.5 which have been applied by various investigators; they are: (1) the fully compressible flow method [169], (2) the momentum and channel integral method [62,117,170], and (3) the single mass flow-rate method [117, 143].

In the fully compressible flow model, the multiple point difference equation approximation to the conservation equations is solved directly for variable  $W$ ,  $P$ , and  $h$  using the appropriate equation of state for density:

$$\rho = \rho (h, P) \quad (6.8)$$

and rewriting the mass continuity equation (6.5) using,

$$\frac{\partial \rho}{\partial t} = \left(\frac{\partial \rho}{\partial h}\right)_p \frac{\partial h}{\partial t} + \left(\frac{\partial \rho}{\partial P}\right)_h \frac{\partial P}{\partial t} \quad , \quad (6.9)$$

to get,

$$\left(\frac{\partial \rho}{\partial h}\right)_p \frac{\partial h}{\partial t} + \left(\frac{\partial \rho}{\partial P}\right)_h \frac{\partial P}{\partial t} + \frac{1}{A} \frac{\partial W}{\partial x} = 0 \quad . \quad (6.10)$$

Equation (6.9) can be substituted into the energy equation (6.7) and along with (6.10) results in a system of equations which can be solved for  $\partial P/\partial t$  and  $\partial h/\partial t$  to give:

629 136

$$\begin{aligned} \frac{1}{c^2} \frac{\partial P}{\partial t} + \frac{1}{A} \frac{\partial W}{\partial x} + \frac{W}{\rho^2 A} \left( \frac{\partial \rho}{\partial h} \right)_p \frac{\partial P}{\partial x} - \left( \frac{\partial \rho}{\partial h} \right)_p \frac{W}{\rho A} \frac{\partial h}{\partial x} \\ = - \frac{1}{\rho} \left( \frac{\partial \rho}{\partial h} \right)_p \frac{\partial q}{\partial y} , \end{aligned} \quad (6.11)$$

and

$$\begin{aligned} \frac{1}{c^2} \frac{\partial h}{\partial t} + \frac{1}{\rho A} \frac{\partial W}{\partial x} - \frac{W}{\rho^2 A} \left( \frac{\partial \rho}{\partial P} \right)_h \frac{\partial P}{\partial x} + \frac{W}{\rho A} \left( \frac{\partial \rho}{\partial P} \right)_h \frac{\partial h}{\partial x} \\ = \frac{1}{\rho} \left( \frac{\partial \rho}{\partial P} \right)_h \frac{\partial q}{\partial y} , \end{aligned} \quad (6.12)$$

where  $C$  is the isentropic sonic velocity defined as

$$C = \frac{1}{\sqrt{\frac{1}{\rho} \left( \frac{\partial \rho}{\partial h} \right)_p + \left( \frac{\partial \rho}{\partial P} \right)_h}} . \quad (6.13)$$

Equations (6.6), (6.8), (6.11) and (6.12) can be solved for the three unknowns:  $W(x,t)$ ,  $P(x,t)$ ,  $h(x,t)$ .

The only drawback from using this method is its numerical stability (explicit methods), and accuracy (implicit methods); since the required integration timesteps are on the order of the time for a sonic wave to pass through one space step; that is,

$$\Delta t \leq \frac{\Delta x}{C + |u|} \quad (6.14)$$

629 137

Therefore, it is obvious that the computational time requirements will be prohibitively long for fluid with high sonic velocity.

To remove the timestep dependency on the sonic velocity, one can assume that the fluid density is a function of enthalpy only,

$$\rho = \rho (h, Pr) \quad (6.15)$$

where  $Pr$  is a spatially constant reference pressure [117].

This approximation removes the spatial pressure distribution in the flow region and hence simplifies the overall momentum and energy equations, leading to the removal of acoustic wave phenomena as described by Meyer [117]. Recently an extension to this method has been considered by Weaver, et al. [62,171] in which the time rate of change of the spatially constant reference pressure has been included.

The momentum integral model is limited by numerical stability considerations to integration timesteps of the order of the fluid residence time, that is:

$$\Delta t \leq \frac{\Delta x}{|u|} \quad (6.16)$$

This improvement in the integration timestep makes this method's applicability to large system studies quite feasible, while retaining the essential physical features of the process for transients in which the duration of significant changes in pressures and velocities are longer than the time for several sonic waves to pass through the system [117].

Further computational simplification can be achieved by neglecting the mass flow rate distribution along the flow path (single mass flow-rate model). That is:

629 138



$$\frac{\partial p}{\partial t} = - \frac{1}{A} \frac{\partial W}{\partial x} = 0 \quad (6.17)$$

This assumption leads to a considerable simplification in the energy and momentum equations, which allows the determination of temporal variation of mass flow rate through solution of a single ordinary differential equation of the form [117,143]:

$$\frac{1}{A} \frac{dW}{dt} + \frac{W^2}{A^2} \frac{d(1/\rho)}{dx} + \frac{dP}{dx} + g \rho \frac{dz}{dx} + \frac{f}{di} \frac{W|W|}{2\rho A^2} = 0 \quad (6.18)$$

which may be integrated over a flow length  $\Delta x$ , using the appropriate pressure boundary conditions as discussed in Reference [143].

Numerical comparisons of the momentum integral and single mass flow rate models have demonstrated that a general agreement exists, and it is highly dependent on the transient under consideration.

Figure 6.5 illustrates a transient when the flow channel is subject to a sudden decrease in pressure drop as computed by Meyer [117]. It is apparent that the agreement between the two models is quite good except for a very short period of time when some deviation is observed.

Another approach to the solution of the conservation equations is the step-wise analytical method. This method can be quite advantageous since the solution of the conservation equations is unhampered by the numerical stability and convergence problems of the finite difference techniques; leading to a considerable reduction in computer running time without affecting the stability of the solution as considered by Agee [172,173]. An excellent review of the numerical solution techniques for the conservation equations is given by Ybarrondo, Solbrig and Isbin [175].

629 139

The thermodynamic state of the steam drum or steam-water separators can be determined using the conservation of mass and energy equations (due to the stagnant nature of the fluid inside the steam drum or separators the momentum equation need not be considered) along with an equation of state which relates the specific internal energy,  $e$ , the specific volume,  $v$  ( $v=1/\rho$ ), and the steam drum pressure  $P$  together [62,143,152].

This model is based on an equilibrium thermodynamics with perfect separation. A model can be incorporated to account for bubble distribution in the steam-water mixture, such as the one developed by Moore and Rose [174].

It can be concluded that the treatment of LMFBR steam generating transients can be accomplished by several numerical and physical models, and the choice of model is dependent on the transient and the conditions of interest.

The purely compressible analysis is not feasible except during blowdown or rapid pressurization, e.g., turbine trip, and a combination of a momentum integral and a single-mass flow rate method seems to be the most desirable approach for slowly varying transients.

#### 6.4 Empirical Considerations for Two-Phase Flows

The true thermodynamic state of the two-phase flow in a channel is highly dependent on the heat transfer and the two-phase flow nature. The effect of flow regime on heat transfer performance and the effect of void fraction on slip ratio and the pressure drop characteristics are of extreme importance in two-phase flow analysis.

To date, the theoretical models have not been able to adequately predict the actual condition, and the semi-empirical approach has proven to be more accurate and reliable.

629 140

### 6.4.1 Heat Transfer Correlations

The formation of a two-phase mixture by vapor generation in a vertical heated tube is shown in Figure 6.6 .

It is observed that the flow pattern undergoes seven different regimes causing variations in the heat transfer process as discussed by Collier [176].

Single-phase forced convection heat transfer is encountered in the inlet of the tube where the fluid enthalpy is below that of saturated water. Despite marked progress in the understanding of turbulence, it is not yet possible to make accurate predictions of forced convection heat transfer coefficient from fundamental principles; therefore empirical correlations must be used. The most extensively used correlation is a modified form of the Dittus and Boelter equation ( $Re > 10^4$ ,  $L/D > 50$ ):

$$Nu = 0.023 Re_b^{0.8} Pr_b^{0.4} \quad (6.19)$$

For laminar flow a variety of relationships are available depending on the boundary conditions and the type of flow (developing or fully developed). The following empirical equation is based on experimental data that takes into account the effect of physical property variations across the flow stream and the influence of natural convection as suggested by Collier [176]:

$$Nu = 0.17 Re_b^{0.33} Pr_b^{0.43} (Pr_b/Pr_w)^{0.25} Gr_b^{0.1} \quad (6.20)$$

where b and w correspond to the conditions at the bulk fluid temperature and

629 141

the temperature adjacent to the wall, and  $Gr$  is the fluid Grashof number. Equation (6.20) is valid for  $L/D > 50$  and  $Re < 2000$  for vertical tubes.

The heat transfer coefficient in the intermediate range Reynolds number ( $2000 \leq Re \leq 10,000$ ) is quite controversial and not very well understood. One approach involves a smooth interpolation between the two correlations for continuity. Another method developed by Colburn [177] is based on the similarity of heat and momentum transfer in the transition region. He discusses the controlling variables in this region in the light of then available data.

The effect of subcooled boiling can normally be neglected due to uncertainties in the prediction methods. The reader is referred to an excellent review of the subcooled boiling heat transfer by Collier [176].

In the bubbly flow region (regions B and C of Figure 6.6), the bubbles can become crowded in the vicinity of the heating surface and form a moving bubble layer, as shown in Figures 6.6, and 6.7a. When the bubble layer becomes thick enough to impede cooling liquid contacting the hot surface, boiling changes from subcooled nucleate boiling to film boiling. Thus, this type of boiling crisis is specifically called Departure from Nucleate Boiling (DNB).

At high-vapor fractions, the flow pattern in the tubes is such that a vapor core exists surrounded by an annulus of water. The velocity of vapor in the core can be so high that the turbulence at the vapor-liquid surface causes the heat transfer mechanism to change to evaporation heat transfer before the occurrence of dryout as illustrated by Figures 6.6 and 6.7b.

The suppression of nucleate boiling occurs at high values of the liquid Reynolds number,  $Re_2$  and  $(1/X_{tt})$ , where  $X_{tt}$  is the Lockhart-Martinelli parameter given as:

629 142

$$\frac{1}{x_{tt}} = \left( \frac{x}{1-x} \right)^{0.9} \left( \frac{\rho_l}{\rho_v} \right)^{0.5} \left( \frac{\mu_v}{\mu_l} \right)^{0.10} \quad (6.21)$$

where  $\rho$  and  $\mu$  are the saturated density and viscosity of liquid and vapor.

Chen [178] proposed the following method where the heat transfer coefficient in this region is a combination of a nucleate boiling component and a forced convection counterpart; thus:

$$h = S \cdot h_{NB} + F \cdot h_c \quad (6.22)$$

where the nucleate boiling coefficient  $h_{NB}$ , originally developed by Foster and Zuber [179] for pool boiling and modified by Chen [178] to account for convective boiling effect given as:

$$h_{NB} = 0.0012 \left[ \frac{k_l^{0.79} c_l^{0.49} \rho_l^{0.49}}{\sigma^{0.5} \mu_l^{0.29} \lambda_{fg}^{0.24} \rho^{0.24}} \right] \Delta P^{0.75} \quad (6.23)$$

where:

$c_l$  = specific heat of liquid,

$k_l$  = thermal conductivity of liquid,

$\sigma$  = surface tension,

$\lambda_{fg}$  = latent heat of vaporization, and

$\Delta P$  = difference in saturation pressure corresponding to the wall superheat.

The Reynolds number correction factor  $F$ , and the nucleate boiling suppression factor  $S$  given by Figure 6.8 are represented as [143]:

629 143

$$F = \begin{cases} 2.84 \frac{1}{X_{tt}}^{0.45} & \frac{1}{X_{tt}} < 2 \\ 2.57 + 0.7643 \frac{1}{X_{tt}} & \frac{1}{X_{tt}} \geq 2 \end{cases} \quad (6.24)$$

$$S = \begin{cases} 1.05 - 1.3 \times 10^{-5} Re & Re \leq 2.5 \times 10^4 \\ 0.83 - 4.3 \times 10^{-6} Re & 2.5 \times 10^4 < Re \leq 10^5 \\ 0.32 \exp(-1.92 \times 10^{-6} Re) & 10^5 < Re \leq 6 \times 10^5 \\ 0.09 & Re > 6 \times 10^5 \end{cases} \quad (6.25)$$

and,

$$Re = Re_{\ell} \cdot F^{1.25} \quad (6.26)$$

The convective coefficient  $h_c$ , should be calculated from Dittus-Boelter Equation (6.19) based on liquid thermodynamic properties.

In annular flow, a liquid film normally covers and cools the heating surface. The boiling crisis occurs when the liquid film becomes too thin and breaks down into dry patches (Figure 6.6 region D to F and Figure 6.7b). Thus, this type of boiling crisis is specifically termed "Dryout."

The flow regime encountered at heat flux levels above the critical heat flux is usually called the post dryout regime. Post dryout heat transfer can be subdivided into transition boiling, where the heated surface is wetted intermittently, and stable film boiling where the heated surface is dry and the liquid phase is carried by the vapor.

629 144

The post dryout heat transfer can be predicted from empirical correlations or from theoretical models. Since the theoretical models are rather complex and the physical mechanisms on which they are based are not yet fully understood, the heat transfer coefficients after the dryout are normally predicted from empirical relationships.[180]

Lack of sufficient experimental data applicable to the partial film-boiling (the transition from nucleate boiling to stable film boiling regime) has led the designers to make the conservative assumption that the stable film boiling begins as soon as the critical heat flux is exceeded. Tong [181] proposes a simplified correlation of transition boiling-heat transfer to water at a pressure of 138 bars:

$$h = h_f + 95736.70 \exp[-0.01 (T_w - T_s)] \quad (6.27)$$

where  $h_f$  is the stable film boiling coefficient (see Equation 6.28) and  $(T_w - T_s)$  is the degree of superheat.

Ganic and Rohenow [182] have studied the post dryout heat transfer, employing a drop deposition model for the migration of liquid drops toward the heated wall and its associated size and distribution. Based on their model and experiment they developed a semi-empirical expression for the heat flux from the wall to the dispersed flow which includes the radiative heat transfer between the wall and the dispersed flow.

As the wall superheat increases the heat transfer mechanism approaches the stable film regime. In this regime, the heat transfer surface is entirely covered by a stable vapor film. At low wall superheat it is possible for the droplets to wet the heating surface, while at the higher superheat

629 145

the hot surface causes rapid evaporation of steam between the liquid droplet and the wall form a vapor cushion that supports the water droplets and keeps the liquid from the heated surface. This is normally referred to as the "Leindofrost point."

For film boiling at high-mass velocities, particularly when the wall temperature is below the Leindofrost point, the following correlation of Bishop et al. [183] is suggested:

$$Nu_f = 0.0193 Re_f^{0.80} Pr_f^{1.23} \left( \frac{\rho_v}{\rho_b} \right)^{0.68} \left( \frac{\rho_v}{\rho_l} \right)^{0.068} \quad (6.28)$$

where  $f$  refers to the film temperature, which equals  $(T_w + T_b)/2$ .

#### 6.4.2 Critical Heat Flux

The prediction of the critical heat flux in the two-phase convective flows is an important consideration for design and safety analysis of steam generators. Numerous boiling heat-transfer and two-phase flow studies have put emphasis on development of models and understanding of the mechanism for improving the critical heat flux predictions. Thus far no overall analytical solution method has been obtained, and the reliable prediction method has remained empirical.

The limited experimental data for sodium heated steam generators required more detailed experimental studies for the development of critical heat flux correlations applicable for LMFBR steam generator design and transient analysis. Geometry of the tubes has relatively great importance on the thermodynamic performance. Among the various arrangements, the behavior of straight, vertical tubes, for instance, is quite different from the corresponding behavior of coiled tubes; in this last type of once-through steam

629 146



generators, the thermal crisis begins at higher qualities with minor effects on the heat transfer coefficient (wall temperature jump and oscillation). At the same time, for the coiled tube geometry, the centrifugal effects on the two phase flow are dependent on the coil slope and diameter [184].

The critical heat flux is one of the most sensitive parameters to the experimental circumstances and the testing method and assumptions. The simulation of thermal boundary condition using an indirect heating by means of a hotter fluid, or the direct electrical Joule heating, alters the mechanism of the heat transfer. The critical heat flux is greater in indirect fluid heating (actual) as compared to the direct electrical Joule heating under the same experimental conditions, depending on pressure and specific mass flow rate.

Most of the existing critical heat flux correlations have been developed for light water reactor core applications which are characterized by much shorter lengths (a few meters, instead of several meters) and higher heat fluxes (hundreds of  $W/cm^2$ , instead of tens of  $W/cm^2$ ). These substantial differences influence the development of two-phase convective boiling flow in the tubes and hence, vary the critical quality.

It is generally believed that the critical heat flux,  $q_{CHF}''$ , is a function of the following:

$$q_{CHF}'' = \text{Function} (X_{CHF}, G, P, D, L) \quad (6.29)$$

where  $X_{CHF}$  is the critical quality,  $G$  the mass flux of water-steam mixture in the tube,  $D$  the tube inner diameter, and  $L$  the tube boiling length.

Alternatively, the critical quality can be expressed in terms of the critical heat flux, the length, mass flux, latent heat of vaporization and the fluid inlet subcooling through an energy balance equation

629 147

leading to:

$$x_{CHF} = \frac{4L_{CHF}}{DG} \frac{q_{CHF}''}{\lambda_{fg}} - \frac{\Delta H_{isc}}{\lambda_{fg}} \quad (6.30)$$

where  $\lambda_{fg}$  is the latent heat of vaporization, and  $\Delta H_{isc}$  is the inlet sub-cooling. The effect of various system parameters on the critical heat flux is discussed by Lee [185], and Tong [186].

Harty [187] correlated the experimental data obtained from a modular sodium heated steam generator unit and found that the critical quality can best be represented in terms of the system parameters as follows:

$$x_{CHF} = \begin{cases} \frac{3.210 \times 10^{12}}{\lambda_{fg} (\rho_v/\rho_l) \sqrt{G}} \bar{q}''^{-1.5} & \bar{q}'' < 6.31 \times 10^5 \text{ W/m}^2 \\ \frac{6.406 \times 10^3}{\lambda_{fg} (\rho_v/\rho_l) \sqrt{G}} & \bar{q}'' \geq 6.31 \times 10^5 \text{ W/m}^2 \end{cases} \quad (6.31)$$

where  $\bar{q}''$  is the average heat flux from the saturation point up to the dryout location. The dryout is predicted to occur anywhere along the tube length where the critical quality  $x_{CHF}$  is equal to the local average quality  $x_{local}$ .

The Harty correlation (Equation 6.32) has been compared [188] to the Bailey and Lee correlation which is of the following form:

$$x_{CHF} = \frac{18.15}{\lambda_{fg}} \left[ 1 - 4.011 \times 10^{-5} G^{-0.575} \bar{q}'' \right] \quad (6.32)$$

$$1.58 \times 10^5 \leq \bar{q}'' \leq 3.15 \times 10^6 \text{ W/m}^2$$

Bein and Yahalom [188] found a close agreement in the dryout prediction to within 5% for a typical LMFBR steam generator condition.

For a straight vertical water test section ( $d = 0.012$  m,  $L = 11$  m), Campolunghi et al. [184] found two separate pressure ranges that are evident from the experimental data:  $4.9 \times 10^{12} < p < 8.8 \times 10^{12}$  N/m<sup>2</sup> and  $9.8 \times 10^{12} < p < 1.76 \times 10^{13}$  N/m<sup>2</sup>, separated by a transition region, in which the critical qualities are substantially different and two different physical dryout mechanisms exist, resulting in the following correlations:

$$x_{CHF} = \begin{cases} 0.494 \bar{q}^{5/13} G^{-3/5} p^{-4/700} & 4.9 \times 10^{12} < p < 8.8 \times 10^{12} \text{ N/m}^2 \\ 0.202 \bar{q}^{8/9} G^{-14/17} p^{-1/7} & 9.8 \times 10^{12} < p < 1.76 \times 10^{13} \text{ N/m}^2 \end{cases} \quad (6.33)$$

Other correlations are summarized by Lee [185] and Tong [186]; it can be concluded that due to the importance of two-phase flow and heat transfer mechanisms in the prediction of LMFBR transient performance, further experimental and theoretical studies are warranted.

#### 6.4.3 Two-Phase Flow Pressure Drop

Analysis of two-phase flow pressure drop is vastly more complicated than that for single phase flow. This is due in part to the multi-dimensional variation in mass and velocity distribution, further hampered by nonuniformity in heat transfer in convection two-phase flows. A number of correlations for the prediction of pressure drops in two-phase flows are available. The investigators have been able to use their own experimental test data to verify their correlations. Unfortunately, there is very little agreement among the methods used for calculating frictional pressure losses. For example,

629 149

within certain pressure and quality ranges, the two-phase frictional loss computed by the Martinelli-Nelson method is 100% larger than that given by the Armand method. Within other pressure and quality ranges the agreement is fairly good. However, at the present time there is no evidence as to which correlation is the most reliable.

One important point to be noted is that the effect of an overestimation in two-phase frictional pressure loss does not necessarily lead to a conservative design and analysis [143]. In steam generator stability analysis, the inclusion of large pressure losses in the heating zone and riser can lead to unstable dynamic operation. Consequently, if the design is just stable with an overestimated frictional loss, it will have a sizable stability margin under actual plant operating conditions, leading to an increase in the total plant cost [189]. However, in the case of a steam generator blowdown accident, an overestimated two-phase pressure loss leads to reduced discharge flow rate through the ruptured pipe with subsequently longer calculated blowdown time, which is certainly not conservative.

The two-phase flow multiplier concept essentially provides a means to determine the total frictional pressure drop for the two-phase flow by multiplying the total flow frictional pressure drop, considered as saturated liquid, by a multiplier,  $\phi_{tp}$ , as follows:

$$(\Delta P/\Delta L)_{tp} = \phi_{tp} (\Delta P/\Delta L)_{lp} \quad (6.34)$$

where  $(\Delta P/\Delta L)$  is the pressure gradient for two-phase (tp) and the saturated liquid phase (lp) with the total mass flow rate.

The following research has contributed to the development of the two-phase flow pressure drop models: (1) Lockhart-Martinelli [190],

629 150

(2) Martinelli-Nelson [191], (3) Armand [192], (4) Levy [193], (5) McMillan [194], (6) Thom [195], and (7) Barcozy [196].

Among these correlations, Martinelli's is by far the most widely used general method for estimating pressure drop and void fraction in two-phase flow. Many modifications or improvements on Martinelli's basic approach have been proposed, and the applications of this technique have been made over conditions much different from that assumed in the original model.

Barcozy [196] compared the Martinelli-Nelson correlation with experimental data for various systems over a wide range of quality and flow rates. He found very strong dependence of the two-phase pressure drop multiplier  $\phi_{tp}$  on the flow rate and quality. That is:

$$(\Delta P/\Delta L)_{tp} = \phi_{tpm} (\Delta P/\Delta L)_{lp} \quad (6.35)$$

where:

$$\phi_{tpm} \equiv \phi_{tp} (\Lambda, \chi, G = 1356) \cdot \Omega(\Lambda, \chi, G) \quad (6.36)$$

which is a modified two-phase flow multiplier, accounting for mass flux and quality variations with the physical property index  $\Lambda$  defined as:

$$\Lambda = \left( \frac{\rho_v}{\rho_l} \right) \left( \frac{\mu_l}{\mu_v} \right)^{0.2} \quad (6.37)$$

Figure 6.9 shows the two-phase flow multiplier,  $\phi_{tp}$  (at  $G = 1356 \text{ kg/m}^2\text{-s}$ ), and the multiplier ratio,  $\Omega$  as a function of  $\Lambda$ ,  $G$ , and  $\chi$ .

The graphical forms of Figure 6.9 are not readily amendable for digital computer applications. Fortunately the following approximation by

629 151

Heat Transfer and Fluid Services (HTFS) yields a suitable analytical expression [197]. That is,

$$\phi_{\text{tpm}} = \left(1 + \frac{\bar{C}}{\bar{X}} + \frac{1}{\bar{X}^2}\right) (1 - \chi)^2 \frac{f_{\ell 0}}{f_{\ell p}} \quad (6.38)$$

with:

$$\bar{C} \equiv -2 + (28 - 0.3 G^{1/3}) \exp \left[ -\frac{(\log \Lambda + 2.5)^2}{2.4 - 10^{-4} G} \right] \quad (6.38a)$$

and

$$\bar{X}^2 \equiv \frac{(\Delta P/\Delta L)_{\ell 0}}{(\Delta P/\Delta L)_{v 0}} = \frac{f_{\ell 0}}{f_{v 0}} \frac{\rho_v}{\rho_\ell} \left(\frac{1 - \chi}{\chi}\right)^2 \quad (6.38b)$$

where subscripts,  $\ell 0$ ,  $v 0$ , and  $\ell p$  refer to the parameter being evaluated based on the flow of liquid, flow of vapor and the total flow as liquid, respectively. That is:

$$f_{\ell 0} = \text{Function} \left( \frac{(1 - \chi) G D}{\mu_\ell} \right) \quad (6.39a)$$

$$f_{v 0} = \text{Function} \left( \frac{\chi G D}{\mu_v} \right) \quad (6.39b)$$

$$f_{\ell p} = \text{Function} \left( \frac{G D}{\mu_\ell} \right) \quad (6.39c)$$

Assuming that friction factor may be expressed in terms of Reynolds number by the following relation,

$$f \sim \text{Re}^{-0.20} \quad (6.40)$$

629 152

it can be shown easily that combining Equations (6.38), (6.39) and (6.40) yields:

$$\phi_{t_{pm}} = (1 - x)^{1.80} + \frac{\bar{C}}{\sqrt{\Lambda}} \left[ x (1 - x) \right]^{0.9} + \frac{x}{\Lambda}^{1.3} \quad (6.41)$$

where  $\bar{C}$  and  $\Lambda$  are given by Equations (6.37) and (6.33a).

A much simpler approach based on the homogeneous flow model considers the two phases to flow as a single phase possessing mean fluid properties. In this model, the two-phase flow multiplier can be defined as [176]:

$$\phi_{tp} = \left[ 1 + x \left( \frac{\rho_l}{\rho_v} - 1 \right) \right] \left[ 1 + x \left( \frac{\mu_l}{\mu_v} - 1 \right) \right]^{-0.20} \quad (6.42)$$

Figure 6.10 shows the ratio of the two-phase flow multiplier to that calculated from the homogeneous model (Equation 6.42),  $R$ , for both Barcozy theory (Equation(6.35)and Figure 6.9) and the HTFS correlation (Equation 6.41) for  $P=74.5 \times 10^5 \text{ N/m}^2$  and  $G=1356 \text{ kg/m}^2\text{-s}$ .

It is seen that the HTFS correlation is smooth as compared to the Barcozy and yields the correct limits for saturated liquid condition ( $x=0$ ) and the saturated vapor condition ( $x=1$ ).

629 153

## 7. NUMERICAL CONSIDERATIONS AND METHODS

### 7.1 Background and Requirements

Physically, an LMFBR plant consists of many systems and subsystems which are interconnected with each other through various processes and/or components. Each of these subsystems is represented by a set of conservation equations. The total number of equations required in simulating the entire plant depend, of course, on the level of modeling details used in individual subsystems. These equations then must be solved numerically to obtain pressures, temperatures and flow rates in the plant. This section is devoted to a brief discussion of the needs and methods that have been used for digital computer simulation models.

Perhaps the most important requirement of numerical method used is the accuracy. The solution obtained must be accurate, within a user-specified error control band, and must be numerically stable. It is noted that the term accuracy used in this section refers to numerical accuracy and as such this should not be confused with the quality or accuracy of modeling assumptions. Another concern that enters into the picture is the efficiency of the method used. A reasonably good measure of simulation efficiency is the ratio of the computing time to reactor simulation time for a given transient. It is pointed out that there is no absolute measure of computing efficiency - for rapid transients the above mentioned ratio can be large, while for flow transients this ratio should be less than unity.

Prior to the discussions of numerical methods, it is helpful to define certain terms. One of the most important terms used is the 'time constant'. Using the terminology of Meyer [64], one can define the time constant for fuel



(blanket or control) rod in two different ways:  $\tau_q$ , a heat flux time constant; and  $\tau_b$ , a bulk coolant time constant. These definitions are illustrated in Figures 7.1. Consider a case in which the fuel rod is operating at steady state. Then begin increasing the heat generation rate linearly with time with bulk coolant temperature  $T_B$  fixed. Initially, the heat flux,  $\phi_0$ , will not respond, but at large time,  $\phi_0$  will also be increasing linearly with time (with the same slope as  $q''$ ). The time lag between  $q''$  and  $\phi_0$  is the time constant  $\tau_q$ . The time constant  $\tau_b$  is defined in a similar manner. However, here  $T_B$  is increased linearly with time,  $q''$  is held constant and the time lag between  $T_B$  and  $\bar{T}$  is the time constant  $\tau_b$  (see Figure 7.1). While in general these two time constants are different, for the one node fuel rod model, they are the same. For this one node model,

$$\tau_q = \tau_b = [m_a c_p / U] \quad , \quad (7.1)$$

where  $m_a$  is the rod mass per unit clad outside surface area ( $\text{kg}/\text{m}^2$ ),  $c_p$  is an average specified heat ( $\text{J}/\text{kg K}$ ), and  $U$  is an average overall heat transfer coefficient ( $\text{W}/\text{m}^2\text{K}$ ).

Similarly, an "enthalpy transport time constant,"  $\tau_h$ , can be defined for a particular system component as:

$$\tau_h = \left( \frac{V}{Wv} \right) \quad , \quad (7.2)$$

where  $V$  is the coolant volume within the component ( $\text{m}^3$ ),  $W$  is the mass flow rate of coolant through the component ( $\text{kg}/\text{s}$ ), and  $v$  is the coolant specific volume ( $\text{m}^3/\text{kg}$ ). This time constant is equivalent to the "fluid transport time" or "transport delay time" for a pipe-like component as defined in Section 5.2. It is equivalent to a "fill time" for a plenum-like component.

629 155

An estimate of the magnitude for these time constants can be obtained for particular plant specifications. Table 7.1 lists some of the major ones, as computed by Meyer, for CRBRP-type conditions. Two sets of values are noted in this table - one set for the normal full power/full flow conditions and the other set to represent conditions at very low flows and power values somewhat typical of the long-term natural circulation conditions. These values are generated for the purpose of illustration and, hence, they need not be taken literally for the CRBRP. Note that the heat flux time constants for the fuel, blanket and control rods are governed largely by geometric characterization and hence, they are not very sensitive to low flow or power conditions. The enthalpy transport time constants, on the other hand, are directly dependent on the fluid velocity.

The application of a numerical method or approximation to a particular process is determined by the relationship between its time constant and the speed of transient or time for significant change. Meyer [64] has defined three ratios of times - the quasi-steady state ratio,  $R_Q$ , and the explicitness ratio,  $R_E$ , and the transient speed ratio,  $R_S$ , as:

$$\left[ \begin{array}{c} \text{Quasi-Steady} \\ \text{State Ratio} \\ (R_Q) \end{array} \right] = \left[ \frac{\text{time constant}}{\text{time for significant change}} \right], \quad (7.3)$$

$$\left[ \begin{array}{c} \text{Explicitness} \\ \text{Ratio} \\ (R_E) \end{array} \right] = \left[ \frac{\text{time step}}{\text{time constant}} \right], \quad (7.4)$$

and,

$$\left[ \begin{array}{c} \text{Transient} \\ \text{Speed Ratio} \\ (R_S) \end{array} \right] = \left[ \frac{\text{time step}}{\text{time for significant change}} \right]. \quad (7.5)$$

629 156

The time step in Equations (7.4) and (7.5) refer to the computational time step used.

The significance of these ratios can be qualitatively interpreted in the following way. If  $R_Q$  were to be small ( $\ll 1$ ), a quasi-steady state calculation may be performed; an explicit calculation would be required otherwise. If the explicit ratio,  $R_E$ , is very small ( $\ll 1$ ) then the differential equations can be integrated by using explicit numerical methods. If nonlinearities are present, a relatively low cost improvement in accuracy can sometimes be obtained by predictor-corrector methods. However, both explicit and many predictor-corrector methods become unstable or experience other numerical irregularities if used for  $R_E$  much in excess of one. For integrations with  $R_E$  larger than one, implicit numerical methods can often be adopted. Computing time per time step tends to increase. Such extra computations can be justified if large enough time steps can be employed. The third ratio characterizing temporal discretization gives a feel for how large the time step is in relation to the transient speed. It would seem surprising, during a complicated simulation, to be able to use  $R_S$  greater than, say,  $1/3$ , which would give three time steps during the time for a significant change. It is recognized, in stating this, that it may be very difficult, especially during a simulation, to define what a significant change is. However, once output is available, such a judgment can probably be made, and the problem rerun, if necessary. A point to emphasize here is that one or all of these ratios can, and do, change during the course of a transient.

As noted earlier, the time step size to be used depends upon the transient under investigation. Agrawal [74] has reported approximate time step values for some of the processes of interest in simulating the flow coastdown

629 157

to natural circulation in an LMFBR plant. The total time span of simulation covers up to an hour of reactor time after the loss-of-electric power followed by reactor scram. The ranges of the time step sizes are shown in Table 7.2. The time step size depends not only on time but also on the process under investigation, i.e.,  $\Delta t(t, \text{process})$ . For very long-term simulations (say up to days of reactor time), the required timestep sizes can be considerably longer than the ones shown in Table 7.2.

A final comment on the desirability of computing time requirements is noted here. For short-term transients (up to an hour of reactor time) the computer time (CPU), on machines such as a CDC-7600, can be in the range from equality with simulated time (SIM) to five times simulated time (i.e.,  $1 < (\text{CPU}/\text{SIM}) < 5$ ). Examples of transients that may fall under this category are (1) the pipe rupture of a sodium-carrying pipe, and (2) a flow coastdown to natural circulation. For long-term transients that may last up to days of reactor time, such as an eventual shutdown or a loss-of-heat-sink, the computer time to simulated time ratio must be much smaller (say,  $0.05 < (\text{CPU}/\text{SIM}) < 0.5$ ). For these events, some combination of reduced detail, longer time steps and/or shorter CPU time per step must be employed to achieve the necessary improvements in computational speed.

## 7.2 Steady-State Solution Methods

The need for an accurate steady-state solution, prior to starting transient computation, is obvious. There appear to be two distinct methods for obtaining initial conditions. In one case, the steady state solution is obtained by reducing, through successive iterations, the time-dependent terms to zero within a specified tolerance. Hence, numerical techniques for solving

time-dependent equations only need to be developed and programmed. The major drawback of this technique is inefficiency of the method rather than the accuracy of results thus obtained, although the errors will propagate in transients. For a stable set of equations, error due to the inaccuracy of steady-state solution diminishes with time.

Another method for obtaining pretransient conditions is to solve the time-independent conservation equations for the entire system. All  $\partial/\partial t$  terms appearing in conservation equations are set to zero. These equations then reduce to ordinary differential equations that are then solved numerically. Although this method requires separate programming for the steady state, it has merits in large computer programs. This method has been used in the SSC-L [62,198,199] and CURL [126,143] system codes for LMFBRs. The DEMO code [97], on the other hand, uses the steady-state conditions as input to the code, or alternately a steady-state solution is generated by running the transient calculations till time-dependent terms are reduced to a small number. Recently, the plant initialization capability has been added [200] to the DEMO code.

A method employed by Guppy, et al [199] in the SSC-L code is described here to illustrate the steady state solution methodology. The main objective of preaccident calculations is to provide a unique and stable plant-wide solution for the initialization of the transient analysis. The preaccident calculations for the entire plant including all of the essential components in the primary, secondary, and intermediate heat transport system (HTS) can be time consuming if the overall conservation equations are solved simultaneously. One way to reduce demand on computing time is to take advantage of special features of the plant.

629 159

For example, the energy and momentum equations for liquid sodium can be decoupled since thermal properties are independent of pressure. Thus, the energy conservation equations for the primary and intermediate sodium loops can be solved first. The required pumping head is obtained by solving the momentum conservation equation. The energy and momentum equations for the water loop, however, cannot be decoupled since the pressure-dependent nature of the two-phase water properties must be considered.

The resulting system of equations to be solved is a typical set of "m" nonlinear coupled algebraic equations with "n" unknowns ( $n > m$ ). Certain groups of these equations representing the IHX and steam generator (on a component basis) must be solved iteratively. As the number of unknowns is greater than the number of independent equations, some plant variables must be known (i.e., specified) "a priori." Since uncertainties may exist as to which operating conditions are known or unknown, the user should be allowed some flexibility in the selection of plant variables which are input and those which are to be calculated.

The overall logic for the plant thermal and hydraulic steady-state balance is as follows:

1. Determine the exact initialization scheme for the plant thermal balance from the input option the user has specified.
2. Iterate with the detailed steam generator and IHX thermal balances and the core gross thermal balance to achieve an overall plant thermal balance.
  - (a) The steam generator water-side hydraulic balance must be determined in conjunction with the thermal balance due to the pressure-dependent nature of water-side properties and correlations.

629 160

- (b) The detailed thermal balance in the core is not required during the iterative phase of the overall thermal balance.
- 3. Determine the detailed in-core thermal and hydraulic balance.
- 4. Initialize:
  - (a) primary loop hydraulics;
  - (b) secondary loop hydraulics.
- 5. Initialize:
  - (a) primary pump speed;
  - (b) secondary pump speed.

Guppy, et al [199] have applied this technique to initialize the entire plant in the SSC-L code. For a significant detailed nodalization of the plant, a stable steady-state solution required only a few seconds of computing time on a CDC-7600 machine. Because of the efficiency of this method, this technique can be readily used in the early phase of a large number of parametric design calculations.

### 7.3 Transient Solution Method

Numerical methods that may be used in transient simulation of the entire plant can be divided into development of techniques for solving (a) parabolic, (b) hyperbolic, and (c) ordinary differential equations. Note that the following discussions are specifically tailored for their current applications and, hence, need not be considered as a general approach. Some discussions on numerical techniques have already been made in Sections 4,5, and 6. A new approach for system integration based on the multiple timestep scheme (MTS) is also discussed [98].

629 161

### 7.3.1 Parabolic Equation

For the purpose of illustration here, the heat conduction equation is rewritten as

$$\frac{\partial T(r,t)}{\partial t} = \frac{1}{r} \frac{\partial}{\partial r} \left( r \alpha \frac{\partial T}{\partial r} \right), \quad (7.6)$$

where  $\alpha = K(T)/\rho c$  and the source term is ignored. This equation is integrated over node  $i$  (from  $r_i$  to  $r_{i+1}$ ), and the following finite difference approximations for time and spatial derivatives are written as

$$\frac{\partial T}{\partial t} = \frac{T_i^{k+1} - T_i^k}{\Delta t} \quad (7.7)$$

$$\alpha \frac{\partial T}{\partial r} = \frac{(\alpha \Delta T_i)^{k+1} + (1 - \epsilon) (\alpha \Delta T_i)^k}{\Delta r} \quad (7.8)$$

where  $0 \leq \epsilon \leq 1$ ,  $k$  denotes the time step, and  $\Delta t$  is the time-step size. For  $\epsilon = 0$ , the method is explicit; the right side of Equation (7.6) is evaluated at the previous time step only. The time-step requirement for a stable solution is [201]

$$\Delta t \leq \frac{1}{2} \frac{(\Delta r)^2}{\alpha}. \quad (7.9)$$

For  $\epsilon \leq 0$ , the method is at least partially implicit and is unconditionally stable. When  $\epsilon = 1$ , the method reduces to a fully implicit method. A mixed scheme, when  $\epsilon = \frac{1}{2}$ , also known as the Crank-Nicolson scheme, is usually employed.

629 162



When material properties change slowly during a time step, Equation (7.8) can be linearized either by evaluating all properties at the temperature of the previous time step (k) or at a temperature extrapolated at  $(k + \frac{1}{2})$  time step. The latter approximation results in improved accuracy without any significant increase in computational effort. This method has been found to be satisfactory [98].

When Equations (7.6), (7.7) and (7.8) are combined with the linearization approximation, one obtains

$$A_{i-1,i} T_{i-1}^{k+1} + A_{i,i} T_i^{k+1} + A_{i+1,i} T_{i+1}^{k+1} = D_i^k \quad (7.10)$$

for each  $i$  except for the ends. This system of algebraic equations can then be solved by use of standard matrix inversion method (for example, the Gauss elimination procedure).

### 7.3.2 Hyperbolic Equation

The one-dimensional hyperbolic equation is of the form

$$\frac{\partial \Gamma}{\partial t} + \beta \frac{\partial \Gamma}{\partial z} = 0 \quad , \quad (7.11)$$

where  $\beta \neq 0$ . This equation can be written in finite difference form as

$$\begin{aligned} \epsilon_1 \frac{\Gamma_{i-1}^{k+1} - \Gamma_{i-1}^k}{\Delta t} + (1 - \epsilon_1) \frac{\Gamma_i^{k+1} - \Gamma_i^k}{\Delta t} \\ + \beta \left[ \epsilon_2 \frac{\Gamma_i^{k+1} - \Gamma_{i-1}^{k+1}}{\Delta z} + (1 - \epsilon_2) \frac{\Gamma_i^k - \Gamma_{i-1}^k}{\Delta z} \right] = 0 \quad , \quad (7.12) \end{aligned}$$

629 163

where  $0 \leq \varepsilon_1 \leq 1$  and  $0 \leq \varepsilon_2 \leq 1$ . Equation sets for various schemes of integration can be obtained by an appropriate choice for the  $\varepsilon_1$  and  $\varepsilon_2$  values. For example, the explicit scheme of running computation is obtained by choosing  $\varepsilon_1 = \varepsilon_2 = 0$ . Equation (7.12) then reduces to

$$\Gamma_i^{k+1} = (1 - \delta)\Gamma_i^k + \delta\Gamma_{i-1}^k, \quad (7.13)$$

where  $\delta = B\Delta t/\Delta z$ . The stability requirement [201] is that  $\delta < 1$ . A typical time step for a stable solution is obtained by setting  $\delta = \frac{1}{2}$ . Thus, the timestep size for the explicit method should be taken as

$$\Delta t \approx 0.5 \frac{\Delta z}{B}. \quad (7.14)$$

A weighted implicit method is obtained when  $\varepsilon_1 = 0$  and  $\varepsilon_2 = \frac{1}{2}$ . In that case, Equation (7.12) becomes

$$\Gamma_i^{k+1} = (1 + 0.5\delta)^{-1} \left[ 0.5\delta \Gamma_{i-1}^{k+1} + 0.5\delta (\Gamma_i^k - \Gamma_{i-1}^k) \right]. \quad (7.15)$$

This method, also referred to as the Neumann scheme, is of second-order accuracy. Furthermore, it is stable for all time-step sizes.

Note that the numerical scheme is required to give stable and accurate solutions. The stability requirements are determined by the numerical values at a given point, whereas the accuracy requirements are determined by gradients. In the case of fluid flow with small gradients, the time-step size  $\Delta t$  can be large provided the stability condition is met. Since for the explicit method,  $\Delta t$  has to be rather small due to stability requirement, the implicit method is preferred.

629 164

Another method for solving the hyperbolic equation consists of reducing it to an ordinary differential equation by integrating it over the node volume. Thus, Equation (7.12) becomes

$$\frac{d\langle\Gamma\rangle_i}{dt} + \beta \frac{\Gamma_i - \Gamma_{i-1}}{\Delta z} = 0 \quad , \quad (7.16)$$

where

$$\langle\Gamma\rangle_i = \frac{1}{\Delta z} \int_{z_{i-1}}^{z_i} \Gamma(z,t) dz \quad . \quad (7.17)$$

Equation (7.16) can readily be shown to reduce to Equation (7.12) when  $\langle\Gamma\rangle_i$  is expressed as a linear combination of the end values, i.e., when

$$\langle\Gamma\rangle_i = \epsilon_1 \Gamma_{i-1} + (1 - \epsilon_1) \Gamma_i \quad , \quad (7.18)$$

and  $(\Gamma_i - \Gamma_{i-1})$  is evaluated at weighted mean of values at time step  $k$  and  $k + 1$ . In other words, Equation (7.11) can be integrated either by expressing it directly in the finite difference form or by reducing it first to an ODE and then integrating the ODE numerically. The stability requirements would not be changed.

The finite difference form of Equation (7.11), as written above (Equation 7.12), was based on a single-layer formulation, both in space and time, i.e., it involved values of state variable  $\Gamma$  at only one previous time and one space coordinate. A multilayer formulation, particularly in space dimension, may be formulated that would involve  $\Gamma$  values at  $(m + 1)$  space coordinates where  $m$  is the order of layering. It seems that for the sake of computing efficiency and ease in formulation, a single-layer formulation would be superior to a multi-layer treatment.

629 165

### 7.3.3 Ordinary Differential Equation

The ODEs that are encountered in the dynamic simulation of LMFBRs have the form

$$\frac{d\vec{y}}{dt} = \vec{f}(t, \vec{y}) , \quad (7.19)$$

where  $\vec{y}(t=0) \equiv \vec{y}_0$  ,  $\vec{y} = \{y_1, y_2, \dots, y_n\}$  and  $\vec{f} = \{f_1, f_2, \dots, f_n\}$ . A variety of methods (polynomial, one-step, and multistep implicit or explicit) can be used [98] to solve this set of coupled first-order differential equations. Some of the important features and limitations are presented.

The polynomial method consists of expressing  $\vec{y}$  in terms of a polynomial within time step  $\Delta t$ . The differential equations can then be integrated analytically. The coefficients of polynomials are then determined by solving algebraic equations at intermediate time steps. Kaganove [43] used this method for solving space-independent neutronics equations as discussed in Section 3.2.2.

The polynomial method has been found to be a satisfactory one for solving point-kinetics equations. This method allows for larger time-step size than the single-step explicit (Runge-Kutta) method, and it has been found to be almost 600 times faster than the Runge-Kutta method. The stability of this method is still an uncertainty, however. Its application to fluid flow equations, even with higher order approximation, is questionable.

A straightforward single-step explicit method (the Euler method) can be used to solve Equation (7.19). The following difference equation is obtained:

$$\vec{y}^{k+1} = \vec{y}^k + \Delta t \vec{f}(t^k, \vec{y}^k) . \quad (7.20)$$

The stability requirement dictates an upper bound for time step, as for the momentum equation it was discussed in Section 6.3 that :

$$\Delta t \leq \frac{\Delta x}{C + |u|} \quad (7.21)$$

629 166

An implicit solution of the first order is the familiar trapezoidal rule,

$$\vec{y}^{k+1} = \vec{y}^k + \frac{\Delta t}{2} \left[ \vec{f}(t^k, \vec{y}^k) + \vec{f}(t^{k+1}, \vec{y}^{k+1}) \right]. \quad (7.22)$$

This method is stable for all  $\Delta t$  (its value being dictated by the accuracy desired). This method, however, requires a simultaneous solution of a system of equations at each time step. These equations are, for the current application, non-linear, and hence must be solved iteratively.

Substantial savings in computing effort in implicit method can be realized when the differential equations are linearized. For example, all material properties can be evaluated either at previous time step or at an extrapolated condition at time  $(k + 1)$ . Similarly,

$$W^2(t^{k+1}) \approx W^2(t^k) + 2W(t^k) \cdot \left[ W(t^{k+1}) - W(t^k) \right]. \quad (7.23)$$

After linearization, some of the available differential equation solvers, such as GEAR [202,203] or EPISODE [204], can be used for a complete solution. Note that these programs can handle nonlinear equations as well.

#### 7.3.4 System Integration Method

The transient simulation of a system, which requires modeling for a number of components such as the reactor core, fluid flow in piping, heat exchangers, etc., is generally accompanied by performing integration using a single value for time-step size throughout. To satisfy both stability and accuracy

629 167

requirements, the time-step size has to be the smallest of all  $\Delta t$  values for different processes. Depending on the method used, the smallest  $\Delta t$  may or may not be a variable one, i.e.,  $\Delta t(t)$  may or may not be allowed. Nevertheless, the entire system is solved simultaneously by using a single value for  $\Delta t$  at any instant. This scheme is labeled as the single timestep scheme (STS).

A more efficient method, which takes advantage of the fact that different components may have widely varying time-step size requirements has been proposed [74]. It is evident that substantial savings in computing time would result if  $\Delta t(t, \text{process})$  can be used. This multiple timestep scheme (MTS) which is quite closely connected with the method of fractional steps of Yanenko [201] is illustrated by a two-component system.

Figure 7.2 is a sketch of a two-component system coupled together through "inlet" and "outlet" junction points. In the following, the superscripts  $i$  and  $o$  refer, respectively, to these junctions. Fluid flow conservation equations for this system need to be solved. Let  $\Delta t_1(t)$  and  $\Delta t_2(t)$  be the required time-step sizes for these components, respectively. Then one can write

$$\Delta t_2(t) = \left[ I_{\max}(t) + \epsilon \right] \Delta t_1(t) , \quad (7.24)$$

where  $I_{\max}(t)$  is the largest whole integer such that  $\epsilon$  is always less than unity, and it is assumed that  $\Delta t_2$  is greater than  $\Delta t_1$ . The entire system is assumed to be known at  $t = t_0$ , i.e.,  $\Gamma_1(t_0)$  and  $\Gamma_2(t_0)$  are known. It is then desired to calculate  $\Gamma_1$  and  $\Gamma_2$  in the time domain  $t_0 < t \leq t_0 + I_{\max} \Delta t_1$ . The MTS method then proceeds in the following steps:

629 168

1. Assume that  $\Gamma_2(t)$  in  $t_0 < t \leq t_0 + I_{\max} \Delta t_1$  is known. For example, for a linear system,

$$\Gamma_2^i(t) = \Gamma_2^i(t_0) + \left. \frac{d\Gamma_2}{dt} \right|_{t_0} (t - t_0). \quad (7.25)$$

2. With  $\Gamma_2^i(t)$  known from Step 1, solve conservation equations for component 1 as the initial value problem for every  $\Delta t_1$  step, i.e., from  $I = 1, 2, \dots, I_{\max}$ .
3. Step 2 gives a value for  $\Gamma_2^0(t)$  in the desired time domain.
4. Now, solve conservation equations for component 2 as an initial value problem. This step results in a new value for  $\tilde{\Gamma}_2^i(t_0 + I_{\max} \Delta t_1)$ .
5. Compare the assumed value of  $\Gamma_2^i$  with the new value ( $\tilde{\Gamma}_2^i$ ) at  $t = t_0 + I_{\max} \Delta t_1$ . If the two agree within a specified tolerance, the solution is known. Otherwise, replace  $\tilde{\Gamma}_2^i$  for  $\Gamma_2^i$  and repeat the process until a converged solution is obtained.
6. Steps 1 through 6 are repeated for the next time domain of interest from  $(t_0 + I_{\max} \Delta t_1)$  to  $(t_0 + I_{\max} \Delta t_1 + I'_{\max} \Delta t'_1)$ , where  $I'_{\max}$  is the value of  $I_{\max}$  obtained from Equation (7.24) at  $t = t_0 + I_{\max} \Delta t_1$ , and  $\Delta t'_1$  is the new time-step size for component 1.

The MTS method would not require any iteration if the linear approximation of Step 1 is exact. One way of bypassing iterative procedure would be to choose sufficiently small  $I$  so that the approximation of Step 1 is valid. The actual choice between iterative and noniterative procedures should be based on the application of the MTS method to the problem. The MTS method as described here can, of course, be generalized to many

The MTS method of system integration has been efficiently applied to the SSC-L code [62]. The required computations are grouped into five separate categories: (a) loop hydraulic calculations, (b) in-vessel sodium energy and dynamics calculations, (c) in-vessel rod heat conduction and power generation calculations, (d) steam generator thermal and water-side hydraulic calculations, and (e) loop energy calculations. Agrawal et. al., [77] have reported savings in computing time, using the MTS method, of as much as a factor of five over that required for the STS method. They also report that, for a half-hour simulation of flow coastdown to natural circulation with twelve-channel representation in the core, the computing time on a CDC-7600 was about 1785 CPU seconds.

629 130



## 8. SAFETY AND TRANSIENT ANALYSIS

### 8.1 Design Approach to Safety

Classification of accidents in nuclear power reactors is prompted by the necessity of approaching safety design analysis in a systematic manner. The overall safety approach is based on defense in depth philosophy to recognize three levels of design [15].

THE FIRST LEVEL provides adequate and reliable functional design based on the use of proven technology. This level is intended to prevent accidents by providing a quality product that will be relatively fault free.

THE SECOND LEVEL renders protection against equipment or human failures through a reliable and comprehensive protection system and redundant heat removal systems.

THE THIRD LEVEL develops additional protection by considering extremely unlikely faults in the design basis, even though such faults are not expected to occur during the life of a plant. Additional mechanical and thermal loads and geometric constraints are provided as margin in design requirements to provide added protection to the public from events of extremely low probability.

The basic philosophy of multiple protection levels requires that accident severity criteria appropriate to each protection level be devised. The potential accidents have to be grouped together according to their frequency of occurrence and the systems must be designed so that the probability of any potential accident is considered acceptable in terms of damage to the plant, injuries to the plant personnel, and hazard to the public.

The American Society of Mechanical Engineers (ASME) classifies plant conditions into four categories according to their anticipated frequency of

occurrence and the potential radiological consequences to the public [205].

They are:

- I. Normal Conditions: Includes normal operation and operational transients,
- II. Upset Conditions: Includes incidents of moderate frequency,
- III. Emergency Conditions: Includes infrequent incidents, and
- IV. Faulted Conditions: Includes postulated events of extremely low frequency.

A damage severity level must be then associated with each of these categories to create a basis for accident classification [206].

Four damage ranges can be specified without reference to the accidents which could cause them and without reference to any probability for those accidents [207].

a. No Damage - No damage is defined as 1) no significant loss of effective fuel life time; 2) accomodations within the fuel and plant operating margins without requiring automatic or manual protective action; and 3) no planned release of radioactivity.

b. Operational Incident - An operational incident is defined as an occurrence which results in 1) no reduction of effective fuel lifetime below the design values; 2) accomodation with, at most, a reactor trip that assures the plant will be capable of returning to operation after corrective action to clear the trip cause; and/or 3) plant radioactivity release that may approach the limited guideline.

c. Minor Incidents - A minor incident is defined as an occurrence which results in 1) a general reduction in the fuel burnup capability and, at most, a small fraction of fuel rod cladding failures; 2) sufficient plant or fuel rod damage that could preclude resumption of operation for a considerable time

629 172

and/or 3) plant radioactivity releases that may exceed the limiting guidelines, but does not result in interruption or restriction of public use of areas beyond the exclusion boundary.

d. Major Incident - A major incident is defined as an occurrence which results in 1) substantial fuel and/or cladding melting or distortion in individual fuel rods, but the configuration remains coolable, 2) plant damage that may preclude resumption of the plant operations but no loss of safety functions necessary to cope with the occurrence; and/or 3) radioactivity release that may exceed the last two categories but must remain within specified design and regulatory limits.

## 8.2 Event Classification

The event classification by probability alone cannot constitute a full risk criterion since neither industry nor society are accustomed to viewing a spectrum of potential events without some estimate of the consequences of failure [208]. Nevertheless, in many endeavors probability is so high that accommodations must be provided, or the probability is so low that the condition is deemed "incredible." Thus, likelihood classifications are instructive and confine attention to those areas where different levels of potential consequences may be acceptable [206,207].

A prospective list of transients and their respective frequency of occurrence is given in Table 8.1. This list is by no means complete and is included just as an illustration of the class of accidents that usually need to be analyzed as part of an overall safety evaluation for the LMFBR systems [206-211].

629 173

### 8.3 Plant Protection System

The LMFBR Plant Protection System (PPS) is to assure that the results of all postulated fault conditions do not exceed the specified safety limits. It should provide the required protection by sensing the need for, and carrying to completion, reactor scrams, pump trips, turbine generator set trip and isolation.

Safety limits are limits upon important process variables required to reasonably protect the integrity of each of the physical barriers which guard against the uncontrolled release of radioactivity [212]. The maximum safety settings are settings for automatic protective devices related to variables on which safety limits have been placed. A maximum safety setting shall be so chosen that automatic protective action will correct the most severe abnormal situation anticipated before a safety limit is exceeded. Thus, the safety limit on reactor power would be the power level at which operation is deemed to become unsafe, while the maximum safety setting would be the power level at which a trip is initiated. The maximum safety setting must take into account the measurement and instrumentation uncertainties associated with the process variables.

The plant protection system can be thought of as a control system, which, in routine operation, remains an observer acting only if the plant system reaches the limit of permissible operation (maximum safety setting). The following are examples of LMFBR protective functions [15,213].

1. High Neutron Flux subsystem generates a reactor scram signal for positive reactivity insertions at or near full reactor power, that is

$$\phi_m(t) \geq \phi_{\max} \quad (8.1)$$

629 174

where  $\phi_m(t)$  is the measured neutron flux and  $\phi_{max}$  is the specified safety setting.

2. Flux-Delayed Flux subsystem generates a reactor scram signal for rapid sustained reactivity disturbance, either positive or negative, which may occur anywhere in the load range, that is

$$A_1 \int_0^t \phi_m(t') e^{-A_2(t-t')} dt + A_3 \phi_m(t) + A_4 \alpha_m(t) + A_5 \leq 0,$$

for  $\rho > 0$  (8.2a)

$$B_1 \int_0^t \phi_m(t') e^{-B_2(t-t')} dt' + B_3 \phi_m(t) + B_4 \alpha_m(t) + B_5 \leq 0,$$

for  $\rho < 0$  (8.2b)

where  $\alpha_m$  is the measured primary loop pump speed or total reactor coolant flow rate,  $A_1, A_2, \dots, A_5$ , and  $B_1, B_2, \dots, B_5$  are constants associated with the maximum safety settings.

3. Flux -  $\sqrt{\text{Pressure}}$  subsystem provides protection against positive reactivity excursions (increased neutron flux) and/or reduction in pressure at the reactor inlet plenum over the load range, the trip equation is of the form:

$$C_1 \phi_m(t) + C_2 \sqrt{P_m(t)} + C_3 \leq 0 \tag{8.3}$$

where  $P_m$  is the measured pressure and  $C_1, C_2, C_3$  are constants associated with the maximum safety settings.

629 175

4. Flux - Total Flow subsystem initiates a reactor scram signal for positive reactivity excursions or reduction in the primary sodium flow rate over the reactor load range. The trip equation is of the form:

$$D_1 \phi_m(t) + D_2 W_m(t) + D_3 \leq 0 \quad (8.4)$$

where  $W_m$  is the measured primary sodium flow rate, and  $D_1, D_2, D_3$  are constants associated with the maximum safety settings.

5. Primary to Intermediate Speed Ratio subsystem generates a reactor scram signal for imbalance in heat removal capability between primary and intermediate circuits on the same loop (for loop designs only). The protective function is of the form:

$$E_1 \alpha_{pm}(t) + |E_2 \alpha_{pm}(t) + E_3 \alpha_{IM} + E_4| + E_5 \leq 0 \quad (8.5)$$

where  $\alpha_{pm}$  and  $\alpha_{IM}$  are the measured primary and intermediate loop pump speeds and  $E_1, E_2, E_3, E_4, E_5$  are constants associated with the maximum safety settings.

Other possible protective functions may include low sodium level in the reactor upper plenum, high sodium temperature at the reactor outlet, the IHX outlet, the steam generator outlet, low water level in the steam separators, and the turbine trip and loss of electrical power to the pumps.

#### 8.4 Example of Transients

Various reactor design events ranging from normal to faulted conditions are described in this section with regard to resulting plant temperatures, pressures, and flows, including overpower and undercooling events for both loop and pool type LMFBR concepts.

629 176

#### 8.4.1 Normal Reactor Scram

Transient results obtained for a reactor scram shutdown which can be caused by events that take place in the LMFBR plant outside of the primary system (e.g., turbine trip, steam generator tube rupture, etc.) are shown in Figures 8.1. These calculations were performed by the DEMO [97] code and are reproduced from Tang, et al., [63].

The Clinch River Breeder Reactor Plant (CRBRP) PPS System initiates an automatic scram signal following a transient initiation. Due to the inherent time lags associated with the process instrumentation and circuitry, a 200 ms scram time delay is assumed.

In order to assure a power to flow ratio close to unity early in the transient and, yet allow for the core outlet temperature to decrease at an acceptable rate, the primary coolant pumps are tripped 300 ms after the control rod insertion begins; this reduces the possible thermal cycling of the reactor and hot leg structural material [63].

A typical variation in total reactor power and sodium flow rate with time is shown in Figure 8.1a. Following the reactor scram at 200 msec the reactor power drops and then decays quite rapidly to the fission product  $\beta$ - and  $\gamma$ -heating level of about 7%. The core flow rate starts decreasing following the deenergizing of the coolant pumps at 500 msec; the rate of flow reduction is considerably slower than that of reactor power, which is due to the stored rotational kinetic energy of the pump impeller and the fluid momentum, it eventually levels-off at about 30 seconds to the auxiliary pony motor driven condition of nearly 10% core flow rate.

The variation in sodium temperatures at the outlet of an average fuel assembly, a fuel assembly hot channel, a radial blanket hot channel, and an

629 177

average of the highest power radial-blanket assembly are also shown in Figure 8.1b.

The fuel assembly coolant temperatures follow the power to flow ratio quite closely, while the radial-blanket assembly coolant temperatures behave in a different manner. This is because the difference in radial blanket pellet diameter gives the radial blanket elements a larger thermal capacity and, in effect, a slower response time, leading to a continuous heat rejection to the coolant before the temperatures start to monotonically decrease at about 15 to 20 seconds into the transient.

Concepts using uranium-carbide instead of an oxide blanket have been studied [63,214]; and it was observed that the difference in the thermal conductivity of the two compounds leads to a substantially quicker cool-down after scram for the uranium-carbide blanket, which is indicative of the smaller heat capacity and time constant.

#### 8.4.2 Control Assembly Withdrawal at Full Power

During full power reactor operation, the in-core primary control rods can be moved by either the automatic control system or manually by the plant operators.

Inadvertant control assembly withdrawal at full power caused by malfunctioning of the control rod drive system (automatic mode) or by operator error (manual mode) can lead to undesirable transient over-power situations.

The automatic reactor control system and the control rod withdrawal blocks will normally limit the results of this type of events. For example, in the CRBRP design, for reactivity insertions of less than approximately  $5\text{¢}/\text{s}$  occurring when the controllers are in automatic, the automatic control system will correct

629 178



the disturbance with less than 10% power overshoot and restore the power to the initial operating condition [15].

For small reactivity insertions, the trend of the variation in reactor power and increase in maximum fuel assembly cladding and fuel temperatures are shown by Figures 8.2.

It is important to note, that all operator and automatic corrective actions were neglected and reactor shutdown occurred due to the plant protection system only. These results are reproduced from calculations that were performed using the FORE-II [215] simulation code as described elsewhere [15,63].

It is observed that the highest temperatures result from the smallest ramp insertion rates since the smaller the insertion rate the greater the total amount of stored energy before the scram occurs, as shown by the power time histories of various cases. However, in a more realistic situation, the smaller ramp insertion rates should be terminated (corrected) either by the reactor automatic power control system or manually by the operator before temperatures can attain values as high as those indicated in Figure 8.1. This latter means of control is viable since it takes a fairly long time for small insertions to effect the PPS action.

Also shown is the relative effect of primary and secondary shutdown systems on the maximum core power and temperatures. Note that failure of the primary shutdown system leads to substantial elongation of the transient and overpower conditions for all cases.

#### 8.4.3 Protected Loss-of-Flow Transient

The expected mode of decay-heat removal in most of the current LMFBR designs is via forced circulation of liquid sodium through the main coolant pumps

629 119

driven by auxiliary pony motors (CRBRP, FFTF, etc.) or via alternate means like electromagnetic pumps (EBR-II). However, in the event of a complete loss-of-forced cooling, the plants are designed to utilize buoyancy forces to provide free convection as a redundant and diverse means of decay-heat removal.

The thermophysical properties of liquid metals and the design parameters of LMFBR systems cause coolant buoyancy and natural convection to be of some limited interest at full power operating condition; since the body forces are often negligible compared to typical frictional losses at full flow. At post-scrum or under shutdown decay heat removal conditions the buoyancy effects become more significant and often dominant.

Many recent experimental and computational studies have assessed the physical mechanisms and also difficulties in predicting buoyancy-induced natural circulation flow and temperature fields in both loop and pool type LMFBR designs [143,164,216-239].

In predicting the natural convection state of the system some of the following problems must be considered as discussed in the previous sections:

1. Strongly coupled hydrodynamics and temperature fields lead to the existence of forced, mixed, and free convection modes of heat transport.
2. Low flow phenomena and non-uniform heat generation along with the inter-subassembly interactions may lead to significant interassembly dynamic flow redistribution.
3. Non-uniform temperature distribution may lead to intersubassembly heat transfer which in effect causes a flattening of radial temperature profile at the subassembly outlets.

4. Uncontrolled thermal interaction in the two flow domains of the pool-type reactors introduces a strong sensitivity for the mixed convection flow in one domain to the variations in the adjacent domain.
5. Thermal stratification in the upper plenum of the loop-type reactor, the hot and cold pool regions of the pool-type reactor has a significant influence under low flow conditions.

To demonstrate some of these important phenomenon, we will attempt to discuss both numerical and experimental examples of both pool and loop designs under natural convection conditions.

a. Numerical Simulation of Natural Circulation in CRBRP

The sequence of failures leading the plant into a natural circulation decay-heat removal mode for this analysis is loss-of-electric power supply to the plants primary, intermediate and tertiary loop coolant pumps at time zero; causing an automatic scram due to the loss-of-electric power signal 0.75 seconds later. The entire system response was calculated up to 1800 seconds after the initiation of the event using the SSC-L code [227].

The CRBRP reactor core consists of 198 fuel and 150 blanket assemblies arranged in a homogeneous configuration. The fuel assemblies are serviced by five orifice zones; the blanket assemblies by four orifice zones. These assemblies are grouped together for an SSC-L simulation. The grouping can proceed according to either similar hydraulic characteristics or similar power characteristics. In this study, the assemblies were grouped by hydraulic characteristics. These channels are:

Channel 1 - It represents hot fuel channel,

Channel 2-6 - These represent average fuel assemblies in each of the five orifice zones,

629 181

Channel 7 - It represents hot blanket channel,

Channel 8-11 - These represent average blanket assemblies in each of the four orifice zones for blanket, and

Channel 12 - It represents all control and shielding assemblies.

In addition, an unheated bypass channel between the thermal liner and the reactor vessel is used.

Figure 8.3 shows various orifice zones and the SSC-L channel number for a 30° sector of the CRBRP core. The power and flow fractions assigned to the twelve-channel model are noted in Table 8.2. It should be pointed out that only one fuel assembly in the entire core was used to represent the hot fuel channel. The location of this assembly is shown in Figure 8.3 at the interface of the inner and outer core zones. Other assemblies (eleven of them) in this location are grouped with Channel 2. Similarly, the hot blanket channel represents only one blanket assembly in the core. Its location is shown in Figure 8.3 (Row 11). The remaining eleven assemblies in this location are grouped with Channel 10. Note that the power fraction values are expressed in terms of fraction of core-generated heat of 964 MW(t). When heat generated by sodium pumps (six of them) are included, the total power becomes 975 MW. Total in-vessel flow of coolant is 5224 kg/s. A steady-state plant characterization is done by the code from the above information and other design information, including power shapes. All of the conditions used here are representative of the end-of-equilibrium core cycle. This condition was chosen so that the blanket assemblies will have maximum power generation. The decay heat values were taken to be 125% of the nominal values for the fission product heating and 110% of the nominal values for decay of the transuranic elements. The peak axial power in hot fuel and blanket channels are 39.70 kW/m and 36.37 Kw/m, respectively. It should be noted that

629 182

there are 217 pins and 61 pins in each of the fuel and blanket assemblies, respectively. The calculated steady-state values of the coolant temperature rise across the channels are also shown in Table 8.2. For the present grouping of assemblies, it is seen that the coolant temperatures for all of the channels, with the exception of the fuel and blanket hot channels, are reasonably uniform. The hot channels are in some sense only mathematical channels as they may not be easily identifiable. These were obtained by combining all of the statistical factors with the parameters for the peak channel. Since, in the SSC-L, a channel represents at minimum, one assembly, the entire assembly in which the hot channel resides was mocked-up as operating at the hot conditions.

The effect of interchannel flow redistribution during the natural circulation transient was shown in Figure 3.29. The normalized flows, coolant flow fractions,  $f_i(t)/f_i(0)$ , for the hot fuel (#1) and hot blanket (#7) channels, a typical fuel channel (#2) and two blanket channels (#8 and #11) are displayed as a function of time. Since the hot blanket channel was operating at the hottest temperature, it draws more coolant from other channels. The hot channels also draw coolant from other colder channels (including the bypass channel), at least for the first four to five hundred seconds into the transient. The relative amount of sodium flow in a channel is determined by the coolant flow in all other channels.

The axial temperature profiles of sodium in a fuel and a blanket assembly are shown in Figure 8.4 and 8.5, respectively, at various times during the transient. It is seen that the maximum coolant temperature gradually passes from the active fuel region to the fission-gas plenum region and eventually out of the assembly into the reactor outlet plenum. Temporal plots of the maximum coolant temperature in hot fuel and hot blanket channels are shown in

629 183

Figures 3.30 and 8.6, respectively. Also included in these figures are the corresponding temperatures that would have been computed if no credit was taken for the interchannel flow redistribution. In the case of the hot fuel channel, the effect of flow redistribution is seen to lower the maximum temperature by 110 K (200 F). For the hot blanket channel, the effect is much more pronounced. Without flow redistribution, sodium would boil in this channel. It should be added here that the inter-assembly flow redistribution and heat transfer were not included in these calculations. When these effects are considered, the maximum temperature should show an additional margin of safety.

Figure 8.7 shows the normalized sodium flow rates in the primary and intermediate heat transfer loops. It is seen that the primary loop flow reaches its lowest value around 80 to 100 seconds, and, as the natural circulation builds up, it shows a slight increase. For long times, it begins to taper off since the buoyancy head begins to diminish as the rate of heat generation decreases. Similar phenomenon is observed for the intermediate loop sodium flow. The IHX serves as the heat sink for the primary sodium. The temperature distributions in the primary and secondary sodium side are shown in Figures 8.8 and 8.9. An important thing to note is that most of the heat is transferred in the top sections of the IHX. Therefore, a sufficient number of nodes should be allowed here, otherwise unrealistic temperatures will result. In these analyses, a total of 40 equi-distant nodes were used.

Figure 8.10 is a temporal plot of the sodium temperatures in the hot legs of the loops. Included in this graph are the temperatures at the reactor vessel outlet, primary inlet to the IHX, secondary outlet from the IHX and the superheater inlet. At steady state, the first two temperatures are almost identical since the heat losses from pipings were neglected but the temperature rise

629 184

due to the primary pump was included ( $\sim 1$  K). The secondary sodium outlet temperature is identical, at steady state, with the inlet temperature at the superheater. The transient effects, including the effect of time-delays, on these temperatures are also seen here. After about twenty or twenty-five minutes into the transient, all of these temperatures indicate a monotonic downward behavior.

Similarly, Figure 8.11 is a temporal plot of the sodium temperatures in the cold legs. The following temperatures are shown in this figure: the reactor vessel inlet, primary outlet from the IHX, secondary inlet to the IHX, and the evaporator outlet. As expected, the first two and the last two temperatures at the steady state, are almost equal to each other. The transient effects are seen to diminish to within a few degrees of each other in about 30 minutes.

For very long times, the system response will depend upon the conditions in the steam generator where the reactor generated decay heat is rejected from the system. In this analysis, the steam generating system was assumed to operate as if the reactor were in the normal, power producing mode. The only exception to this was that the recirculation pump in the evaporator loop was shutdown so that the evaporator operated as a natural circulation boiler rather than a forced circulation boiler. The consequences of operating the steam generator in this mode rather than the normal shutdown mode is to continue to remove heat from the intermediate sodium using the superheater as well as the evaporator. Under normal decay heat removal conditions, the superheater is isolated so that no heat is rejected through this module. The sodium temperature distribution in the cold side of the intermediate sodium loop is altered resulting in a different natural convection flow rate in the intermediate sodium loop. The different sodium flow rates in the intermediate loop under the two operating conditions is believed to have only a small influence on the sodium temperatures and flow rates in the primary heat transport system.

629 185

The influence of overcooling prior to the events leading to natural circulation has been studied numerically by Khatib-Rahbar, et al., [228] and experimentally in the EBR-II reactor by Singer, et al., [230]. Both studies showed that continuous overcooling due to the operation of plant decay-heat removal systems lead to substantial lowering of the system wide temperature levels. However, the maximum sodium temperatures remain well below the sodium saturation temperature. Figure 8.12 shows the maximum sodium temperature in the radial blanket as a function of pony motor trip time for the end-of-equilibrium cycle condition in CRBRP corresponding to the minimum core flow shown in Figure 8.13. It is seen that maximum sodium temperature drops considerably as the pony motor trip time is increased, while the minimum sodium flow rate in the core decreases until around the pony motor trip time of about an hour, at which time the minimum core flow appears to become insensitive to overcooling.

The impact of the primary and intermediate loop pump inertia on natural circulation has been investigated by Madni et al., [229]. Figure 8.14 illustrates the minimum core flow to the reactor power ratio (at the same instant) as a function of primary and intermediate loop pump inertias. It is evident that increasing the inertia leads to unfavorable temperature distributions in the system and thus has a detrimental effect on natural circulation heat removal capabilities, as also seen from Figure 8.15. This study demonstrates that, although long coastdown times may be desirable for unprotected loss-of-flow events, they have a detrimental impact on the plant's decay heat removal capability.

Similar calculations have been performed by Durham [217,218] for PFR (a pool-type LMFBR). He discusses that the major difficulties in established natural circulation are first, the favorable temperature distribution within the

629 186



circuit, and second, the level difference in the two free surfaces exposed to the same cover gas of the inner and outer pools which can lead to unfavorable conditions opposing convective flow in the reactor.

Here, as in the loop-type design, he shows that the one parameter which can significantly affect the temperature distribution in the primary system is the flywheel inertia (pump stored-kinetic energy) since this governs the flow coast-down following the pump trip. The pump inertia should be such that to maintain the temperature of the inner pool at its value prior to the reactor trip, as this region forms part of the hot leg of the natural circulation loop. The intermediate loop behavior also changes the primary cold leg temperature distribution according to its heat removal abilities.

The level difference between the free surfaces of the inner and outer pools, which is necessary to drive the flow through the IHXs, act as adverse head upon the core flow and this will be reduced as the flow coasts down. The variation in this level is caused by the difference in flow rate in the core and the IHXs, and it decreases when the IHX flow is greater than the core flow. Thus, the IHX flow which is affected by the hot pool (inner pool) conditions can have a significant impact on natural circulation.

Figure 8.16 shows the effect of long pump coastdown time on core outlet temperature as predicted by the MELANI code [217]. For the coastdown time of about 120 seconds flow reversal through the core is predicted some 22 seconds before the pump stops. Transition to natural circulation without flow reversal is predicted for both the longer coastdown times, with maximum core outlet temperatures of 1000 K and 913 K.

629 187

Results for the shorter coastdown times are also shown in Figure 8.17. It is shown that natural circulation gets established for pump coastdown times of 24 s, 29s and 36 s with core outlet temperature rising to around 1030 K.

The intermediate heat exchanger primary side flow resistance also effects the natural convection driven flow conditions, for example in PFR, a 50% decrease in resistance results in 8% reduction in core temperature rise, while a 50% increase in resistance results in core flow reversal [232]. Increase in the elevation of IHX inlet above the core outlet reduces the core temperatures significantly. For example, in PFR an increase in elevation of 1.5 meters reduces core temperature rise by about 25% [232].

The influences of inner pool heat capacity and mixing in natural circulation has not yet been established and requires further investigations, but it is believed some minor differences in the core temperature can occur due to fluid mixing, volume of inner pool, and the heat capacity of the upper reactor internals.

#### b. Experimental

Unfortunately, there are virtually no experimental natural circulation test results available in the open literature except the results of the recent tests with the non-prototypic EBR-II reactor in the U.S. and, it will remain the only source of data for sometime until more useful measurements with the French PHENIX or the U.S. FFTF reactor plants become available in the near future.

The overall low-flow natural convection behavior of sodium-cooled reactors can very well be demonstrated using the EBR-II facility; therefore, the wealth of experimental data that has been gathered over the years can serve a very useful purpose in the future design, operation and safety analysis of the demonstration or commercial size plants.

629 188

Table 8.2 summarizes the EBR-II whole core/whole plant tests and events that have been simulated up to this writing.

A schematic representation of the EBR-II primary vessel and the essential elements of the primary heat transport system are shown in Figure 8.18. From this sketch, it is apparent that EBR-II is of the pool design with all of the components submerged in a large pool of sodium. Primary coolant flow is provided by two centrifugal pumps operating in parallel, with one IHX transferring the energy generated in the reactor to the secondary sodium system and ultimately to the steam generators and the turbogenerator. The reactor itself consists of 16 rows of subassemblies, the inner 7 constituting the active core and the outer 9 containing reflector and blanket subassemblies as shown in Figure 8.19.

The experimental subassembly, designated XX07, as shown in Figure 8.20 consists of 61 elements, 56 of which contain metal fuel. The diameter of these elements is 4.42 mm and similar to the driver fuel, they are spaced with 1.24 mm wire wound on a 152 mm lead. The 61 elements are contained within a hexagonal can which measures 46.4 mm across its inside flats. These dimensions result in a channel hydraulic diameter of 2.75 mm. Within this subassembly there are two inlet, permanent magnet flow meters, 10 fuel centerline thermocouples located 21.7 mm below the top of the fuel, and 13 coolant thermocouples mounted as wire-wrap spacers [231].

Subassembly XX08 is a fueled and instrumented subassembly designed primarily for an ongoing program to investigate the thermal-hydraulic core environment within EBR-II under normal and off-normal plant operating conditions. Figure 8.21 shows that, XX08 resembles its predecessor, subassembly XX07 (Figure 8.20), the major difference being that XX08 contains 58 xenon-tagged, EBR-II Mark-II driver-fuel elements whereas XX07 contained 57 Mark-IA fuel elements. The

629 189

Mark-II fuel is expected to provide XX08 with an irradiation lifetime three times as great as that attained with XX07, i.e., 9 versus 2.9 atom percent burn-up. A burnup of 9 atom percent is equivalent to about 29000 Mwt days of EBR-II reactor operation, which corresponds to 11 reactor runs at 2700 MWd per run.

Instrumentation within XX08 includes 16 spacer-wire coolant thermocouples with junctions at various axial and radial locations within the fuel-element bundle, six top-of-core-location fuel-pin thermocouples, two subassembly-outlet-coolant thermocouples, two permanent-magnet flow meters for measuring subassembly flow, and two sodium self-powered detectors for neutron-flux determination [233].

Figure 8.22 shows the schematics of the instrumented subassembly XX08. It was designed to occupy a vacant control rod position in row 5 of EBR-II, this being one of several available locations for an instrumented assembly within EBR-II core.

Together with the regular EBR-II plant instrumentation, the added in-core instrumentation capabilities of XX07 and more recently XX08 has permitted the conduct of a special series of plant simulations initiated either from a shutdown reactor at decay power levels or from an at-power reactor with fission power.

The test results for a number of experiments summarized in Table 8.2 have been compiled in a series of recent reports [234-239].

During testing of EBR-II over a wide range of powers and flows, the core-wide temperature distribution has been measured extensively. Data were collected under steady state [220,231] as well as transient conditions [226,230,234, 235]. Some of the typical steady state temperature distributions measured [231] at the subassembly outlets over rows 1-16 are shown in Figure 8.23. In this

629 190

figure, the normal full power temperature distribution is indicated by the open circles, revealing a large variation across the reactor core. The subassembly temperature rises cover the range from about 59-154°K, with considerable scatter. The solid circles represent the profile measured under reduced power and flow operation, and a markedly reduced scatter is noted. Similar measurements under natural convection conditions are shown in Figure 8.24 where the temperature profile is seen to flatten even further.

Singer and Gillette [231] have attributed the temperature flattening effect to radial intersubassembly heat transfer with additional effects due to dynamic flow redistribution at low flow conditions.

More recently, Gillette et al., [226] reported similar results under transient natural convection conditions in EBR-II. The results were compared for two tests (1A,1E) which were essentially identical except at slightly different decay-power levels (0.16% for 1A versus 0.19% for 1E). Immediately before the experiment, the following plant conditions were established: the coolant flow rate through the reactor was maintained using the auxiliary E-M pumps at approximately 5.5 to 6% of nominal full flow for decay heat removal. Intermediate-system flow was adjusted to accommodate the decay power from the reactor and at the same time maintain the bulk sodium temperature in the primary tank at or near its 644°K operating temperature. The steam turbine was bypassed, and the steam system was on automatic control to accept and dump the decay-heat load (Table 8.3).

The testing sequence consisted of the following series of events. First, the intermediate-system flow rate was adjusted to a prescribed level. Following a short stabilization period, the auxiliary E-M pump power was turned off, leading to a transition from forced to convective flow cooling of the primary system. Table 8.4 summarizes the initial conditions for both the tests.

629 191

The experiment 1A was conducted about 6-3/4 days after a reactor shutdown. At this time the reactor decay power was estimated to be 0.16% of nominal full power. Subassembly XX08 had been installed for the first time before this test and, therefore had no fission-product inventory of its own. It was only a susceptor of gamma and beta activity emitted by its neighbors. This activity was estimated to be 145 W, or 21% of the decay power that would have been present if XX08 had been irradiated for one reactor run (~2700 MWd) before the test [226].

Experiment 1E, was begun about 5 days after another and later reactor shutdown. At this time, the reactor decay power was estimated to be 0.19% of nominal full power, and the XX08 power corresponding was estimated to be 750 W.

The flow response and temperature rise for several selected XX08 sensors are reproduced from Gillette et al., [226] and compared in Figures 8.25 and 8.26. The top-of-core temperatures were measured by the top-of-core elevation spacer-wire thermocouples on fuel element 31 which is in the center of the fuel bundle, as observed from Figure 8.22. The outlet temperatures refer to measurements taken by one of the two subassembly coolant outlet thermocouples in XX08.

The effect of heat removal rate at the IHX on the primary system free convective-flow level can be seen from Figure 8.25. It is evident that higher intermediate loop flow, leads to better heat removal at the IHX and, hence, higher level of convective-flow in the reactor. The transition period from forced to free convection is also reduced significantly due to a more favorable condition for natural circulation at higher heat removal rates at the IHX, a trend also predicted by Madni et al., [229] for a loop-type LM<sup>2</sup>BR.

The ratio of the corresponding temperature rises (top of the core and subassembly outlet) for the two tests are seen to be about 4 or 5 to 1 at steady state, and are reduced to 2 or 3 to 1 in the period of transition from forced

629 192

to natural convection conditions. Since the power level of the reactor was nearly identical and the hydrodynamics of the reactor and the XX08 were essentially unchanged between the two tests, the only phenomenon that could explain the significantly reduced temperature rise ratios at the convective-flow levels is the intersubassembly heat transfer.

The effect of radial intersubassembly heat transfer in larger reactors may not be as pronounced as it is in EBR-II reactor since the typical fuel assembly for a large LMFBR is about 3 to 3.5 times bigger than the subassemblies in the EBR-II reactor and also the specific design of the EBR-II inlet plenum reduces the large dynamic flow redistribution effect leading to a larger radial temperature gradient and, hence, enhanced radial heat transfer. However, it is important to note that the intersubassembly heat transfer reduces the radial temperature gradient and provides an extra safety margin, and neglecting its effect for simulation purposes only adds to the conservatism of the analysis.

#### 8.4.4 "Calculated" Loss-of-Piping Integrity

Due to the lack of extensive operational experience with LMFBR systems, the current analyses of loss-of-piping integrity must rely heavily on the present state of art and understanding of stainless-steel material properties and stress behavior at LMFBR operating temperatures and pressures. The analysis of LMFBR primary piping integrity has been the subject of a special session of a meeting of the American Nuclear Society [240]. Recent advances in reliability studies have led to some quantitative estimates of the reliability of the LMFBR primary system piping [241,242], but such quantification and assessment is extremely sensitive to the assumed values for the probabilistic parameters. Thus, it appears that the assessment of the likelihood of a rupture of the piping system requires further investigation and analysis.

629 193

In this section, the dynamic response of typical loop-type LMFBRs to the coolant flow perturbations, initiated by the rupture of the primary heat transport systems piping is examined within the framework of protected transients.

Hummel and Kalimullah [243] compared the predicted thermal response of the CRBR core to transients initiated by pipe breaks using the DEMO and SAS3A computer codes. They found, in agreement with previous calculations, that the hot channel of the DEMO code model of the CRBR is well into the boiling range, and boiling is just about attained for the peak channel. They also showed that the situation improves rapidly as the break moves away from the inlet nozzle because inertial and static pressures maintain inlet plenum pressure long enough to permit stored pin heat to be removed. Parallel calculations with SAS3A were performed by supplying the transient power and flow time histories obtained from the output of DEMO. They found that the two codes agreed quite well in their prediction of the average channel thermal behavior considering the coarseness of the mesh in the DEMO pin heat transfer calculations.

More recently, Albright and Bari [200] considered a spectrum of initial conditions, such as break size, break location, the degree of operability of the plant protection system, the number of heat transport loops, the power level and the reactor fuel burn-up history including sensitivity analyses to determine the uncertainty in both physical properties and simulation models using the DEMO code [97]. This analysis is in good agreement with previous predictions for CRBRP and provides an excellent insight in the study of pipe breaks for LMFBRs.

Additon and Chien [244] studied hot-leg ruptures for FFTF using the IANUS Code [96]. Their conclusions included the impact of hot-leg pipe break location on the plant protection system response and consequently on the core thermal behavior.

629 194



It is important to note that the existing pipe rupture simulation models remain generally, experimentally unverified. Therefore, the general validity and accuracy of their predictions needs further investigation and experimental support.

629 195

## 9. CODE VERIFICATION

There is a need for simulating the response of the entire plant for all normal and off-normal transients. Such a simulation is generally achieved through model development and application, thereof, to the plant under consideration. A high degree of accuracy and reliability is needed in calculating consequences of an event. In the case where modeling capability is not matured enough, an estimate of uncertainties in consequence (e.g., pressures and temperatures) needs to be known. One possible way of gaining confidence in computer simulation is through application of models to a variety of experimental conditions. The model predicted results can then be compared with the test data. As the data base grows, so will the confidence and ultimately the computer codes can become more matured and more acceptable.

The simulation of various processes as well as the interplay between different processes and/or components for the entire plant is obviously a complex task. The experimental verification of such simulations is equally complex, if not more so. Clearly, the best set of data for a plant can be obtained by subjecting the plant under investigation to a variety of transients. This procedure is not feasible for two reasons: (1) the data base is often needed prior to building the plant, and (2) it may not be prudent to simulate all off-normal transients. Therefore, alternate procedures are employed.

Figure 9.1 is a schematic representation showing the relationship between the model development and its verification. A system simulation code, which incorporates simulation for individual processes and components, can be verified either on a modular or parts basis, or it can be checked against integrated data from similar thermohydraulic conditions for another plant. There is a direct

exchange of data or feedback of information from one part to another. In just about most situations, one is likely to find areas where improvements would be needed. These improvements can be in the form of updating a physical model or developing an improved correlation. The resulting improvement is then incorporated into the system code and the entire process is repeated. The process of code verification is a continuing one but not an endless one. One would expect that as the data base is enlarged, there will be a continual decrement in improving models or correlations.

Experiments may be performed in existing plants such as a part of the pre-operational testings prior to full power operation. By and large, these integral or in-plant experiments will provide a very adequate data base and these data will be prototypical of a type of plant. Alternately, tests may also be done for a single process or a component in a simulated environment. The laboratory tests are generally inexpensive and readily doable. Perhaps one of the most significant drawbacks of the laboratory tests is a potential for non-prototypical testing conditions. Nevertheless, it should be added that both in-plant as well as laboratory tests should be performed.

Table 9.1 indicates various parts of the LMFBR system that require verification. Included in this table are the key parameters and their importance. This list is not intended to be an exhaustive one, rather it shows some of the most crucial ones. The importance rating is subjective in that it strongly depends upon the plant transient under investigation. The importance rating included in Table 9.1 is perhaps more representative of a natural circulation transient.

Several attempts have been made to quantify the validation process. Coffield and Planchon [245] have reviewed U.S. LMFBR natural circulation

629 197

verification programs. They have included, in this review, a description of both in-plant and laboratory test facilities. Recently, a special session was held to identify needs for simulation and verification of transients in fast breeder reactors. Some of the most useful in-plant experimental data have been obtained and additional data will be obtained from a number of years of operating and testing experiences in reactors such as EBR-II, PHENIX, PFR, MONJU, FFTF, SNR-300 etc. Extensive laboratory tests have also been done and continue to generate additional data. One of the most interesting tests done in a laboratory facility was a  $120^\circ$  sector mock-up of SNR-300 to verify decay heat removal capability [247].

A very important and useful tool in assessing plant safety is the use of sensitivity analyses. The objective here is to determine importance of a variable or a process in the overall system response. Such investigations can be performed either by a straight forward sensitivity analysis or a sophisticated process which allows for varying a number of variables in a certain manner so that the combined effect of uncertainties may be assessed. Krieger, Durston and Albright [248] have applied a statistical technique to determine effective variables for a given transient simulation. These types of analyses can lead to, at least, a qualitative estimate of "weak" spots in data base. Ultimately, one is interested in generating a graph such as Figure 9.2 for a given event under consideration. This schematic figure shows that for a natural circulation transient, say, the maximum cladding temperature or consequence may be calculated with a varying degree of confidence level. The best estimate level is an indication of best engineering judgement while the  $3-\sigma$  level indicates factoring in  $3-\sigma$  level uncertainties in models and data. Although Figure 9.2 is drawn not-to-scale, it is hoped that a quantified curve such as this may be producible in next few years, at least for some of the key safety transients.

629 198

## 10. SUMMARY AND FUTURE AREAS OF INTEREST

The steady state and dynamic simulation of the entire liquid-metal-cooled fast breeder reactor system have been reviewed and discussed. After a brief discussion on various designs and simulation techniques, critical review of various phenomenological, physical and mathematical approaches was made. An extensive list of useful semi-empirical correlations for pressure drops and heat transfer in both liquid metal as well as steam-water system was also included. Numerical methods as applied to integration of steady state and transient equations for large system simulation studies were discussed. Safety analysis and accident classification approaches were reviewed along with several examples of numerical and experimental transient and steady state results with emphasis on special effects (flow redistribution, radial heat transfer, fluid mixing, etc.). Finally, various steps involved in code verification were briefly outlined.

A review of more than twenty years of research and development in LMFBR technology reveals a large variety of possible designs and geometric configurations with a rather limited large scale operational and system experience. However, it was argued that the phenomenological understanding in this field have matured to a point that numerical and computer simulation of these systems are quite feasible and can provide sufficient insight into the problems associated with plant design, operation and safety analysis.

Some of the problems which deserve further thought and analysis are summarized as follows:

- (1) Experimental measurements with liquid metals to determine the fluid mixing and thermal stratification effects in the upper plenum (loop-type), hot cold regions (pool-type) and the piping systems.

(2) Experimental measurements supported by calculation of inter- and intra-assembly dynamic flow redistribution and heat transfer effects.

(3) Subassembly internal flow recirculation and hydrodynamic instability effects at natural convection low flow conditions.

(4) Experimental measurements on rod bundle heat transfer and friction coefficients at low Reynolds numbers, especially, in the transition range.

(5) Experimental verification of pipe break models.

(6) Experimental and analytical studies for two-phase flow pressure drop and critical heat flux in liquid metal heated test models at LMFBR thermodynamic conditions.

(7) Impact of Nonequilibrium effects on LMFBR steam generator thermo-hydraulic transients.

(8) A systematic classification of events and accident progression in LMFBR plants.

(9) Detailed inter-code comparisons of existing LMFBR system simulation models under various design, operational and accident conditions.

(10) Systematic experimental validation of system codes following increasing availability of plant steady state and transient data.

It is hoped that all of the problems that may arise have been fully recognized and that sound and adequate means to solve those that may yet appear can be obtained from planned and existing research and development efforts, along with construction of new test facilities, and/or large scale plant operational experience from the American Fast Flux Test Facility, and the French PHENIX and SUPERPHENIX reactors.

Finally, it is the authors belief that more international cooperative effort is needed to overcome many of the remaining obstacles surrounding LMFBR

629 200

development; and the solution of these tasks will contribute significantly to the safe and economic production of nuclear energy in commercial fast breeder power stations.

629 201

## REFERENCES

1. International Meeting on Fast Reactor Safety Technology, Seattle Washington, USA, August 19-23, 1979.
2. International Symposium on Design, Construction and Operating Experience of Demonstration Liquid Metal Fast Breeder Reactors, Bologna, Italy, April 10-14, 1978.
3. International Meeting on Fast Reactor Safety and Related Physics, Chicago, Illinois, USA, October 5-8, 1976, CONF-761001.
4. Fast Reactor Safety Meeting, Beverly Hills, California, USA, April 2-4, 1974, CONF-740401.
5. Sodium-Cooled Fast Reactor Engineering, Monaco, March 23-27, 1970, International Atomic Energy Agency, Vienna.
6. KAZACHKOVSKY, O.D., and LYTKIN, V.B., "Fast Power Reactors," Atomic Energy Review, Vol. 3, Issue 4, 47 (1965).
7. Atomic Energy Review, Vol. 4, Commemorative Issue (1966).
8. OKRENT, D., "Design and Safety in Large Fast Power Reactors," Atomic Energy Review, 7, 135 (1969).
9. WILSON, R., "Physics of Liquid Metal Fast Breeder Reactor Safety," Rev. Mod. Phys., 49, 893 (1977).
10. MULLER, R. A., and SCHNAUDER, H., "The Evolution of Heat-Exchanger Design for Sodium-Cooled Reactors," Atomic Energy Review, 13, 215 (1975).
11. BEKEY, G. A., and KARPLUS, W. J., "Hybrid Computation," John Wiley & Sons, Inc., New York (1968).
12. GUPPY, J. G., "FFTF Normal Operation Control Study," Advanced Reactors Division, Westinghouse Electric Corporation Report FPC-1275, (1974).
13. BRUKX, J.F.L.M., "Post-Scram LMFBR Heat Transport System Dynamics," The Eighteenth ASME/AIChE National Heat Transfer Conference, San Diego, California, August 5-8, (1979).
14. SESONSKE, A., and YEVICK, J. G., "Description of Fast Reactors," in Fast Reactor Technology: Plant Design, Ed. by Yevick, J.G., and Amorosi, A., The M.I.T. Press, Cambridge, Massachusetts, Chapter 11 (1966).
15. Clinch River Breeder Reactor Plant - Preliminary Safety Analysis Report, Project Management Corporation, USA (1975).



16. VENDRYES, G. A., "SUPERPHENIX: A Full-Scale Breeder Reactor," *Sci. Am.* 236, 26 (1977).
17. LU, Y. S., COWAN, C. L., and BAILEY, H. S., "Nuclear Characteristics of Large LMFBRs - Homogeneous and Heterogeneous Designs," *Proc. of an ANS Topical Meeting on Advances in Reactor Physics, Gatlinburg, Tennessee, April 10-12, 1978, CONF-780401*, p. 527 (1978).
18. BARTHOLD, W. P. and BEITEL, J. C., "Physics Aspects in the Design of Heterogeneous Cores," *Proc. of an ANS Topical Meeting on Advances in Reactor Physics, Gatlinburg, Tennessee, April 10-12, 1978, CONF-780401*, p. 423 (1978).
19. MOUGNIOT, J. C., BARRE, J. Y., CLAUZON, P., GIACOMETTI, C., NEVIERE, G., RAVIER, J., et SICARD, B., "Gains de Regeneration des Reacteurs Rapides a Combustible Oxyde et a Refrigerant Sodium," *Proceedings of the European Nuclear Conference*, p. 133, Vol. 4 (April 1975).
20. TZANOS, C. P. and BARTHOLD, W. P., "Design Considerations for Large Heterogeneous Liquid-Metal Fast Breeder Reactors," *Nucl. Technology*, 36, 262 (1977).
21. CASPERSON, S. A., NOYES, R. C., and VITTI, J. A., "Economic and Nuclear Performance Characteristics of 500-MWe Oxide, Carbide, and Nitride LMFBRs," *Proc. of the International Conference on Advanced Reactors: Physics, Design and Economics*, Ed. by Kallfelz, J.M., and Karam, R.A., p. 125, Pergamon Press, New York (1975).
22. CASPERSON, S. A. and KULWICH, M. R., "Performance Potential of (Th,U) Carbide and (Th,U) Nitride Fuel in 1200 MWe LMFBRs," *Proc. of an ANS Topical Meeting on Advances in Reactor Physics, Gatlinburg, Tennessee, April 10-12, 1978, CONF-780401*, p. 539 (1978).
23. SEHGAL, B. R., LIN, C., NASER, J., and LOWENSTEIN, W. B., "Low Sodium Void Coefficient LMFBR Cores," in *Proceedings of the International Meeting on Fast Reactor Safety and Related Physics, Chicago, Illinois, October 5-8, 1976, CONF-761001*, p. 565 (1976).
24. ADAMS, C. H., "Current Trends in Methods for Neutron Diffusion Calculations," *Nucl. Sci. Eng.*, 64, 552 (1977).
25. LEWIS, E. E., "Progress in Multidimensional Neutron Transport Computation," *Nucl. Sci. Eng.*, 64, 279 (1977).
26. GYFTOPOULOS, E.P., "General Reactor Dynamics" in *The Technology of Nuclear Reactor Safety*, Ed. by T.J. Thompson and J. G. Beckerly, The M.I.T. Press, Cambridge, Massachusetts, Vol. 1, Chapter 3 (1964).
27. FERGUSON, D. R., "Multidimensional Reactor Dynamics Today: An Overview" in *Proceedings of the Conference on Computational Methods in Nuclear Engineering, Charleston, South Carolina, April 15-17, 1975, CONF-750413, Vol. II*, p. VI-49 (1975).

629 203

28. HENRY, A. F., "Review of Computational Methods for Space-Dependent Kinetics," in Dynamics of Nuclear Systems, Ed. by Hetrick, D.L., The University of Arizona Press, Tucson, Arizona, p. 9 (1972).
29. HANSEN, K. F., "Finite-Difference Solutions for Space-Dependent Kinetics Equations," in Dynamics of Nuclear Systems, Ed. by Hetrick, D.L., The University of Arizona Press, Tucson, Arizona, p. 165 (1972).
30. HENRY, A. F., Nuclear Reactor Analysis, The M.I.T. Press, Cambridge, Massachusetts (1975).
31. HETRICK, D. L., Dynamics of Nuclear Reactors, The University of Chicago Press, Chicago (1971).
32. STACEY, W. M. Jr., Space-Time Nuclear Reactor Kinetics, Academic Press, New York (1969).
33. OTT, K. O., "Quasistatic Treatment of Spatial Phenomena in Reactor Dynamics," Nucl. Sci. Eng., 26, 563 (1966).
34. OTT, K. O. and MENELEY, D. A., "Accuracy of the Quasistatic Treatment of Spatial Reactor Kinetics," Nucl. Sci. Eng., 36, 402 (1969).
35. MENELEY, D.A., OTT, K., and WIENER, E.S., "Space-Time Kinetics, the QX1 Code," Argonne National Laboratory, ANL-7310 (1967).
36. MENELEY, D. A., LEAF, G. K., LINDENBAUM, A. J., DALY, T. A., and SHA, W.T. "A Kinetics Model for Fast Reactor Analysis in Two Dimensions," in Dynamics of Nuclear Systems, Ed. by Hetrick, D.L., The University of Arizona Press, Tucson, Arizona, p. 483 (1972).
37. MAYER, L., and BACHMAN, H., "KINTIC-1, A Program for the Calculation of Two-Dimensional Reactor Dynamics of Fast Reactors with Quasistatic Method," Kernforschungszentrum, Karlsruhe, KFK-1627 (1972).
38. FULLER, E. L., "One-Dimensional Space-Time Kinetics Benchmark Calculations," Argonne National Laboratory, ANL-7910, p. 497 (1971).
39. DODDS, H. L. Jr., STEWART, J. W., and BAILEY, C. E. "Comparison of the Quasistatic and Direct Methods for Two-Dimensional Thermal Reactor Dynamics," Trans. Am. Nucl. Sci., 15, 786 (1972).
40. OKRENT, D., COOK, J. M., SATKUS, D., LAZARUS, R. B., and WELLS, M. B., "AX-1, A Computing Program for Coupled Neutronics-Hydrodynamics Calculations on the IBM-704," Argonne National Laboratory, ANL-5977 (1959).
41. DORNING, J. J., and SPIGA, G., "The Relationship between Point Kinetics and Space-Dependent Kinetics for Large Reactors," in Proc. of an American Nuclear Society Topical Meeting on Advances in Reactor Physics, Gatlinburg, Tennessee, April 10-12, 1978, CONF-780401, p. 107 (1978).

629 204

42. KEEPIN, G. R., Physics of Nuclear Kinetics, Addison-Wesley, Reading, Massachusetts (1965).
43. KAGANOVE, J. J., "Numerical Solution of the One-Group, Space-Independent Reactor Kinetics Equations for Neutron Density Given the Excess Reactivity," Argonne National Laboratory, ANL-6132 (1960).
44. WAY, K., and WIGNER, E.P., "The Rate of Decay of Fission Products," Phys. Rev., 73, 1318 (1948).
45. MARR, D.R, and BUNCH, W.L., "FTR Fission Product Decay Heat," HEDL-TME 71-27, Hanford Engineering Development Laboratory (1971); see also Marr, D.R., "A User's Manual for Computer Code RIBD-II, A Fission Product Inventory Code", Hanford Engineering Development Laboratory, HEDL-TME 75-26, (1975).
46. ENGLAND, T.R., WILCZYNSKI, R., and WHITTEMORE, N.L., "CINDER-7; An Interim User's Report", Los Alamos Scientific Laboratory, LA-5885-MS, (1975).
47. BELL, M.J., "ORIGEN-The ORNL Isotope Generation and Depletion Code", Oak Ridge National Laboratory, ORNL-4628, (1973).
48. ROSE, P.F., and BURROWS, "ENDF/B Fission Product Decay Heat", Brookhaven National Laboratory, BNL-NCF-50545, Vol. I and II, (1976).
49. SCHMITTROTH, F., and SCHENTER, R.E., "Uncertainties in Fission Product Decay-Heat Calculations, Nucl. Sci. Eng., 63, 276 (1977).
50. MCCARTHY, W.J., and OKRENT, D., "Fast Reactor Kinetics", in The Technology of Nuclear Reactor Safety, Ed. by Thompson, T.J., and Beckerly, J.G., The M.I.T. Press, Cambridge, Massachusetts, vol. 1, Chapter 10 (1964).
51. HUMMEL, H.H., and OKRENT, D., Reactivity Coefficients in Large Fast Power Reactors, American Nuclear Society (1970).
52. GREEBLER, P., and PFLASTERER, G.R., "Doppler and Sodium Void Reactivity Effects in Fast Reactors in Reactor Physics in the Resonance and Thermal Regions, Ed. by Goodjohn, A.J., and Pomraning, G.C., The M.I.T. Press, Cambridge, Massachusetts, p. 343 (1966).
53. LeSAGE, L.G., WADE, D.C., MCKNIGHT, R.D., and FREESE, K.E., "Assessment of Nuclear Data Files via Benchmark Calculations - A Preliminary Report on the NEACRP/IAEA International Comparison Calculation of a Large LMFBR", in Proc. of an American Nuclear Society Topical Meeting on Advances in Reactor Physics, Gatlinbury, Tennessee, April 10-12, 1978, CONF-780401, p.1 (1978).
54. Proceedings of the International Symposium on Physics of Fast Reactors, October 16-23, 1973, Tokyo, Japan, Vol. 1, p. 19, Power Reactor and Nuclear Fuel Development Corporation, Tokyo, Japan (1973).

629 205

55. CHA, B.K., and McLENAN, G.A., "NUBOW-2D Inelastic: A Computer Program for the Bowing History of Reactor Core", *Trans. Am. Nucl. Soc.*, 27, 756 (1977).
56. Clinch River Breeder Reactor Plant Project - 1977 Technical Progress Report, Westinghouse Electric Corporation, CRBRP-ARD-0211 (1977).
57. SHIELDS, J.A., and ARMSTRONG, J.R., "Relationship between Fuel Handling and Reactivity", in *Reactor Development Progress Report - May 1978*, Argonne National Laboratory, ANL-RDP-71, p. 1-17 (1978).
58. GOLDMAN, A.J., "Reactivity Effects of Protactinium -233 Buildup in U<sup>233</sup> Fast Breeder Reactors", *Nucl. Sci. Eng.*, 10, 91 (1961).
59. PEARSON, A., and LENNOX, C. G., "Sensing and Control Instrumentation," in *The Technology of Nuclear Reactor Safety*, Ed. by Thompson, T.J., and Beckerly, J.G., The M.I.T. Press, Cambridge, Massachusetts, Vol. I, Chapter 6 (1964).
60. SCOTT, C. C., "Plant Instrumentation and Control," in *Fast Reactor Technology: Plant Design*, Ed. by Yevick, J.G., and Amorosi, A., The M.I.T. Press, Cambridge, Massachusetts, Chapter 9 (1966).
61. KHATIB-RAHBAR, M., AGRAWAL, A. K., and SRINIVASAN, E. S., "Feedback Control Systems for Non-Linear Simulation of Operational Transients in LMFBRs," in *Proc. of International Meeting on Fast Reactor Safety Technology*, August 19-23, 1979, Seattle, Washington (in preparation).
62. AGRAWAL, A. K., et al., "An Advanced Thermohydraulic Simulation Code for Transients in LMFBRs (SSC-L Code)," Brookhaven National Laboratory, BNL-NUREG-50773 (1978).
63. TANG, Y. S., COFFIELD, R. D. Jr., and MARKLEY, R. A., *Thermal Analysis of Liquid Metal Fast Breeder Reactors*, American Nuclear Society (1978).
64. MEYER, J. E., "Some Physical and Numerical Considerations for the SSC-S Code," Brookhaven National Laboratory, BNL-NUREG-50913 (1978).
65. FRIEDLAND, A. J., "Coolant Properties, Heat Transfer and Fluid Flow of Liquid Metals," in *Fast Reactor Technology: Plant Design*, Ed. by J. G. Yevick and A. Amorosi, The M.I.T. Press, Cambridge, Massachusetts, Chapter 2, (1966).
66. LEVY, S., "Fluid Flow," in *The Technology of Nuclear Reactor Safety*, Ed. by Thompson, T.J. and Beckerly, J.G., The M.I.T. Press, Cambridge, Massachusetts, Vol. 2, Chapter 15 (1973).
67. NOVENDSTERN, E. H., "Turbulent Flow Pressure Drop Model for Fuel Rod Assemblies Utilizing a Helical Wire-Wrap Space System," *Nucl. Eng. & Design*, 22, 19 (1972).

629 206

68. AXFORD, R. A., "Two-Dimensional Multiregion Analysis of Temperature Fields in Reactor Tube Bundles," Nucl. Eng. & Design, 6, 25 (1967).
69. YANG, J. W., Brookhaven National Laboratory, Personal Communication (1977).
70. REHME, K., "Pressure Drop Correlations for Fuel Element Spacers," Nucl. Technology, 17, 15 (1973).
71. CHIU, C., TODREAS, N. E., and ROHSENOW, W. M., "Pressure Drop Measurements in LMFBR Wire-Wrapped Blanket Bundles," Trans. Am. Nucl. Soc., 30, 541 (1978).
72. ENGEL, F. C., MARKLEY, R. A., and BISHOP, A. A., "Laminar Transition, and Turbulent Parallel Flow Pressure Drop Across Wire-Wrap-Spaced Rod Bundles, Nucl. Sci. Eng., 69, 290 (1979).
73. HOFMANN, H., "Experimental Investigation on Coolant Cross Mixing and Pressure Drop in Rod Bundles with Helical Spacers," Kernforschungszentrum Karlsruhe, EURFNR-1161 (KFK-1843), (1973).
74. AGRAWAL, A. K., "Numerical Considerations in LMFBR Advanced Thermal Transient Code SSC," Trans. Am. Nucl. Soc., 21, 219 (1975).
75. YANG, J. W., and AGRAWAL, A. K., "Buoyancy-Induced Flow Redistribution in Reactor vessel of an LMFBR," Trans. Am. Nucl. Soc., 26, 450 (1977).
76. GUPPY, J. G., and AGRAWAL, A. K., "Confirmatory Simulation of Safety and Operational Transients in LMFBR Systems," Paper presented at the ENS/ANS International Topical Meeting on Nuclear Power Reactor Safety, Brussels, Belgium, October 15-19, 1978.
77. AGRAWAL, A.K., GUPPY, J.G., MADNI, I.K., and WEAVER, W.L., III, "Dynamic Simulation of LMFBR Plant Under Natural Circulation," The Eighteenth ASME/AIChE National Heat Transfer Conference, San Diego, California, August 5-8, (1979).
78. MURAOKA, J., et al., "FLODISC - A Dynamic Core Flow Distribution Code: Evaluation of the Total Loss-of-Electric Power Event," Hanford Engineering Development Laboratory, HEDL-TC-8-74 (1977).
79. Staff of EBR-II, " EBR-II Performance Experiments and Analysis," Trans. Am. Nucl. Soc., 22, 588 (1975).
80. WHEELER, C. L., et al., "COBRA-IV-I: An Interim Version of COBRA for Thermal-Hydraulic Analysis of Rod Bundle Nuclear Fuel Elements and Cores," Battelle Pacific Northwest Laboratories, BNWL-1962 (1976).
81. SHA, W. T., and SCHMITT, R. C., "THI-3D - A Computer Program for Steady State and Transient Thermal Hydraulic Multichannel Analysis," Argonne National Laboratory, ANL-8112 (1974).

629 207

82. KHAN, E., "A Porous Body Model for Predicting Temperature Distributions in Wire Wrapped Fuel and Blanket Assemblies of a Liquid Metal Fast Breeder Reactor," PhD Thesis, Massachusetts Institute of Technology (Jan. 1975).
83. NOVENLSTERN, E. H., "Mixing Model for Wire-Wrap Fuel Assemblies, Trans. Am. Nucl. Soc., 15, 866 (1972).
84. BOWRING, R. W., "HAMBO: A Computer Programme for the Subchannel Analysis of the Hydraulic and Burn Out Characteristics of Rod Clusters, Part I: General Description," AEEW-R-524, U. K. Atomic Energy Establishment, Winfrith (1967); "Part II: The Equation," AEEV-R 582, U. K. Atomic Energy Establishment, Winfrith (1968).
85. CHELEMER, H., WEISMAN, J., and TONG, L. S., "Subchannel Analysis," Nucl. Eng. Design, 27, 3 (1972).
86. LORENZ, J. J., "MIX: A Computer Code for Transient Thermal Hydraulic Analysis of the LMFBR Outlet Plenum," Argonne National Laboratory, ANL-CT 75-41 (1975).
87. COOK, J. L., and NAKAYAME, P. I., "VARR II: A Computer Program for Calculating Time Dependent Turbulent Fluid Flows with Slight Density Variation," U.S. Department of Energy, CRBRP-ARD-0106 (1976).
88. DOMANUS, H.M., SCHMITT, R.C., and SHA, W.T., "Numerical Results Obtained from the Three Dimensional Transient Single Phase Version of the COMMIX Computer Code," Argonne National Laboratory, NUREG-0355, ANL-CT-78-3 (1977).
89. YANG, J. W., and AGRAWAL, A. K., "An Analytical Model for Transient Fluid Mixing in Upper Outlet Plenum of an LMFBR," in Proc. Int. Conf. on Fast Reactor Safety and Related Physics, Chicago, Illinois, October 5-8, 1976, CONF-761001, p. 1448 (1977).
90. YANG, J.W., "Comparative Studies of FFTF Upper-Plenum Mixing and Stratification," Trans. Am. Nucl. Soc., 30, 535 (1978).
91. LORENZ, J.J., and HOWARD, P.A., "A Study of the Density Interface in a Stratified LMFBR Outlet Plenum," American Society of Mechanical Engineers, ASME paper No. 77-HT-23, AIChE/ASME Heat Transfer Conference, Salt Lake City, Utah, August 15-17, 1977.
92. JONES, P., "A Study of Transient, Buoyancy-Induced Flow Stratification Relevant to the Primary Pool of a Liquid-Metal-Cooled Fast Breeder Reactor," The Sixteenth International Heat Transfer Conference, ASME, August 7-11, 1978, Toronto, Canada.
93. DWYER, O. E., "Liquid Metal Heat Transfer," in Sodium Flow, Heat Transfer, Intermediate Heat Exchangers, and Steam Generators, Sodium-NaK Engineering Handbook, Vol II, Chapter 2, Gordon and Breach, Science Publishers, Inc., New York, N.Y. (1976).

629 208

94. KAZIMI, M. S., and CARELLI, M. D., "Heat Transfer Correlations for Analysis of CRBRP Assemblies," U.S. Energy Research and Development Administration, CRBRP-ARD-0034 (1976).
95. HETRICK, D. L., and SOWERS, G. W., "BRENDA: A Dynamic Simulator for a Sodium-Cooled Fast Reactor Power Plant," U.S. Nuclear Regulatory Commission, NUREG/CR-0244 (1978).
96. ADDITON, S.L., McCALL, T.B., and WOLFE, C.F., "Simulation of the Overall FFTF Plant Performance," Hanford Engineering Development Laboratory, HEDL-TC-556 (1976).
97. "LMFBR Demonstration Plant Simulation Model, DEMO," Westinghouse Advanced Reactors Division, WARD-D-0005 (Rev. 4), (1976).
98. AGRAWAL, A.K., GUPPY, J.G., MADNI, I.K., QUAN, V., WEAVER III, W.L., and YANG, J.W., "Simulation of Transients in Liquid-Metal Fast Breeder Reactor Systems," Nucl. Sci. Eng., 64, 480 (1977).
99. CARELLI, M. D., and BACH, C. W., "LMFBR Core Thermal-Hydraulic Analysis Accounting for Interassembly Heat Transfer," Trans. Am. Nucl. Soc., 28, 560 (1978).
100. WEI, J. P., "A Practical Model of Interassembly Heat Transfer in LMFBR Assemblies," Trans. Am. Nucl. Soc., 28, 562 (1978).
101. KHAN, E., et al., "A Simplified Approach for Predicting Temperature Distribution in Wire Wrapped Assemblies," COO-2245-3, U. S. Atomic Energy Commission (Sept. 1973).
102. ROWE, D. S., "COBRA-III- A Digital Computer Program for Steady and Transient Thermal-Hydraulic Subchannel Analysis of Rod Bundles Nuclear Fuel Elements," BNWL-1695, Battelle Pacific Northwest Laboratories (1973).
103. WANTLAND, J. L., "ORRIBLE - A Series of Computer Programs for Flow and Temperature Distribution in LMFBR Fuel Bundles of Different Sizes and Configurations," ORNL-TM-4384, Oak Ridge National Laboratory (Mar. 1974); see also Trans. Am. Nucl. Soc., 15, 407 (1972).
104. GRAVES, A. W., and CATTON, I., "An Explicit Method for Predicting the Thermal Performance of FBR Wire-Wrapped Fuel Rod Assemblies," Trans. Am. Nucl. Soc., 15, 404 (1972).
105. FRANCE, D. M. and GINSBERG, T., "Evaluation of Lumped Parameter Heat Transfer Techniques for Nuclear Reactor Applications," Nucl. Sci. Eng., 51, 41 (1973).
106. MAGEE, P. M., "Modeling of Flow Sweeping Effects in Wire-Wrapped Rod Bundles," Trans. Am. Nucl. Soc., 15, 406 (1972).
107. HENRY, R. E., "A Subassembly Interchannel Mixing Program," Trans. Am. Nucl. Soc., 15, 866 (1972).

629 209

108. MARKLEY, R.A., and ENGEL, F.C., "LMFBR Blanket Assembly Heat Transfer and Hydraulic Test Data Evaluation," Presented at the IAEA Specialists' Meeting on Thermodynamics of FBR Fuel Subassembly under Nominal and Non-Nominal Operating Conditions, February 5-7, 1979 in Karlsruhe, Federal Republic of Germany.
109. COFFIELD, R.D., MARKLEY, R.A., and KHAN, E.U., "Natural Convection Analyses and Verification for LMFBR Cores," Presented at the IAEA Specialists' Meeting on Thermodynamics of FBR Fuel Subassembly under Nominal and Non-Nominal Operating Conditions, February 5-7, 1979, in Karlsruhe, Federal Republic of Germany.
110. HAN, J.T., "Blockages in LMFBR Fuel Assemblies - A Review of Experimental and Theoretical Studies," Oak Ridge National Laboratory, ORNL/TM-5839 (1977); see also HAN, J.T., and FONTANA, M.H., "Blockages in LMFBR Fuel Assemblies Symposium on the Thermal and Hydraulic Aspects of Nuclear Reactor Safety, Volume 2, Liquid Metal Fast Breeder Reactors, ed. by Jones, O.C., Jr., and Bankoff, S.G., The American Society of Mechanical Engineers, New York (1977).
111. SHA, W. T., DOMANUS, H. M., SCHMITT, R. C., ORAS, J. J., and LIN, E. I. H., "COMMIX-I: A Three-Dimensional, Transient Single-Phase Component Computer Program for Thermal-Hydraulic Analysis," Argonne National Laboratory, ANL 7-96, NUREG-0415 (1978).
112. FENECH, H., and ROHSENOW, W. M., "Heat Transfer" in Technology of Nuclear Reactor Safety, Ed. by Thompson, T.J., and Beckerly, J.G., The M.I.T. Press, Cambridge, Massachusetts, Vol 2, Chapter 16 (1973).
113. NEIMARK, L. A., LAMBERT, J. D. B., MURPHY, W. F., and RENFRO, C. W., "Performance of Mixed-Oxide Fuel Elements to 11 at. % Burnup," Nucl. Technology, 16, 75 (1972).
114. BROKAW, R. S., "Estimating Thermal Conductivities for Non-Polar Mixtures: Simple Empirical Method," Ind. Eng. Chem. 47, 2398 (1955).
115. BIANCHERIA, A., NAYAK, U. P., and BECK, M. S., "Effects of Burnup on Fuel Pin Thermal Performance," Proc. Fast Reactor Fuel Element Technology, New Orleans, Louisiana, p. 363, April 1971, American Nuclear Society.
116. JACOBS, G., and TODREAS, N., "Thermal Contact Conductance in Reactor Fuel Elements," Nucl. Sci. Eng., 50, 183 (1973).
117. MEYER, J.E., "Hydrodynamic Models for the Treatment of Reactor Thermal Transients," Nucl. Sci. Eng., 10, 269 (1961).
118. WALLIS, G.B., One-Dimensional Two-Phase Flow, Mc-Graw-Hill Book Company, New York (1969).

629 210



119. FRAAS, A.P., and OZISIK, M.N., Heat Exchanger Design, John Wiley & Sons, New York (1968).
120. PEARSON, E.N., and MOORE, H., "Intermediate Heat Exchangers (IHX's)," in Sodium Flow, Heat Transfer, Intermediate Heat Exchangers and Steam Generators, Sodium-NaK Engineering Handbook, Vol II, Chapter 3, Gordon and Breach, Science Publishers, Inc., New York, N.Y. (1976).
121. KOCH, L.J., "EBR-II - An Experimental LMFBR Power Plant," Reactor Technology, 14, No. 3., 286 (1971).
122. HENRY, H.J., "Technical Description of PFR," Nucl. Eng. Int., 16, 632 (1971).
123. LEIPUNSKII, A.I. et al., "The Atomic Power Station BN-600," in Development and Construction of Atomic Power Plants in USSR, JPRS 46, 747, Joint Publications Research Service (1968).
124. FOSTER, K.N., "Thermal Performance of the SRE Main Intermediate Heat Exchanger," USAEC Report NAA-SR-11396 (1960).
125. ALEXANDERSON, E.L. et. al., "Enrico Fermi Atomic Power Plant Operating Experience through 100 MW," in Fast Reactor National Topical Meeting, San Francisco, California, April 10-12, 1967, CONF-670413.
126. CADY, K.B., KHATIB-RAHBAR, M., PAVLENCO, G.F., and RABER, J.R., "CURL: A Transient Simulation Code for LMFBRs," Trans. Am. Nucl. Soc., 27, 543 (1977).
127. ABUROMIA, M.M., CHO, S.M., and SAWYER, R.H., "Thermal/Hydraulic Design Considerations for Clinch River Breeder Reactor Plant Intermediate Heat Exchangers," ASME Paper 75-WA/HT-101 (1975).
128. SKIRIVIN, S.C., "Users Manual for Version D of the Transient Heat Transfer Computer Program," General Electric R&D Center, 69-C-205, Schenectady, New York (1969).
129. ABUROMIA, M.M., CHU, A.W., and CHO, S.M., "Heat Transfer in Tube Bundles of Heat Exchangers with Flow Baffles Induced Mixing," ASME Paper 76-WA/HT-73 (1976).
130. GUNBY, A.L., "Intermediate Heat Exchanger Modeling for FFTF Simulation," Battelle Northwest Laboratory, BNWL-1367 (1970).
131. GEBHART, G., Heat Transfer, 2nd Edition, McGraw Hill Book Co., New York, New York (1971).
132. LYON, R.N., "Liquid Metal Heat Transfer Coefficient," Chem. Eng. Prog. 47, 75 (1951).

629 211

133. DWYER, O.E., "Eddy Transport in Liquid-Metal Heat Transfer," AICHE Journal, 9, 2, 261 (1963).
134. AOKI, S., "Current Liquid-Metal Heat Transfer Research in Japan," Progress in Heat and Mass Transfer, 7, 569, (1973).
135. SUBBOTIN, V.I., PAPOVYANTS, A.K., KIRILLOV, P.L., IVANOVSKII, N.N., "A Study of Heat Transfer to Molten Sodium in Tubes," Atomic Energy (USSR), 13, 380 (1962).
136. SELLARS, J.R., TRIBUS, M., and KLEIN, J.S., "Heat Transfer to Laminar Flow in a Round Tube or Flat Conduit - The Graetz Problem Extended," Trans. ASME, 441 (1956).
137. MARESCA, M.W., and DWYER, O.E., "Heat Transfer to Mercury Flowing In-Line Through A Bundle of Circular Rods," Trans. ASME, 180 (1964).
138. FRIEDLAND, A.J., and BONILLA, C.F., "Analytical Study of Heat Transfer Rates for Parallel Flow of Liquid Metals Through Tube Bundles, Part II, AICHE Journal, 7, 1, 107 (1961).
139. GRABER, H., and RIEGER, M., "Experimental Study of Heat Transfer to Liquid Metal Flowing In-Line Through Tube Bundles," Progress in Heat and Mass Transfer, 7, 151 (1973).
140. SPARROW, E.M., LOEFFLER, A.L. JR., and HUBBARD, H.A., "Heat Transfer to Longitudinal Laminar Flow Between Cylinders," Trans. ASME, 415 (1961).
141. DAWSON, B.E., and WOLOWODIUK, W., "Flow Model Testing for FFTF Intermediate Heat Exchanger," ASME Paper 74-PWR-21 (1974).
142. KASZA, K.E., CHEN, M.M., and BINDER, M.J., "Initial Considerations on the Influence of Thermal Buoyancy on Heat Exchanger Performance (Relevant Geometric, Operational, Thermal-Hydraulic Phenomena and Modeling Considerations)," Technical Memorandum, ANL-CT-78-47 (1978).
143. KHATIB-RAHBAR, M., "System Modeling for Transient Analysis of Loop-Type Liquid-Metal-Cooled Fast Breeder Reactors," Cornell University Nuclear Reactor Laboratory, CURL-53, Ithaca, New York (1978).
144. MADNI, I.K., "Transient Analysis of Coolant Flow and Heat Transfer in LMFBR Piping Systems," Topical Report, Brookhaven National Laboratory, (in preparation).
145. PAVLENCO, G.F., "Transient Analysis of the Primary System of a Liquid Metal-Cooled Fast Breeder Reactor Plant," Cornell University Nuclear Reactor Laboratory, CURL-49, Ithaca, N.Y. (1976).
146. LANGHAAR, H.L., "Steady Flow in the Transition Length of a Straight Tube," Journal of Applied Mechanics, 64, A55 (1942).

629 212

147. CHASE, W.L., "Heat-Transport Systems," in Fast Reactor Technology: Plant Design, Ed. by YEVICK, J.G. and Amorosi, A., The M.I.T. Press, Cambridge, Massachusetts, Chapter 4 (1966).
148. STREETER, V.L., and WYLIE, E.B., Hydraulic Transients, McGraw Hill Book Co., New York (1967).
149. STEPANOFF, Centrifugal and Axial Flow Pumps, John Wiley and Sons, Inc. New York (1957).
150. MADNI, I.K., CAZZOLI, E.G., AGRAWAL, A.K., "A Single-Phase Sodium Pump Model for LMFBR Thermal-Hydraulic Analysis," in Proc. of International Meeting on Fast Reactor Safety Technology, August 19-23, 1979, Seattle, Washington.
151. DONSKY, B., "Complete Pump Characteristics and the Effects of Specific Speeds on Hydraulic Transients," ASME Transactions, Journal of Basic Engineering, 685 (1967).
152. RELAP3B Manual, "A Reactor System Transient Code," Brookhaven National Laboratory, RP-1035 (1974).
153. QUAN, V., and AGRAWAL, A.K., "A Pipe-Break Model for LMFBR Safety Analysis," Brookhaven National Laboratory, BNL-NUREG-50688 (1977).
154. WING, P., "Control Valve Sizing," in Process Instruments and Control Handbook, Ed. by CONSIDINE, D.M., McGraw-Hill Book Co., pp. 9-43 (1974).
155. WING, P., "Control Valve Characteristics," in Process Instrument and Control Handbook, Ed. by CONSIDINE, D.M., McGraw-Hill Book Co., pp. 9-53, (1974).
156. HARRIOT, P., Process Control, McGraw-Hill Book Co., New York (1964).
157. POOL, E.B., et al., "Prediction of Surge Pressure from Check Valve for Nuclear Loops," ASME paper No. 62-WA-219 (November 1962).
158. POOL, E.B., "Minimization of Surge Pressure from Check Valves for Nuclear Loops," ASME paper No. 62-WA-220 (November 1962).
159. BALL, J.W., and TRELIS, J.P., "Report of Hydraulic Tests: 16-Inch Cold Leg Valve," Report No. 36, Hydro-Machinery Laboratory, Colorado State University, Fort Collins, Colorado, (June 1974).
160. KASZA, K.E., SCHMITT, R.C., and SHA, W.T., "Thermal Buoyancy Phenomena in a Horizontal Pipe During a Flow Coastdown, Thermal-Hydraulic Transient," ANL-CT-77-31 (1977).
161. DOMANUS, H.M., SCHMITT, R.C., and SHA, W.T., "Numerical Results Obtained from the Three Dimensional Transient Single Phase Version of COMMIX Computer Code," NUREG-0355, ANL-CT-78-3 (1978).
162. TRENT, D.S., "TEMPEST, 3-D Hydrothermal Code Development Project," Personal Communication, Pacific Northwest Laboratory (1979).

629 213

163. TRENT, D.S., Personal Communication, Pacific Northwest Laboratory, (1979).
164. LOWRIE, R.R., and SEVERSON, W.J., "A Preliminary Evaluation of the CRBRP Natural Circulation Decay Heat Removal Capability," Westinghouse Advanced Reactors Division, WARD-D-0132 (1976).
165. KHATIB-RAHBAR, M., MADNI, I. K., and AGRAWAL, A. K., "Impact of Multi-Dimensional Effects in LMFBR Piping Systems," To be published in the Transactions of the American Nuclear Society.
166. BUDNEY, G.S., and MARVOSH, J., "Steam Generators," in Sodium Flow, Heat Transfer, Intermediate Heat Exchangers and Steam Generators, Sodium-NaK Engineering Handbook, Vol. II, Chapter 4, Gordon and Breach Science Publishers Inc., New York, N.Y. (1976).
167. BAILEY, N.A., and COLLIER, J.G., "The Estimation of Tube Wall Temperatures in the Evaporator Region of Subcritical Once-Through Sodium Heated Steam Generators," U.K. Atomic Energy Establishment, AEEW-M-1000, Winfrith (1976).
168. WEINBERG, L., DURAND, R.E., and GABLES, M.J., "Vibration Tests of a Full-Scale Water Model of a Steam Generator Module," Clinch River Breeder Reactor Plant, Technical Review, CRBRP-PMC77 (Winter 1977).
169. PORSHING, T.A., MURPHY, J.H., REDFIELD, J.A., and DAVIS, V.C., "FLASH-4: A Fully Implicit FORTRAN IV Program for the Digital Simulation of Transients in a Reactor Plant," WARD-TM-840 (March 1969).
170. HOELD, A., "A Theoretical Model for Calculations of Large Transients in Nuclear Natural Circulation U-Tube Steam Generators (Digital Code UTSG)," Nucl. Eng. and Design 47, 1 (1978).
171. WEAVER, W.L. III, MEYER, J.E., and AGRAWAL, A.K., "A Few-Pressure Model for Transient Two-Phase Flows in Networks," Trans. Am. Nucl. Soc. 28, 273 (1978).
172. AGEE, L.J., "An Analytical Method of Integrating the Thermal-Hydraulic Conservation Equations," Nucl. Eng. and Design 42, 195 (1977).
173. AGEE, L.J., "Power Series Solutions of the Thermal-Hydraulic Conservation Equations," Paper Presented at the Second ORCD/NEA Specialists Meeting on Transient Two-Phase Flow, Paris, France (June 1978).
174. MOORE, K.V., and ROSE, R.P., "Application of a Lumped Parameter Bubble-Rise Model," Trans. Am. Nucl. Soc. 9, 2, 559 (1966).
175. YBARRONDO, L.J., SOLBRIG, C.W., and ISBIN, H.S., "The Calculated Loss-of-Coolant Accident: A Review," AIChE Monograph Series 7, 68 (1972).
176. COLLIER, J.G., Convective Boiling and Condensation, McGraw-Hill Book Co., United Kingdom (1972).
177. COLBURN, A.P., "A Method of Correlating Forced Convection Heat Transfer Data and a Comparison with Fluid Friction," AIChE Transactions 29, 174 (1933).

629 214

178. CHEN, J.G., "Correlation for Boiling Heat Transfer to Saturated Fluids in Convective Flow," I&EC Process Design and Development 5, 322 (1966).
179. FOSTER, W.K., and ZUBER, N., "Dynamics of Vapor Bubbles and Boiling Heat Transfer," AIChE Journal 1, (4), 531 (1955).
180. GROENEVELD, D.C., "Post-Dryout Heat Transfer: Physical Mechanisms and a Survey of Prediction Methods," Nucl. Eng. and Design 32, 283 (1975).
181. TONG, L.S. and WEISMAN, J., Thermal Analysis of Pressurized Water Reactors, American Nuclear Society Monograph Series, Illinois (1970).
182. GANIC, E.N., and ROHSENOW, W.M., "Post Critical Heat Flux Heat Transfer," Massachusetts Institute of Technology, Report No. 82672-97, Cambridge, Mass. (1976).
183. BISHOP, A.A., SANDBER, R.O., and TONG, L.S., "Forced Convection Heat Transfer at High Pressure After the Critical Heat Flux," ASME Paper No. 65-TH-31 (1965).
184. CAMPOLUNGI, F., CUMO, M., and FERRARI, G., "On the Thermal Design of Steam Generators for LMFBRs," Trans. Am. Nucl. Soc. 26, 137 (1975).
185. LEE, D.H., "Prediction of Burnout," in Two-Phase Flow and Heat Transfer, Edited by D. Sutterworth and G.F. Hewitt, Harwell Series, Oxford University Press (1977).
186. TONG, L.S., Boiling Crisis and Critical Heat Flux, AEC Critical Review Series, TID-25887, U.S. Atomic Energy Commission (1972).
187. HARTY, R.B., "Modular Steam Generator Final Project Report," Atomic International Division of Rockwell International, TR-097-330-010 (September 1974).
188. BEIN, M., and YAHALOM, R., "Some Aspects of Modeling Power Plant Thermal Hydraulics," Nucl. Eng. and Design 44, 187 (1977).
189. NAHAVANDI, A.N., "The Loss-of-Coolant Accident Analysis in Pressurized Water Reactors," Nucl. Sci. Eng. 36, 159 (1969).
190. LOCKART, R.W., and MARTINELLI, R.C., "Proposed Correlation of Data for Isothermal Two-Phase, Two-Component Flow in Pipes," Chem. Eng. Prog. 45(1), 39(1949).
191. MARTINELLI, R.C. and NELSON, D.B., "Prediction of Pressure Drop During Forced Circulation Boiling of Water," Trans. ASME (1948).
192. ARMAND, A.A., "The Resistance During the Movement of a Two-Phase System in Horizontal Pipe," AERE, Translation, 828, U.K. Atomic Energy Authority Research Group Translation (1959).
193. LEVY, S., "Steam Slip-Theoretical Prediction from Momentum Model," J. of Heat Transfer 113 (May 1960).

629 215

194. MCMILLAN, H.K., FONTAINE, W.E., and CHADDOK, J.B., "Pressure Drop in Isothermal Two-Phase Flow," ASME Paper No. 64-WA/FE-4 (1964).
195. THOM, J.R.S., "Prediction of Pressure Drop During Forced Circulation Boiling of Water," Int. J. of Heat Mass Transfer 7, 709 (1964).
196. BARCOZY, C.J., "A Systematic Correlation for Two-Phase Pressure Drop," Chem. Eng. Prog. Ser. 64, 62, 232 (1966).
197. WULFF, W., "THOR-1 (PWR): A Computer Code for Predicting the Thermal Hydraulic Behavior of Nuclear Reactor Systems," Vol. 2, Process Modeling and Verification, Brookhaven National Laboratory, BNL-NUREG-24760 (1978).
198. AGRAWAL, A.K., et. al., "Preaccident Modeling of an LMFBR Plant for SSC-L," Brookhaven National Laboratory, BNL-NUREG-50602 (1976).
199. GUPPY, J.G., AGRAWAL, A.K., MADNI, I.K., WEAVER, W.L., and YANG, J.W., "Preaccident Modeling of an LMFBR Plant," Trans. Am. Nucl. Soc., 24, 257 (1976).
200. ALBRIGHT, D.C., and BARI, R.A., "Primary Pipe Rupture Accident Analysis for the Clinch River Breeder Reactor," Nucl. Technology, 39, 225 (1978).
201. YANENKO, N.N., The Method of Fractional Steps, Springer-Verlag, New York (1971).
202. GEAR, C.W., Numerical Initial Value Problems in Ordinary Differential Equations, Prentice-Hall, Inc., Englewood, Cliffs, New Jersey (1971).
203. HINDMARSH, A.C., "GEAR: Ordinary Differential Equation System Solver," Lawrence Livermore Laboratory, UCID-30001, Rev. 3 (1974).
204. HINDMARSH, A.C., and BYRNE, G.D., "EPISODE: An Experimental Package for the Integration of Systems of Ordinary Differential Equations," Lawrence Livermore Laboratory, UCID-30112 (1975).
205. ASME Boiler and Pressure Vessel Code, Section III, Subsection NA, Div. 1-1974 Edition.
206. GRAHAM, J., Fast Reactor Safety, Academic Press, New York (1971).
207. GRAHAM, J., ZEMANICK, P. P., "The Role of Reliability and Risk Assessment in LMFBR Design: Implementation of Reliability in LMFBR Design, in Nuclear Systems Reliability Engineering and Risk Assessment, Edited by J. B. Fussell and G. R. Burdik, pp. 676-709, Society for Industrial and Applied Mathematics, Philadelphia, PA (1977).
208. FARMER, F. R., Reactor Safety and Siting: A Proposed Risk Criterion. Nuclear Safety, Vol. 8, No. 6, pp. 539-548 (1976).
209. CRBRP, Primary Pipe Integrity Status Report, Westinghouse Advanced Reactors Division, WARD-D-C127, Madison, PA (1975).

629 216

210. PERKINS, K. R., BARI, R. A., and ALBRIGHT, D. C., "Uncertainties in the Calculated Response of the Clinch River Breeder Reactor During Natural Circulation Decay Heat Removal, BNL-NUREG-22715 (Informal Report) April 1977.
211. HAYEN, E. W., "Anticipated Transients Without Scram: Status Quo, Nuclear Safety Vol. 17, No. 1, pp. 43-54, January-February (1976).
212. Code of Federal Regulation, Section 50.36(d) of IOCFR50, Licensing of Production and Utilization Facilities, U. S. Federal Register (31), 158-10891, (1966).
213. KHATIB-RAHBAR, M., and AGRAWAL, A. K., "Plant Protection and Control System Modeling" in Reactor Safety Research Programs, Quarterly Progress Report, April 1-June 30, 1978, NUREG/CR-0316, BNL-NUREG-50883, pp. 136-140, U. S. Department of Commerce, Springfield, Virginia (August 1978).
214. CAPERSSON, S. A. et al., "A Carbide Radial Blanket for a Demonstration LMFBR," Trans. Am. Nucl. Soc. 18, 277 (1974).
215. FOX, J. N., LAWER, B. E., and BUTS, H. R., "FORE-II; A Computational Program for the Analysis of Steady State and Transient Reactor Performance," General Electric Co. GE-AP-5273 (1966).
216. KHAN, E. U., ROHSENOW, W. M., SONIN, A. A. and TODREAS, N. E., "A Porous Body Model for Predicting Temperature Distribution in Wire-Wrapped Rod Assemblies Operating in Combined Forced and Free Convection," Nucl. Eng. and Design 35, pp. 199-211 (1975).
217. DURHAM, M. E., "Influence of Reactor Design on the Establishment of Natural Circulation in Pool-Type LMFBR," J. Br. Nucl. Energy Soc., 15, No.4, pp. 305-310, (1976).
218. DURHAM, M. E., "Optimization of Reactor Design for Natural Circulation Decay Heat Removal in a Pool-Type LMFBR," in Optimization of Sodium-Cooled Fast Reactors, British Nuclear Energy Society, pp. 45-53, London (1977).
219. ADDITON, S. L., and PARZIALE, E. A., "Natural Circulation in FFTF, A Loop Type LMFBR," Symposium on the Thermal and Hydraulic Aspects of Nuclear Reactor Safety, Vol. 2: Liquid Metal Fast Breeder Reactors, pp. 265-283, ASME Winter Meeting, Atlanta, Georgia (November 27-December 2, 1977).
220. SINGER, R. M. et al., "Steady State Natural Circulation Performance of the EBR-II Primary Heat Transport Circuit, Nucl. Sci. and Eng. 63, pp. 75-82 (1977).
221. SINGER, R. M., GRAND, D., and MARTIN, R., "Natural Circulation Heat Transfer in Pool-Type LMFBRs," Symposium on the Thermal and Hydraulic Aspects of Nuclear Reactor Safety, Vol. 2: Liquid Metal Fast Breeder Reactors, pp. 239-264, ASME Winter Meeting, Atlanta, Georgia (November 27-December 2, 1977).

629 217

222. PERKINS, K. R., BARI, R. A., and ALBRIGHT, D. C., "Natural Circulation Decay Heat Removal in an LMFBR," Trans. Am. Nucl. Soc., 27, 542-543 (1977).
223. KHATIB-RAHBAR, M., and CADY, K. B., "Establishment of Buoyancy-Induced Natural Circulation in Loop-Type LMFBRs, Trans. Am. Nucl. Soc., 28, 432-433 (1978).
224. BOUCHEY, G. D., ADDITON, S. L., and PARZIALE, E. A., "Planned Natural Circulation Testing in the Fast Flux Test Facility," Trans. Am. Nucl. Soc. 28, 592-594 (1978).
225. GUPPY, J. G., and AGRAWAL, A. K., "Confirmatory Simulation of Safety and Operational Transients in LMFBR Systems," Paper presented at the International ENS/ANS Topical Meeting on Nuclear Power Reactor Safety, Brussels, (October 16-19, 1978).
226. GILLETE, J. L., TOKAR, J. V., and SINGER, R. M., "Experimental Observations of Intersubassembly Heat Transfer Effects During Natural Circulation," Trans. Am. Nucl. Soc. 30, 537-538 (1978).
227. AGRAWAL, A. K., GUPPY, J. G., MADNI, I. K., and WEAVER, W. L. III, "Dynamic Simulation of LMFBR Plant Under Natural Circulation," Proceedings of the 18th ASME National Heat Transfer Conference, San Diego, California, August 5-8, 1979.
228. KHATIB-RAHBAR, M., MADNI, I. K., AGRAWAL, A. K., and CAZZOLI, E. G., "Transition to Natural Convection From Low-Temperature, Low-Flow Conditions in Loop-Type LMFBRs, Trans. Am. Nucl. Soc. 31 (1979).
229. MADNI, I. K., KHATIB-RAHBAR, M., and AGRAWAL, A. K., "Effect of Pump Stored-Kinetic Energy on Natural Circulation Decay-Heat Removal in Loop-Type LMFBRs, Trans. Am. Nucl. Soc. 31 (1979).
230. SINGER, R. M., MOHR, D., and TOKAR, V., "LMFBR Transition to Natural Circulation from an Initial Isothermal State, Trans. Am. Nucl. Soc., 30, pp. 412-413 (1978).
231. SINGER, R. M., and GILLETE, J. L., "Experimental Study of Whole Core Thermal-Hydraulic Phenomena In EBR-II, Nucl. Eng. and Design 44, pp. 177-186, 1977.
232. SINGER, R. M., "Natural Circulation and Decay Heat Removal in LMFBRs, Seminar Presented at Brookhaven National Laboratory, Jan 30, 1979.
233. SMAARDYK, A. et al., "EBR-II Environmental Instrumented Subassembly XX08: Engineering and Assembly, ANL-78-9, (May 1978).
234. GILLETTE, J.L., SULLIVAN, J.E., TOKAR, and SINGER, R.M., "Compilation of Data From EBR-II Natural-Circulation-Test Procedure EX-140, Section IV, Addendum 1A, ANL/EBR-101, (May 1978).

629 218



235. GILLETTE, J.L., SULLIVAN, J.E., TOKAR, J.V., and SINGER, R.M., "Compilation of Data from EBR-II Natural-Circulation-Test Procedure EX-140, Section IV, Addendum 1E, ANL/EBR-102 (September 1978).
236. BETTEN, P.R., "A Tabulation of XX07 and EBR-II Core Parameters for the EBR-II Core Natural Circulation Experiment; XX07 Test F, Letter from P.R. Betten to R.J. Neuhold, ANL (July 25, 1978).
237. GILLETTE, J.L., SULLIVAN, J.E., SINGER, R.M., TOKAR, J.V., and DEAN, E.M., "Compilation of Data From EBR-II Natural-Circulation-Test Procedure EX-140, Section IV, Addendum 7A, under publication (July 1979).
238. BETTEN, P.R., GILLETTE, J.L., MOHR, D., and SINGER, R.M., "A Tabulation of XX08 Parameters and Experimental Data for the EBR-II Natural Circulation Experiment, Test 7A, under publication (January 1979).
239. MOHR, D., BETTEN, P.R., GILLETTE, J.L., and SINGER, R.M., "Boundary Conditions, Driving Functions and Calculated Results for an Average Driver in the EBR-II Natural Circulation Experiment, Test 7A, under publication (January 1979).
240. "Piping Integrity for LMFBRs, Special Session," Trans. Am. Nucl. Soc. 23, 380 (1976).
241. "Primary Pipe Integrity Status Report," Westinghouse Advanced Reactors Division, WARD-D-0127 (1975).
242. ZEMANICK, P. P., WITT, F. J., and SACRAMO, R. F., "Probabilistic Assessments of Primary Piping Integrity," Trans. Am. Nucl. Soc., 23, 382 (1976).
243. HUMMEL, H. H., and KALIMULLAH, "Pipe Rupture Studies for the CRBR Using DEMO and SAS," in Proceedings of the International Meeting on Fast Reactor Safety and Related Physics, Chicago, Illinois, October 5-8, 1976, CONF-761001, P. 1101 (1976).
244. ADDITON, S. L., and CHIEN, Y. M., "Simulation of FFTF Hot-Leg Ruptures, and Loss-of-Flow Events," Trans. Am. Nucl. Soc., 28, 594 (1978).
245. COFFIELD, R.D., and PLANCHON, H.P., "LMFBR Natural Circulation Verification Program (NCVP) - Review of Experimental Facilities and Testing Recommendations," Westinghouse Advanced Reactors division, WARD-NC-3045-1, Madison, Pennsylvania, USA.
246. "FBR Systems Simulation and Verification," Special Session held at San Diego, California during 1978 Annual Meeting of the American Nuclear Society, Trans. Am. Nucl. Soc., 28, 587 (1978).
247. HAIN, H., HOFMANN, F., KIRSCH, D., KLEEFELDT, K., KRAMER, W., and MEYER, R., "Modellversuche zum tankinternen Notkuehlensystem des Prototyp-Reactors SNR-300," Gesellschaft fur Kernforschung M.B.H., Karlsruhe, KFK-1895 (June, 1974).
248. KRIEGER, T.J., DURSTON, C., and ALBRIGHT, D.C., "Statistical Determination of Effective Variables in Sensitivity Analysis," Trans. Am. Nucl. Soc., 28, 515 (1978).

629 219

APPENDIX A

629 220

## LIST OF TABLES

### Table No.

- |      |   |
|------|---|
| 1.1  | LMFBR Projects Throughout the World   |
| 2.1  | Attributes of Analog and Digital Computers  |
| 3.1  | Key Core Parameters for LMFBRs  |
| 3.2  | Material Properties for Different LMFBR Fuels   |
| 3.3  | Design and Nuclear Performance Comparison of Oxide, Carbide and Nitride Fuels               |
| 3.4  | Design and Nuclear Characteristics of Different Large LMFBR Designs                         |
| 3.5  | Delayed-Neutron Half-Lives and Decay Constants  |
| 3.6  | Doppler Coefficient for Oxide, Carbide and Nitride U-Pu Fuels in a 500 MWe Design           |
| 3.7  | Calculated Doppler Coefficient for CRBRP  |
| 3.8  | Isothermal Sodium Temperature Coefficient of Reactivity for CRBRP                           |
| 3.9  | Isothermal Temperature Coefficients of Reactivity in EBR-II and FERMI                       |
| 3.10 | Reactivity Effect Due to Power Operation in the CRBRP                                       |
| 3.11 | Combined Long-Term Reactivity Effects   |
| 3.12 | Flow Distribution in the CRBRP  |
| 3.13 | Correlations for Free Convection in Liquid Metals   |
| 3.14 | Comparison of Thermohydraulic Codes for Wire-Wrapped Assemblies                             |
| 4.1  | Intermediate Heat Exchanger Design Data   |
| 4.2  | Nusselt Number Correlations for Fully Developed Turbulent Flow Inside Round Tubes           |
| 4.3  | Nusselt Number Correlations for Fully Developed Turbulent Flow Through Unbaffled Tube Banks |
| 4.4  | Theoretical Values of the Hydrodynamic Potential Drop [93]                                  |

629 221

LIST OF TABLES (Cont.)

Table No.

- 5.1 Typical Velocity Head Factor Values
- 5.2 Homologous Head and Torque Polynomial Coefficients  
(H, B = Head or Torque Curve; A or V = Division by  $\alpha^2$   
or  $v^2$ ; N, D, T or R = Normal, Energy Dissipation, Turbine,  
or reverse pump region)
- 5.3 Pump Friction Torque Correlations
- 6.1 Steam Generating System Design Data
- 7.1 Examples of Different Time Constants in CRBRP
- 7.2 Range of Time-Step Sizes for LMFBR Systems
- 8.1 Accident Classification
- 8.2 Steady-State Power and Flow Fractions in SSC-L
- 8.3 EBR-II Whole Core/Whole Plant Tests and Events
- 8.4 Initial Conditions for Tests 1A and 1E of EBR-II
- 9.1 LMFBR System Verification Needs

629 222

TABLE 1.1 LMFBR PROJECTS THROUGHOUT THE WORLD

Reactor	Power, MW		Basic Design	Type of Facility	Status
	Thermal	Electrical			
<u>FRANCE</u>					
RAPSODIE	40	-	Loop	Experimental	In operation since 1967.
PHENIX	563	250	Pool	Demonstration	In operation since 1973.
SUPERPHENIX-1	3000	1200	Pool	Commercial	Under construction, Criticality 1982.
<u>GERMANY</u>					
KNK-2	58	20	Loop	Experimental	Converted from the thermal neutron KNK-1, in operation since 1977.
SNR-300	762	327	Loop	Demonstration	Under construction, Criticality 1981 (?).
SNR-2	3750	1300-1500	Loop	Commercial	In design, Criticality 1988.
<u>GREAT BRITAIN</u>					
DFR	60	14	Loop	Experimental	Initial operation 1959, Decommissioned 1977.
PFR	600	250	Pool	Demonstration	In operation since 1974.
CFR	3250	1320	Pool	Commercial	In design, Criticality 1986.

629

225

TABLE 1.1 LMFBR PROJECTS THROUGHOUT THE WORLD (Cont'd)

Reactor	Power, MW		Basic Design	Type of Facility	Status
	Thermal	Electrical			
<u>INDIA</u>					
FBTR	42.5	12.5-15	Loop	Experimental	Under construction, Criticality 1980.
FBR-500	?	500	Pool	Commercial	In design.
<u>ITALY</u>					
P.E.C.	116	-	Loop	Experimental	In construction, Criticality 1980.
<u>JAPAN</u>					
JOYO	100	-	Loop	Experimental	In operation since 1977.
MONJU	714	300	Loop	Demonstration	In design, Criticality 1984.
<u>U.S.S.R.</u>					
BR-5	5	-	Loop	Experimental	Initial operation 1958, It was upgraded to BR-10.
BR-10	10	-	Loop	Experimental	BR-5 was upgraded in 1973.
BOR-60	60	12	Loop	Experimental	In operation since 1969.
BN-350	1000	350	Loop	Demonstration	In operation since 1972.
BN-600	1470	600	Pool	Commercial	Under construction, Criticality 1979.
BN-1600	?	1500	Pool	Commercial	

TABLE 1.1 LMFBR PROJECTS THROUGHOUT THE WORLD (Cont'd)

Reactor	Power, MW		Basic Design	Type of Facility	Status
	Thermal	Electrical			
<u>U.S.A.</u>					
Clementine	0.025	-	Loop	Experimental	First fast reactor, Initial operation 1946, Decommissioned 1953.
EBR-I	1	0.2	Loop	Experimental	Initial operation 1951.
EBR-II	62.5	20	Pool	Experimental	In operation since 1963.
FERMI	200	-	Loop	Experimental	Initial operation 1963, Decommissioned.
SEFOR	20	-	Loop	Experimental	Initial operation 1970, Decommissioned 1975.
FFTF	400	-	Loop	Experimental	In construction, Criticality 1979.
CRBRP	975	350	Loop	Demonstration	?
PLBR				Commercial(?)	

025  
225

TABLE 2.1 ATTRIBUTES OF ANALOG AND DIGITAL COMPUTERS

Attribute	Analog Computer	Digital Computer
Accuracy	Limited by the quality of computer components ( $\approx 0.01\%$ of full-scale)	Determined by the number of bits in memory registers and numerical technique
mode of operation	Parallel	Sequential (future computers do have parallel processing)
Speed	Real-time operation; speed limited by the bandwidth characteristics of the computing elements	Determined by problem complexity
Efficiency	Multiplication, addition, integration, and non-linear functions generations performed efficiently	Limited number of arithmetic operations (addition and multiplication); more complex operations (such as integration) performed by numerical techniques
	Limited ability for logical operations, storage of data	Indefinite storage of numerical and non-numerical data, facility for logical operations
Programming techniques	Consist of substituting analog computing elements for corresponding elements in a physical system	Little direct relationship to the problem under study

629  
226



TABLE 3.1 KEY CORE PARAMETERS FOR LMFBRs

Parameter	CRBRP (Prototypic)	SUPERPHENIX (Commercial)
<u>CORE</u>		
Equivalent diameter (m)	1.87	3.5
Fuel height (m)	0.914	1.0
Volume (L)	2,510	10,000
Fuel and blanket arrangement	Homogeneous	Homogeneous
No. of fuel enrichment zones	2	2
No. of orifice zones		
Fuel/blanket	5/4	
<u>FUEL ASSEMBLIES</u>		
Number inner/outer	108/90	193/171
Flat-to-flat outside distance (mm)	116.2	173
Assembly wall thickness (mm)	3.0	
Assembly pitch (mm)	120.9	179
Number of rods per assembly	217	271
Clad ID/OD (mm)	5.08/5.84	/8.65
Spacer wire diameter (mm)	1.4	1.1
Fuel rods pitch-to-diameter ratio	1.24	1.13
Fuel forms	pellet	annular pellet
Fuel/blanket pellet OD (mm)	4.92/4.92	7.02/7.02
Core region length (m)	0.914	1.0
Fuel type	(U-Pu)O <sub>2</sub>	(U-Pu)O <sub>2</sub>
Fuel density		
nominal (% TD)	91.3	
cold smeared (% TD)	85.5	
Pu enrichment inner/outer Pu/(U + Pu) (%)	17.7/25.6	14.5/18.5
Axial blanket height lower/upper (mm)	355/355	300/300
Blanket pellet material	Depleted UO <sub>2</sub>	Depleted UO <sub>2</sub>
Nominal pellet density (% TD)	96.0	
Fission gas plenum length lower/upper (mm)	-/1220	850/150
Cladding material	20% CW SS 316	SS 316L
<u>BLANKET ASSEMBLIES</u>		
Number	150	233
Number of rods per assembly	61	91
Clad ID/OD (mm)	12.09/12.85	/16.3
Rod pitch-to-diameter ratio	1.072	1.07
Pellet OD (mm)	11.94	14.8
Blanket region length (m)	1.63	1.60
Pellet density		
nominal (% TD)	95.6	
cold smeared (% TD)	93.2	
Pellet material	Depleted UO <sub>2</sub>	Depleted UO <sub>2</sub>
Cladding material	20% CW SS 316	SS 316L
<u>CONTROL ASSEMBLIES</u>		
Number Primary/Secondary	15/4	21/3
Number of absorber rods per assembly		
Primary/Secondary	37/31	31/
Cladding outside diameter		
Primary/Secondary (mm)	15.52/14.04	
Cladding inside diameter		
Primary/Secondary (mm)	12.47/12.56	
Pellet material	B <sub>4</sub> C	Enriched B <sub>4</sub> C
Pellet outside diameter		
Primary/Secondary (mm)	11.66/11.78	
Pellet density (% TD)	92	
Absorber column length (m)	0.914	1.10

629 227

TABLE 3.2 MATERIAL PROPERTIES FOR DIFFERENT LMFBR FUELS

Property	Fuel Type		
	(U-Pu) $O_{1.26}$	(U-Pu) $C_{1.04}$	(U-Pu) $N_{1.00}$
Theoretical density (kg/m <sup>3</sup> )	10.87x10 <sup>3</sup>	13.60x10 <sup>3</sup>	14.30x10 <sup>3</sup>
Heavy metal theoretical density (kg/m <sup>3</sup> )	9.80x10 <sup>3</sup>	12.90x10 <sup>3</sup>	13.50x10 <sup>3</sup>
Thermal conductivity at 1000 K (W/mK)	2.7	17.7	18.5
Melting point (K)	2980	2755	3030
Specific heat at 1000 K (kJ/kg K)	0.33	0.19	0.32

629 228

TABLE 3.3 DESIGN AND NUCLEAR PERFORMANCE COMPARISON OF  
OXIDE, CARBIDE, AND NITRIDE LMFBRs

Parameter	Fuel Type		
	(U-Pu)O <sub>1.96</sub>	(U-Pu)C <sub>1.04</sub>	(U-Pu)N <sub>1.00</sub>
<u>Design</u>			
Fuel pin clad ID/OD (mm)	5.59/6.35	8.23/8.99	7.85/8.61
Fuel bond material	Helium	Sodium	Sodium
Fuel density - cold smeared (% TD)	80.0	79.1	82.2
Heavy metal content in core (kg)	7837	9480	9629
Pu enrichment (%)	15.6	12.4	12.5
<u>Performance</u>			
Average Linear Power (kw/m)	28.9	61.7	61.7
Breeding ratio	1.20	1.42	1.35
Internal breeding ratio	0.66	0.82	0.80
Doubling time (yrs)	28.0	11.4	14.8
Average/peak heavy metal discharge burnup (MWd/kg)	65/100	50/78	47/71
Doppler coefficient, Tdk/dt ( $\Delta k/k$ )	-0.0070	-0.0075	-0.0074
Full power days per cycle (d)	156	218	205
Equilibrium fuel cycle cost (mills/kWhr)	1.80	1.48	1.79

629 229

TABLE 3.4 DESIGN AND NUCLEAR CHARACTERISTICS OF DIFFERENT LARGE LMFBR DESIGNS

Parameter	$(Pu-U)O_2$		$(U^{233}-Th)O_2$	
	Homogeneous Core	Heterogeneous Core	Homogeneous Core	Heterogeneous Core
Reactor Power (MWe) (MWt)	1200 3740	1200 3740	950 3000	950 3000
Number of Fuel Assemblies	414	396	252	222
Number of Blanket (Inner/Outer) Assemblies	-/252	235/306	-/216	121/234
Core diameter (m) height (m)	2.91 1.22	3.64 1.22	3.14 1.22	3.50 1.22
Fuel Rod diameter (mm)	5.84	5.84	8.89	8.64
Number of rods per assembly Core/blanket	271/127	271/127	271/127	271/127
Breeding Ratio	1.176	1.336	1.140	1.190
EOEC Doppler Coefficient ( $\Delta k/k$ )	-0.0065	-0.0081	-0.0085	-0.0095
Core Sodium void worth (\$)	6.16	3.24	-0.09	-1.32

620 230

TABLE 3.5 DELAYED-NEUTRON HALF-LIVES AND DECAY CONSTANTS

Group Index	$U^{235}$		$Pu^{239}$		CRBRP (LWR Fuel)	
	$\lambda_i$ ( $s^{-1}$ )	$\beta_i$	$\lambda_i$ ( $s^{-1}$ )	$\beta_i$	$\lambda_i$ ( $s^{-1}$ )	$\beta_i$
1	0.0127	0.00063	0.0129	0.00024	0.0129	0.000082
2	0.0317	0.00351	0.0311	0.00176	0.0312	0.000776
3	0.115	0.00310	0.134	0.00136	0.133	0.000666
4	0.311	0.00672	0.331	0.00207	0.345	0.001354
5	1.40	0.00211	1.26	0.00065	1.41	0.000591
6	3.87	0.00043	3.21	0.00022	3.75	0.000181
	Total	0.0165	Total	0.0063	Total	0.00365

629 231

TABLE 3.6 DOPPLER COEFFICIENT FOR OXIDE, CARBIDE AND NITRIDE  
U-Pu FUELS IN A 500-MWe DESIGN

Parameter	Fuel Type		
	Oxide	Carbide	Nitride
Fuel form	(U-Pu)O <sub>1.96</sub>	(U-Pu)C <sub>1.04</sub>	(U-Pu)N <sub>1.00</sub>
Fuel-clad bond material	Helium	Sodium	Sodium
Fertile-to-fissile ratio U/Pu	5.4	7.1	7.0
T(dk/dt)                      (Δk/k)	-0.0070	-0.0075	-0.0074
Δβ (1100 → 1500k)              (Δk/k)	-0.0022	-0.0023	-0.0023

629 232

TABLE 3.7 CALCULATED DOPPLER COEFFICIENT FOR CRBRP

Reactor Region	$-T \left( \frac{dk}{dT} \right)_{\text{Dopp}} \times 10^4$			
	BOEC		EOEC	
	Na in	Na out	Na in	Na out
Lower axial blanket	5.2	3.4	5.7	3.9
Upper axial blanket	1.1	1.0	1.7	1.5
Inner core	34.4	16.3	37.0	19.2
Outer core	10.7	6.1	13.1	7.7
Radial blanket	11.0	10.2	12.1	11.9
Total	62.4	37.0	69.6	44.2

629 233

TABLE 3.8 ISOTHERMAL SODIUM TEMPERATURE COEFFICIENT OF REACTIVITY FOR CRBRP

Reactor Region	(dk/dT) Sodium	
	$10^{-6} \Delta k/K$	$10^{-3} \beta/K$
Lower axial blanket	-0.33	-9.0
Upper axial blanket	-0.33	-9.0
Inner Core	1.84	50.4
Outer Core	-1.12	-30.6
Radial Blanket	-0.46	-12.6

629 234



TABLE 3.9 ISOTHERMAL TEMPERATURE COEFFICIENTS OF REACTIVITY IN EBR-II AND FERMI

Mechanism	$(\Delta k/k)/\Delta T$ in $10^{-6} (\Delta k/k)/K$	
	EBR-II	FERMI
<u>Core</u>		
Axial fuel expansion	-3.9	-2.5
Radial fuel expansion (Sodium expulsion)	-0.9	-0.6
Density change of coolant and assembly material	-9.1	-7.1
Structure expansion	-9.7	-6.0
<u>Blanket</u>		
Density change of coolant and assembly material	-9.5	-3.3
Growth of uranium	-1.0	-0.5
Structure expansion	-2.0	-0.6
Total	-36.1	-20.6

629 235

TABLE 3.10 REACTIVITY EFFECT DUE TO POWER OPERATION IN THE CRBRP

Components	Reactivity, cents	
	Initial Isothermal Temperature	
	at 478 K	at 589 K
Doppler		
Inner core	-162.6	-130.9
Outer core	- 38.2	- 29.9
Radial blanket	- 12.1	- 6.1
Axial blankets	- 5.8	- 3.1
Total Doppler	-218.7	-170.0
Sodium temperature	- 2.4	- 1.4
Axial fuel expansion	- 20.0	- 15.4
Radial core expansion	- 69.0	- 29.0
Bowing	+ 50.0*	+ 30.0*
Total	-260.1	-185.8

\*Estimated by the authors

629 236

TABLE 3.11 COMBINED LONG-TERM REACTIVITY EFFECTS

Reactor Type	Atoms/cm <sup>3</sup> Pu plus U (10 <sup>24</sup> )	Burnup, % of Pu + U fissioned	$\Delta k/k$			
			Burnup in core	Buildup in blanket	Fission product buildup	Total
EBR-II (metal)		2	- 0.018	+ 0.007	- 0.002	- 0.013
800-liter (metal)	0.012	5	- 0.054	+ 0.026	- 0.017	- 0.045
1500-liter (oxide)	0.00467	10	- 0.169	+ 0.025	- 0.037	- 0.181
1500-liter (carbide)	0.0069	10	- 0.147	+ 0.031	- 0.028	- 0.144

629

231

TABLE 3.12 FLOW DISTRIBUTION IN THE CRBRP

Component	Number of Assemblies	Flow		
		$10^6$ kg/hr	% Total	per assembly kg/s
Fuel Zone 1	66	5.8	30.6	24.4
2	78	5.9	31.2	21.0
3	36	2.3	12.4	17.7
4	12	0.7	3.9	16.2
5	6	0.3	1.7	13.9
Total	198	15.0	79.8	-
Blanket Zone 6	24	0.7	3.7	8.10
7	30	0.8	4.3	7.41
8	54	0.9	4.8	4.63
9	42	0.3	1.6	1.98
Total	150	2.7	14.4	-
Control Assembly	19	0.3	1.6	4.39
Radial shield	324	0.3	1.6	0.26
Bypass and leakage		0.5	2.6	
Total for Reactor		18.8	100.0	

629 238

TABLE 3.13 CORRELATIONS FOR FREE CONVECTION IN LIQUID METALS

Configuration	Correlation	Range
Free convection in liquid sodium to a cold horizontal plate	$Nu_D = 0.0785 (Ra)^{0.32}$ $Nu_D = \frac{hD}{k}$ D = diameter of horizontal plate	Turbulent regime $5 \times 10^6 \leq Ra \leq 4 \times 10^7$
Free convection to a heated vertical plate	$Nu_x = 0.3 (Ra_x)^{0.25}$ X = plate height	Laminar regime $Ra_x < 10^6$
Free convection from inside wall of a vertical vessel	$Nu_x = 0.16 [(Ra_x)(rx)]^{0.3}$ x = total height of cylindrical wall r = radius of vessel	Both laminar and turbulent regimes
Free convection to a horizontal cylinder	$Nu_D = 0.53 (Ra Pr)^{0.25}$ D = diameter of cylinder	Laminar regime $Re < 10^5$
Free convection across an enclosed liquid-metal gap between plates	Vertical parallel plates: $Nu_D = 0.028 (Ra_D)^{0.355}$ Horizontal parallel plates: $Nu_D = 0.043 (Ra_D)^{0.33}$ D = distance between plates	Turbulent regime $4 \times 10^4 \leq Ra \leq 1 \times 10^8$
Free convection within an open-ended channel	$Nu_D = 0.68 (Ra)^{0.165}$ D = distance between plates	Creeping regime $10^{-3} \leq Ra \leq 25$

629 239

TABLE 3.14 COMPARISON OF THERMOHYDRAULIC CODES FOR WIRE-WRAPPED ASSEMBLIES

Features	Thermohydraulic Computer Codes							
	ENERGY	COBRA-III	ORRIBLE	COTEC	THI-3D	FORCMX	FULMIX	SIMPLE
A. Geometry								
Maximum number of rods		36	217	271	217			
Subchannel Shape	Interior and edge channel	Interior and edge channel	Interior and edge channel	Interior and edge channel	Hexagonal channel around rod			Interior and edge channel
Special edge-channel treatment (separate cross-flow and turbulent mixing coefficient)	yes	no	no	no	yes	yes		yes
Maximum number of flow subchannels	500	60	438	500	271			
	(limit can be readily changed)							
Maximum number of axial steps (exact correlation can be specified)	no limit	91	no limit	no limit	no limit			
B. Flow parameters								
Buoyancy effect		yes	no	no	yes			no
Variable coolant properties		yes	no	yes	yes			
Variable flow area due to wire	no	yes	yes	yes	yes			yes
C. Mixing Characteristics								
Cross-flow diversion	yes	yes	input coefficient	yes	yes	yes	yes	
Axial temperature period		yes	yes	yes	yes	yes	yes	
Flow sweeping coefficient input	yes	yes	yes	yes	yes	yes	yes	
Cross flow swirl	yes	no	no	yes	yes	yes		
D. Heat Flux								
Variable axial and radial	yes	yes	yes	yes	yes	yes		
Transient capability	no	yes	yes	no	no			
E. Reference	101	102	103	83	81	104,105	106	107

629 240

TABLE 4.1 INTERMEDIATE HEAT EXCHANGER DESIGN DATA

PLANT DATA	EBR-II [119]	FFTF [96]	CRBRP [15]	PHENIX [10,16]	SUPERPHENIX [16]	PFR [120]	BN-600 [121]
Country	USA	USA	USA	France	France	UK	USSR
Plant Concept	Pool	Loop	Loop	Pool	Pool	Pool	Pool
Number of IHXs	1	3	3	6	8	6	6
Thermal Load per unit, MWt	62.5	133.3	325	93.8	375	100	100
Design Parameters							
Number of Tubes	3026	1540	2850	2228	5380	1808	---
Tube O.D., mm	15.9	22.	22.	14	14	20	---
Tube Thickness, mm	1.6	1.2	1.14	1	1	1	---
Active Length, m	2.8	5.2	7.47	5.15	6.5	4.4	6.0
Tube Pitch, mm	20.6	33.	33.	20	20	---	---
Pitch/Diameter	1.30	1.50	1.50	1.43	1.43	---	---
Primary Coolant							
Route	Shell	Shell	Shell	Shell	Shell	Tube	Shell
Flow Rate, kg/s	470	734	1741	460	1970	488	1010
Inlet Temperature, K	746	839	808	833	815	835	823
Outlet Temperature, K	640	695	661	673	665	673	653
Intermediate Coolant							
Route	Tube	Tube	Tube	Tube	Tube	Shell	Tube
Flow Rate, kg/s	315	730	1610	368.5	1633	488	883
Inlet Temperature, K	582	648	617	623	618	643	593
Outlet Temperature, K	736	791	775	823	798	805	793
Logarithmic Mean $\Delta T$ , K	27.3	47.5	38.2	24.9	29.50	30	43.3

TABLE 4.2 NUSSELT NUMBER CORRELATIONS FOR FULLY DEVELOPED  
TURBULENT FLOW INSIDE ROUND TUBES

Nusselt Number Correlations		Reference
$Nu = 7. + 0.025 (\bar{\psi} Re \cdot Pr)^{0.8}$	$\bar{\psi} = 1$	Lyon [130]
	$\bar{\psi} = 1 - \frac{1.84}{Pr(\epsilon_m/\nu)_{\max}^{1.4}}$	Dwyer [93,131]
$Nu = 6. + 0.025 (\bar{\psi} Re \cdot Pr)^{0.8}$	$\bar{\psi} = \frac{0.014 (1 - e^{-71.8\beta})}{\beta}$ $\beta = Re^{-0.45} Pr^{-0.2}$	Aoki [132]
$Nu = 5. + 0.025 (\bar{\psi} Re \cdot Pr)^{0.8}$	$\bar{\psi} = 1$	Subbotin, et al., [93,133]



TABLE 4.3 NUSSELT NUMBER CORRELATIONS FOR FULLY DEVELOPED TURBULENT FLOW THROUGH UNBAFFLED TUBE BANKS

Nusselt Number Correlation	Range	Reference
$\text{Nu} = 6.66 + 3.126 (P/D) + 1.184 (P/D)^2$ $+ 0.0155 (\bar{\psi} \text{Re} \cdot \text{Pr})^{0.86}$	$70 \leq \text{Re} \cdot \text{Pr} \leq 10^4$ $1.3 \leq P/D \leq 3.0$	Maresca-Dwyer [135]
$\text{Nu} = 7.0 + 3.8 (P/D)^{1.52}$ $+ 0.027 (P/D)^{0.27} (\bar{\psi} \text{Re} \cdot \text{Pr})^{0.8}$	$0 < \text{Re} \cdot \text{Pr} \leq 10^5$ $1.3 \leq P/D \leq 10$	Friedland-Bonilla [136]
$\text{Nu} = \alpha + \beta (\text{Re} \cdot \text{Pr})^\gamma$ $\alpha = 0.25 + 6.2 (P/D)$ $\beta = -0.007 + 0.032 (P/D)$ $\gamma = 0.8 - 0.024 (P/D)$	$110 \leq \text{Re} \cdot \text{Pr} \leq 4300$ $1.25 \leq P/D \leq 1.95$	Graber-Rieger [137]

TABLE 4.4 THEORETICAL VALUES OF THE HYDRODYNAMIC POTENTIAL  
DROP [93]

P/D	$\phi_u/D$	
	Equilateral Triangular Spacing	Square Spacing
1.25	3.7975	4.2299
1.30	3.5393	3.8988
1.35	3.3311	3.6297
1.40	3.1587	3.4064
1.45	3.0589	3.2776
1.50	2.9690	3.1619
1.55	2.8876	3.0575
1.60	2.8132	2.9630

629 244

TABLE 5.1 TYPICAL VELOCITY HEAD FACTOR VALUES

FITTING	VELOCITY HEAD FACTOR, K
Sudden Expansion	1.0
Sudden Contraction	0.5
Welding Tee Through Branch	1.36
90 Welding Elbow L.R.	0.315
90 Welding Elbow S.R.	0.455
45 Welding Elbow	0.208
Gate Valve, Open	0.208

629 245

TABLE 5.2 Homologous head and torque polynomial coefficients (H,B $\equiv$ head or torque curve  $\alpha$  or V $\equiv$ division by  $\alpha^2$  or  $\nu^2$ ; N,D,T or R $\equiv$ normal, energy dissipation, turbine, or reverse pump region)

(I) Curves	Coeff.					
	$c_0$	$c_1$	$c_2$	$c_3$	$c_4$	$c_5$
1 HVN	-0.556	0.85376	0.82906	-3.7106	7.0593	-3.4776
2 HAN+HAD	1.2897	-0.061907	0.17327	-0.57294	0.033762	0.13865
3 HVD	0.69189	0.43961	0.68459	-0.24701	0.63156	-0.20833
4 HVT	0.69209	-0.46132	0.92592	-0.4308	0.50845	-0.22436
5 HAT	0.63405	0.20178	-0.30242	0.76603	-0.48077	0.19231
6 HAR	0.63405	0.14665	-4.1896	-2.4828	0.89730	0.0
7 HVR	-0.556	0.66362	-0.086081	-0.93928	-0.57381	0.0
1 BVN	-0.37069	0.41741	3.8511	-7.6752	7.0695	-2.2917
2 BAN+BAD	0.44652	0.5065	0.59643	-0.64055	-0.025531	0.11531
3 BVD	0.8658	0.28437	-0.22348	0.45083	-0.70586	0.21562
4 BVT	0.86533	-0.60816	3.1497	-9.3647	10.418	-4.0064
5 BAT	-0.68468	1.8495	0.96871	-8.9653	12.045	-4.7546
6 BAR	-0.684	2.0342	-0.95477	-0.42286	0.0	0.0
7 BVR	-0.372	2.3716	-0.56147	0.0	0.0	0.0

629  
246

TABLE 5.3 PUMP FRICTION TORQUE CORRELATIONS

Frictional Torque,	References
DEMO $\alpha > 0.005$ $14.77\alpha$ $\alpha \leq 0.005$	SSC [150]
$0.023\alpha + 0.012$ $\alpha > 0.0117$ $0.117 - 8.970\alpha$ $\alpha \leq 0.0117$	DEMO [97]
$0.105e^{-100\alpha} + 0.023\alpha + 0.012$	CURL [126, 143]
$0.035\alpha \alpha $	RELAP3B [152]

629 247

TABLE 6.1 STEAM GENERATING SYSTEM DESIGN DATA

	EBR-II [14]	CRBRP [15]	PHENIX [10]	SUPERPHENIX [16]	PFR [10]	BN-600 [121]
Country	USA	USA	France	France	UK	USSR
Plant Concept	Pool	Loop	Pool	Pool	Pool	Pool
Number of Steam Generator Loops	1	3	3	4	3	3
<b>Evaporator</b>						
Number of Units per Loop	8	2	1	1	1	1
Number of Tubes	73	757	84	-	-	-
Tube O.D., mm	36.5	16	28	-	-	16
Tube Thickness, mm	4.7	3	4	-	-	2.5
Active Length, m	6.9	14	-	-	-	-
Tube Pitch, mm	49.2	31	-	-	-	-
Intermediate Coolant Route	Shell	Shell	Shell	Shell	Shell	Shell
Intermediate Flow Rate, kg/s	39.375	805	737	798	976	883
Intermediate Inlet Temp., K	696	730	748	-	728	725
Intermediate Outlet Temp., K	582	617	623	618	643	593
Tertiary Flow Rate, kg/s	3.9	140	208	340	728	178
Tertiary Inlet Temp., K	561	555	519	340	561	514
Tertiary Outlet Temp., K	577	600	648	-	626	573
Thermal Load per Unit, MWt	5.7	117.50	119	-	-	-
<b>Superheater</b>						
Number of Units per Loop	4	2	1	1	1	1
Number of Tubes	109	757	84	-	890	-
Tube O.D., mm	15.1	16	31.8	-	14.3	16
Tube Thickness, mm	2.4	3	3.6	-	2.2	2.5
Active Length, m	7.8	14	-	-	-	-
Tube Pitch, mm	28.2	31	-	-	-	-
Intermediate Coolant Route	Shell	Shell	Shell	Shell	Shell	Shell
Intermediate Flow Rate, kg/s	78.75	1610	737	3266	976	-
Intermediate Inlet Temp., K	736	775	823	798	805	793
Intermediate Outlet Temp., K	696	730	748	-	728	725
Tertiary Inlet Temp., K	577	598	648	-	626	573
Tertiary Outlet Temp., K	722	755	785	508	787	778
Thermal Load per Unit, MWt	4.25	90	187.7	750	200	490

629 248

TABLE 7.1 EXAMPLES OF DIFFERENT TIME CONSTANTS IN CRBRP

Time Constant for	100% Power, 100% Flow (s)	2.4% Power, Natural Circulation Flow (s)
<b>Heat Flux Time Constant</b>		
Fuel Rod	1.3	1.3
Blanket Rod	2.6	2.7
Control Rod	3.8	4.0
<b>Enthalpy Transport Time Constants in PHTS</b>		
Within Reactor Vessel	42.8	1420
Reactor Vessel to IHX	14.3	480
Within IHX	12.2	410
IHX to Reactor Vessel	6.2	210
Total	<u>75.5</u>	<u>2520</u>
<b>Enthalpy Transport Time Constant in IHTS</b>		
Within IHX	14.7	590
IHX to Superheater	35.4	1410
Within Superheater	3.9	160
Superheater to Evaporator	5.3	210
Within Evaporator	7.9	320
Total	<u>93.6</u>	<u>3740</u>
<b>Enthalpy Transport Time Constant in SGS</b>		
Steam Drum	10.5	101
Recirculation Loop	34.6	247
Steam Drum to Turbine Throttle	11.7	195
Total	<u>56.8</u>	<u>543</u>
<b>Grand Total of Enthalpy Transport Time Constant</b>	226	6803

629 247

TABLE 7.2 RANGE OF TIME-STEP SIZES FOR LMFBR SYSTEMS

Process	Time-Step Size (s)
In-Vessel	
Power Generation	$10^{-4} - 10^{-2}$
Heat Conduction/Convection	$10^{-3} - 10^{-2}$
Sodium Boiling	$10^{-6} - 10^{-4}$
Fluid Mixing in Plenum	$10^{-2} - 10^{-1}$
Heat Transport System	
Fluid Flow in Pipings	$10^{-2} - 10^{-0}$
Heat Transfer in Heat Exchanger	$10^{-3} - 10^{-1}$
Fluid Discharge through Break	$10^{-2} - 10^{-1}$
Steam Generator	
Evaporator/Superheater	$10^{-4} - 10^{-2}$
Water/Steam Discharge through Break	$10^{-4} - 10^{-2}$

629 250



TABLE 8.1. ACCIDENT CLASSIFICATION

CATEGORY	FREQUENCY RANGE (EVENTS/REACTOR YEAR)	EXAMPLE OF EVENTS
Normal	$\geq 1$	<ul style="list-style-type: none"> <li>• Plant Startup</li> <li>• Plant Shutdown</li> <li>• Load changing</li> </ul>
Upset	1 - 1/40	<ul style="list-style-type: none"> <li>• Control Assembly Withdrawal at Startup</li> <li>• Control Assembly Withdrawal at Full Power</li> <li>• Small reactivity Insertion</li> <li>• Inadvertent Drop of a Single Control Rod at Full Power</li> <li>• Loss of Off-Site Electrical Power</li> <li>• Spurious Single Pump Trips</li> <li>• Inadvertent Closure of a Steam Generator Isolation Valve</li> <li>• Loss of Normal Feedwater</li> <li>• Turbine Trip</li> </ul>

629 251

TABLE 8.2 STEADY-STATE POWER AND FLOW FRACTIONS IN SSC-L

Channel Number	Number of Assemblies	Power Fraction	Power Per Pin kW	Flow Fraction	Flow Per Pin kg/s	Coolant Temp. Rise K
1	1	0.0067	29.87	0.0033	0.0794	297.8
2	65	0.30916	21.20	0.2994	0.1109	150.8
3	78	0.34651	19.80	0.30842	0.0952	164.1
4	36	0.14894	18.44	0.12308	0.0823	176.9
5	12	0.04459	16.57	0.03902	0.0783	167.0
6	6	0.01939	14.41	0.01651	0.0662	171.6
7	1	0.001644	26.07	0.00073	0.0625	330.5
8	24	0.02961	19.57	0.03414	0.1218	126.5
9	30	0.03259	17.23	0.03965	0.1132	119.8
10	53	0.035346	10.58	0.04275	0.0691	120.5
11	42	0.018760	7.08	0.01772	0.0361	154.6
12	19	0.00676	--	0.0600	--	16.3
Bypass	--	0	--	0.01527	--	0

629 252

TABLE 8.3 EBR-II WHOLE CORE/WHOLE PLANT TESTS AND EVENTS

TEST IDENTIFICATION	STEADY-STATE OR TRANSIENT	PRIMARY SYSTEM CONDITIONS		SECONDARY SYSTEM FLOW CONDITIONS
		FLOW	POWER	
EX-109 (XX07)	Steady-state	All pumps off	.11% decay heating	0.4 to 6.1%, controlled
Test G (XX07)	Steady-state	All pumps off	0.5 to 1.3% fission heating	2.5 to 6.0%, controlled
Test F (XX07)	Transient	Primary pumps off, pri. aux. pump tripped	1.6% decay power	2.0%, controlled
Cover Lift Test (XX07)	Transient	Pri. pumps off, pri. aux. pump on, reactor cover lifted to fuel handle	0.58% decay power	~ 1%, controlled
LOF/Scram of 1/1/75 (XX07)	Transient	Loss of power to pump 1, manual trip of pump 2, from 100% flow. Primary aux. pump on.	Scram from 100% power on low flow signal	Trip from 100% flow with scram
Test 1A (XX08)	Transient	Primary pumps off, pri. aux. pump tripped	0.15% decay power (XX08) unirradiated, with 0.03% power)	3.3 to 10.5%, controlled; also natural convective flow
Tests 1B-1E (XX08)	Transient	Primary pumps off, pri. aux. pump tripped	0.17 to 0.63% decay power	2.6 to 9.0%, controlled also natural convective flow
Test 2 (XX08)	Transient	Primary pumps off, pri. aux. pump on	< 0.1% decay power. Plant isothermal at 580°F	Trip of sec. pump from 30, 50, 100% flow
Test 7A (XX08)	Transient	Primary pumps tripped from 34% flow, pri. aux. pump off	Scram from 29% power	Constant at 33%

629  
253

TABLE 8.3 EBR-II WHOLE CORE/WHOLE PLANT TESTS AND EVENTS (CONT'D)

TEST IDENTIFICATION	STEADY-STATE OR TRANSIENT	PRIMARY SYSTEM CONDITIONS		SECONDARY SYSTEM FLOW CONDITIONS
		FLOW	POWER	
Test 10 (XX08)	Transient	Primary pumps tripped from 34% and 100% flow, pri. aux. pump off	Scram from 100% power preceding LOF by 45 to 215 minutes	Sec. flow controlled at 9%, nat. circ., or loss of flow throttling
LOF/Scram of 10/1/77 (XX08)	Transient	Primary pumps tripped from 100% flow, pri. aux. pump on	Scram from 100% power	Sec. pump trip from 100% flow with scram
LOF/Scram of 11/2/77 (XX08)	Transient	Primary pumps tripped from 100% flow, pri. aux. pump on	Scram from 100% power	Sec. pump trip from 100% flow with scram
LOF/Scram of 1/10/78 (XX08)	Transient	Primary pumps tripped from 100% flow, pri. aux. pump on	Scram from 100% power	Sec. pump trip from 100% flow with scram
Scram of 2/2/78 (XX08)	Transient	Flow constant at 100%	Scram from 100% power	Sec. pump trip from 100% flow with scram
Scram of 5/24/78 (XX08)	Transient	Flow constant at 100%	Scram from 56% power	Sec. pump trip from 58% flow with scram
Scram of 6/3/78 (XX08)	Transient	Flow constant at 100%	Scram from 100% power	Sec. pump trip from 100% flow with scram
Scram of 6/13/78 (XX08)	Transient	Flow constant at 100%	Scram from 100% power	Sec. pump trip from 100% flow with scram
Scram of 7/12/78 (XX08)	Transient	Flow constant at 100%	Scram from 27% power	Sec. pump trip from 100% flow with scram

629 254

TABLE 8.4 INITIAL CONDITIONS FOR TESTS 1A and 1E of EBR-II

TEST	PHASE	XX08 FLOW %	REACTOR INLET TEMP °K	XX08 AVG. TOP-OF-CORE TEMP °K	XX08 S/A AVG. OUTLET TEMP °K	IHX PRIMARY INLET TEMP °K	IHX SECONDARY INLET TEMP.	INTERMEDIATE-SYSTEM FLOW %
1A	1	5.4	646	647	648	647	534	3.3
1E	1	5.5	644	649	649	647	537	2.6
1A	2	5.6	644	644	645	647	540	5.1
1E	2	5.6	638	642	642	643	551	5.8
1A	3	5.8	639	640	640	643	547	7.0
1E	3	5.7	633	637	637	639	562	6.6
1A	4	5.99	633	634	635	637	565	10.4
1E	4	5.95	628	633	633	634	571	9.0

629

255

TABLE 9.1 LMFBR SYSTEM VERIFICATION NEEDS

COMPONENT	PARAMETER	IMPORTANCE
I. <u>IN-REACTOR</u>		
a) Core	Pressure Drops in Reactor Vessel Structures	High
	Pressure Drops in Fuel, Blanket and Control Assemblies	High
	Reactor Power including Decay Power by Assembly	High
	Inter-Assembly Flow/Heat Redistribution	High
	Intra-Assembly Flow/Heat Redistribution	High
	Sodium Boiling	Medium/High
b) Plenum	Mixing/Stratification	Low
II. <u>HEAT TRANSPORT SYSTEM</u> (Primary/Intermediate)		
a) Piping	Pressure Drops in Piping, bends, etc.	Medium
	Heat Transfer to Ambient and Pipe Wall	Medium
b) Pump	Pump Characteristics	High
	Pressure Drop for Locked Rotor	High
c) Check Valve/ Isolation Valve	Pressure Drop Correlations	Medium
d) IHX	Pressure Drops	Medium
	Mixing in Plena	Low/Medium
	Heat Transfer Characterization	Medium
e) Pipe Break	Coolant Discharge Rate - Role of Sleeves/Guard Pipe	Medium
III. <u>STEAM GENERATOR</u>		
a) SG	Pressure Drop Correlations	Medium/High
	Heat Transfer Correlations	Medium/High
IV. <u>PLANT</u>		
a) Overall Performance	All of the above	High

629 256

APPENDIX B

629 257

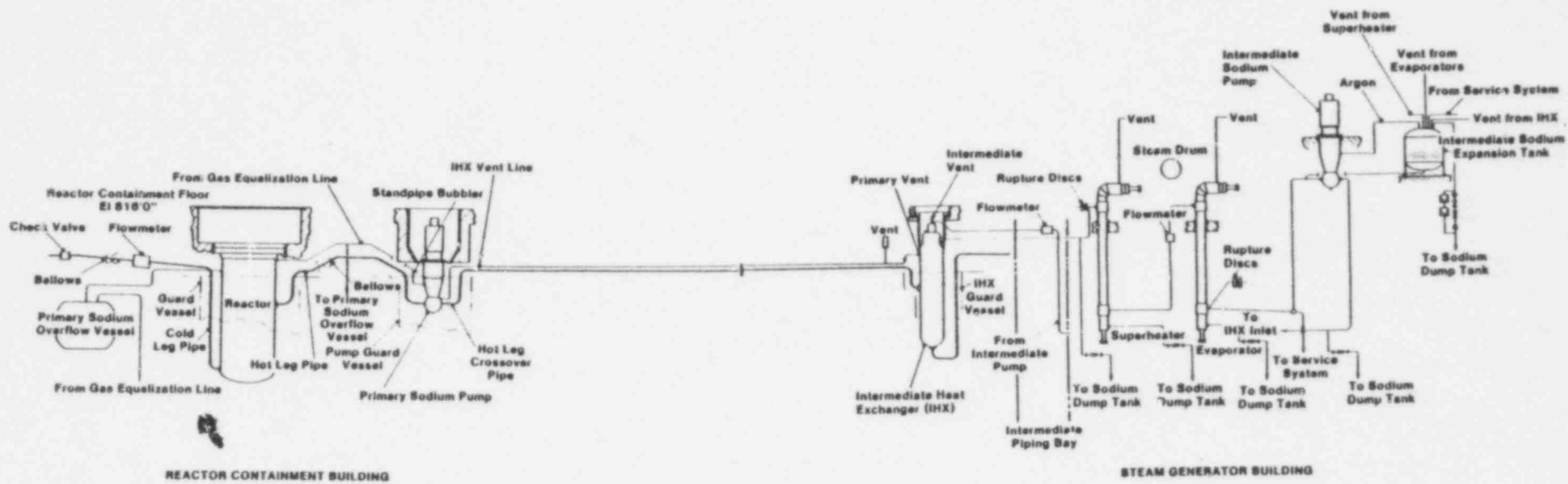
FIGURE CAPTIONS

Figure No.

- 1.1 Schematic Layout of a Loop-Type LMFBR.
- 1.2 Schematic Layout of a Pool-Type LMFBR.

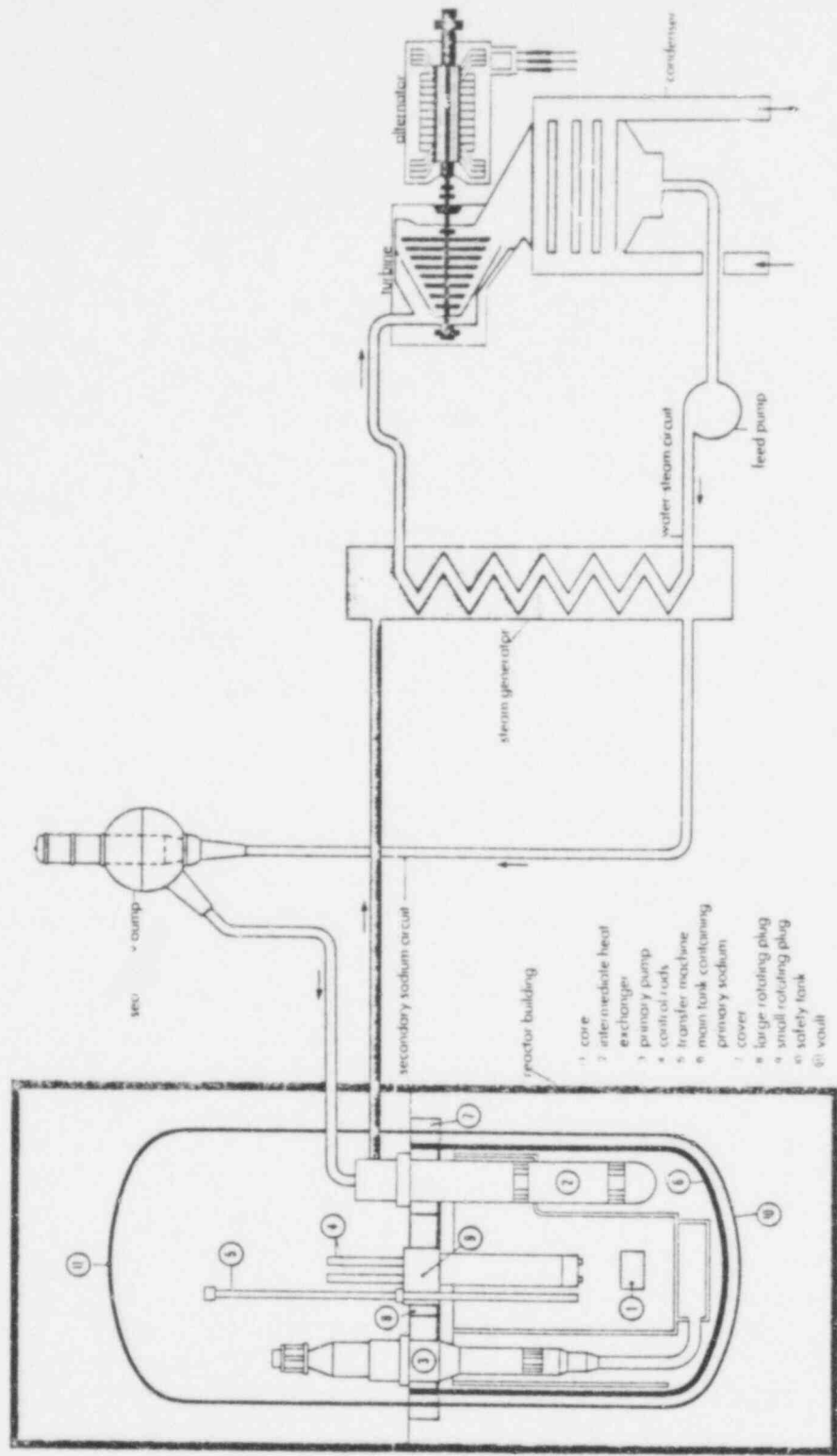
629 258





AGRAWAL & KHATIB-RAHBAR  
Fig. 1.1

629  
259



**containments**

- a) First barrier represented by fuel cladding
- b) Second barrier consisting of main tank, cover and rotating plugs
- c) Third barrier primary containment consisting of safety tank and vault
- d) Fourth barrier secondary containment consisting of reactor building

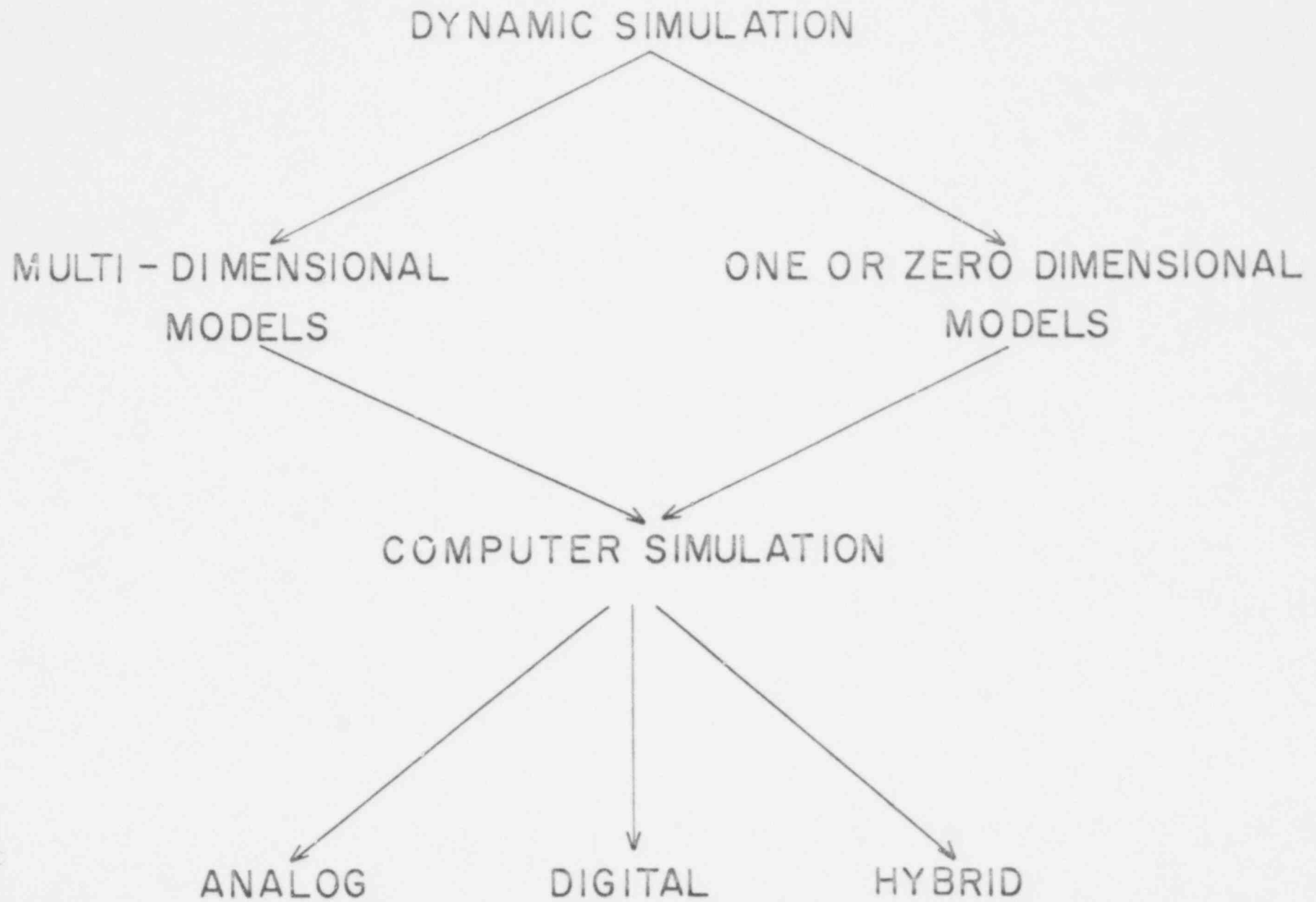
029 260

FIGURE CAPTIONS

Figure No.

2.1            Spectrum of Dynamic Simulation and Computational  
                  Methods.

629 261



625  
262

## FIGURE CAPTIONS

### Figure No.

- 3.1 A Cross Section of CRBRP Core.
- 3.2 A Cross Section of SUPERPHENIX Core.
- 3.3 Schematic Layout of the CRBRP Fuel Assembly.
- 3.4 Schematic Layout of the SUPERPHENIX Fuel Assembly.
- 3.5 Schematic Comparison of Fuel Rods in CRBRP and SUPERPHENIX.
- 3.6 1200 MWe Heterogeneous LMFBR Core Layout.
- 3.7 Power Generation Values in CRBRP.
- 3.8 Assembly Radial Power Factor and Peak Rod Radial Power Factor (with respect to the average rod in the whole core or blanket) at BOEC in CRBRP.
- 3.9 Typical Core Axial Power Shape in CRBRP.
- 3.10 Typical Axial Blanket Power Shape in CRBRP.
- 3.11 Typical Axial Power Shape in CRBRP Radial Blankets.
- 3.12 Fission Product Decay Heat for FFTF.
- 3.13 Overall Scheme for Calculating Reactor Power
- 3.14 LMFBR Core Configuration at 400 Full Power Days.
- 3.15 Bowing Reactivity Contribution for CRBRP Startup.
- 3.16 Measured Power Reactivity Defect versus Run Number in EBR-II.
- 3.17 Reactivity Feedback Calculational Scheme.
- 3.18 Diagram of Reactor Coolant Flow for the CRBRP.
- 3.19 Diagram of Reactor Coolant Flow for the SUPERPHENIX.
- 3.20 Orifice Design for the PHENIX Reactor.
- 3.21 Friction Factor as a Function of Reynolds Number for Pipes.

629 263

FIGURE CAPTIONS (Cont.)

Figure No.

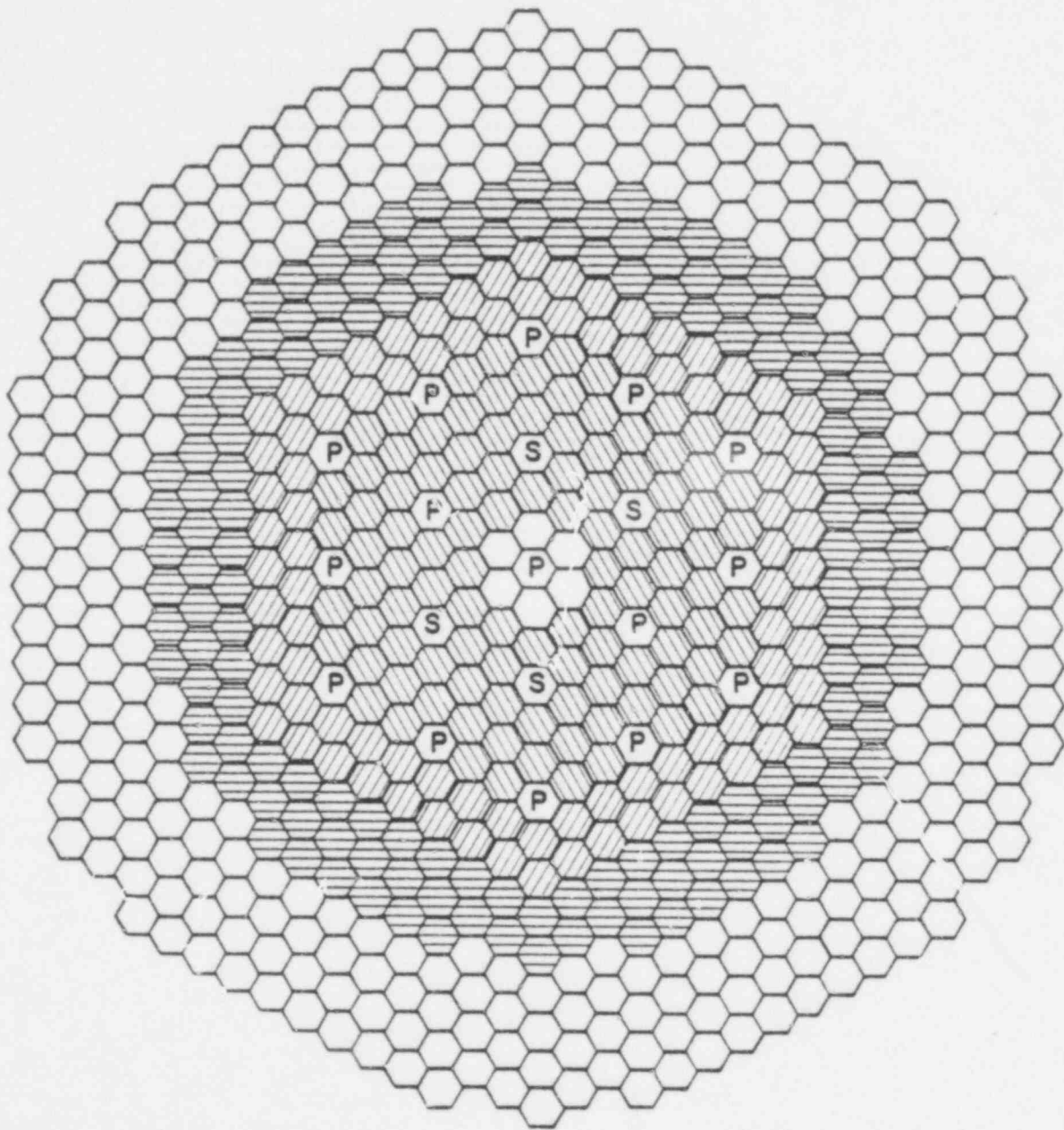
- 3.22 Modified Friction Factor versus Modified Reynolds Number for Rod Bundles.
- 3.23 Rod-Bundle Friction Factor versus Reynolds Number.
- 3.24 A Schematic of Flow Distribution in CRBRP Reactor Vessel.
- 3.25 Electrical Analog of Flow Fields in a Reactor Vessel.
- 3.26 Pressure Drop versus Total Core Flow.
- 3.27 Normalized Flow and Enthalpy Rise in Fuel Channel (1) versus Total Flow.
- 3.28 Normalized Flow and Enthalpy Rise in Blanket Channel (2) versus Total Flow.
- 3.29 Normalized Flow Ratios versus Transient Time in CRBRP.
- 3.30 The Effect of Flow Redistribution in a Hot Fuel Channel Coolant Temperature.
- 3.31 Sketch of Outlet Plenum Flow Patterns for Steady-State and Stratified Conditions.
- 3.32 Comparison for Effective Mixing Volume Between Yang's Model and Experiments.
- 3.33 Representative Nusselt Numbers versus Peclet number for Sodium at 700 K.
- 3.34 Temperature Traverses across Test Assembly ( $Re = 3700$ ,  $T_{in} = 590$  K).
- 3.35 Temperature Traverses Across Test Assembly ( $Re = 990$ ,  $T_{in} = 587$  K).
- 3.36 Temperature Traverses Across Test Assembly ( $Re = 490$ ,  $T_{in} = 589$  K).
- 3.37 Region of Negligible Axial Heat Conduction in Sodium.




629 264



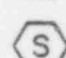
FIGURE CAPTIONS (Cont.)

Figure No.

- 3.38 A Typical Temperature Distribution in a Fuel Rod.
- 3.39 Post-Irradiation Fuel Structure of Mixed Oxide Pellet.
- 3.40 Effect of Restructuring on Mixed-Oxide Fuel Thermal Conductivity.

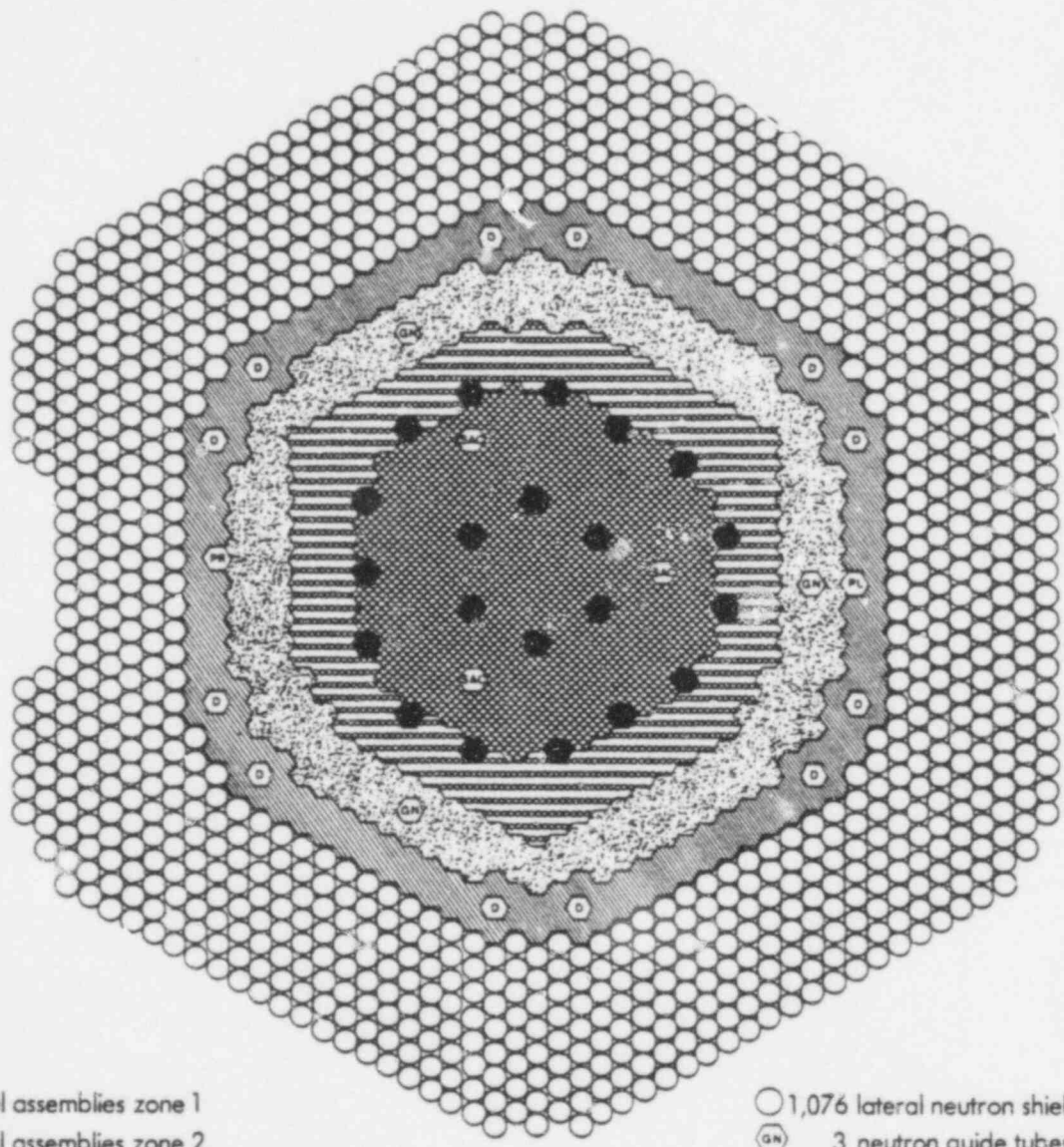


-  INNER CORE 108
-  OUTER CORE 90
-  RADIAL BLANKET 150

-  RADIAL SHIELD 324
-  PRIMARY CONTROL 15
-  SECONDARY CONTROL 4

629 266

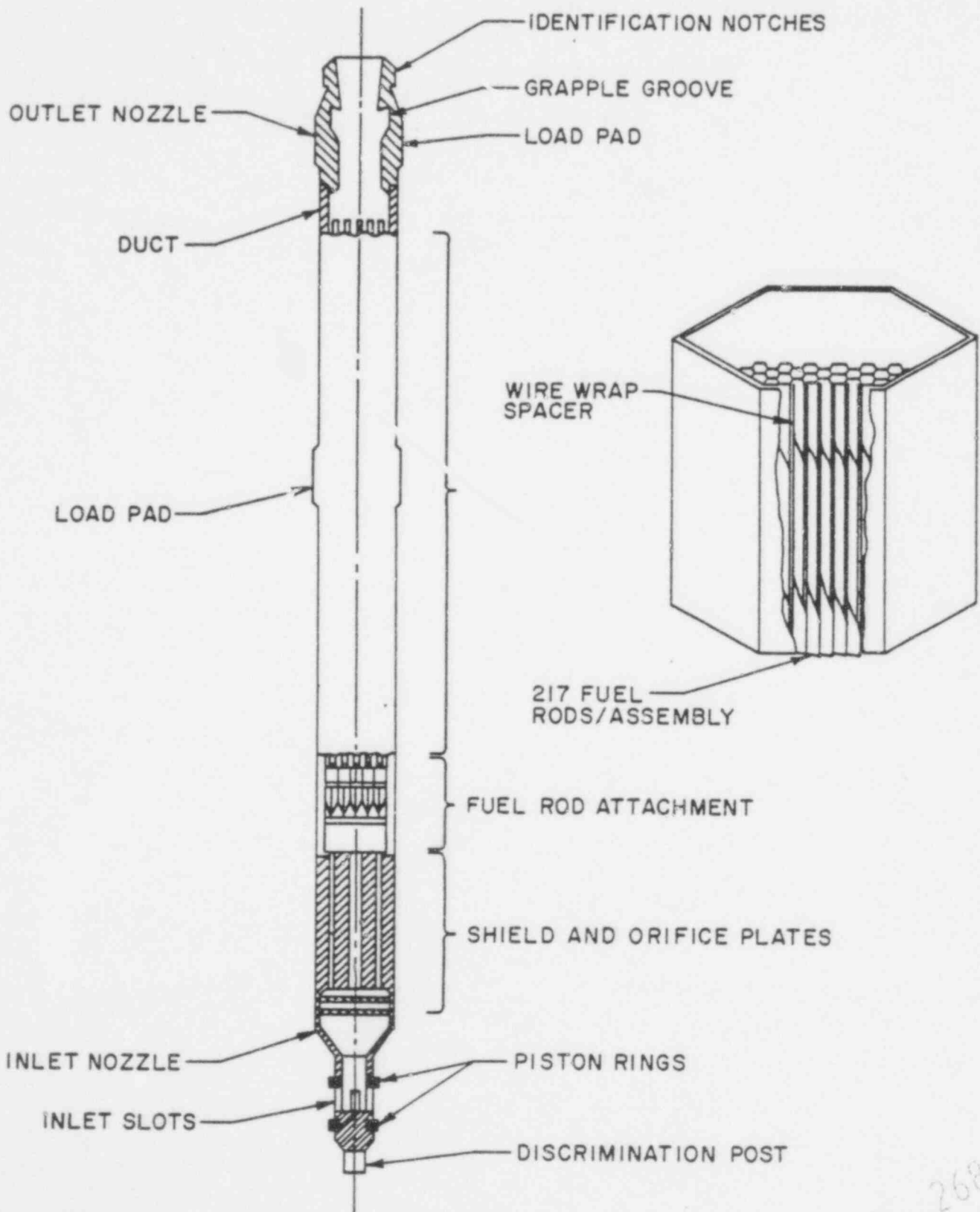




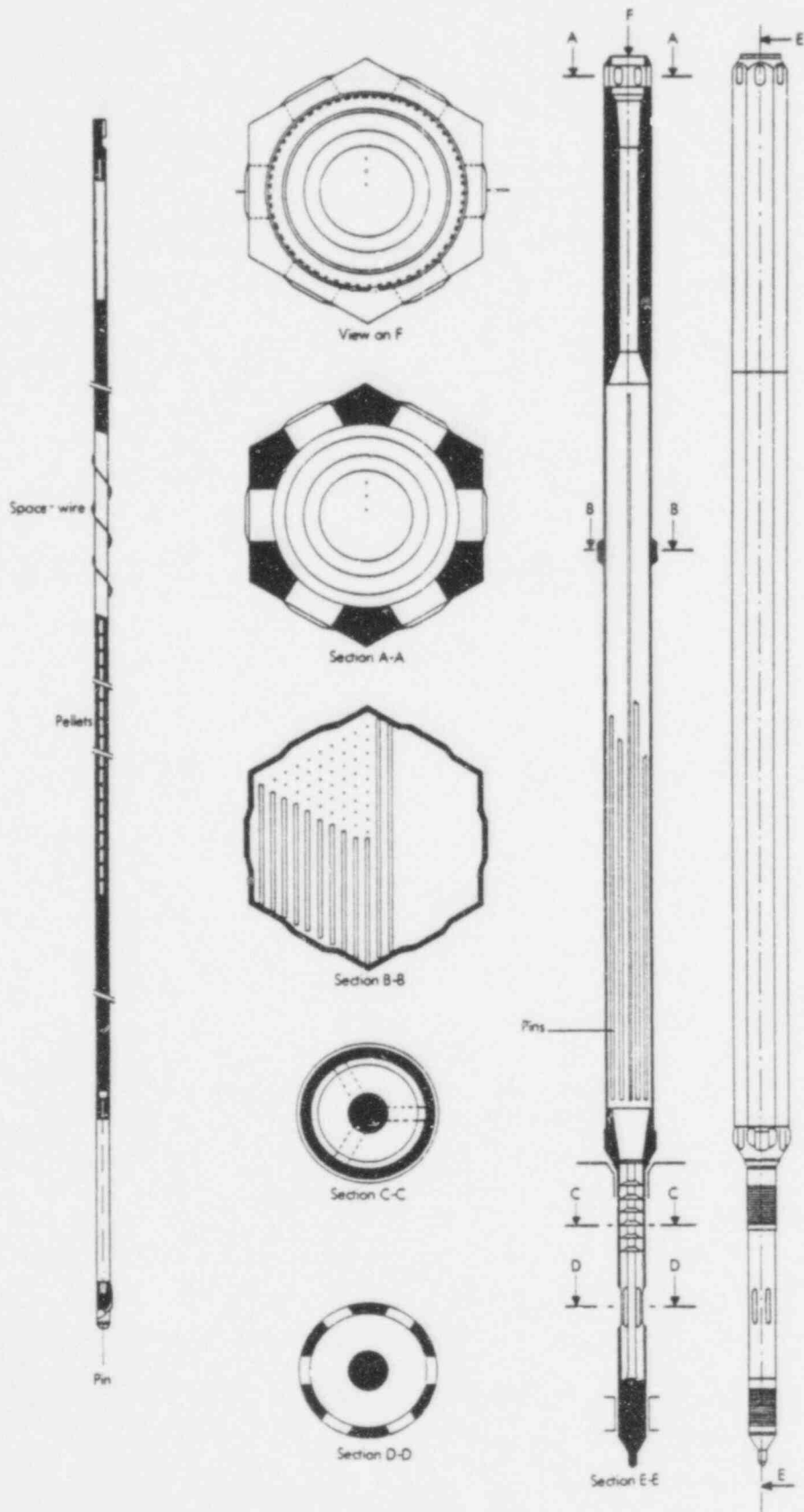
- 193 fuel assemblies zone 1
- ▨ 171 fuel assemblies zone 2
- 21 main control rods
- 233 blanket assemblies
- 198 steel assemblies

- 1,076 lateral neutron shielding assemblies
- GN 3 neutron guide tubes
- D 12 spare fuel assemblies
- SAC 3 backup control rods

629 267

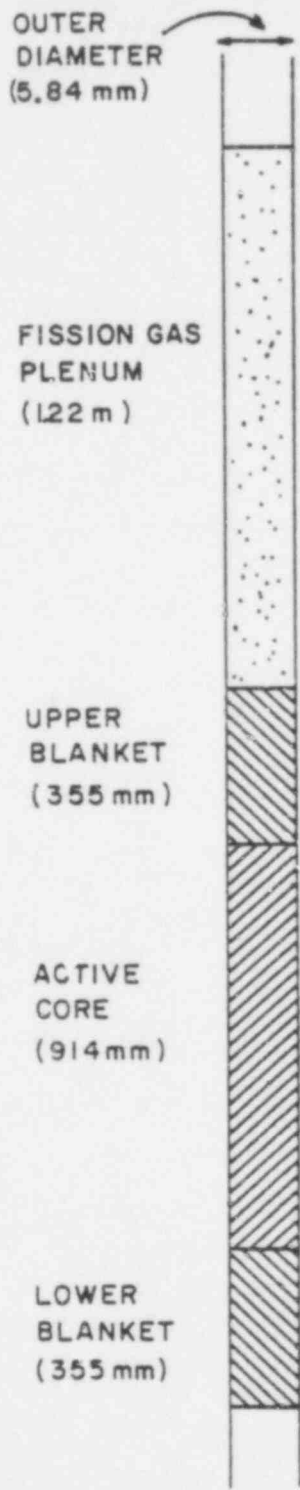


629 268

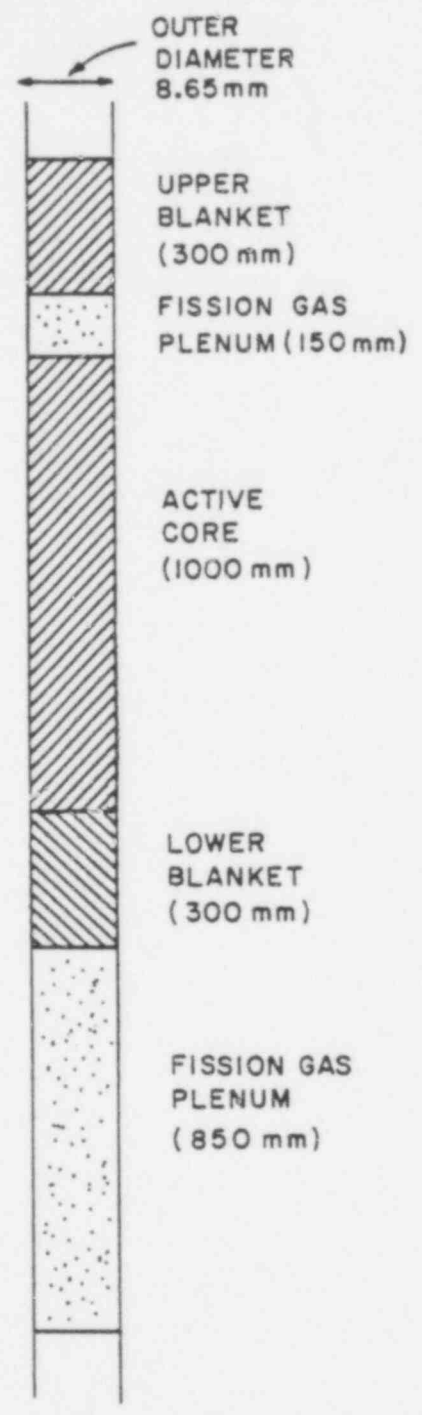


629 269

AGRAWAL & KHATIB-RAHBAR  
Fig. 3.4

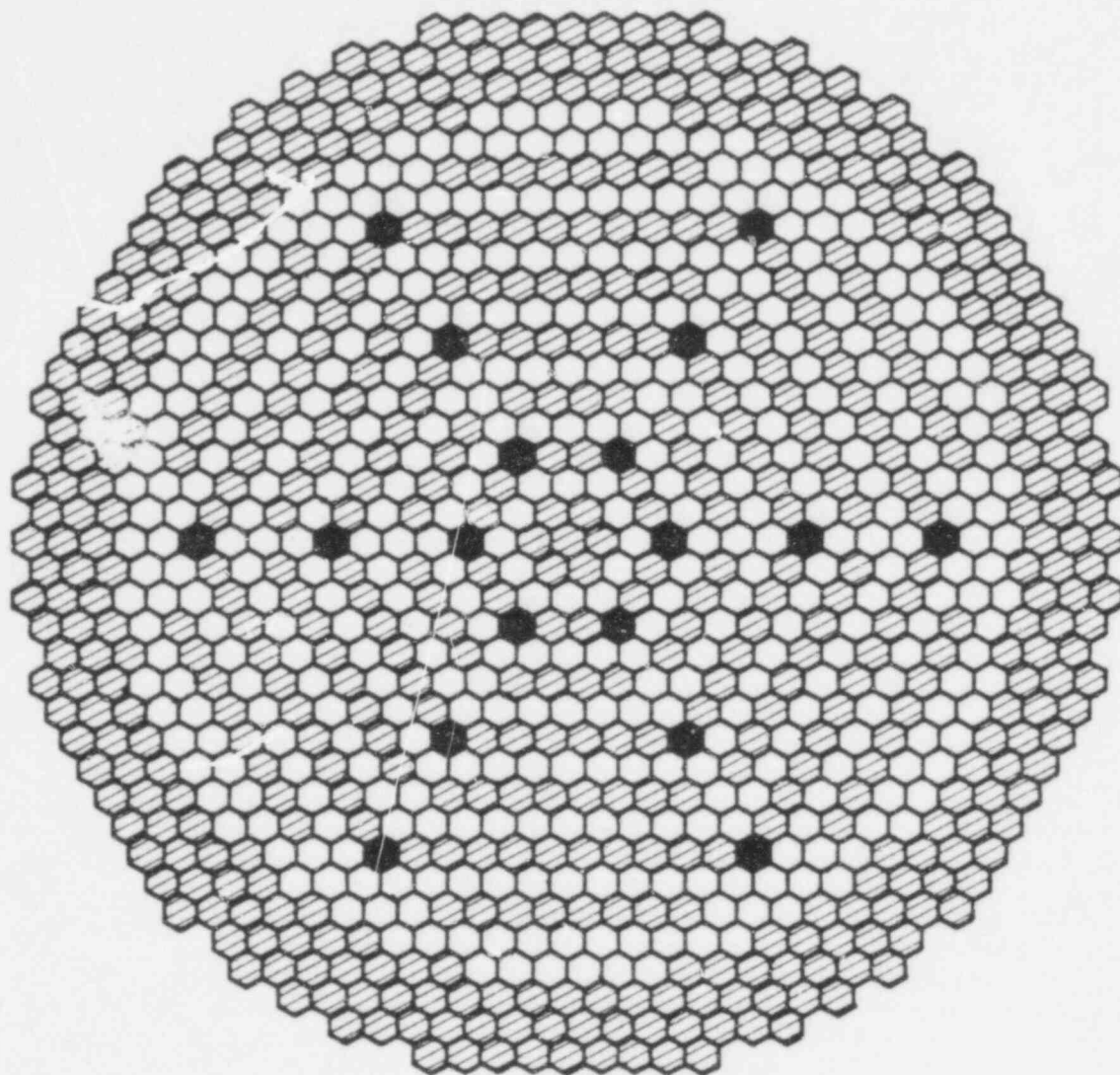


CRBRP

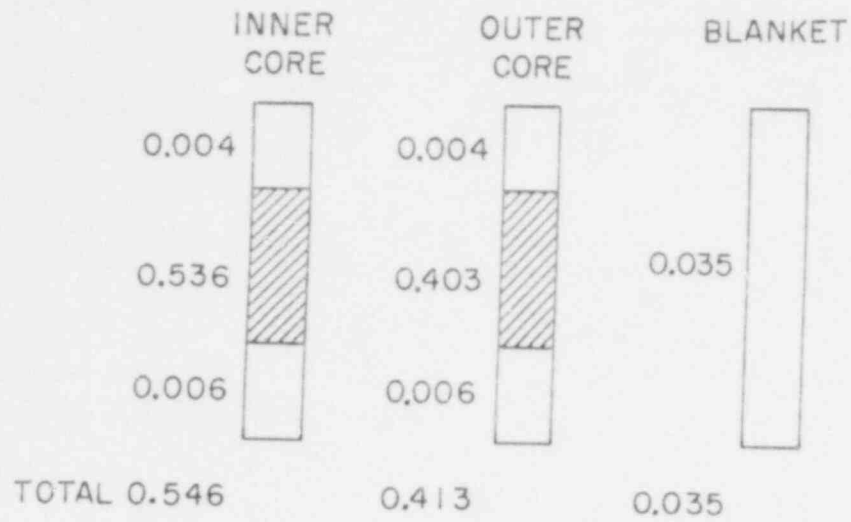


SUPERPHENIX

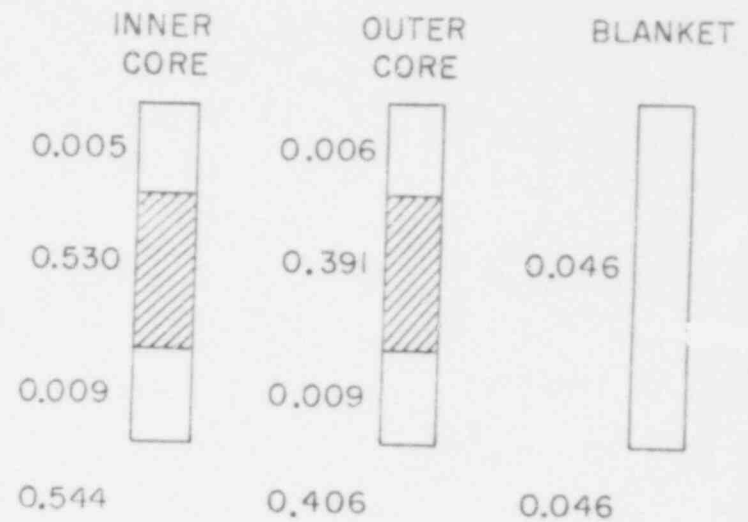
629 270



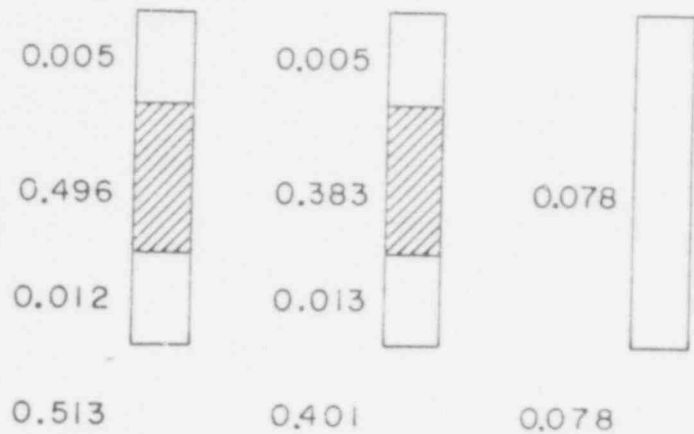
- CORE FUEL 396
- ▨ BLANKET  
INTERNAL 235  
RADIAL 306
- CONTROL 18



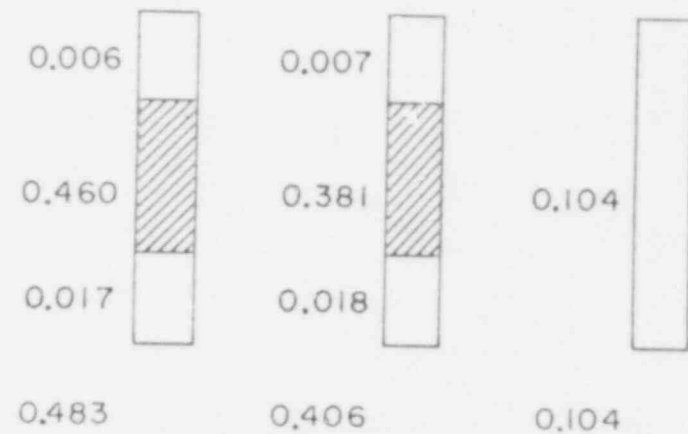
BEGINNING OF FIRST CYCLE



END OF FIRST CYCLE

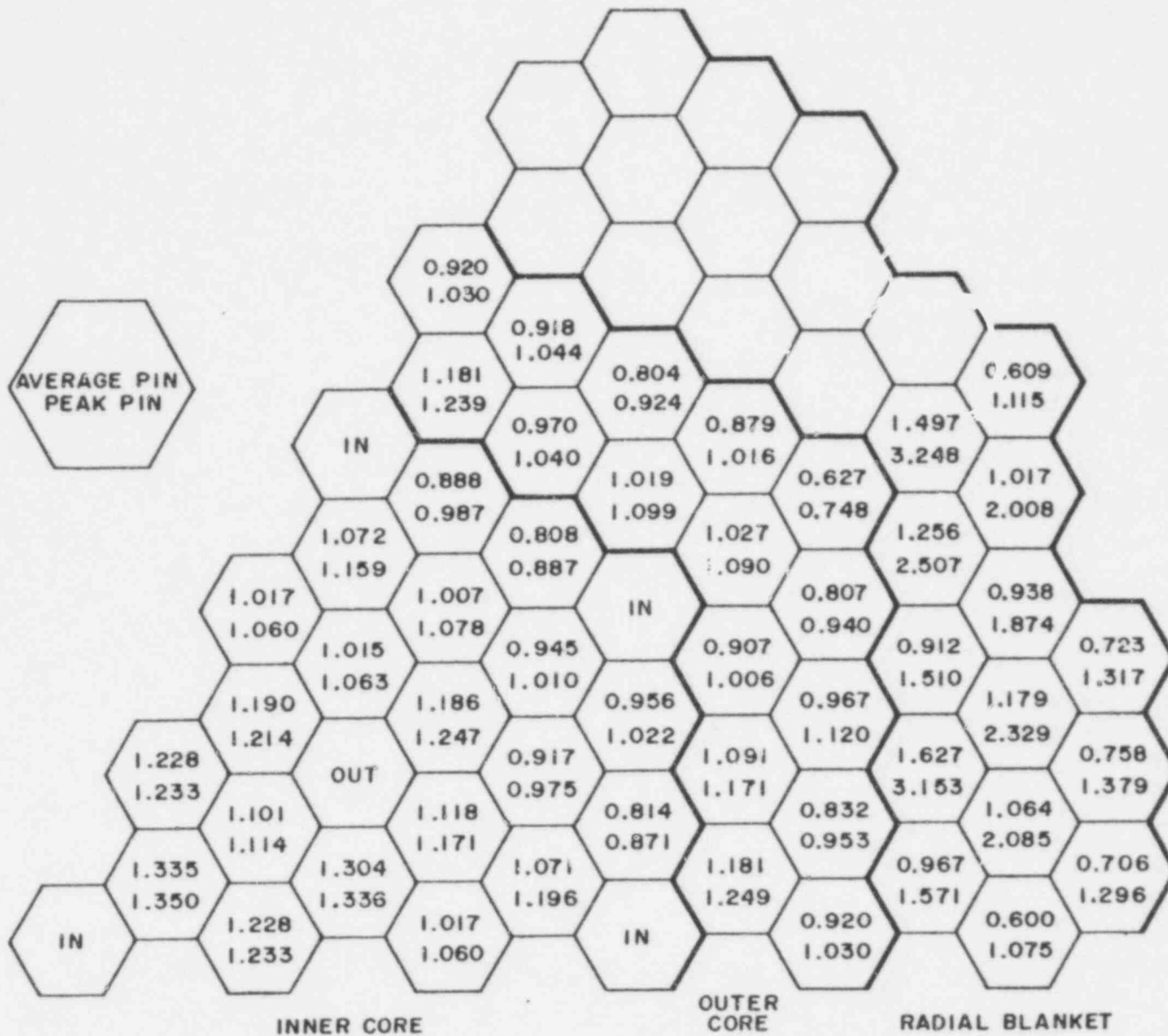


BEGINNING OF EQUILIBRIUM CYCLE

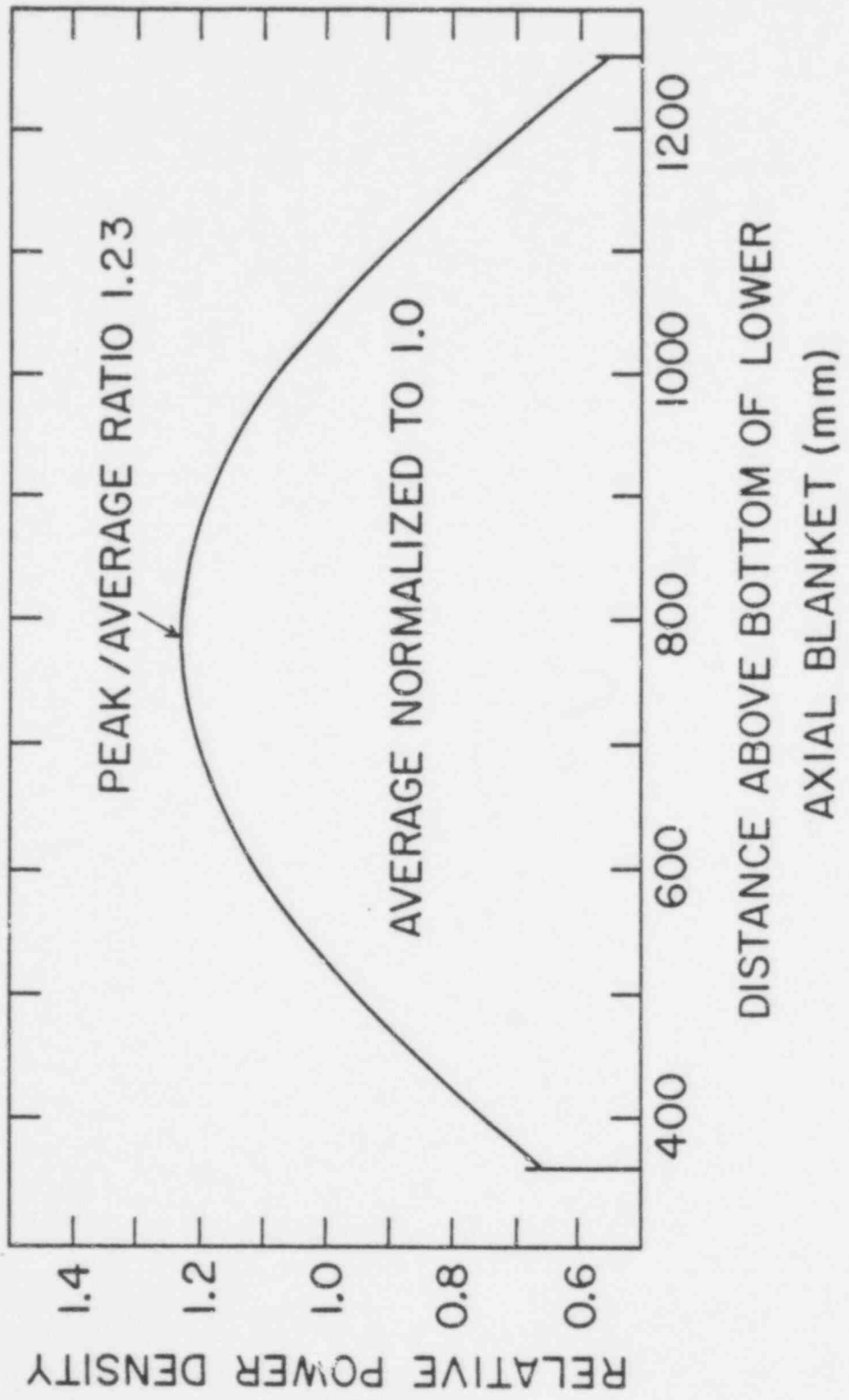


END OF EQUILIBRIUM CYCLE

629  
212

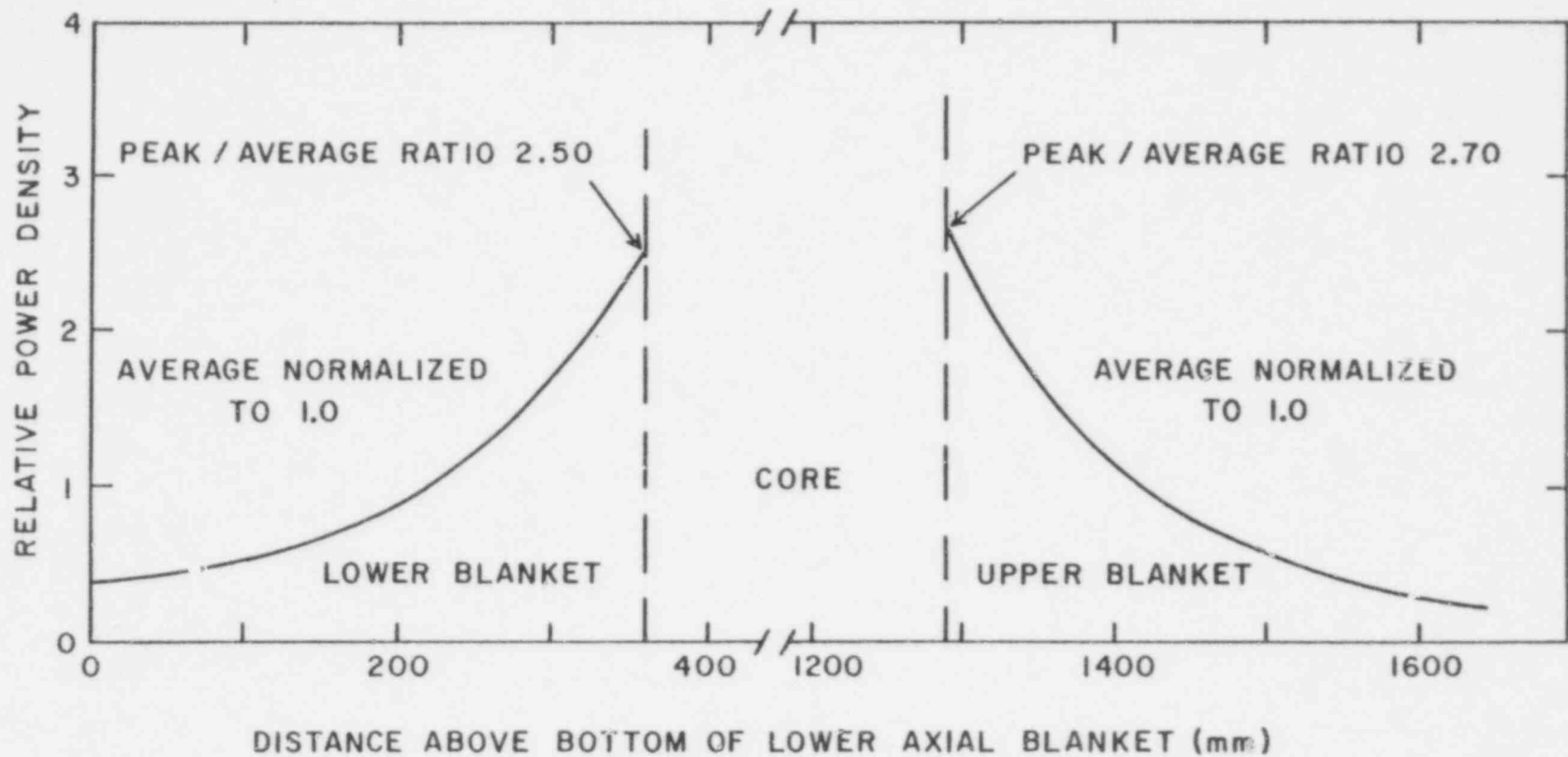


629  
215

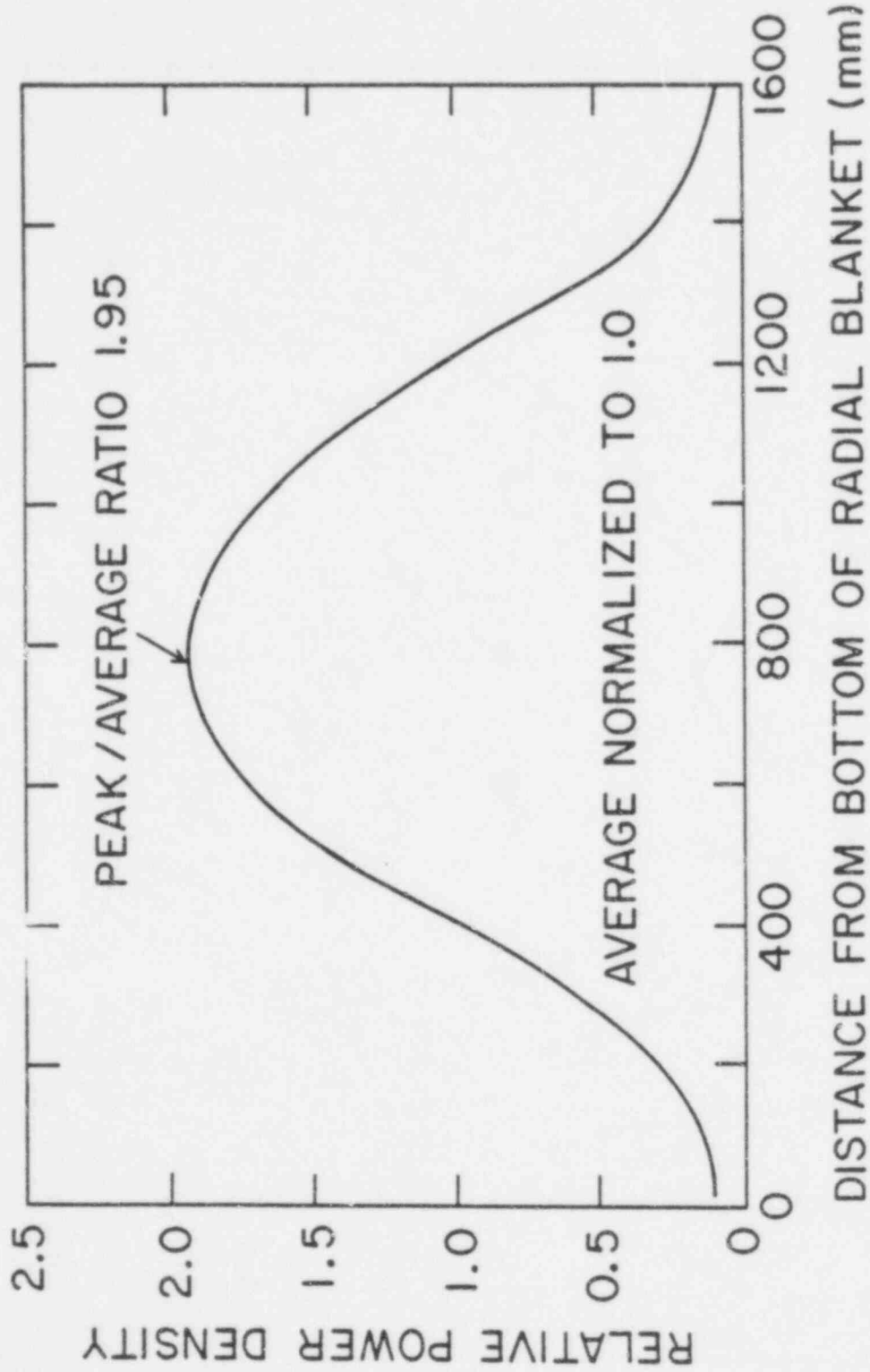


629 274

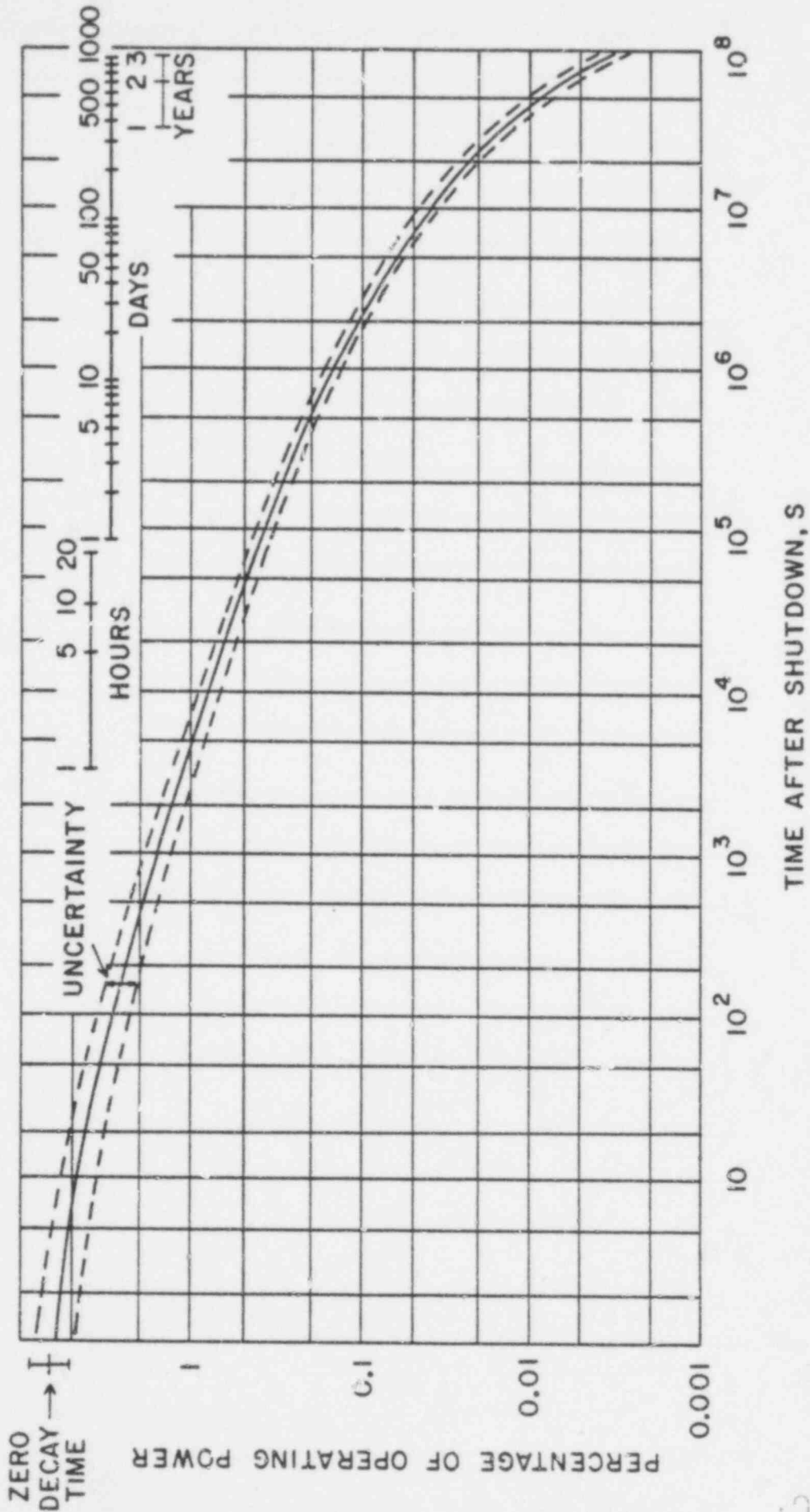




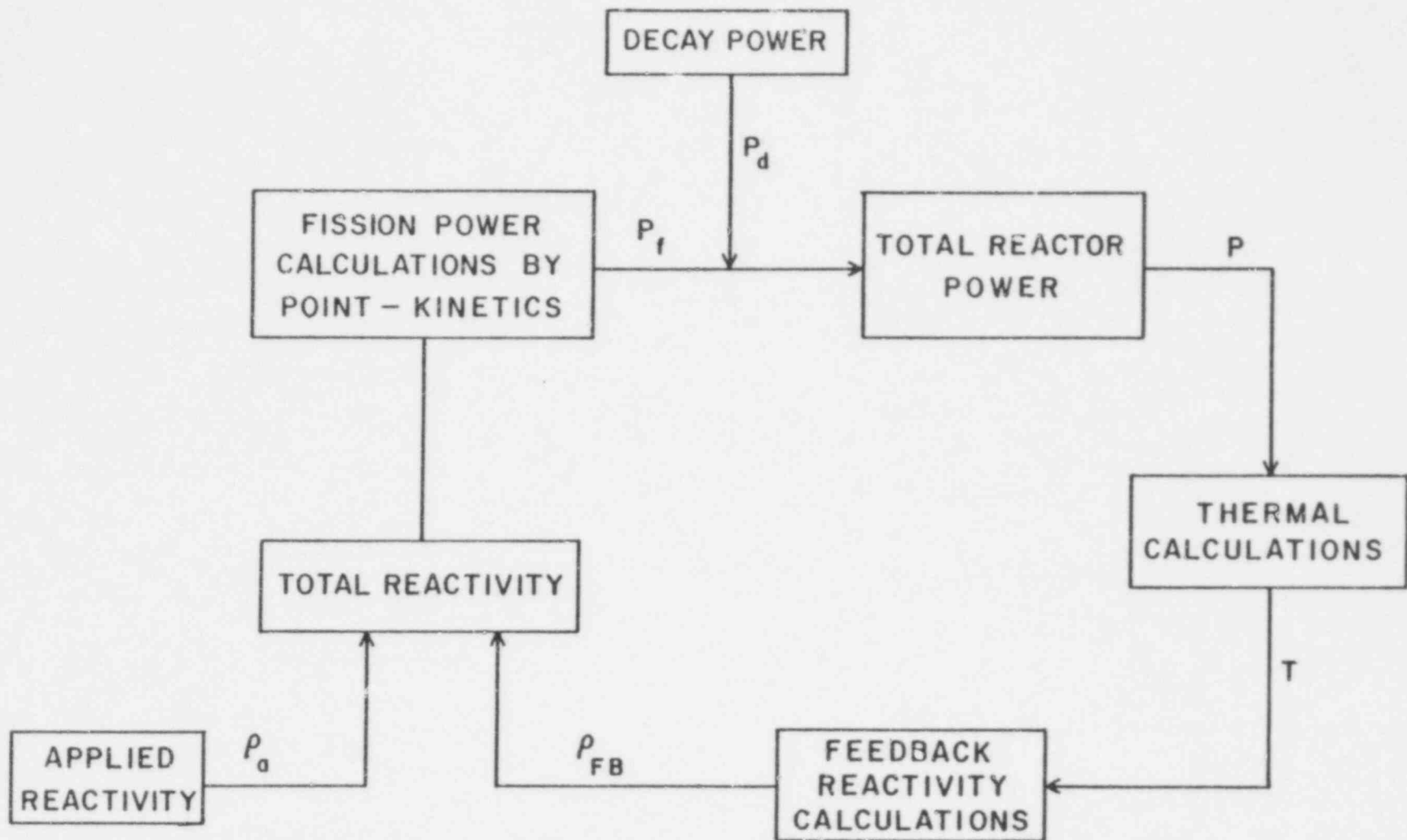
629  
2/25



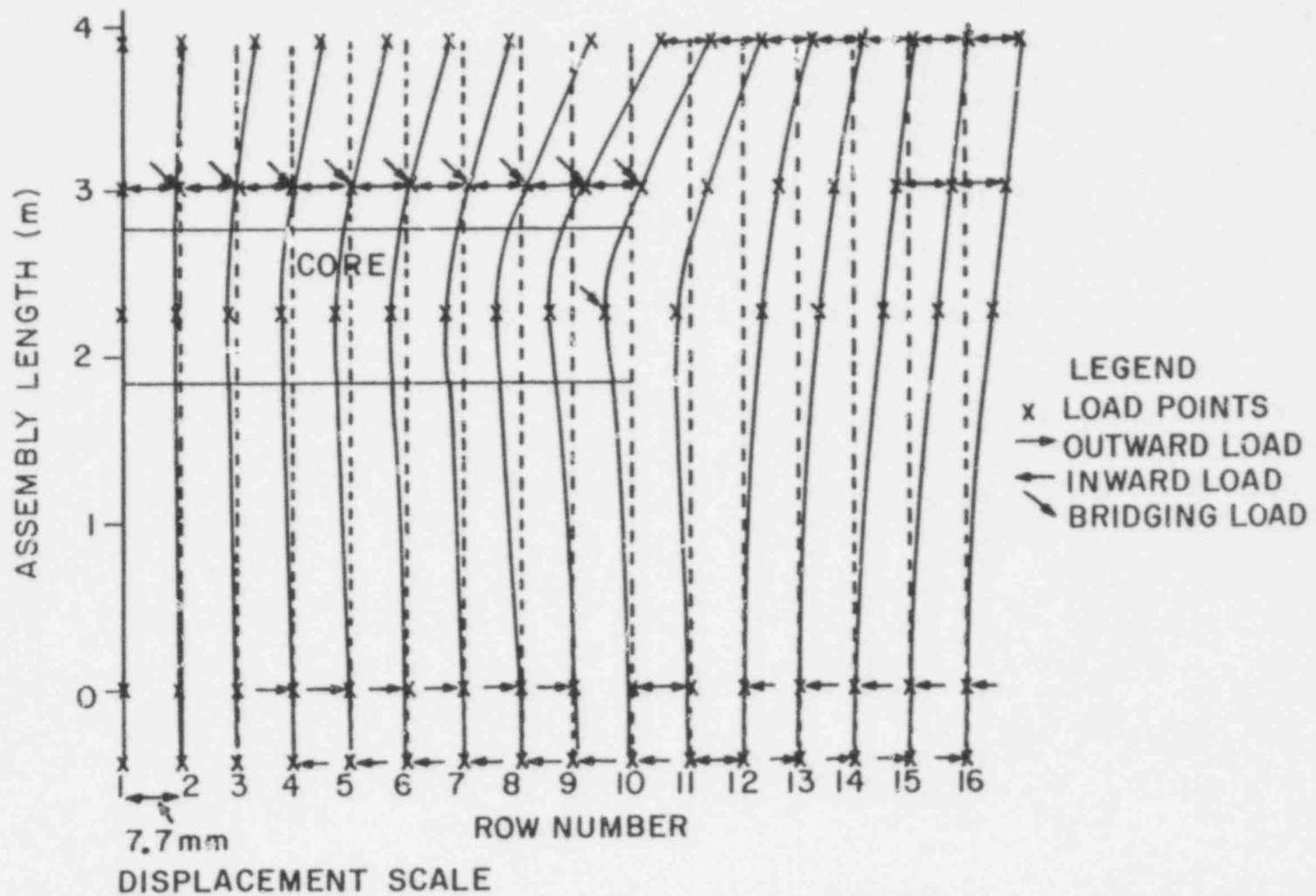
629 276



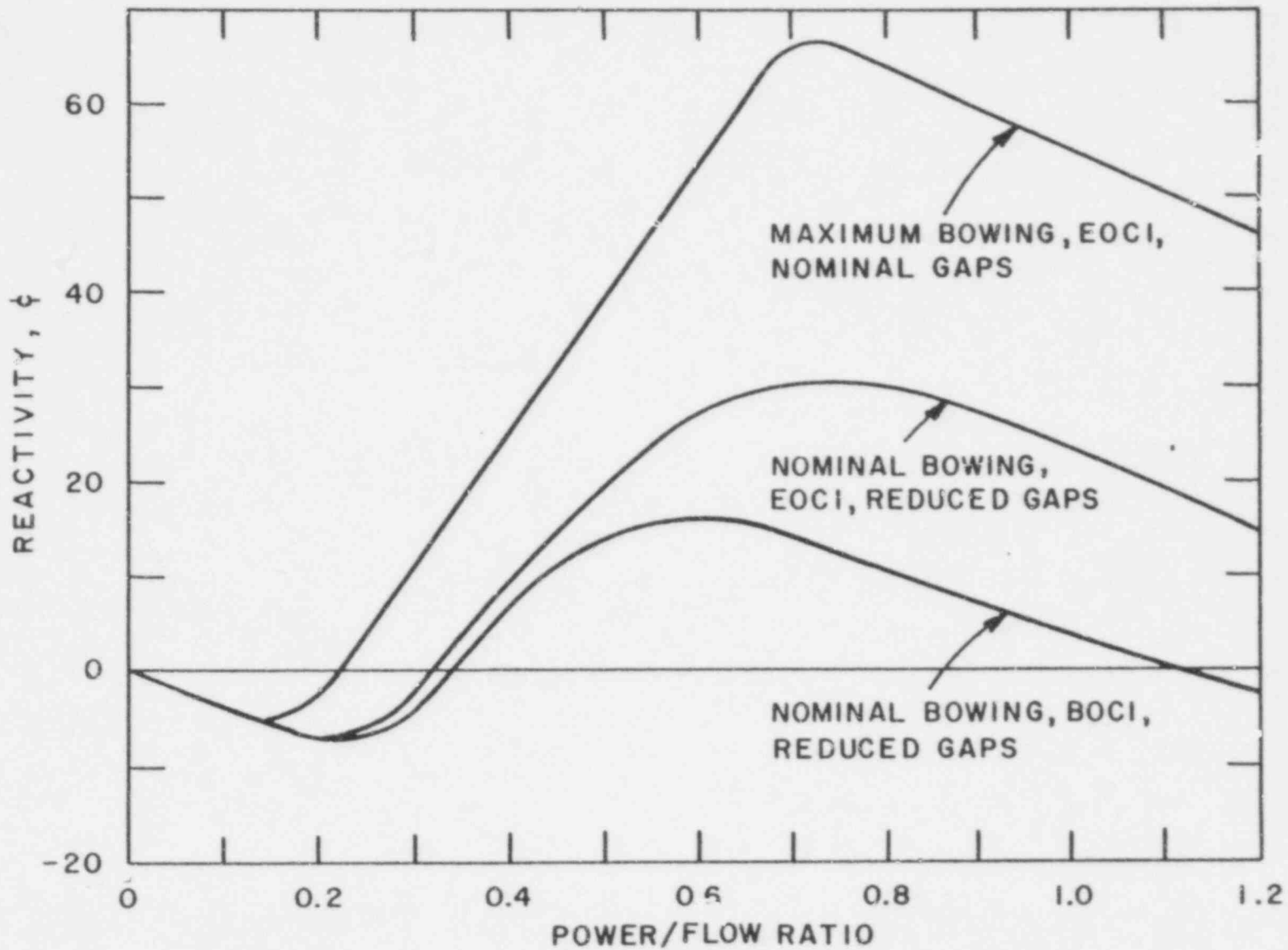
629 277



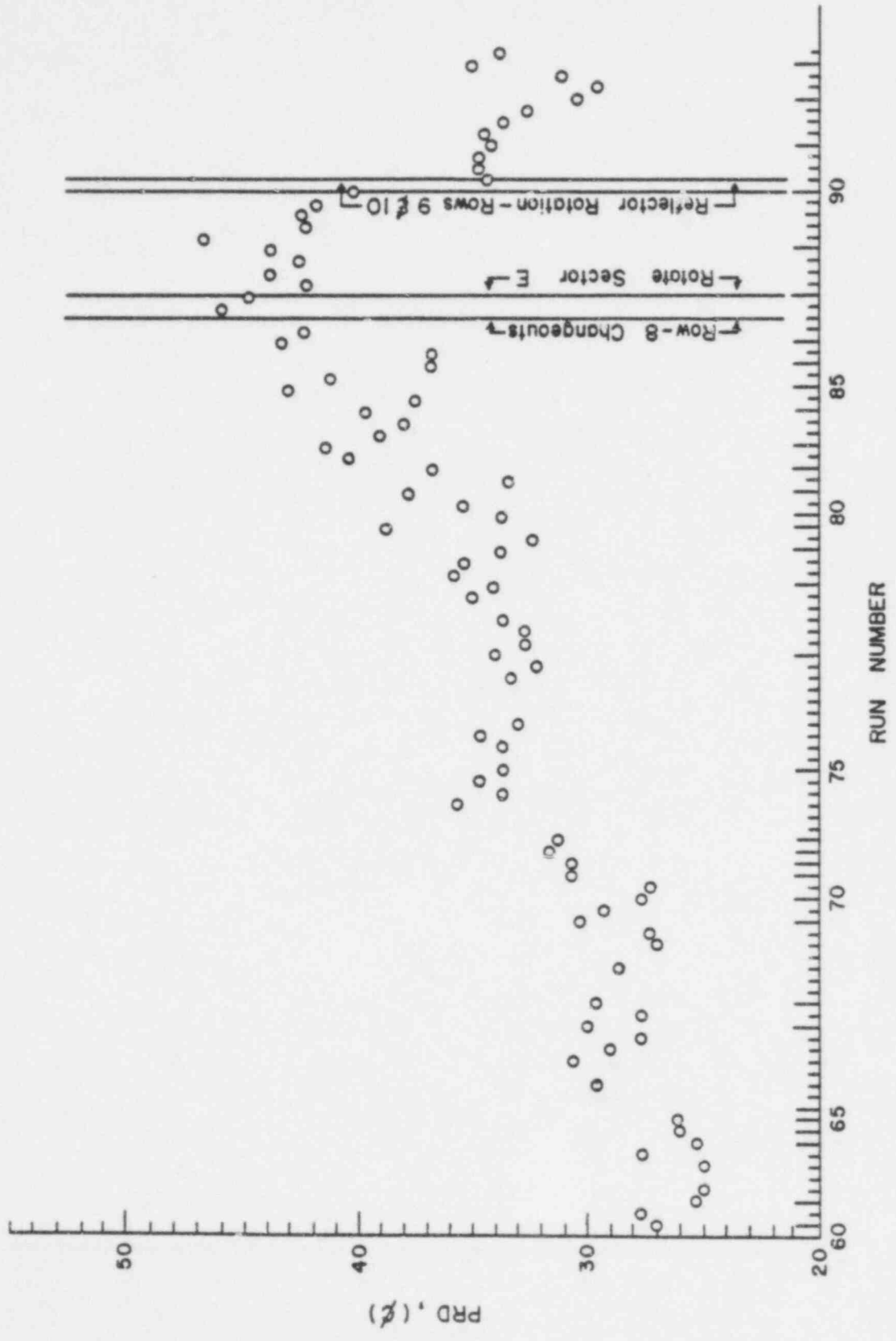
629  
278



AGRAWAL & KHATIB-RAHBAR  
Fig. 3.14

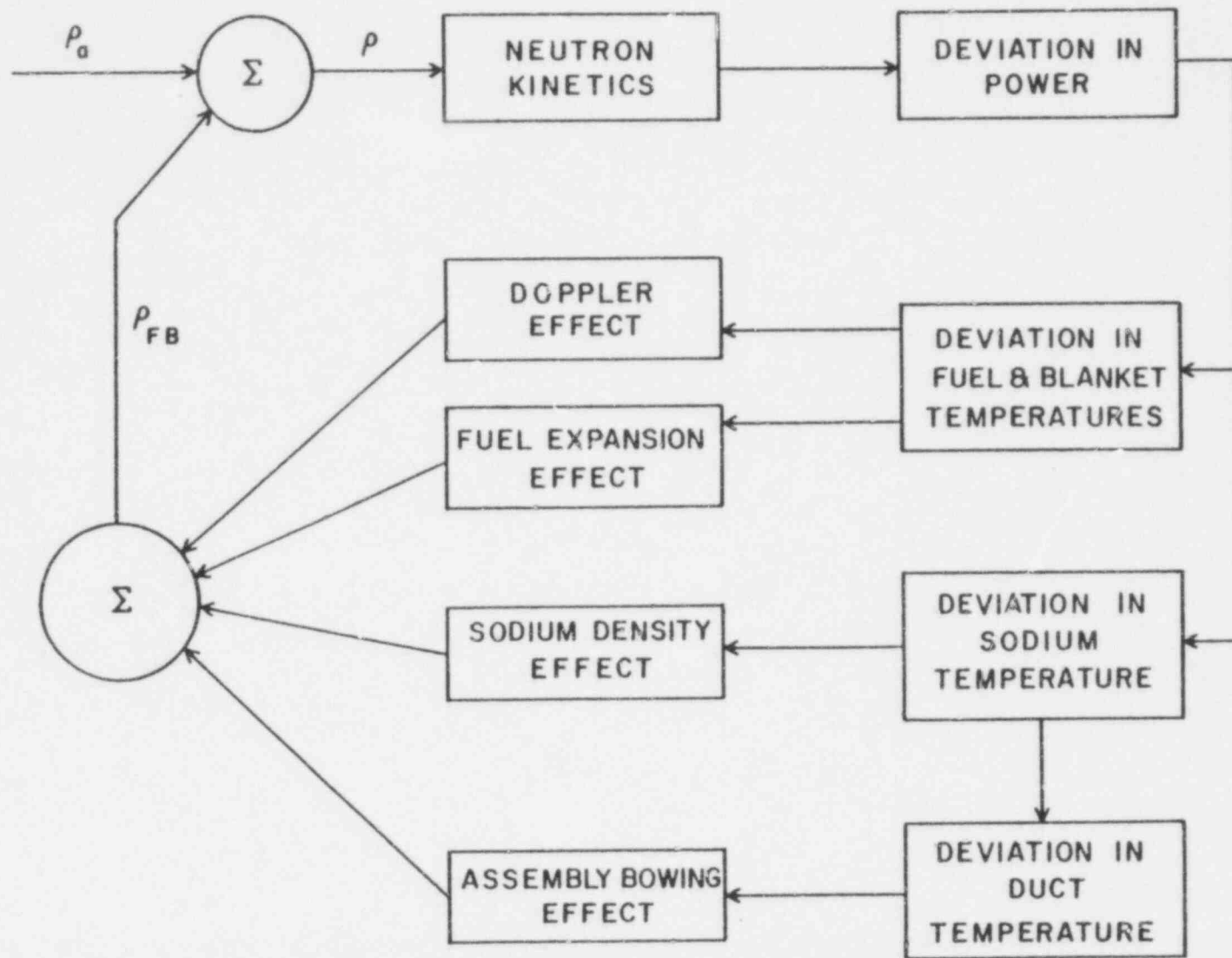


629  
280



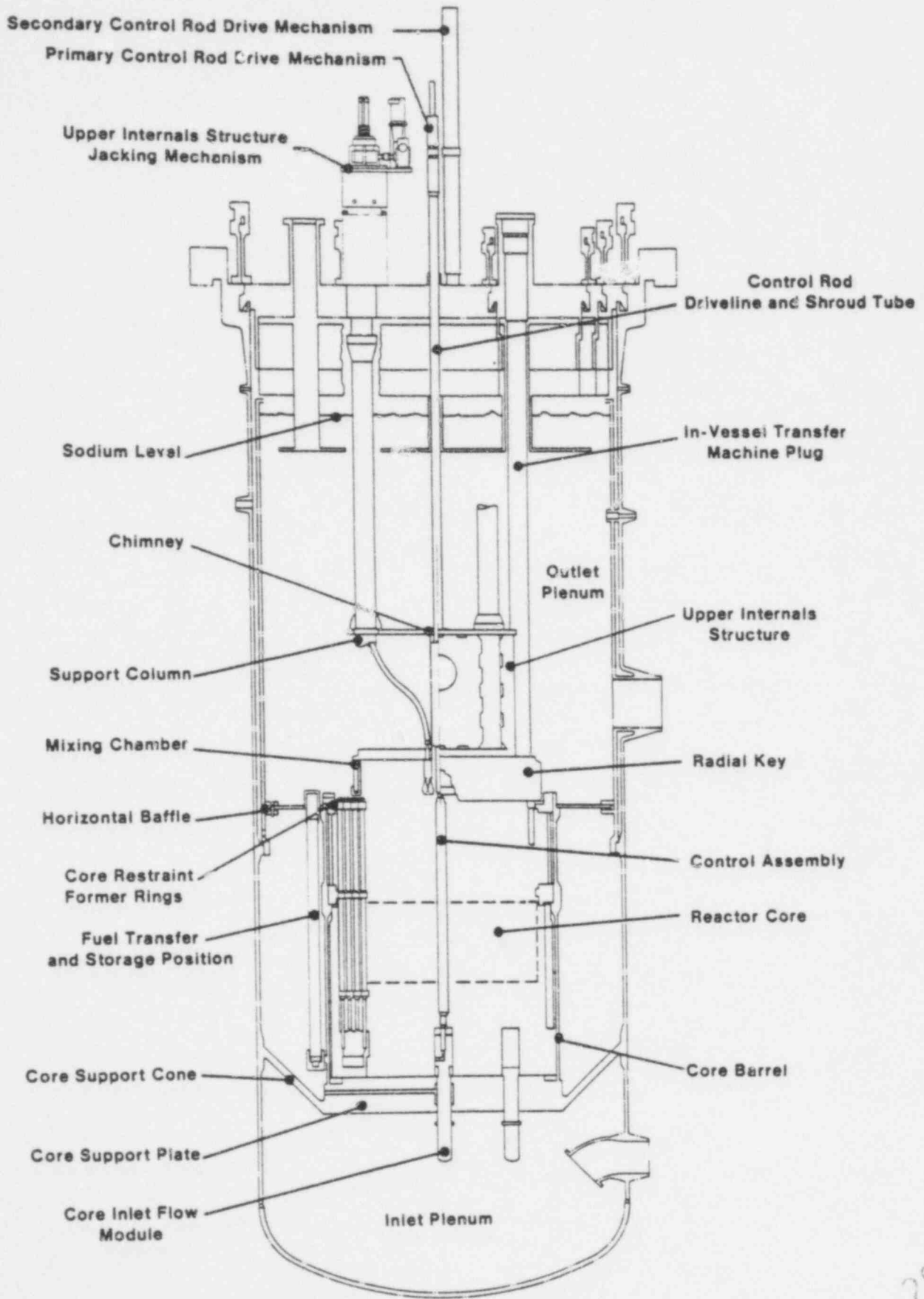
AGRAWAL & KHATIB-RAHBAR  
Fig. 3.16

629 281

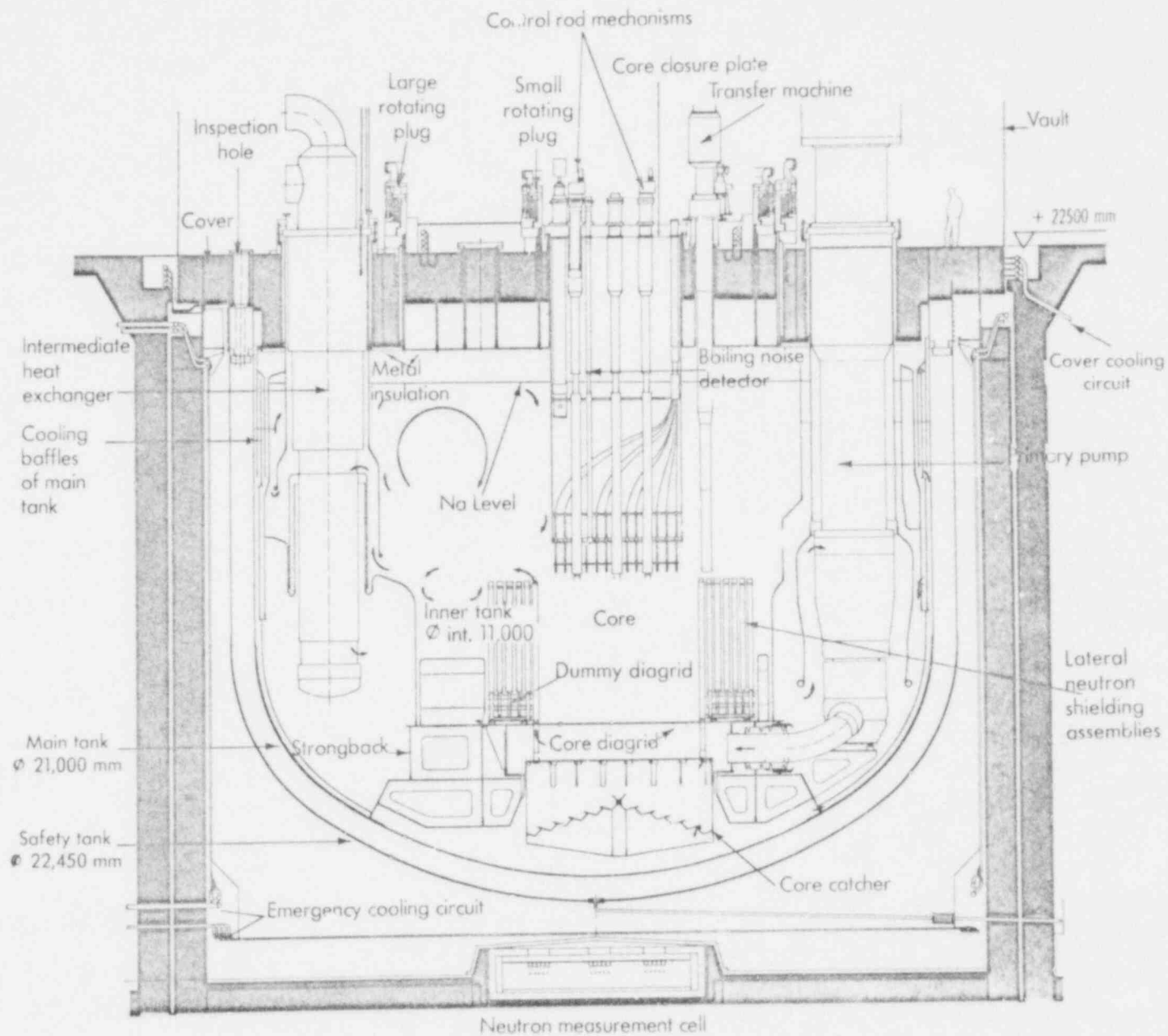


029  
282

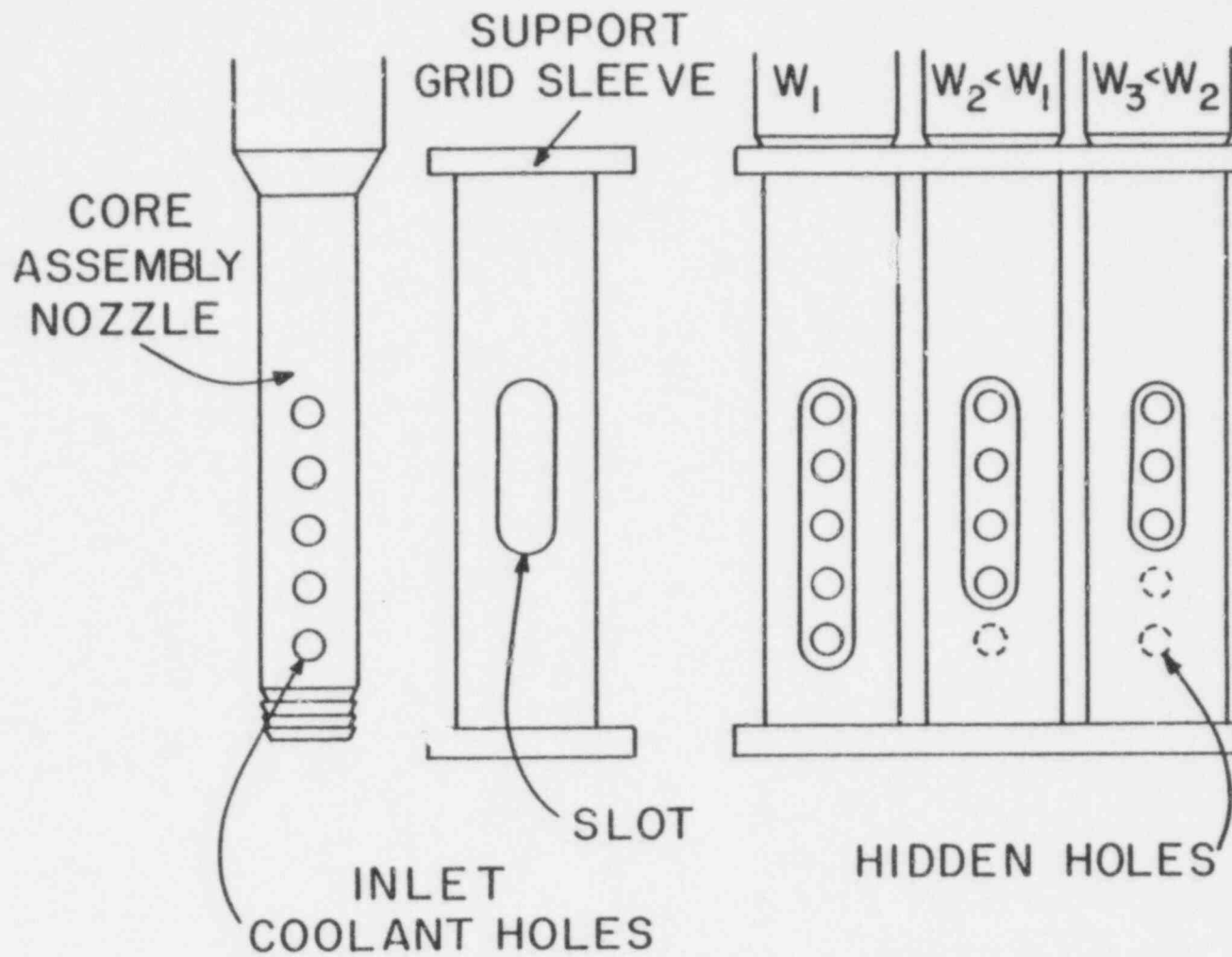




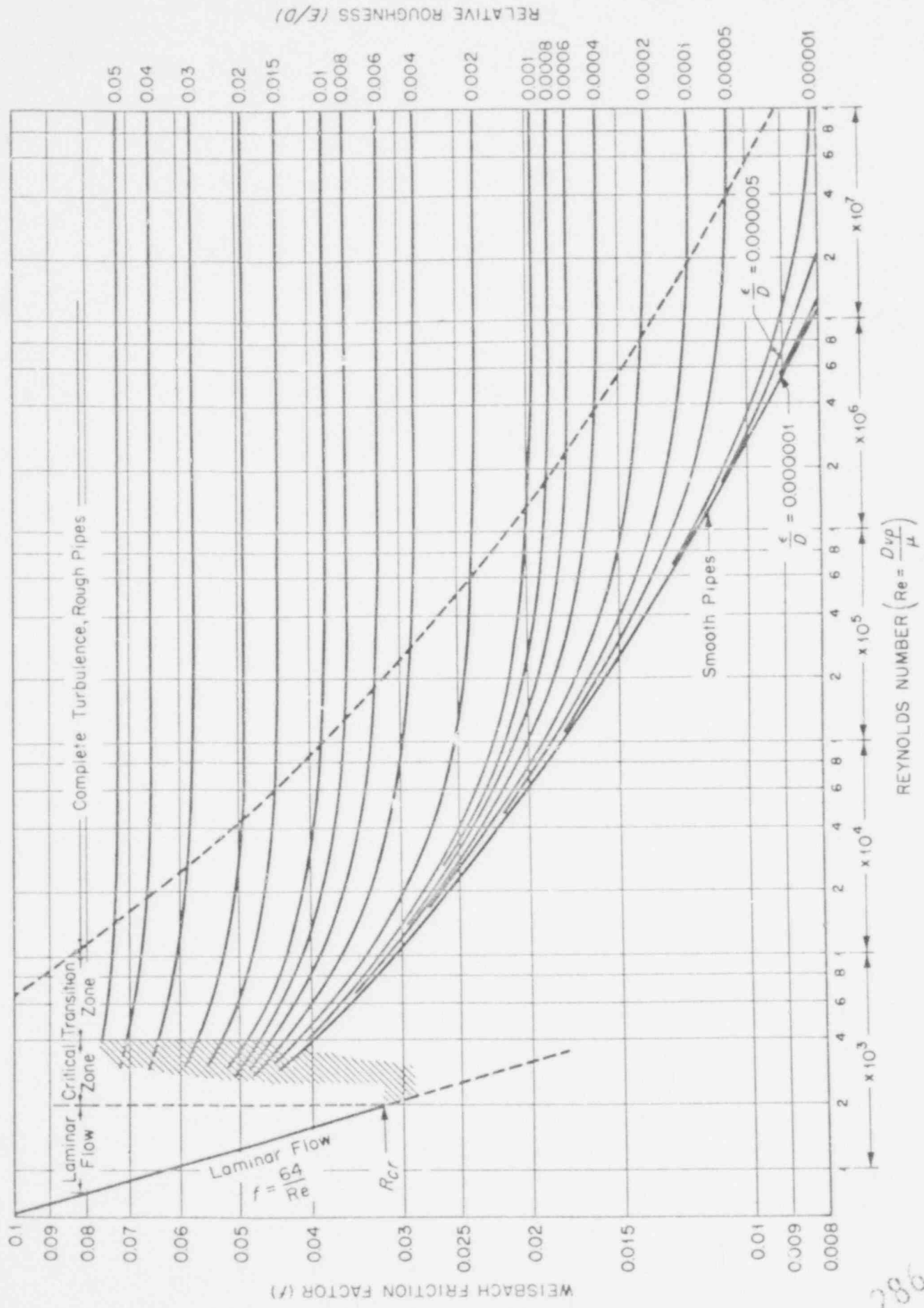
629 283



AGRAWAL & KHATIB-RAHBAR  
Fig. 3.19

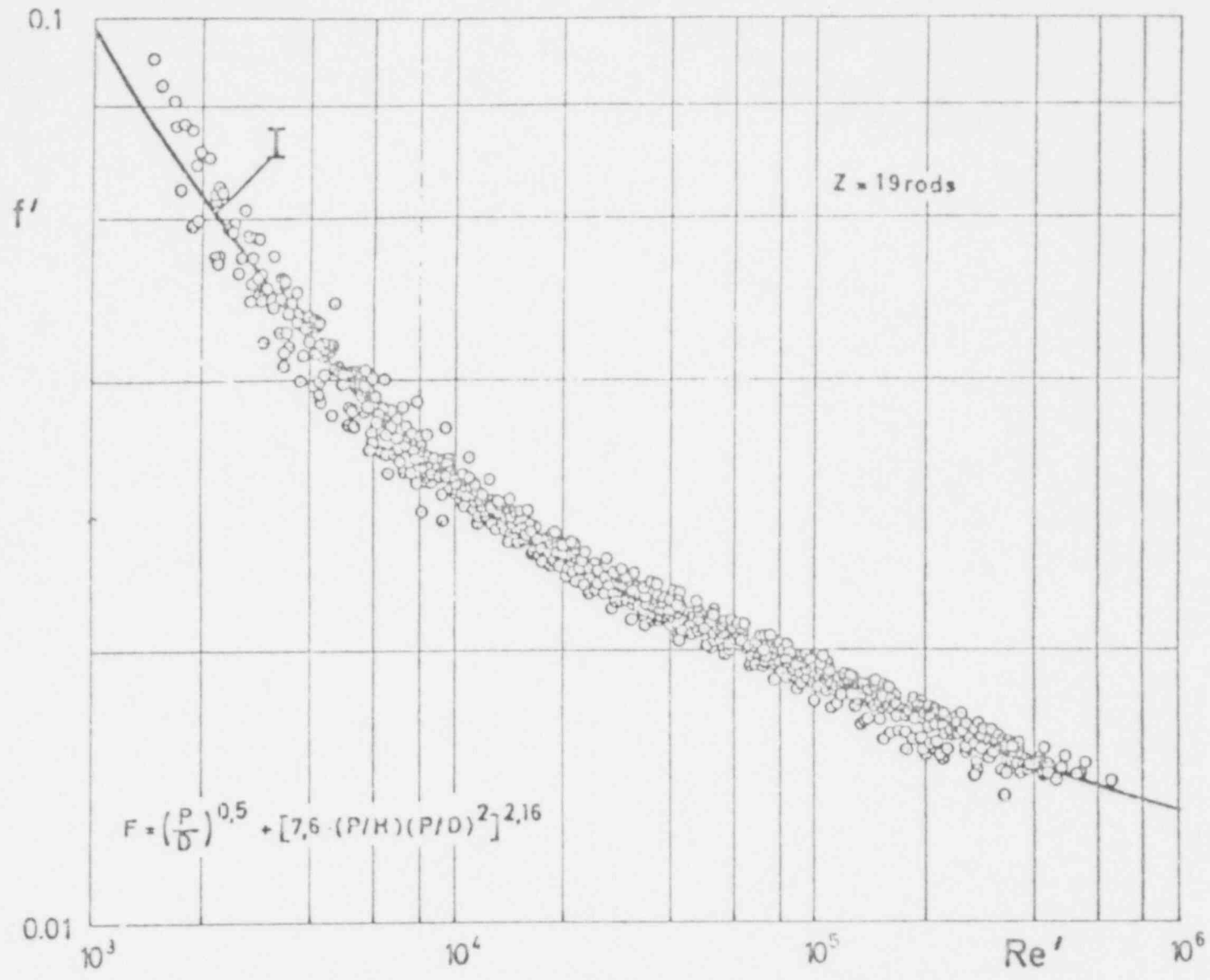


629  
285



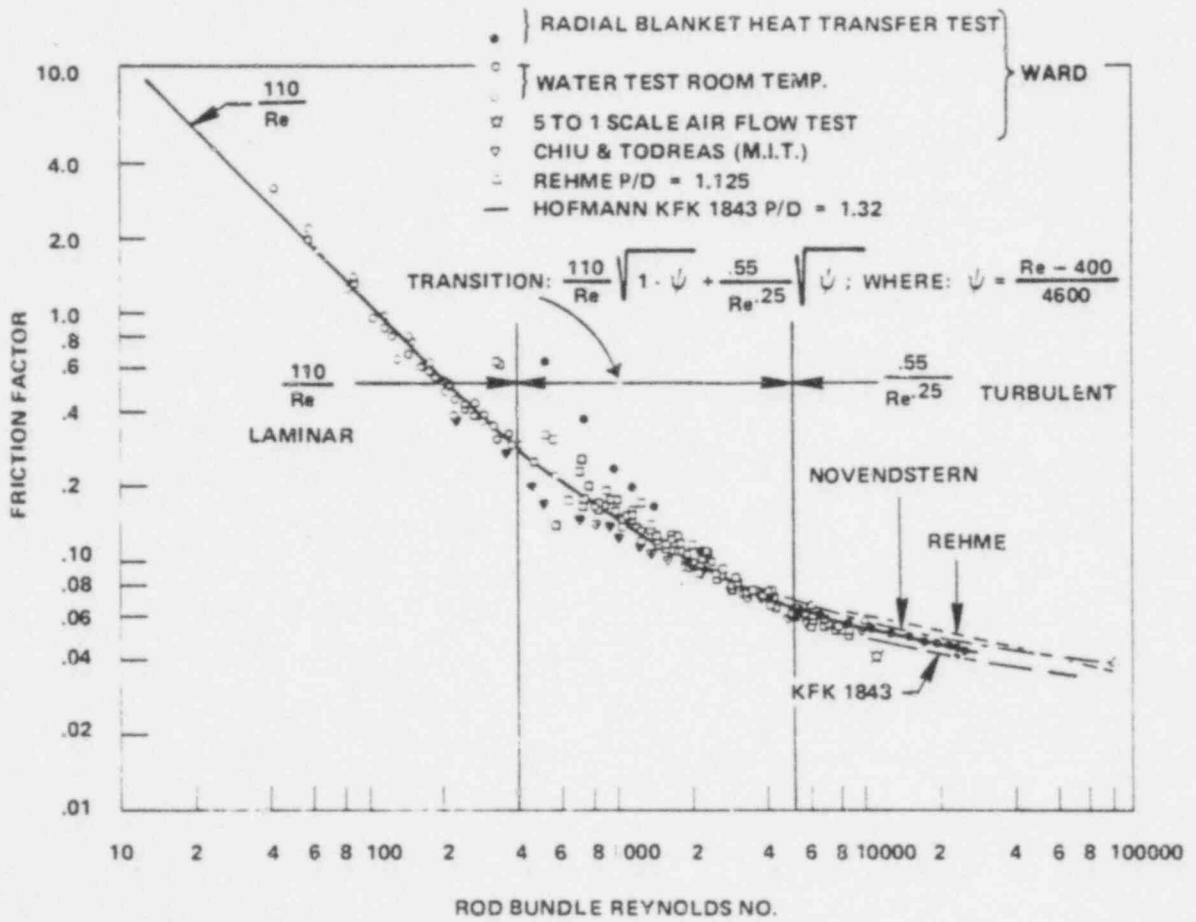
AGRAWAL & KHATTIB-RAHIBAR  
Fig. 3.21

529  
286

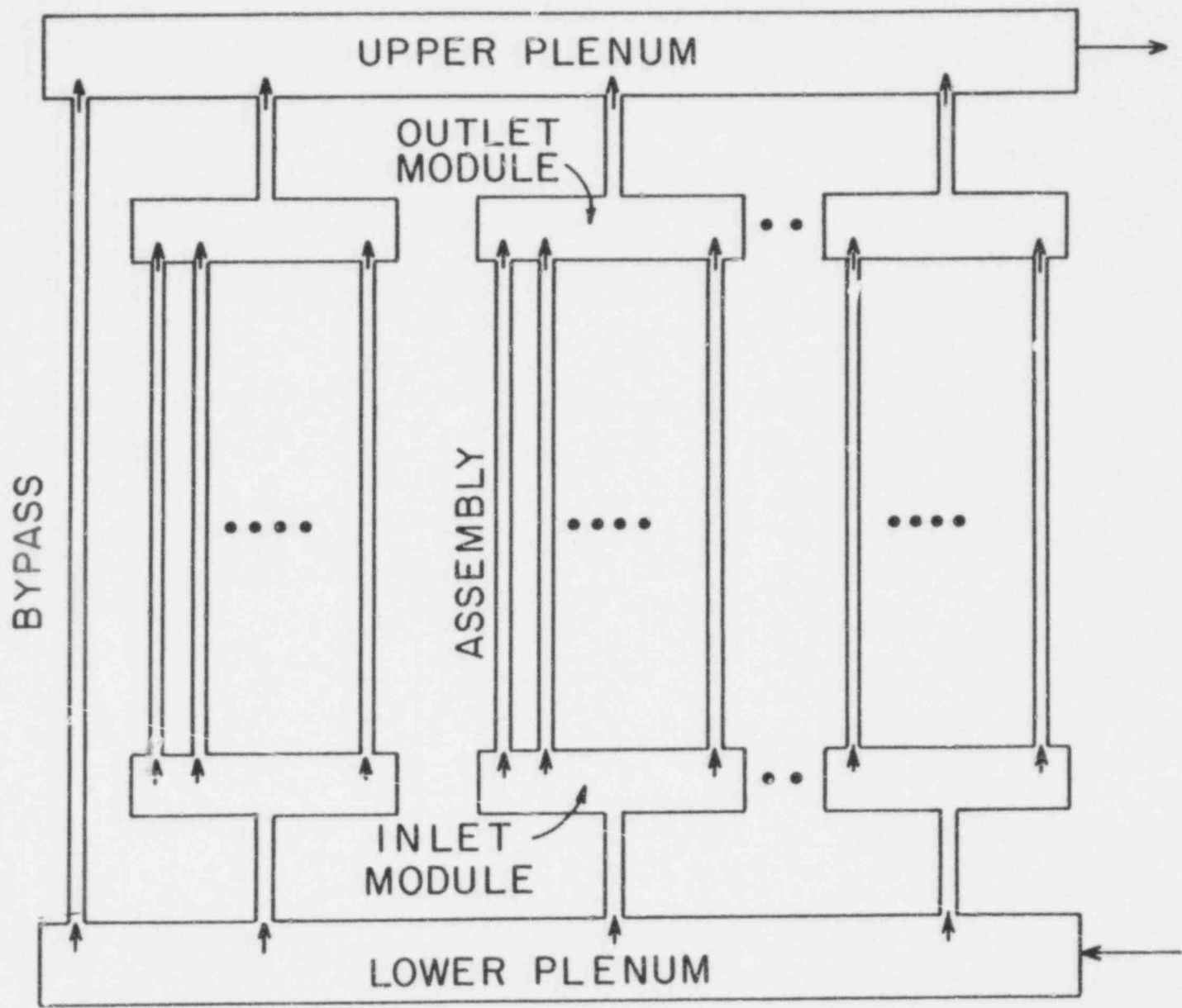


a) wire wraps,  $f' = \frac{f}{F} \cdot \frac{P_{\text{gas}}}{P_B}$ ;  $Re' = Re \cdot F^{0.5}$ ;  $I: f' = 0.1317 \cdot Re'^{-0.17}$

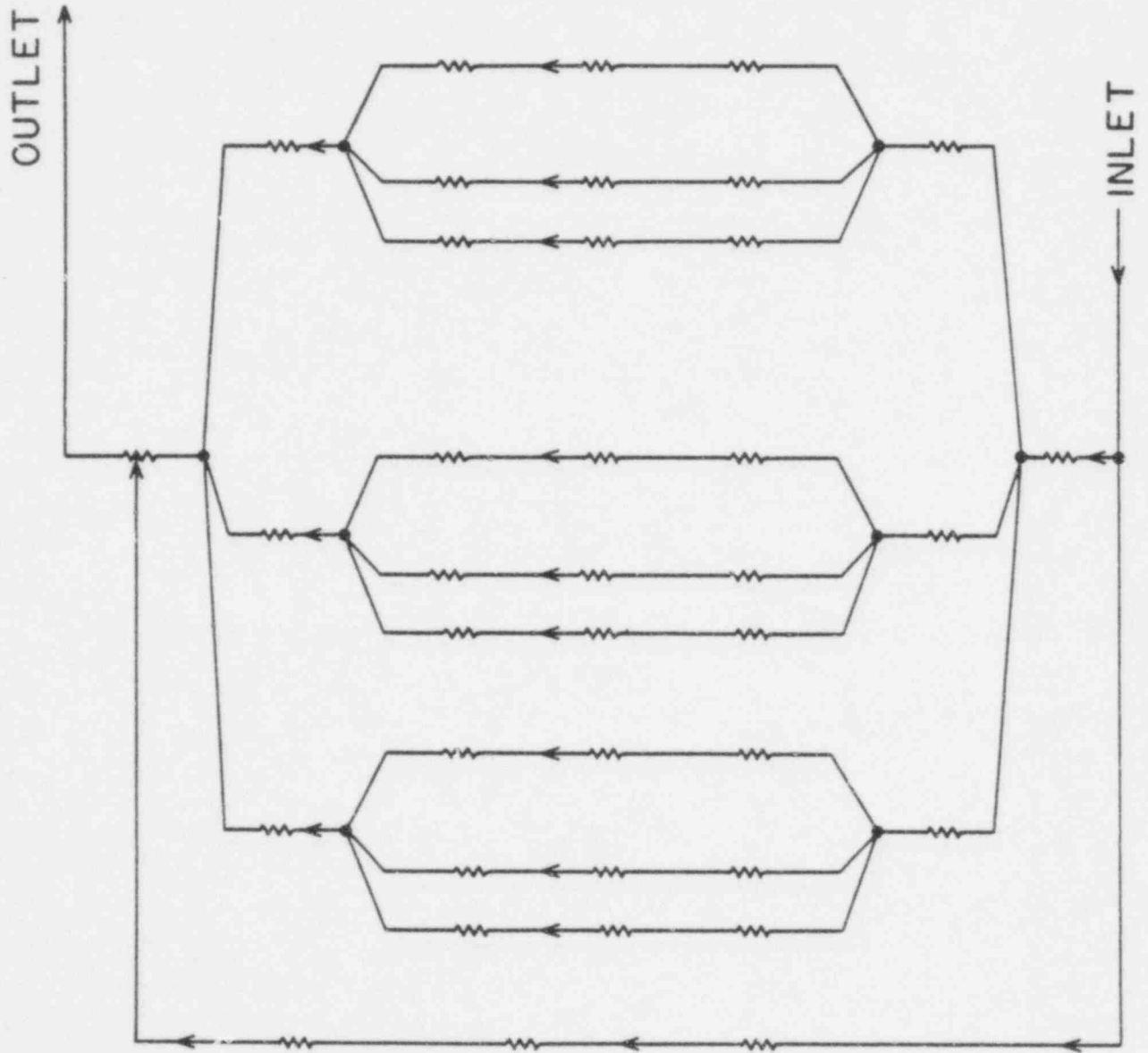
229  
287



629 288  
 AGRAWAL & KHATIB-RAHBAR  
 Fig. 3.23

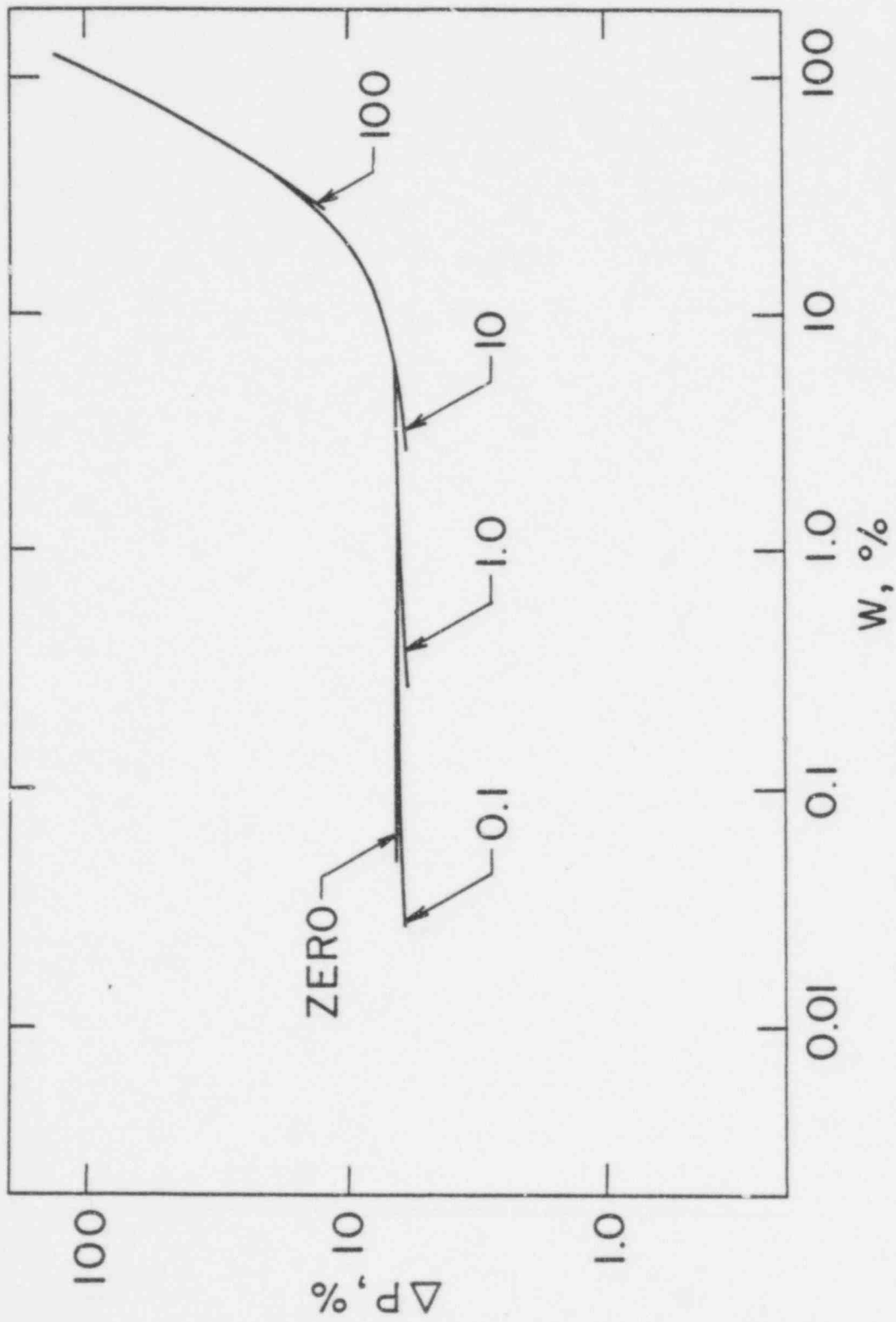


629  
289

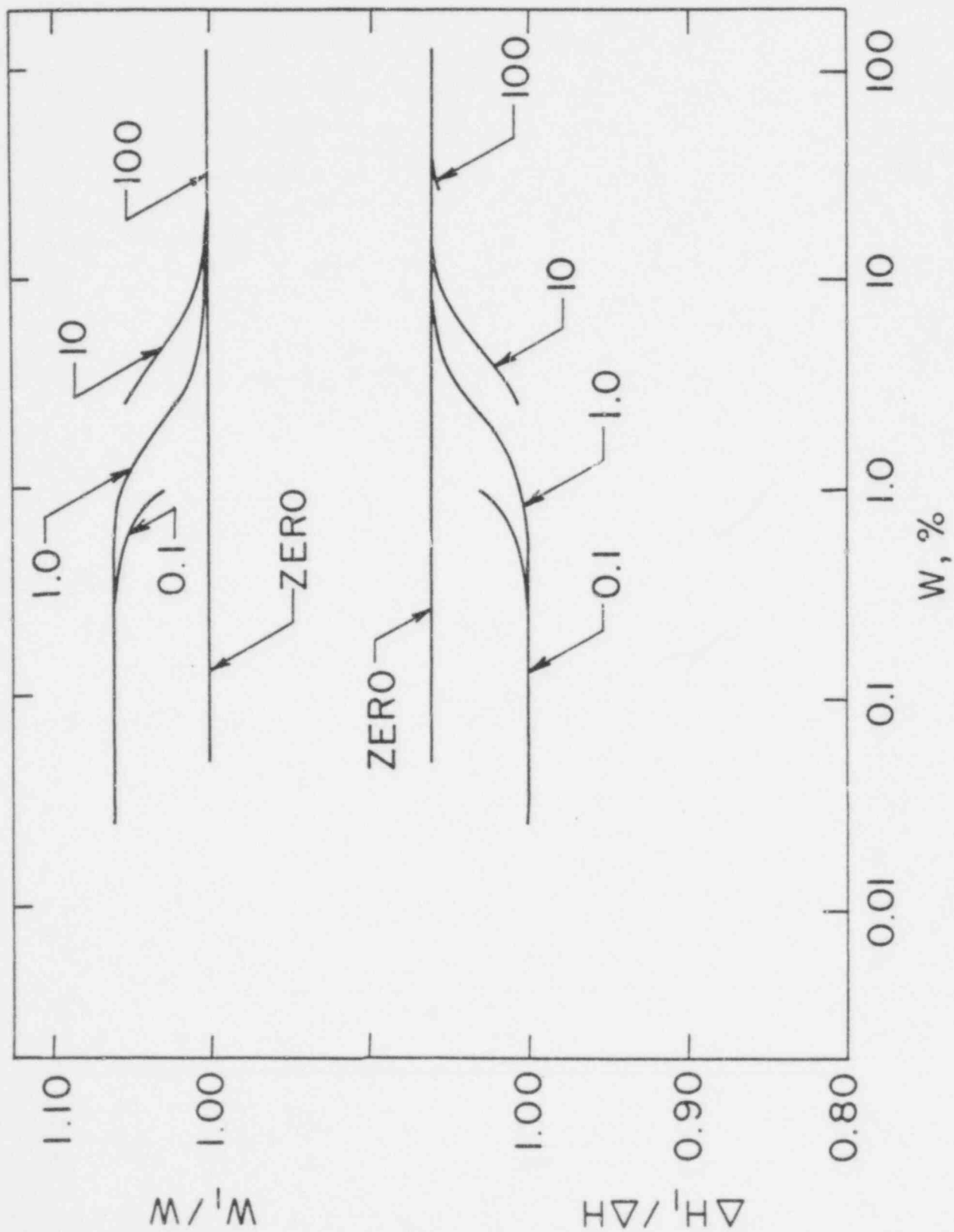


629 290

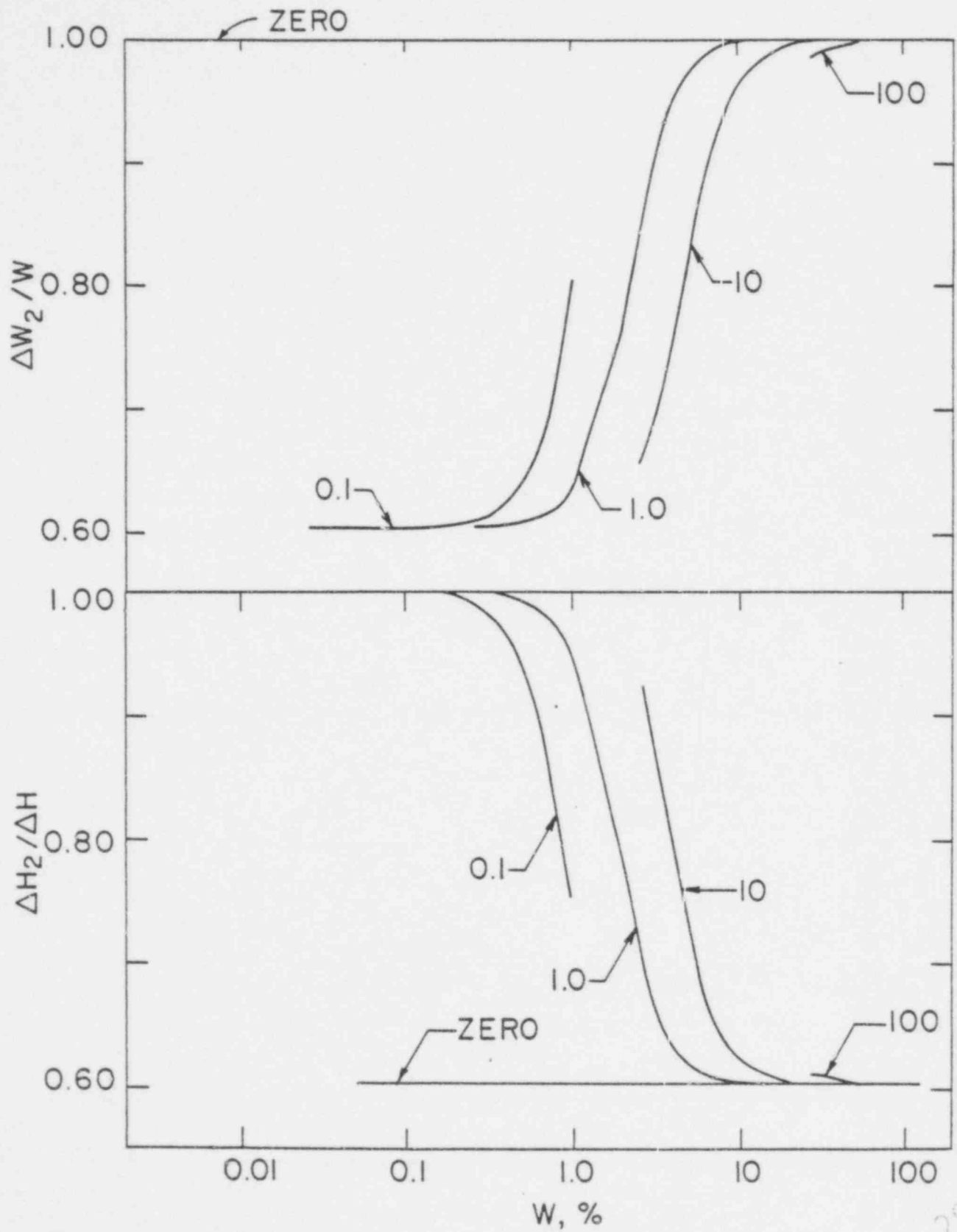


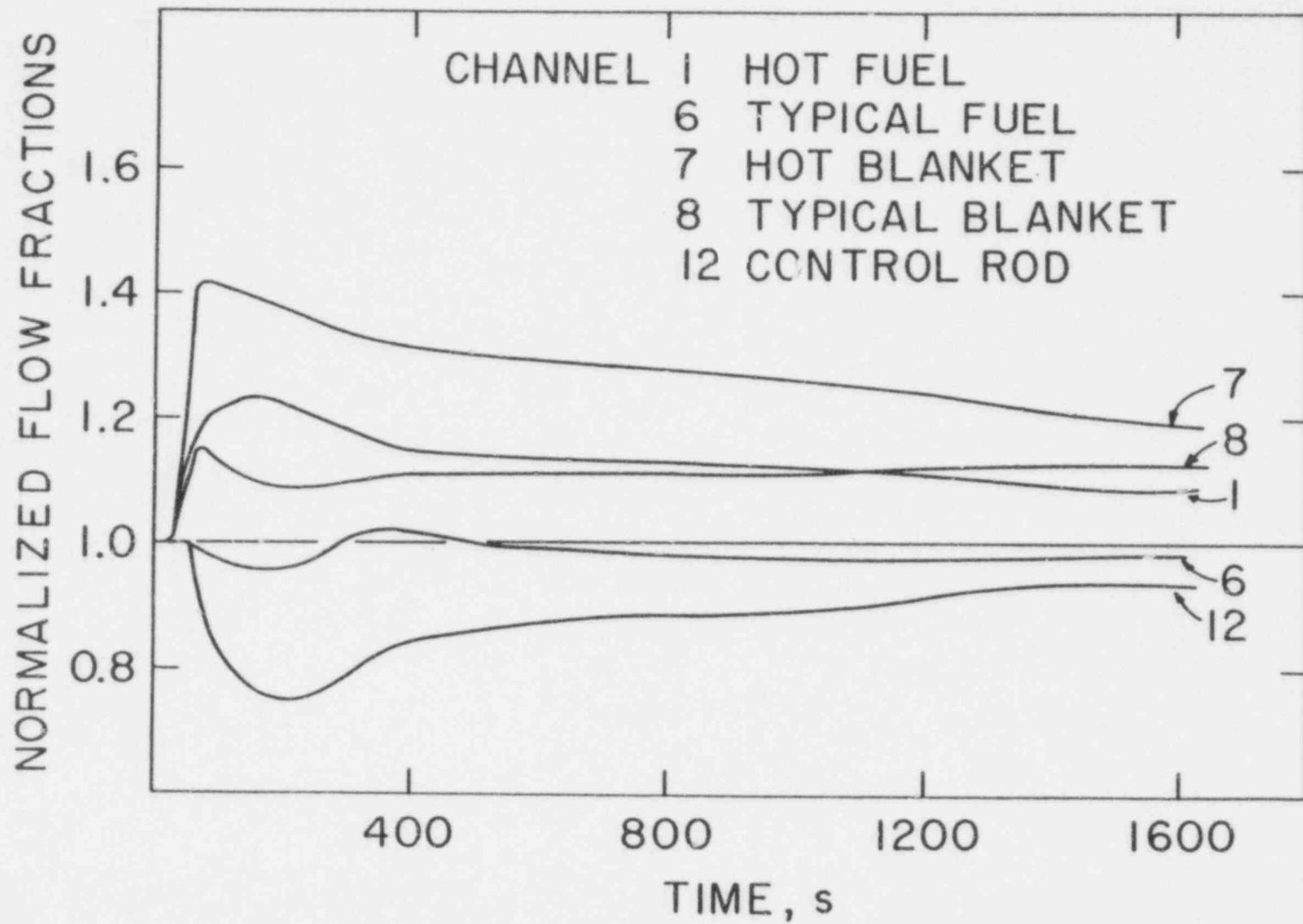


629 291

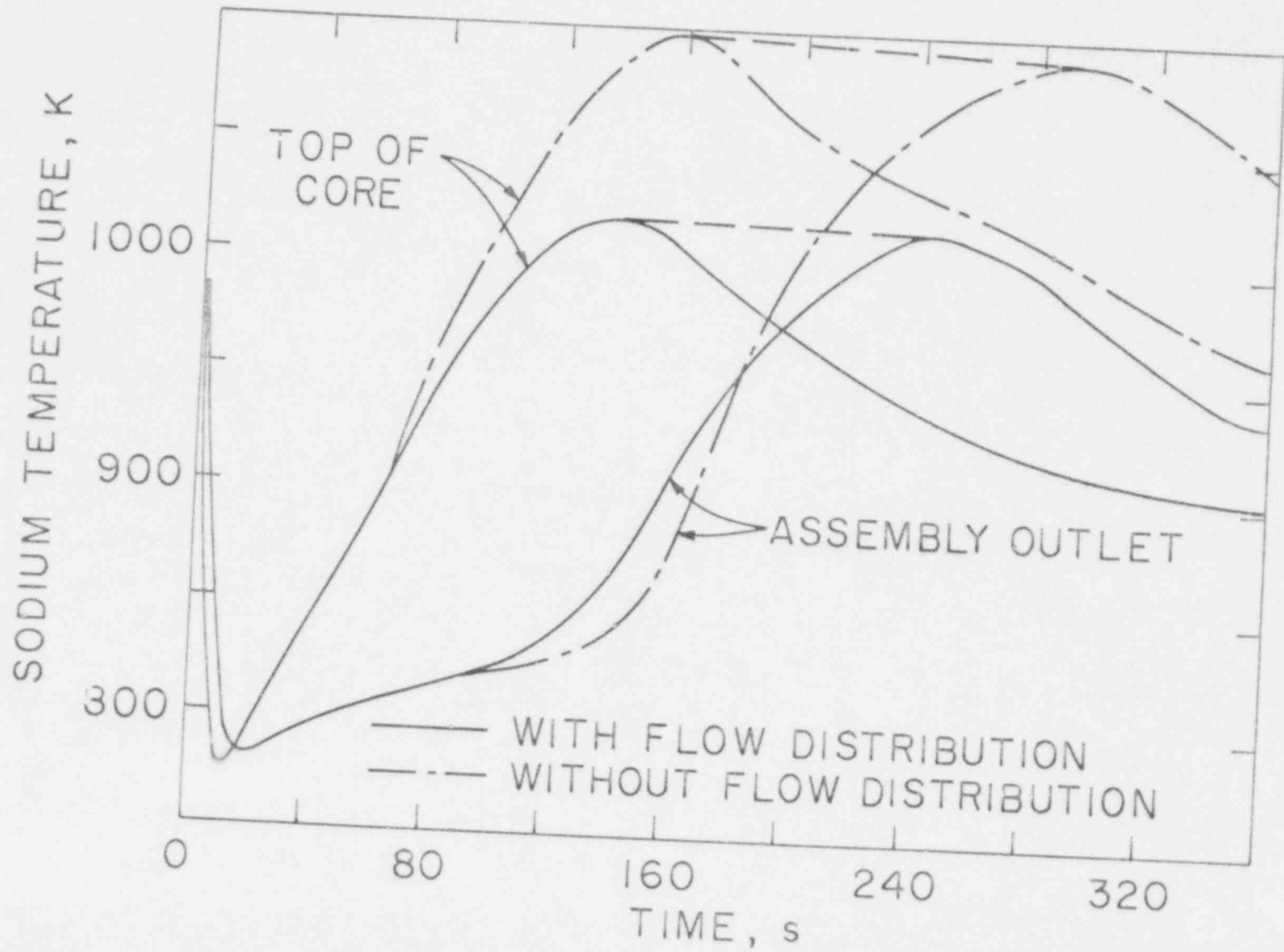


629 292

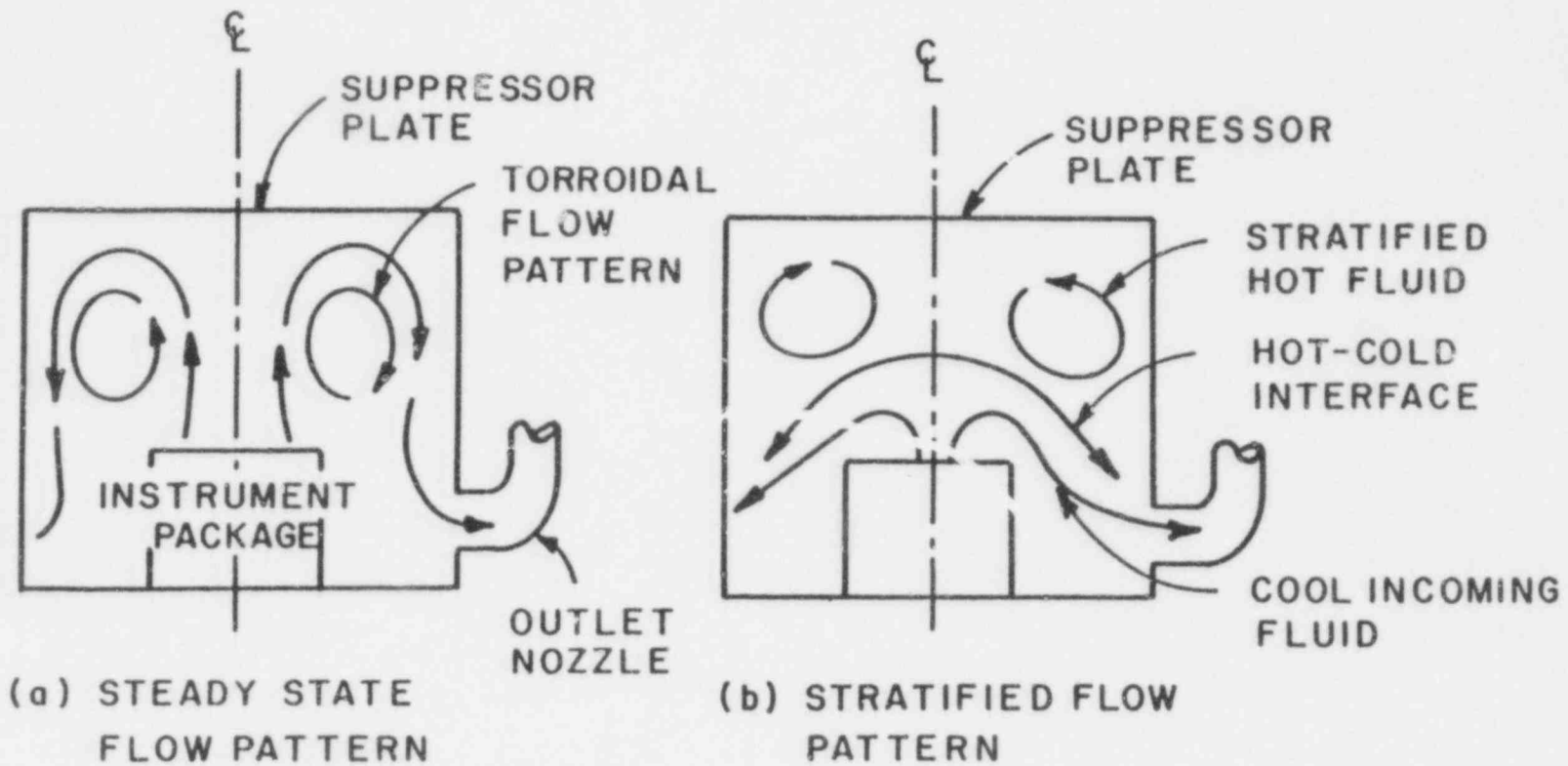




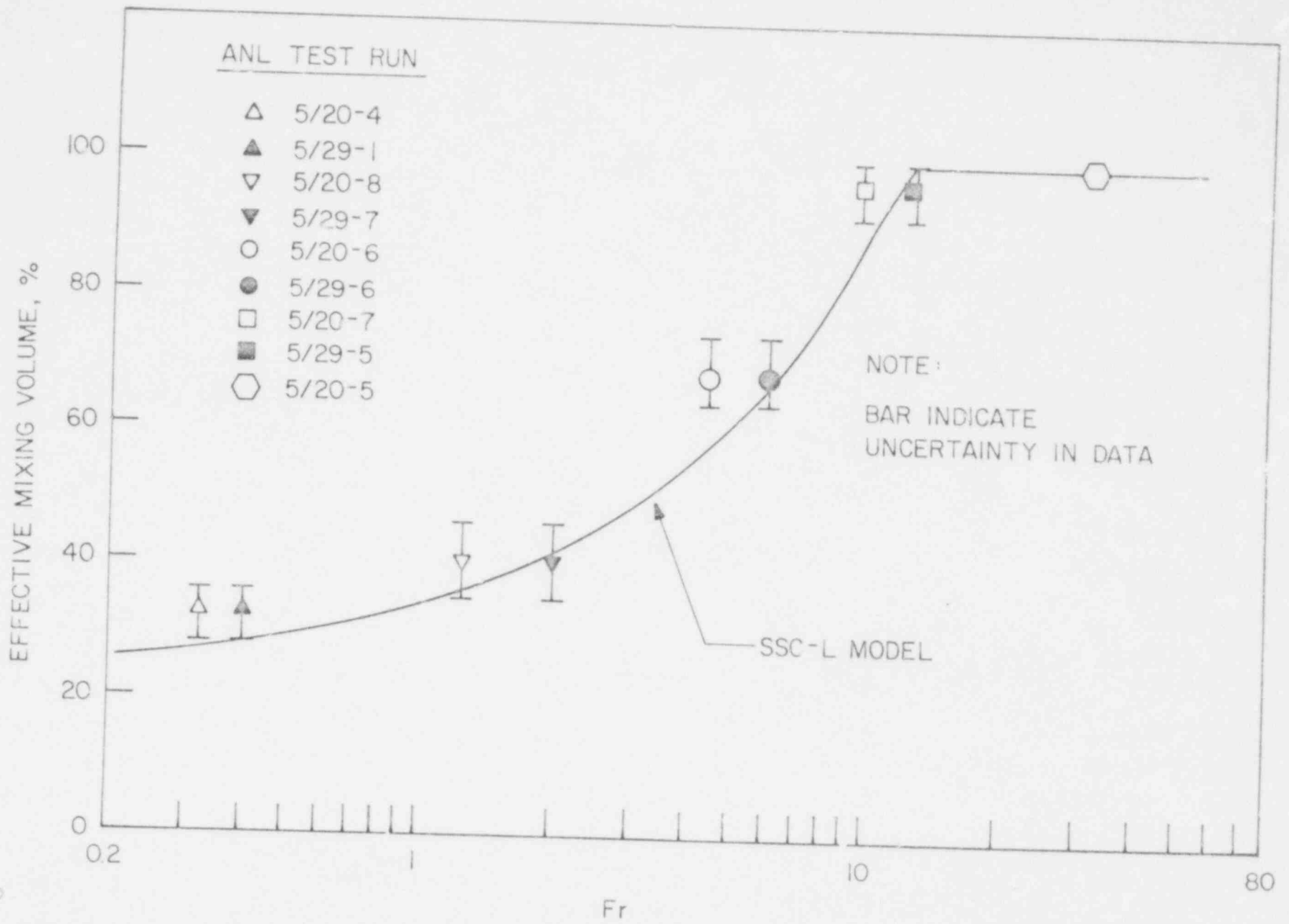
629  
 294



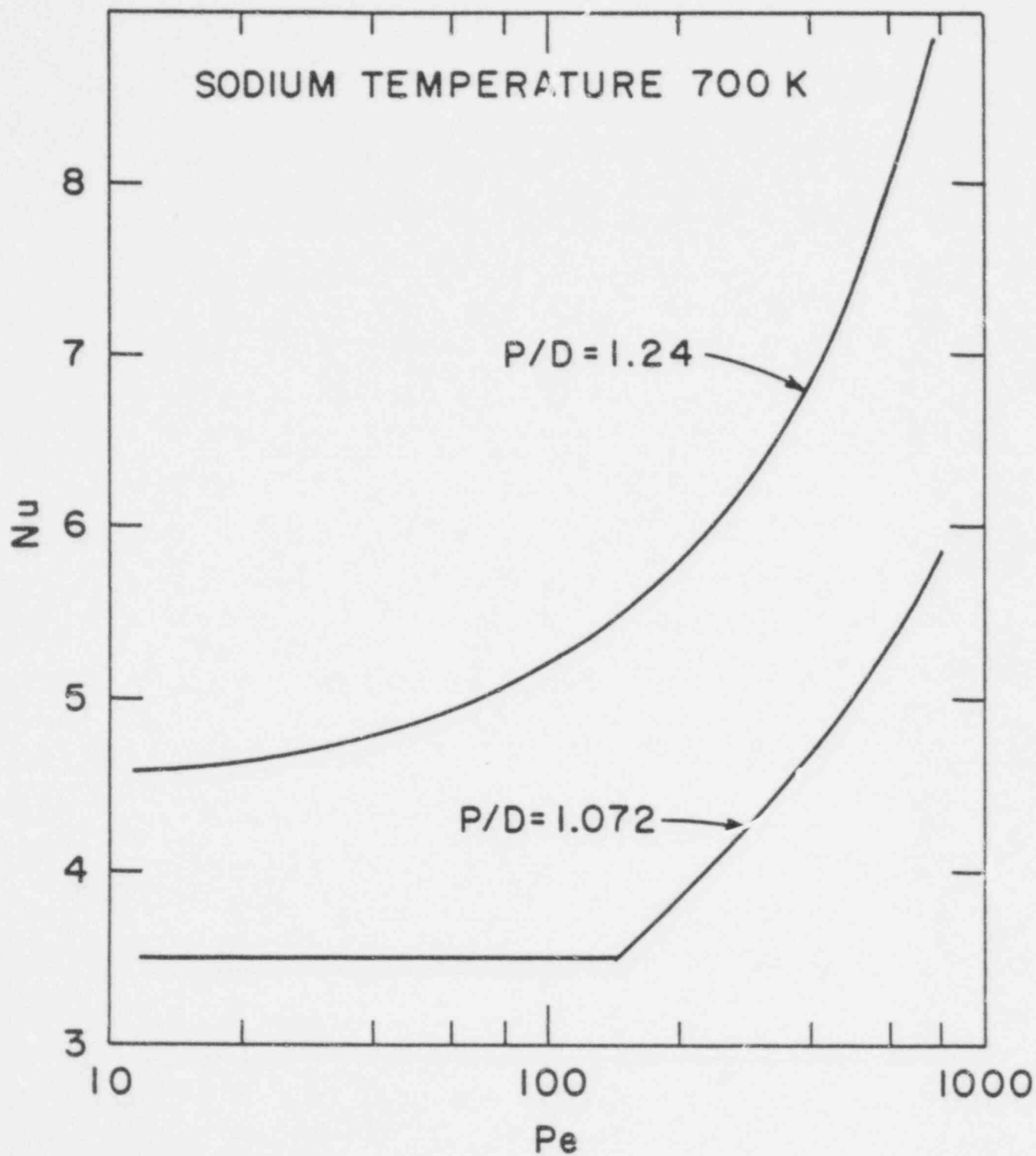
AGRAWAL & KHATIB-RAHBAR  
Fig. 3.30



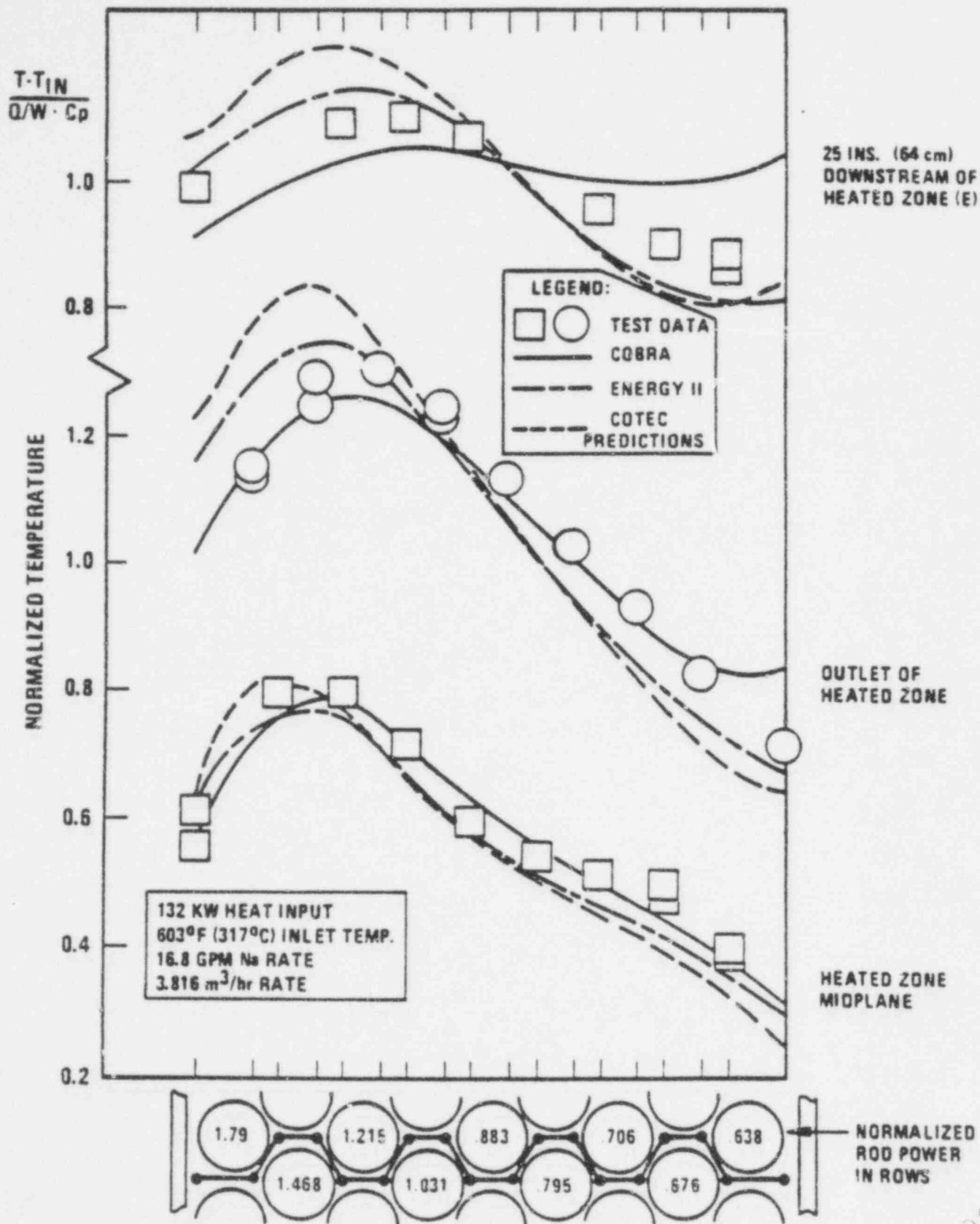
629  
2990



629  
297



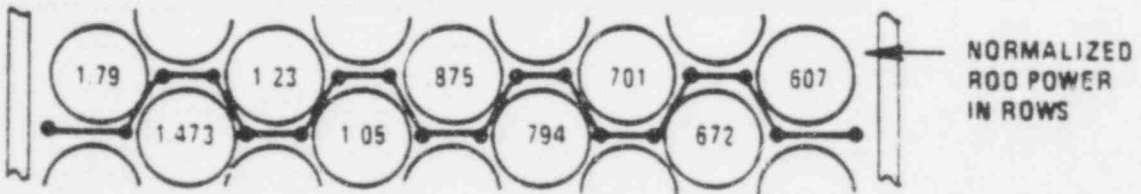
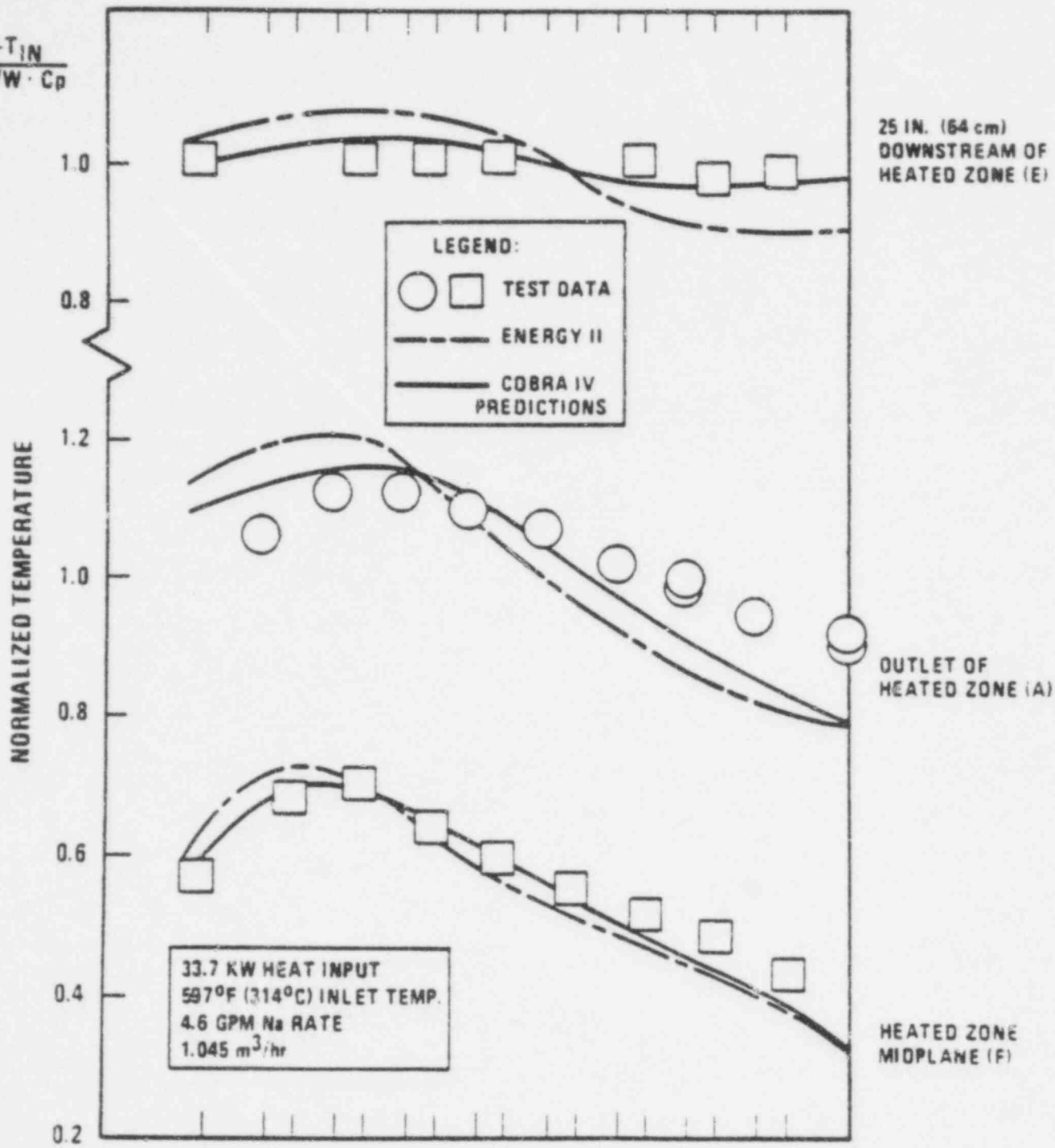




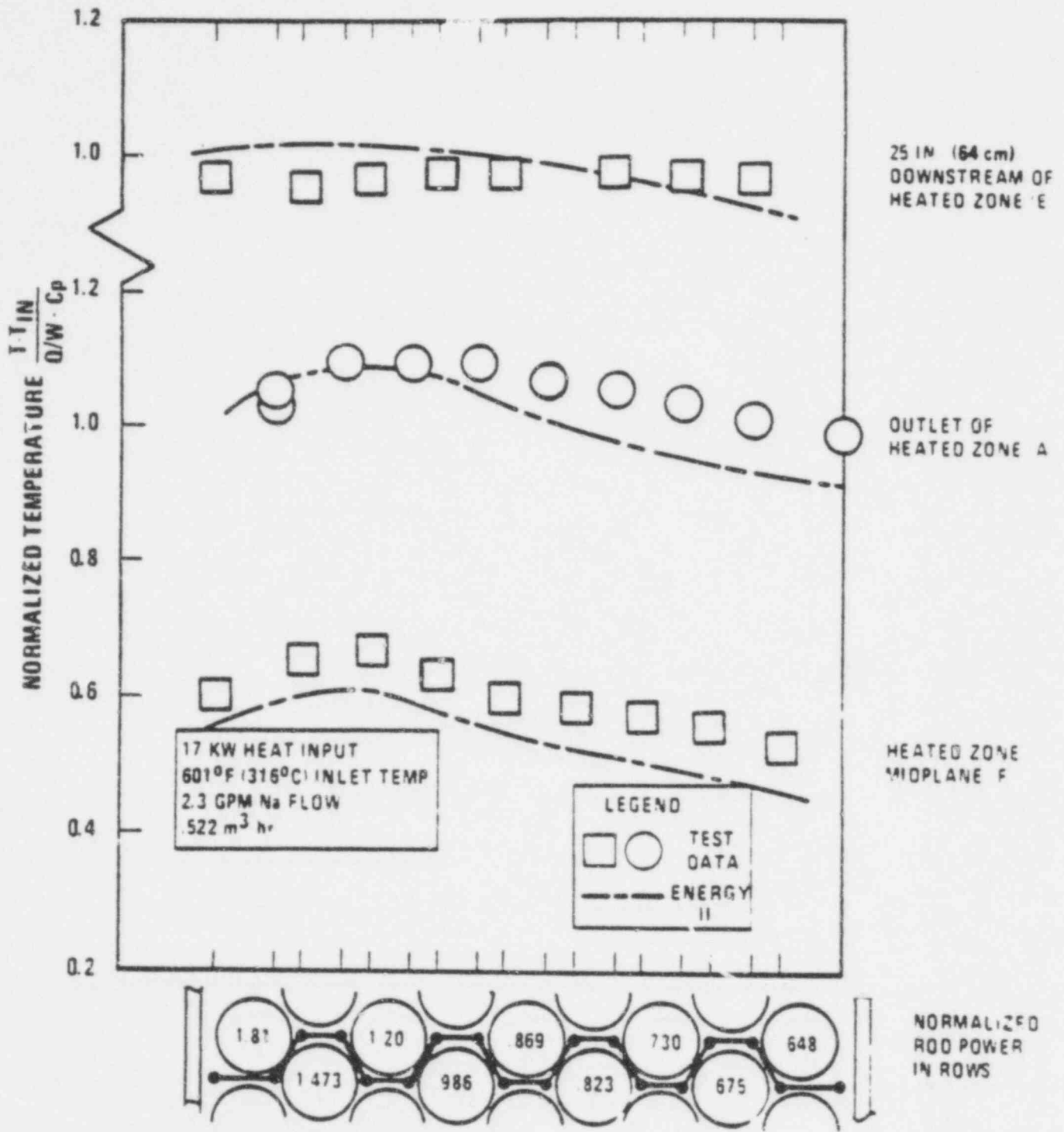
AGRAWAL & KHATIB-RAHBAR  
 Fig. 3.34

629 299

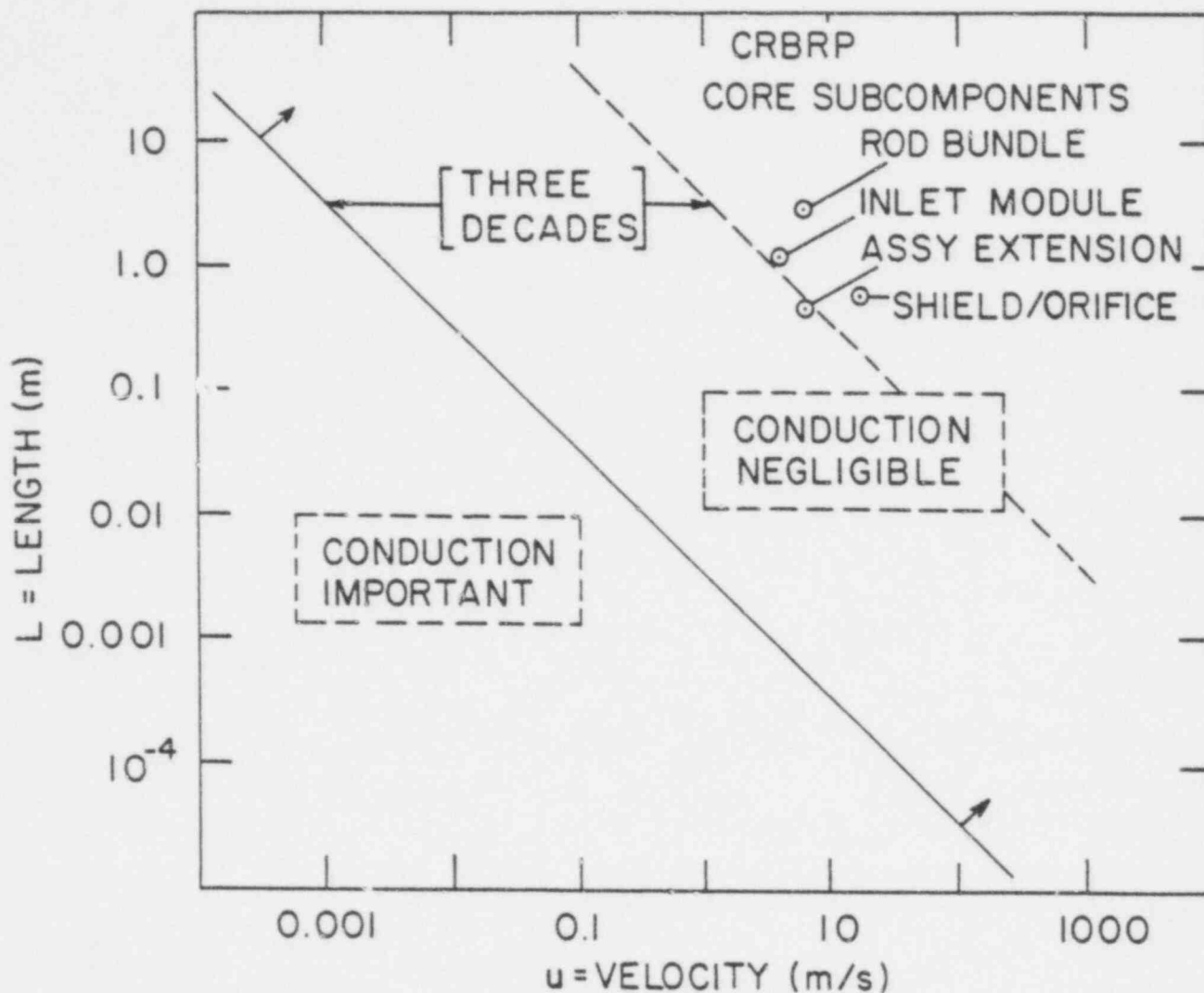
$$\frac{T - T_{IN}}{Q/W \cdot C_p}$$



629 300



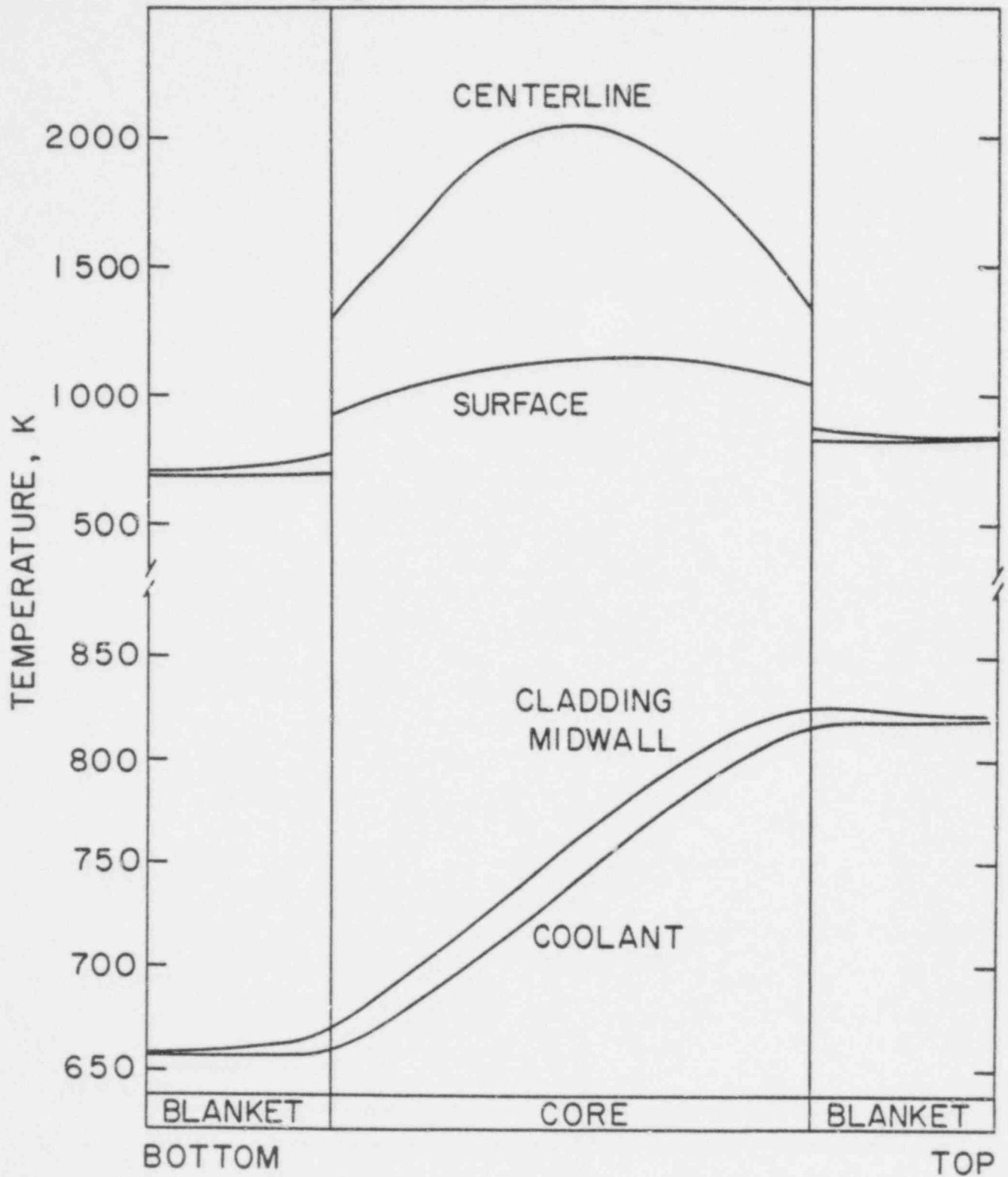
629 301

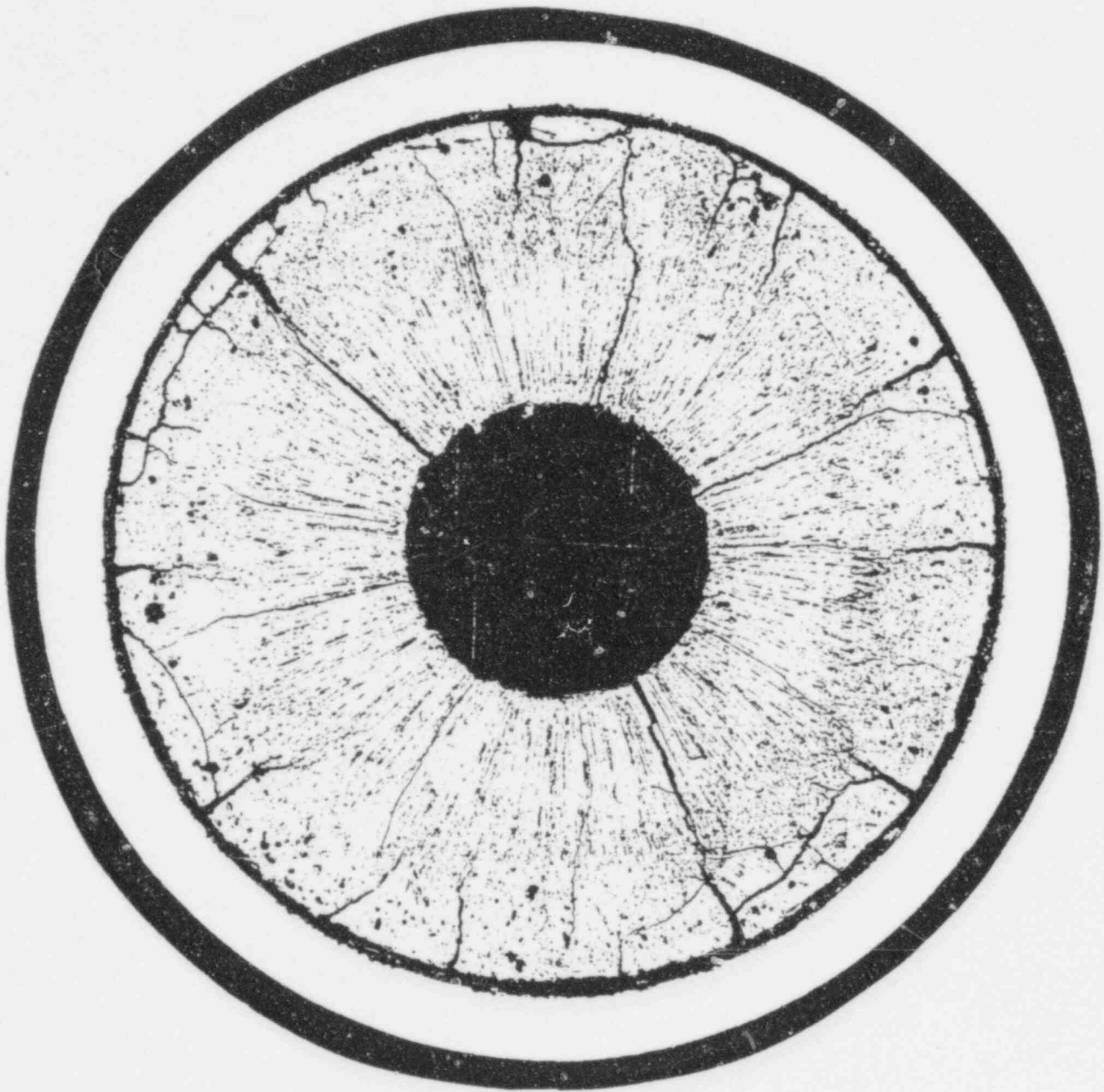


- NOTES (a) LINE IS FOR  $(Pe)_L = 50$   
 (b) ARROWS ARE DIRECTED TOWARD REGION OF NEGLIGIBLE CONDUCTION  
 (c) CRBRP FUEL ASSEMBLY SUBCOMPONENTS CONDITIONS ARE INDICATED FOR FULL FLOW OPERATION

629 302

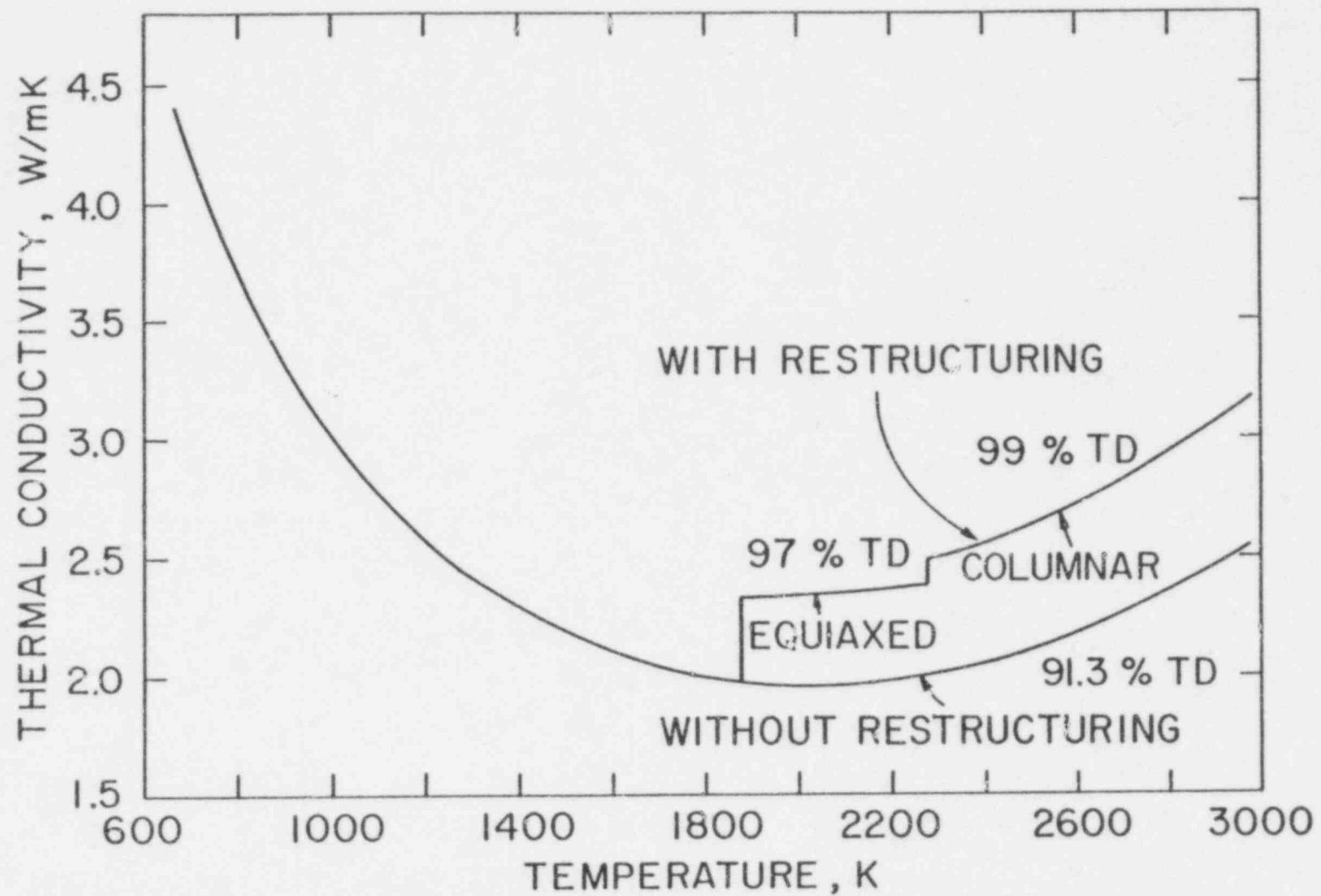
# CRBRP AVERAGE CORE CHANNEL





629 304

AGRAWAL & KHATIB-RAHBAR  
Fig. 3.39



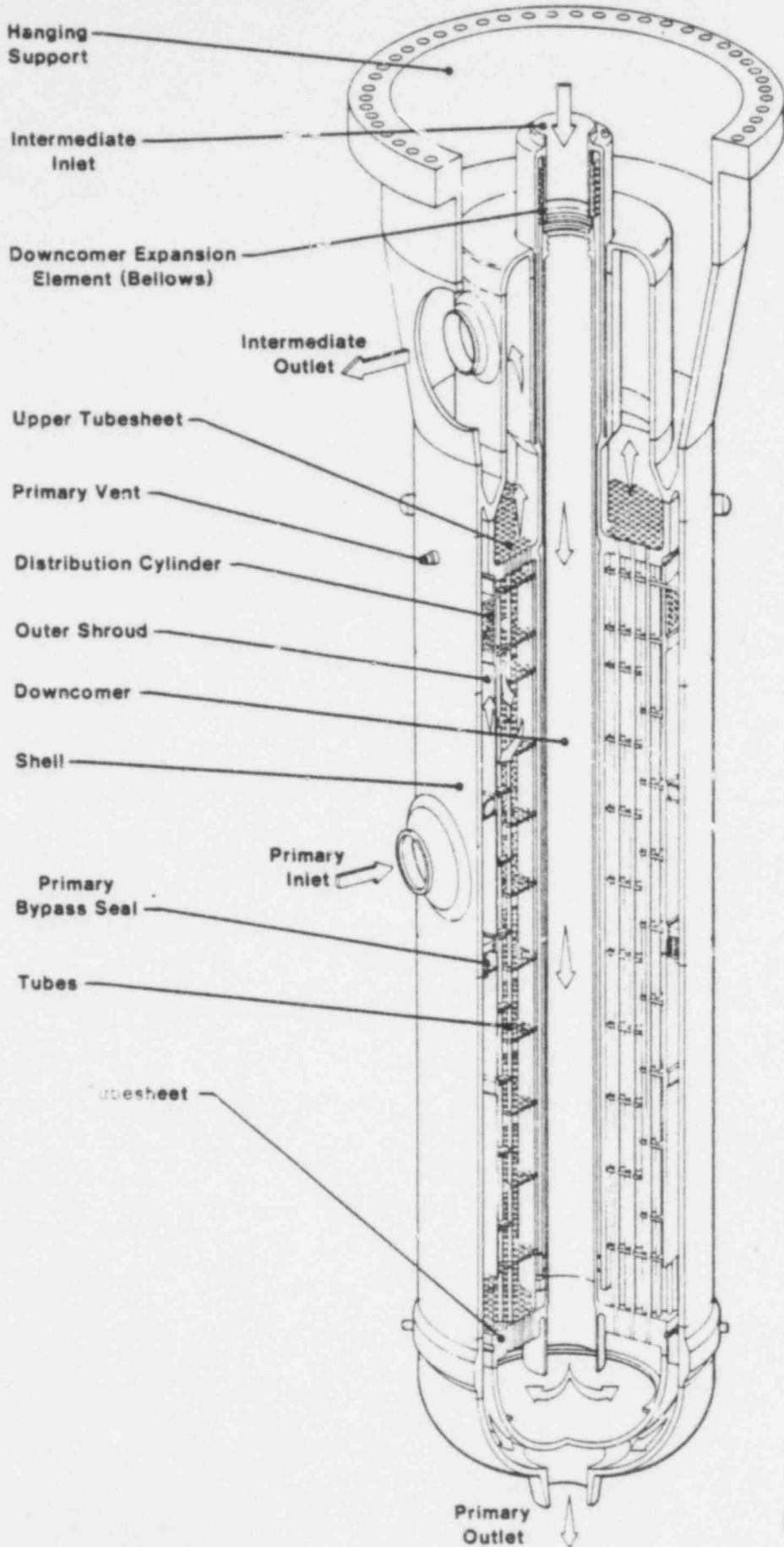
AGRAWAL & KHATIB-RAHBAR  
Fig. 3.40

## FIGURE CAPTIONS

### Figure No.

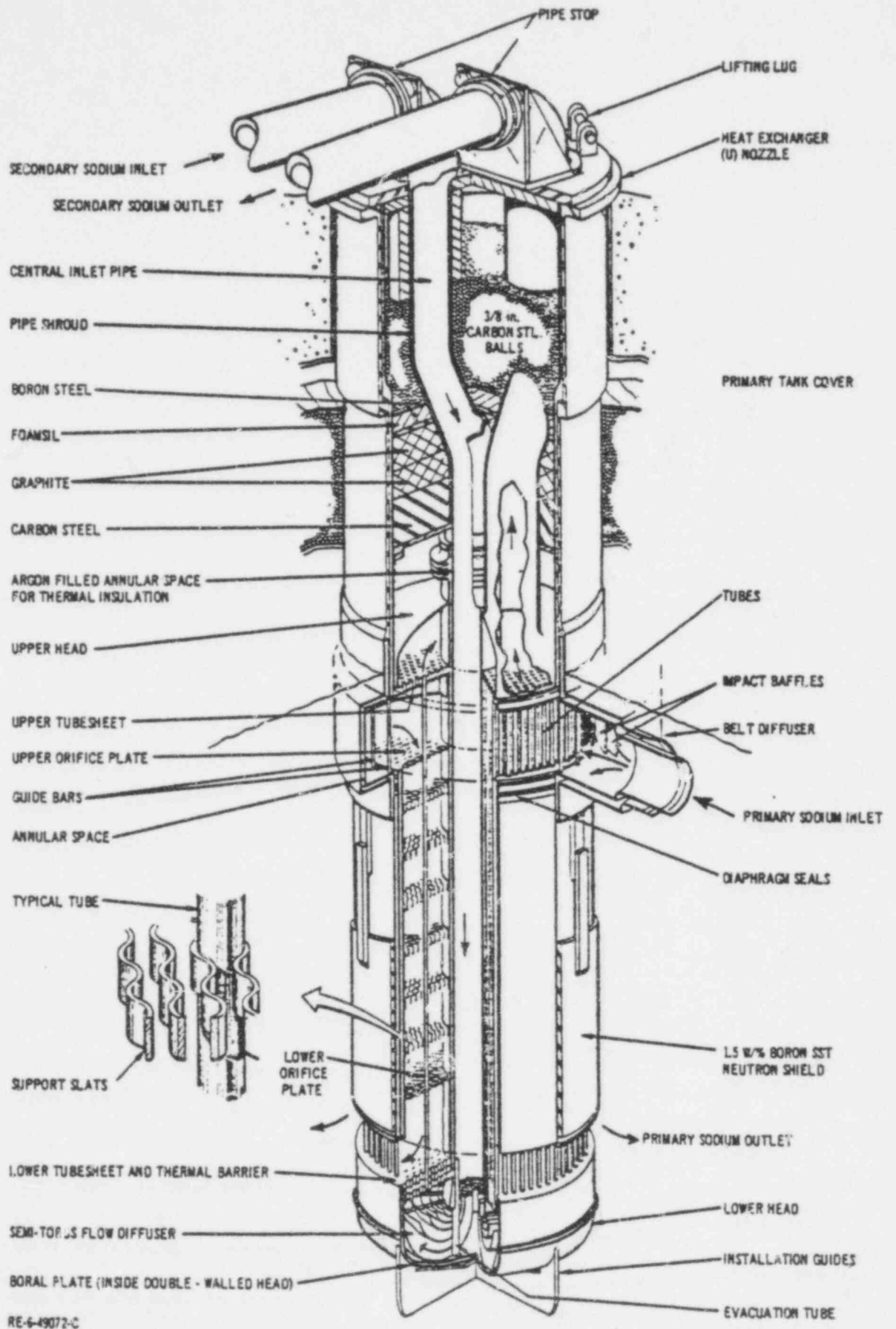
- 4.1 Sectional View of the CRBRP Intermediate Heat Exchanger
- 4.2 Sectional View of the EBR-II Intermediate Heat Exchanger
- 4.3 Tube Wall Mean Temperature Distribution With and Without Forced Mixing for Both Cases of (a) Uniform Flow and (b) Linear Flow Maldistribution
- 4.4 IHX Staggered Mesh Heat Transfer Model
- 4.5 IHX Outlet Temperature Response Using Various Numerical Approximations for the Enthalpy Transport.
- 4.6 Steady-State and Transient Temperature Distribution for the CRBRP Intermediate Heat Exchanger
- 4.7 Schematic Representation of Tube-Bank Geometries, (a) Equilateral-Triangular Spacing, and (b) Square Spacing





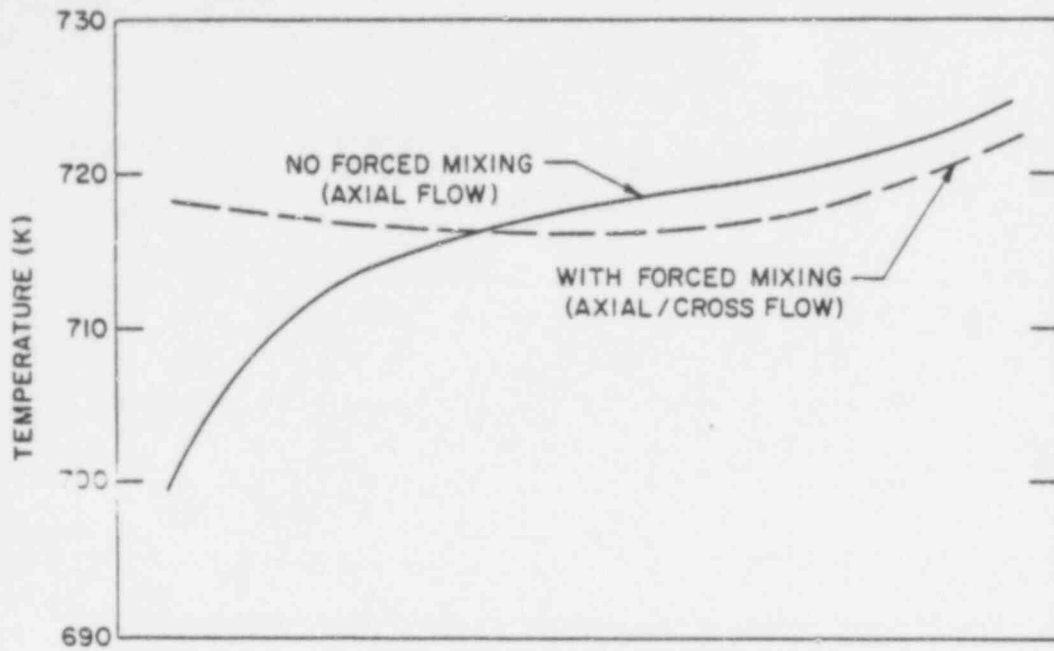
629 307

AGRAWAL/KHATIB-RAHBAR  
Fig. 4.1

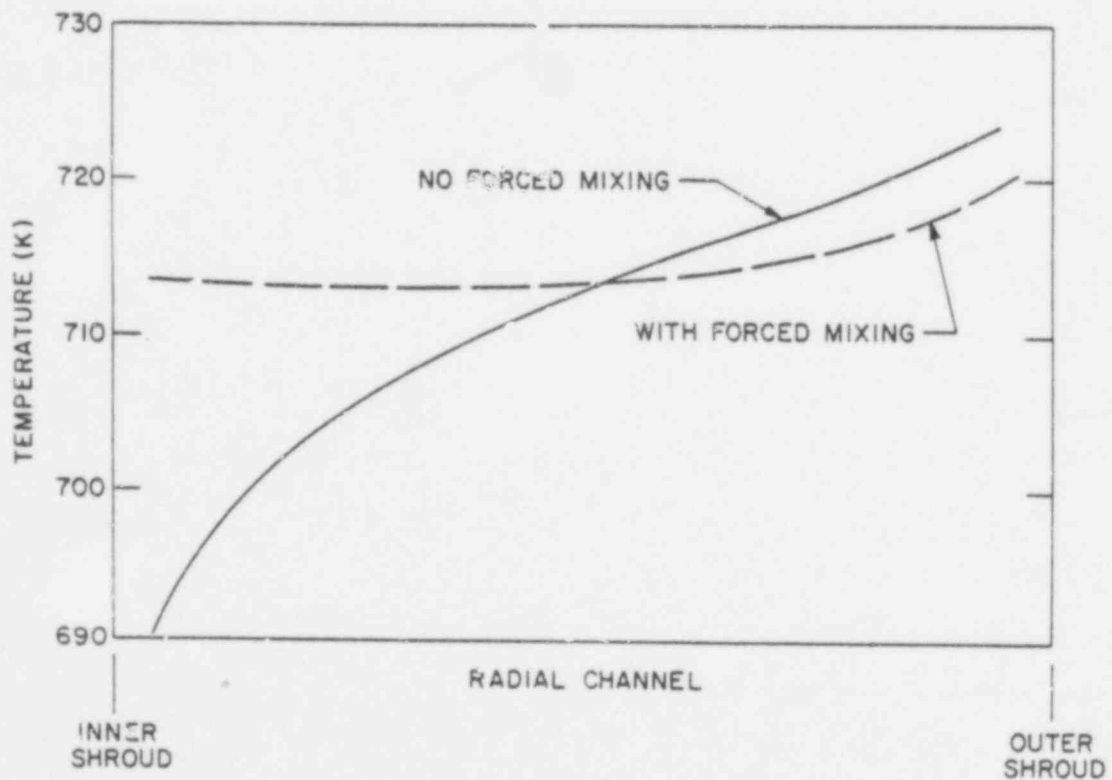


629 308

AGRAWAL/KHATIB-RAHBAR  
Fig. 4.2

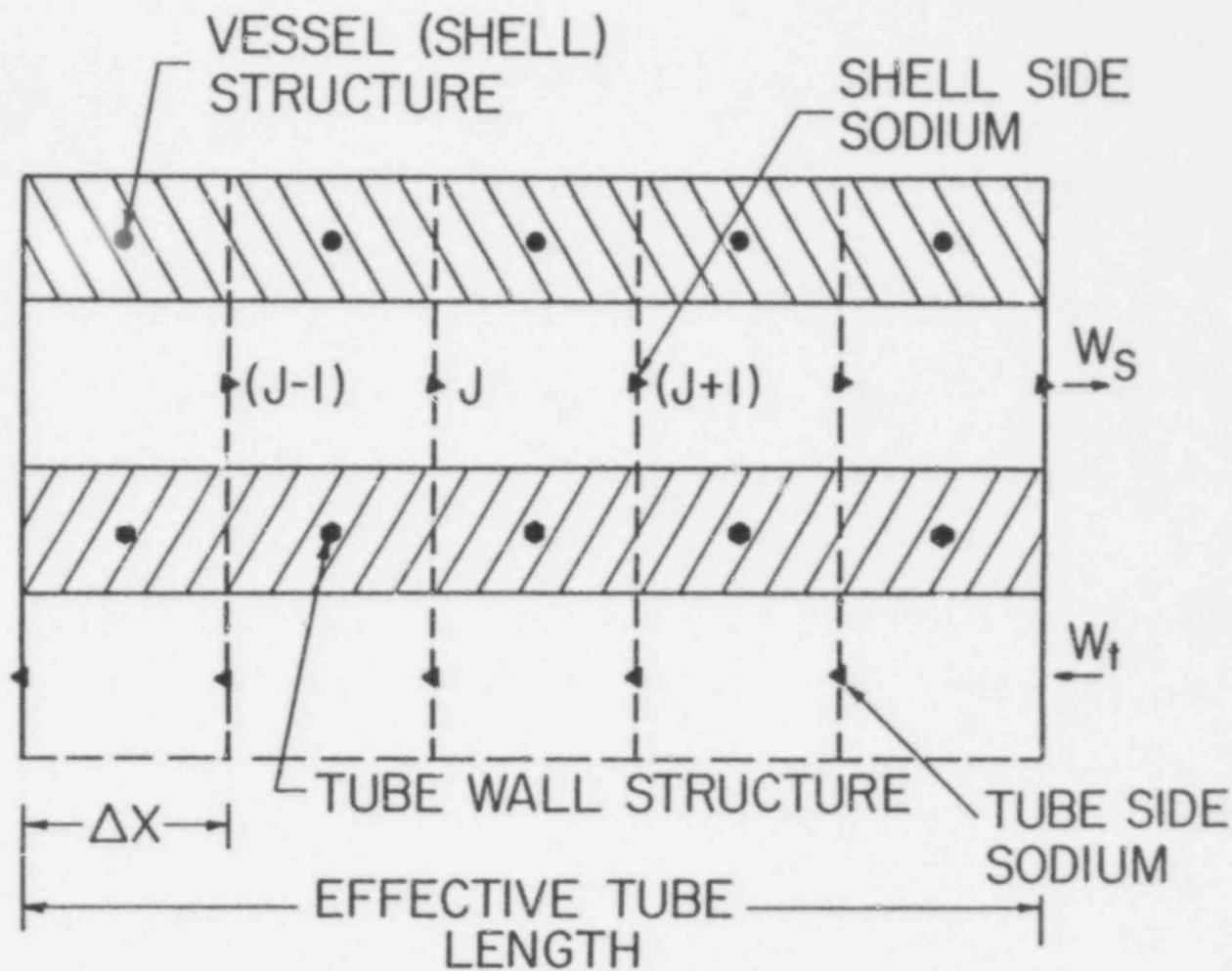
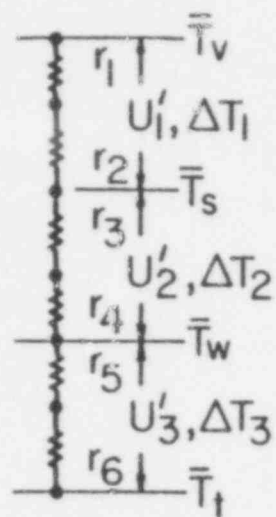


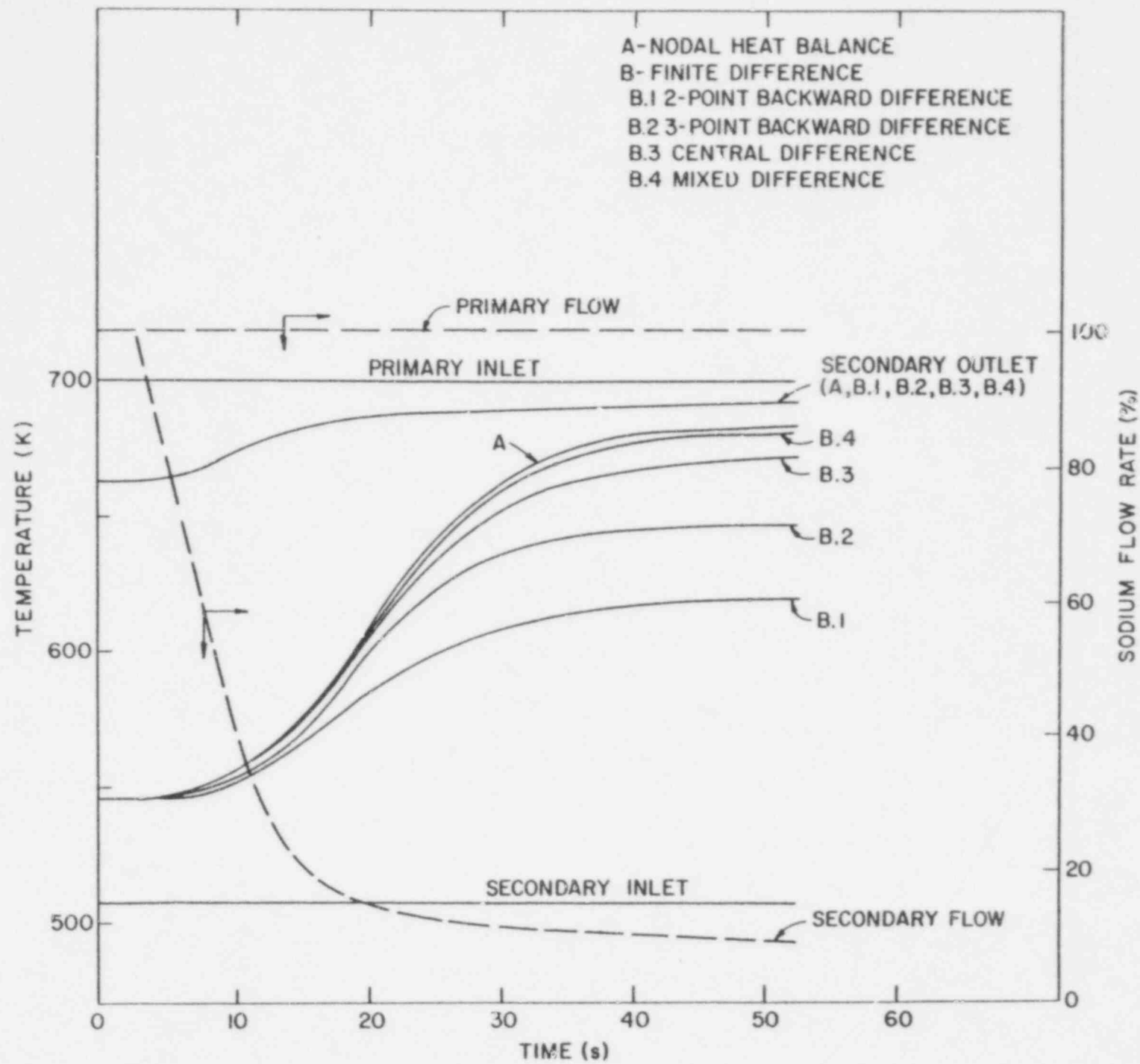
(a) UNIFORM DISTRIBUTED FLOW

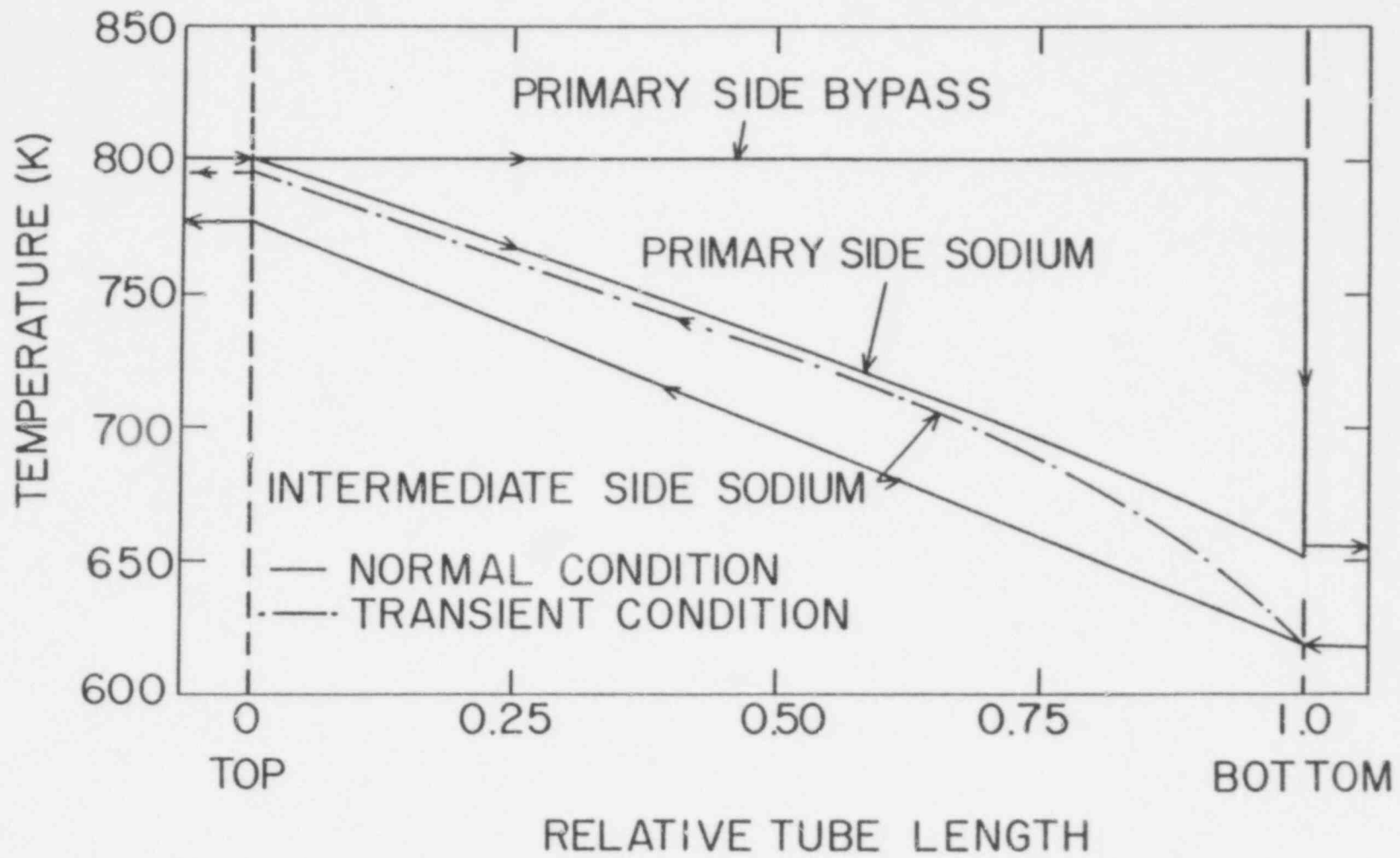


(b) LINEAR FLOW MALDISTRIBUTION

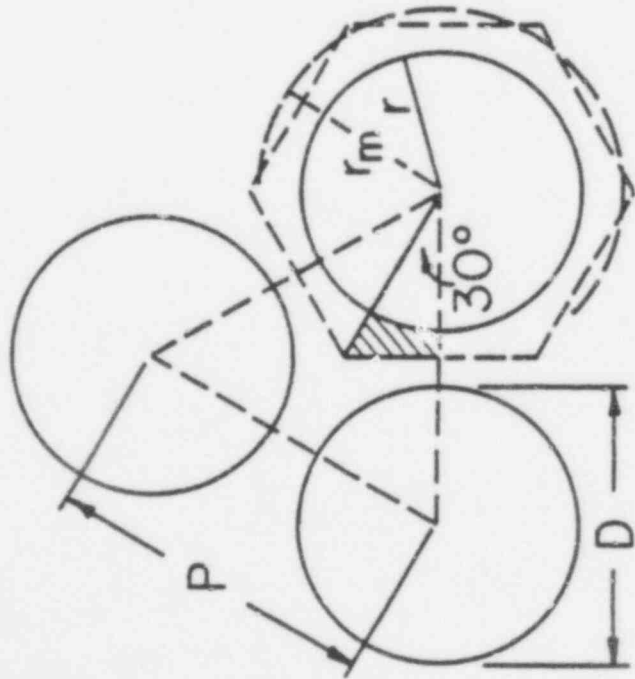
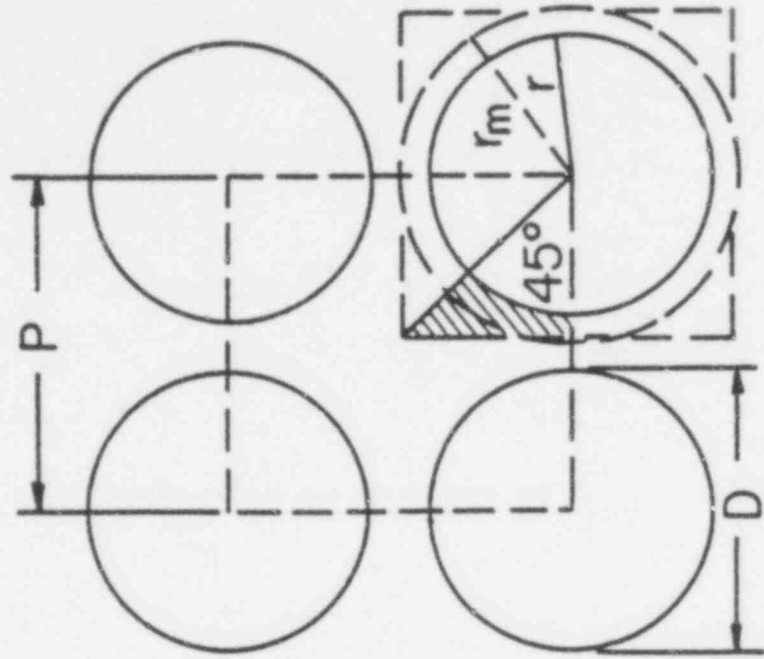
629 309







629  
5/12



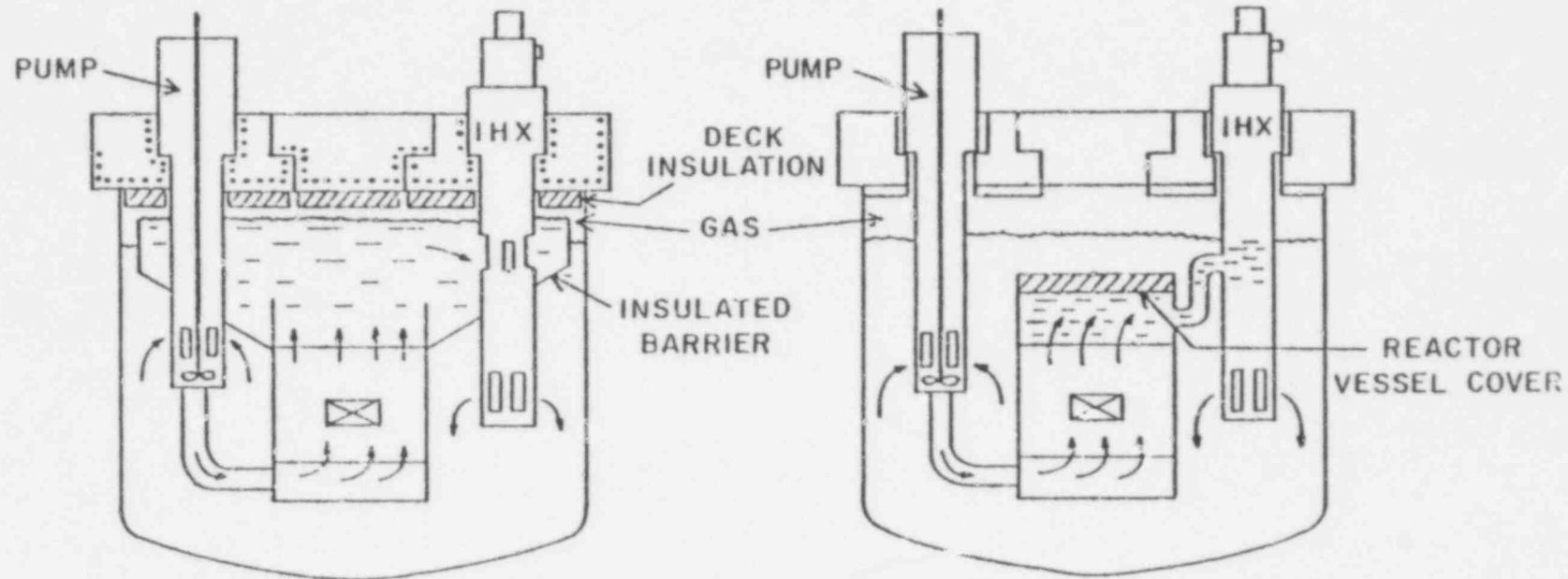
629 313

## FIGURE CAPTIONS

### Figure No.

- 5.1 Configuration Options in Pool-Type LMFBR Primary Systems
- 5.2 Pipe Section Staggered Mesh Heat Transfer Model
- 5.3 Pipe Section Outlet Temperature Response Using Various Thermal Transport Models
- 5.4 Cutaway View of a Primary Sodium Pump in the CRBRP Design
- 5.5 Homologous Representation of Pump Head
- 5.6 Homologous Representation of Pump Torque
- 5.7 Cutaway View of a Primary Loop Check Valve in the CRBRP Design
- 5.8 Pipe Section Inlet Flow and Temperature Transient Boundary Conditions
- 5.9 Pipe Axial Velocity Profile
- 5.10 Temperature Time Histories at Various Axial Positions and Comparisons to the 3-D Calculations for (a) Conducting Pipe Wall, and (b) Adiabatic Pipe Wall

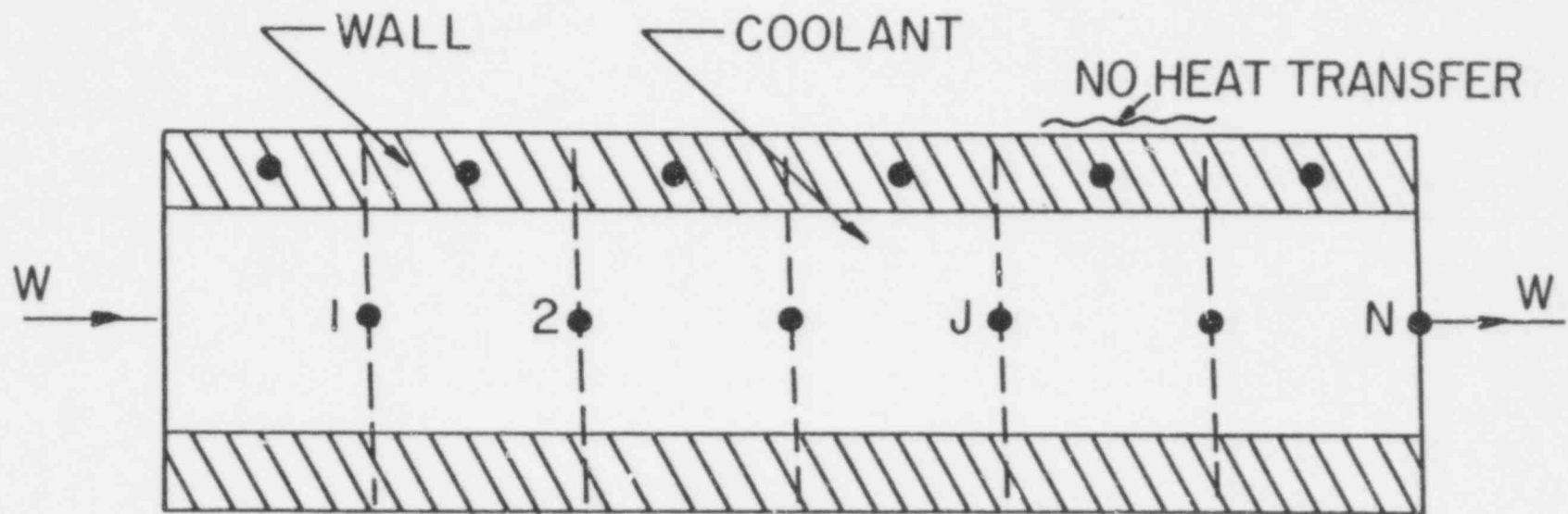


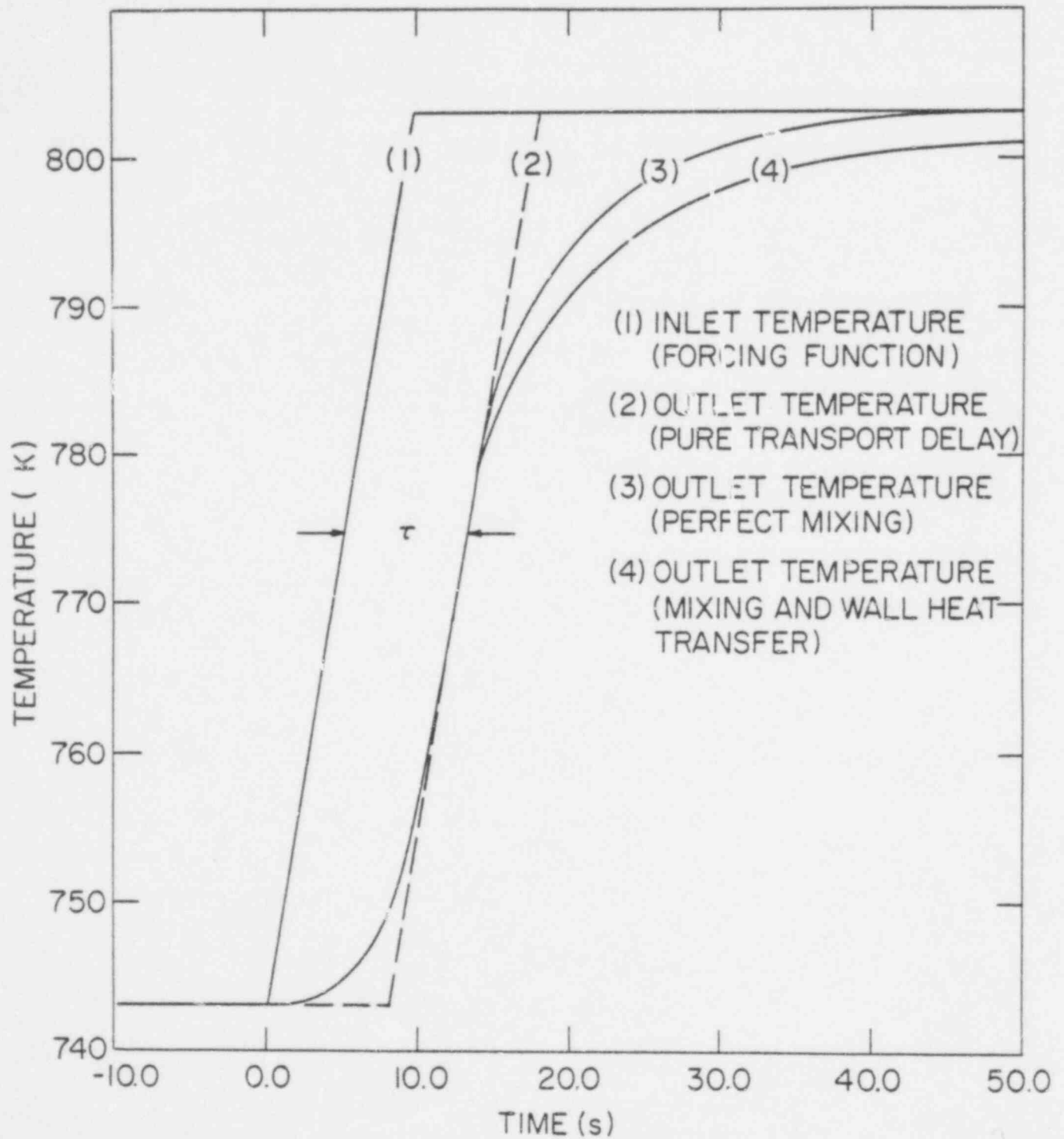


HOT POOL (PFR, SUPERPHENIX)

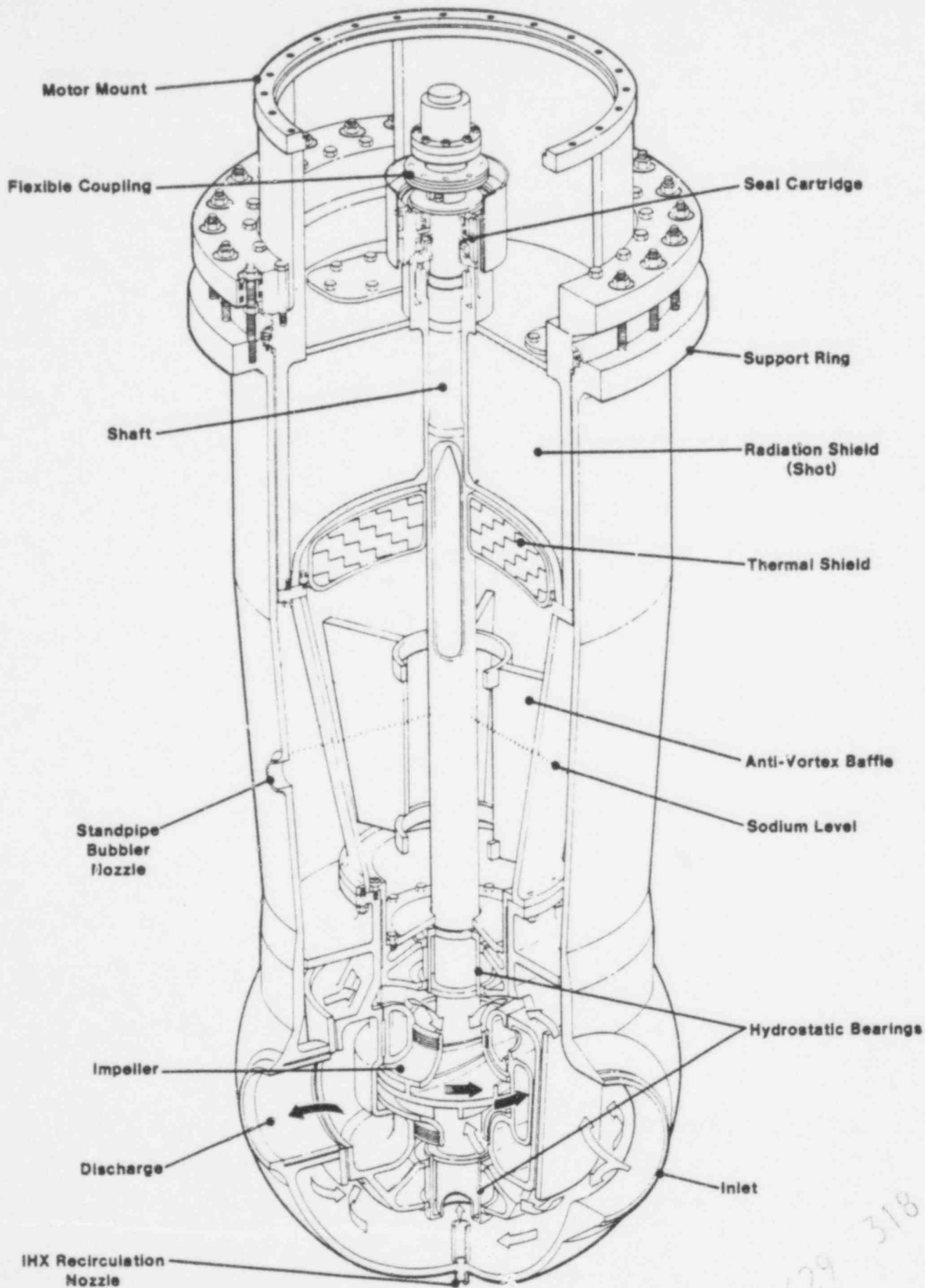
COLD POOL (EBR-II)

629 315

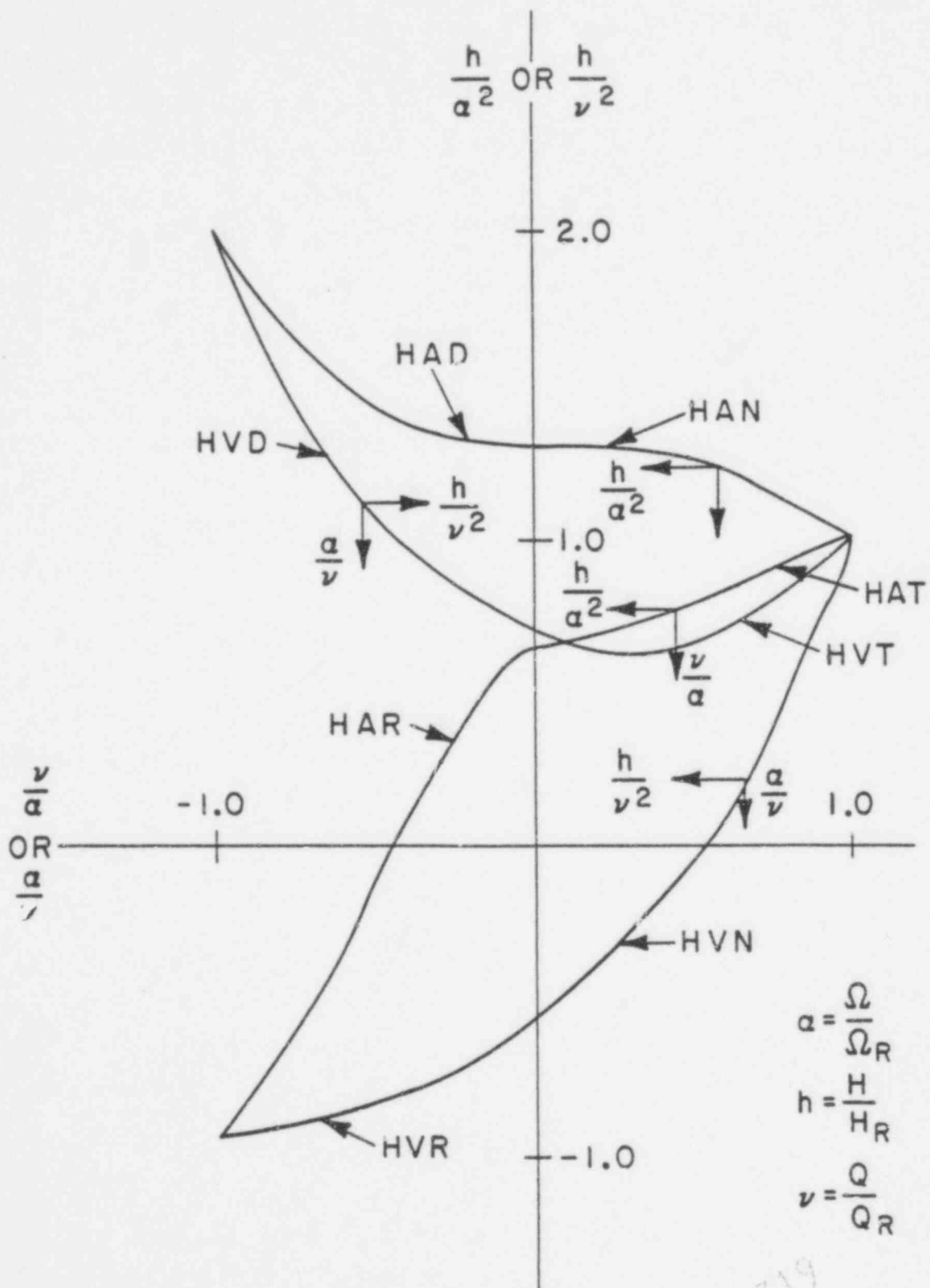




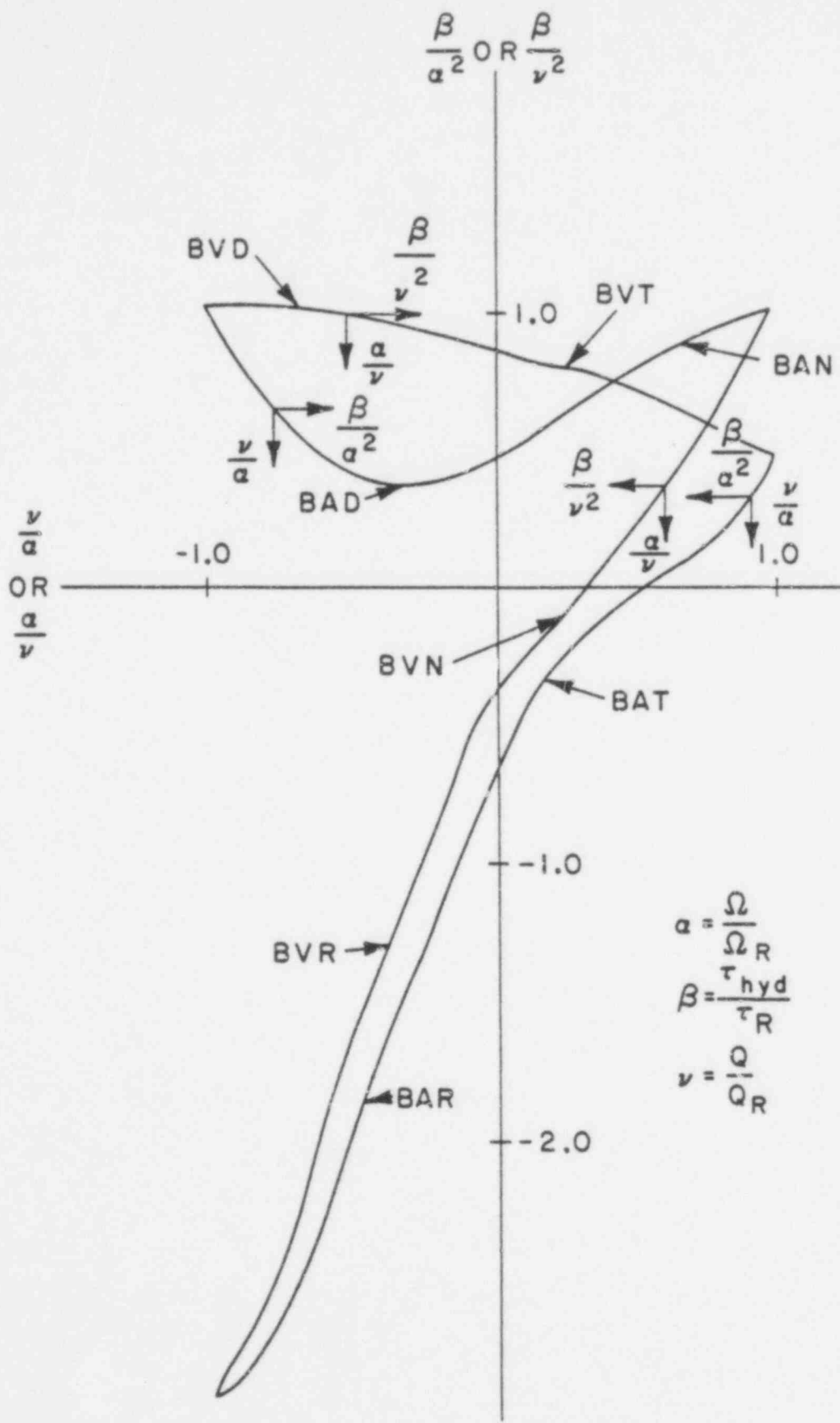
AGRAWAL/KHATIB-RAHBAR  
Fig. 5.3



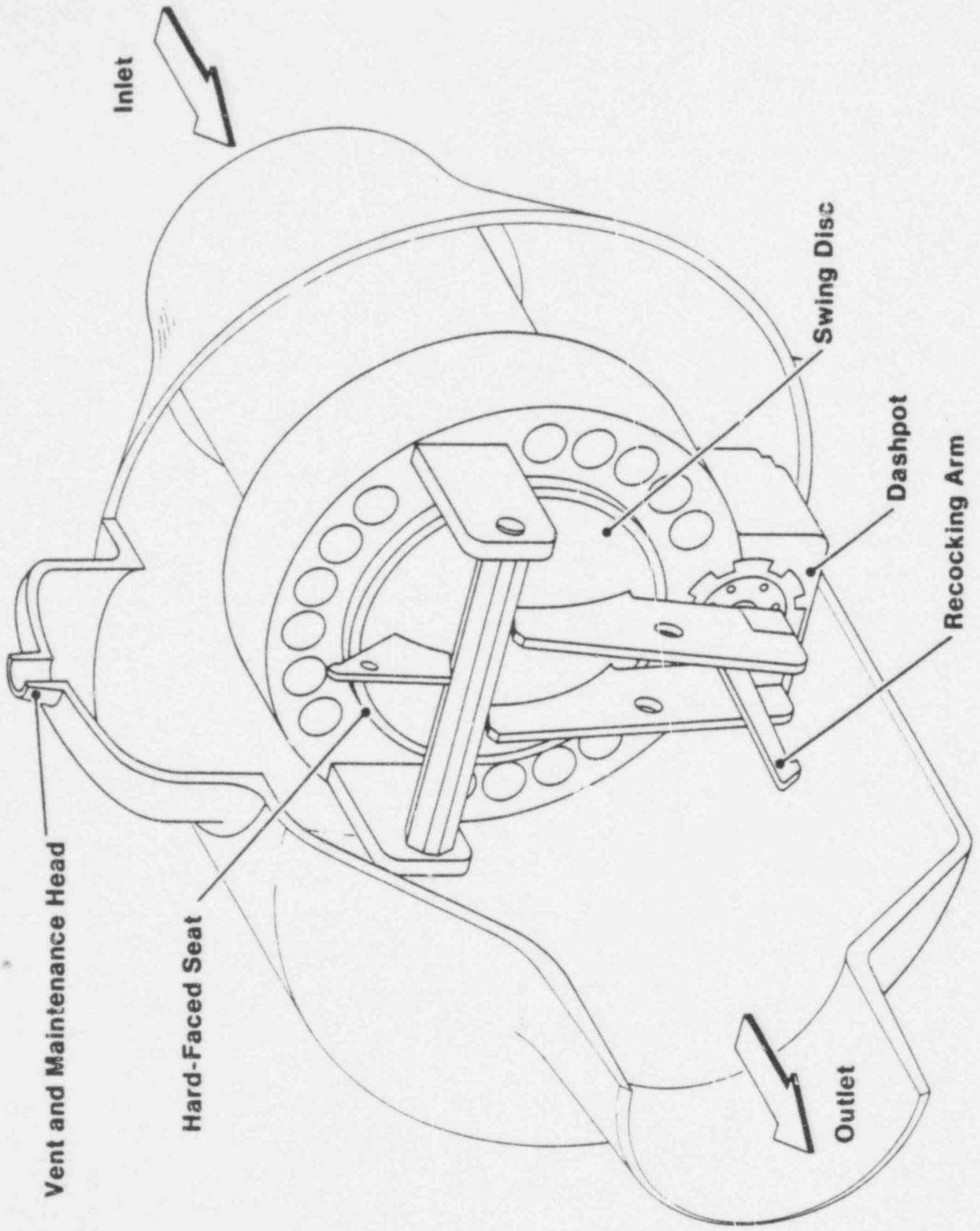
629 318



AGRAWAL/KHATIB-RAHBAR  
Fig. 5.5



629 320



Inlet

Swing Disc

Dashpot

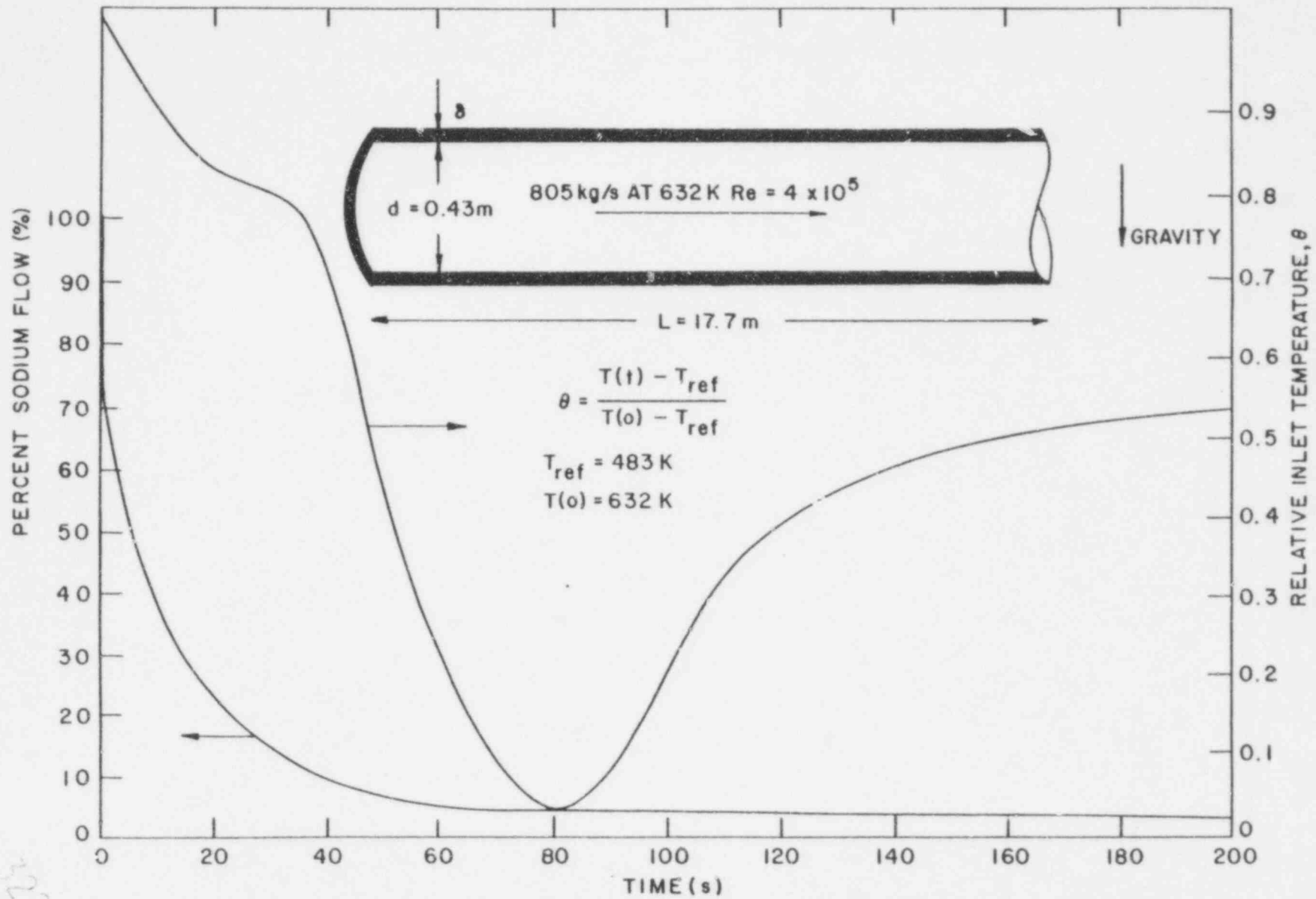
Recocking Arm

Vent and Maintenance Head

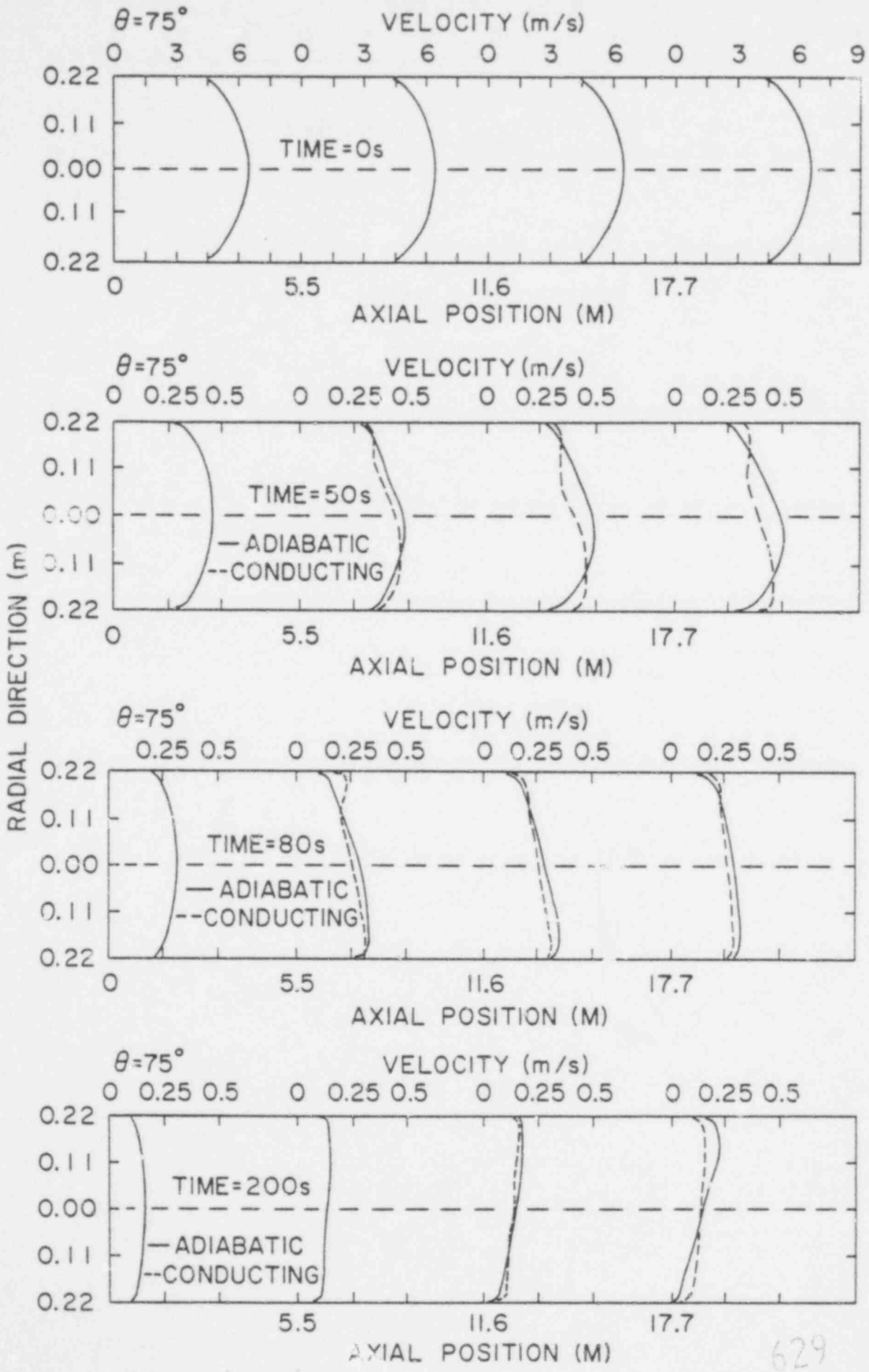
Hard-Faced Seat

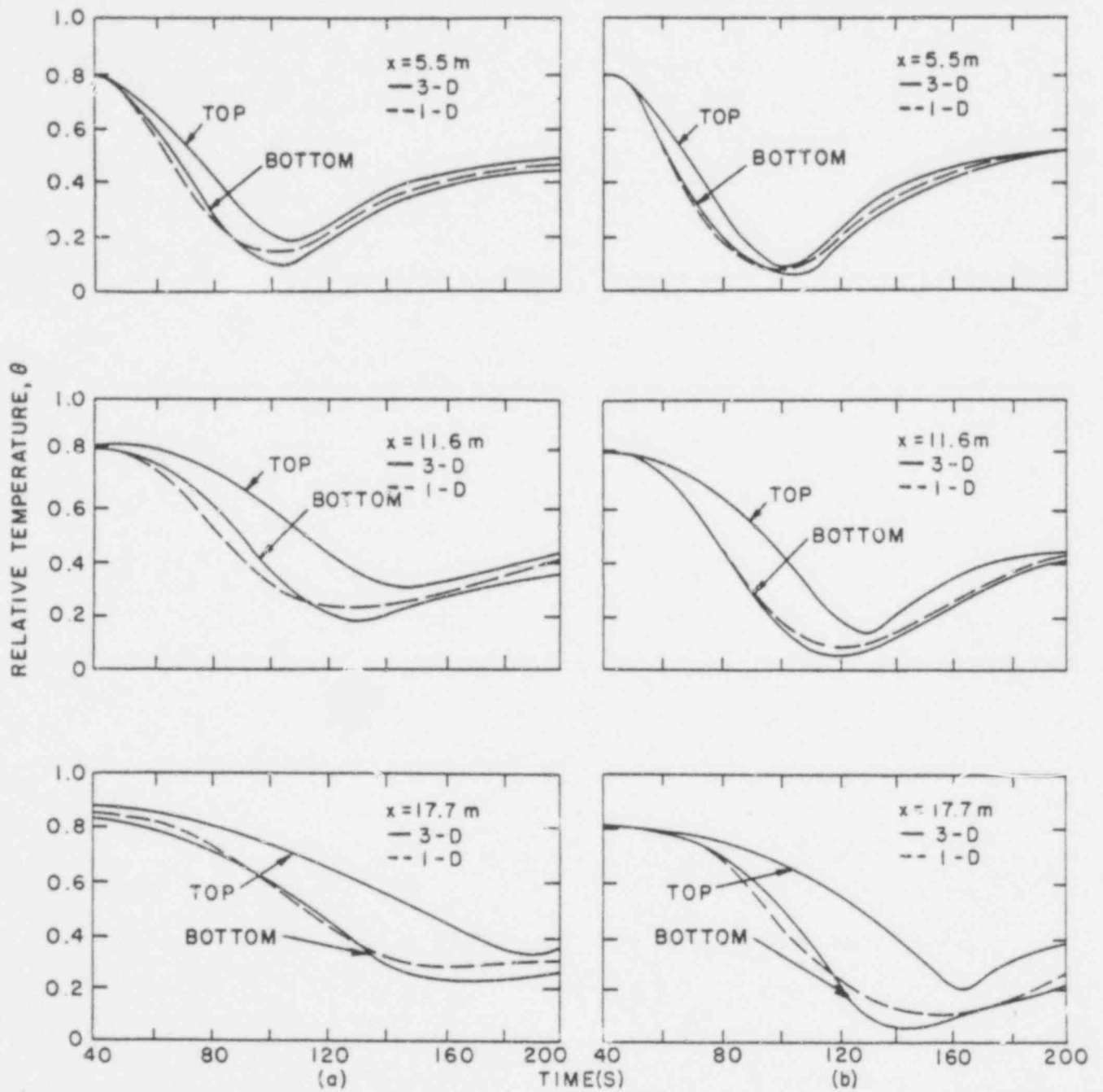
Outlet

529 321









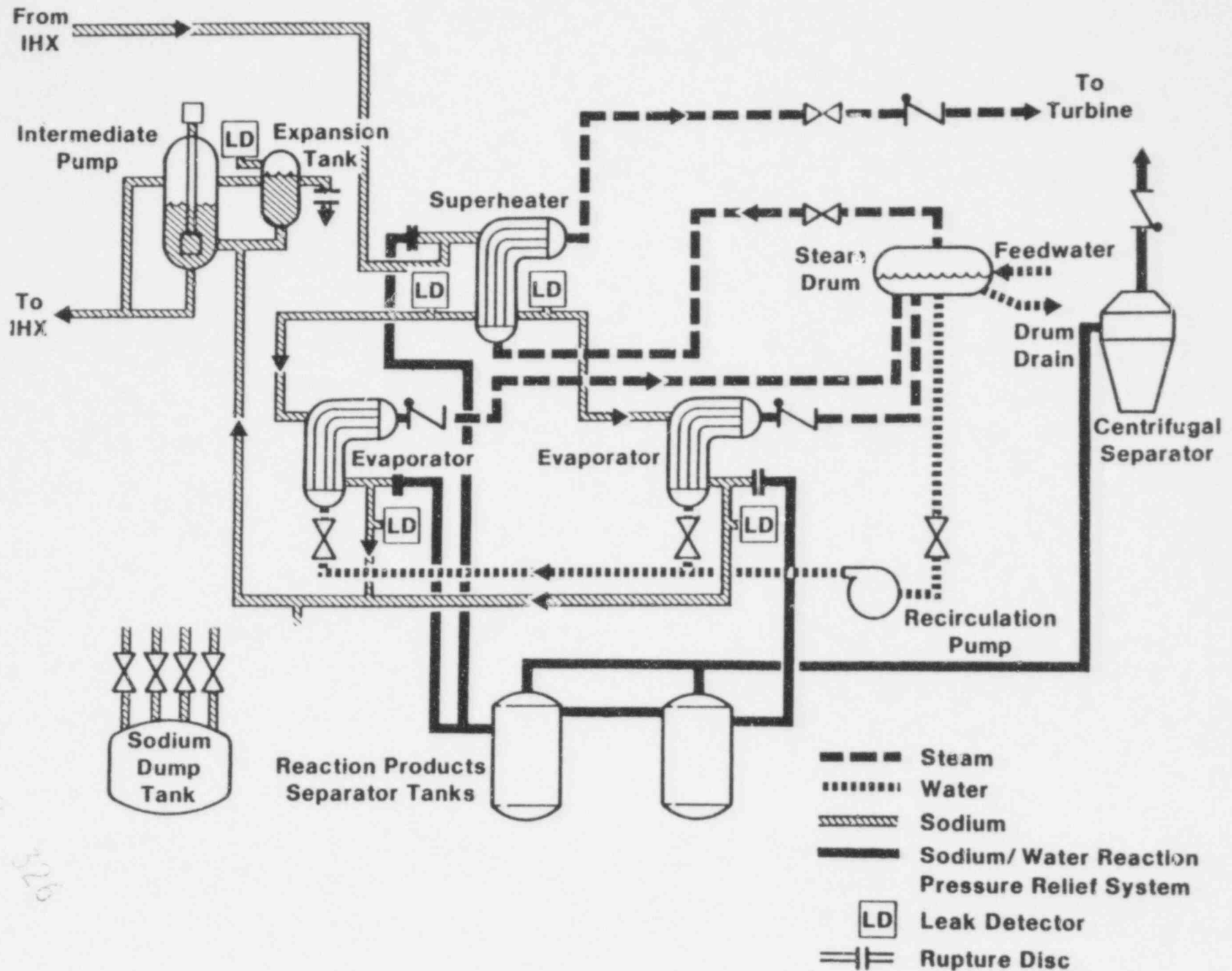
629 324

## FIGURE CAPTIONS

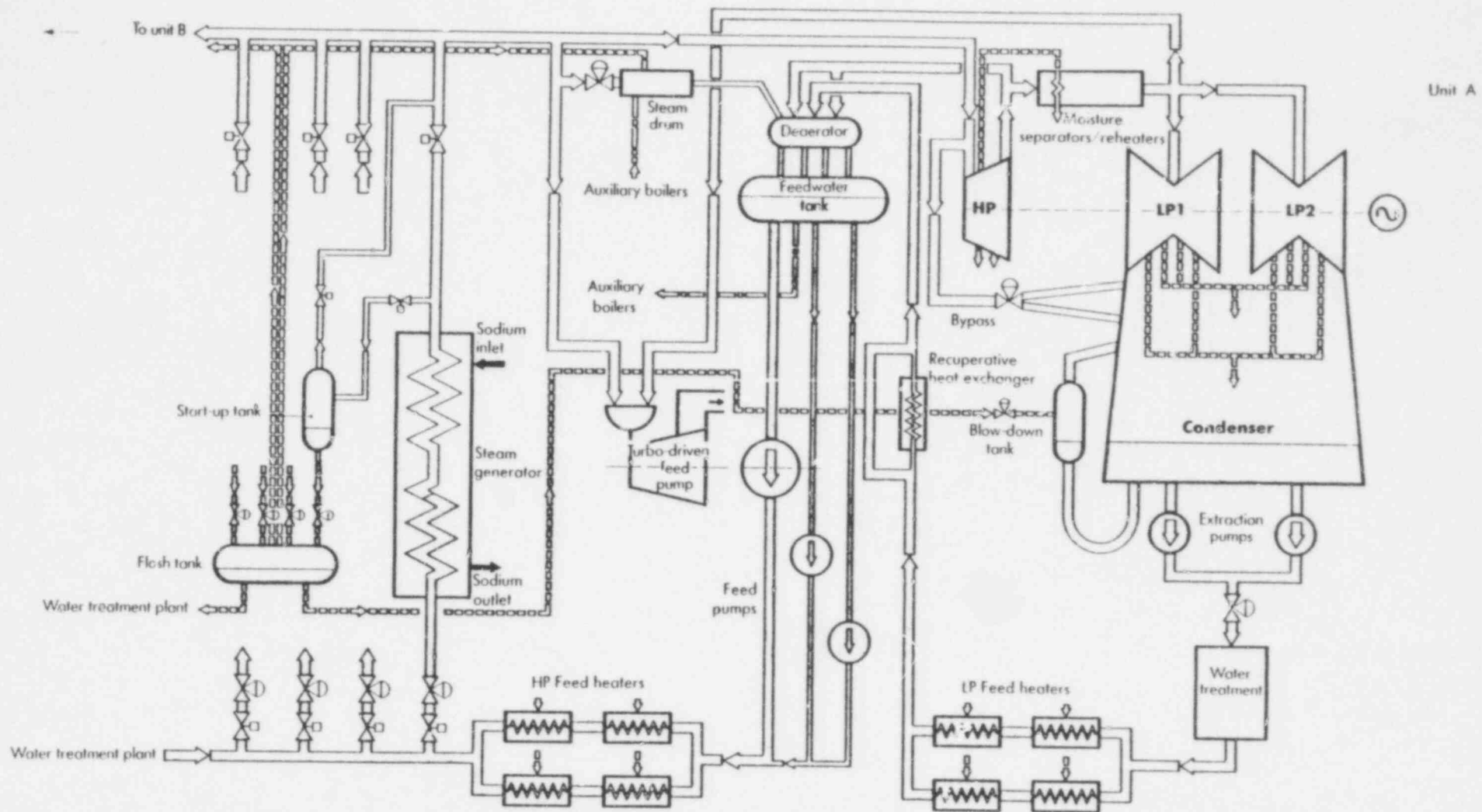
### Figure No.

- 6.1 Schematic of CRBRP Steam Generating System
- 6.2 Schematic of SUPER PHENIX Steam Generating System
- 6.3 Cutaway View of a SUPER PHENIX Steam Generator Module
- 6.4 Cutaway View of a CRBRP Steam Generator Module
- 6.5 Comparison of the Momentum Integral and the Single Mass Flow Rate Models
- 6.6 Regimes of Heat Transfer in Convective Boiling
- 6.7 Comparison of Boiling-Crisis Mechanisms in Various Flow Patterns (a) Subcooled Bubbly Flow, and (b) Annular Flow
- 6.8a Reynolds Number Correction Factor,  $F$
- 6.8b Nucleate Boiling Suppression Factor,  $S$
- 6.9 Graphical Representation of the Two-Phase Multiplier,  $\phi_{tp}$  and  $\Omega$
- 6.10 Comparison of Two-Phase Flow Multiplier Ratio,  $R$ , for both Barcozy and HTFS Correlations

629 325

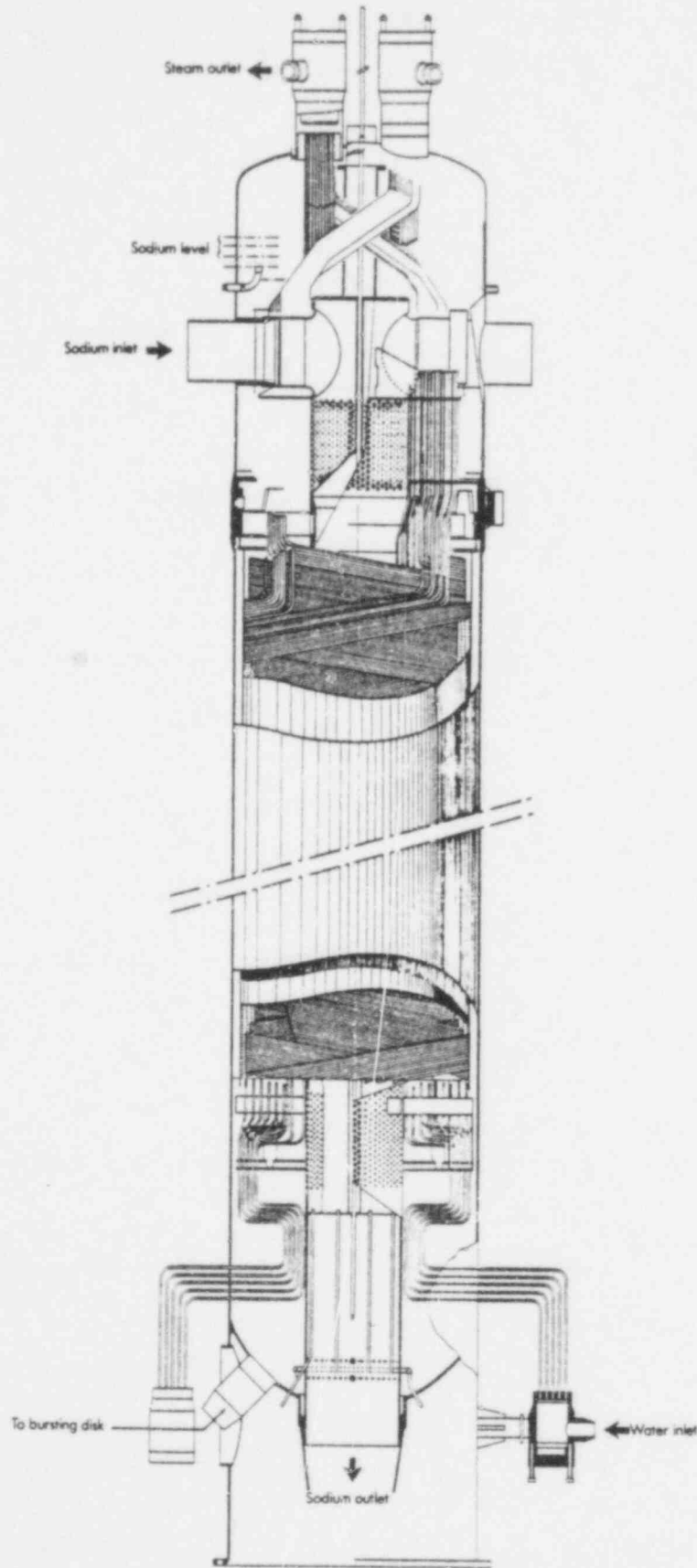


AGRAWAL/KHATIB-RAHBAR  
Fig. 6.1



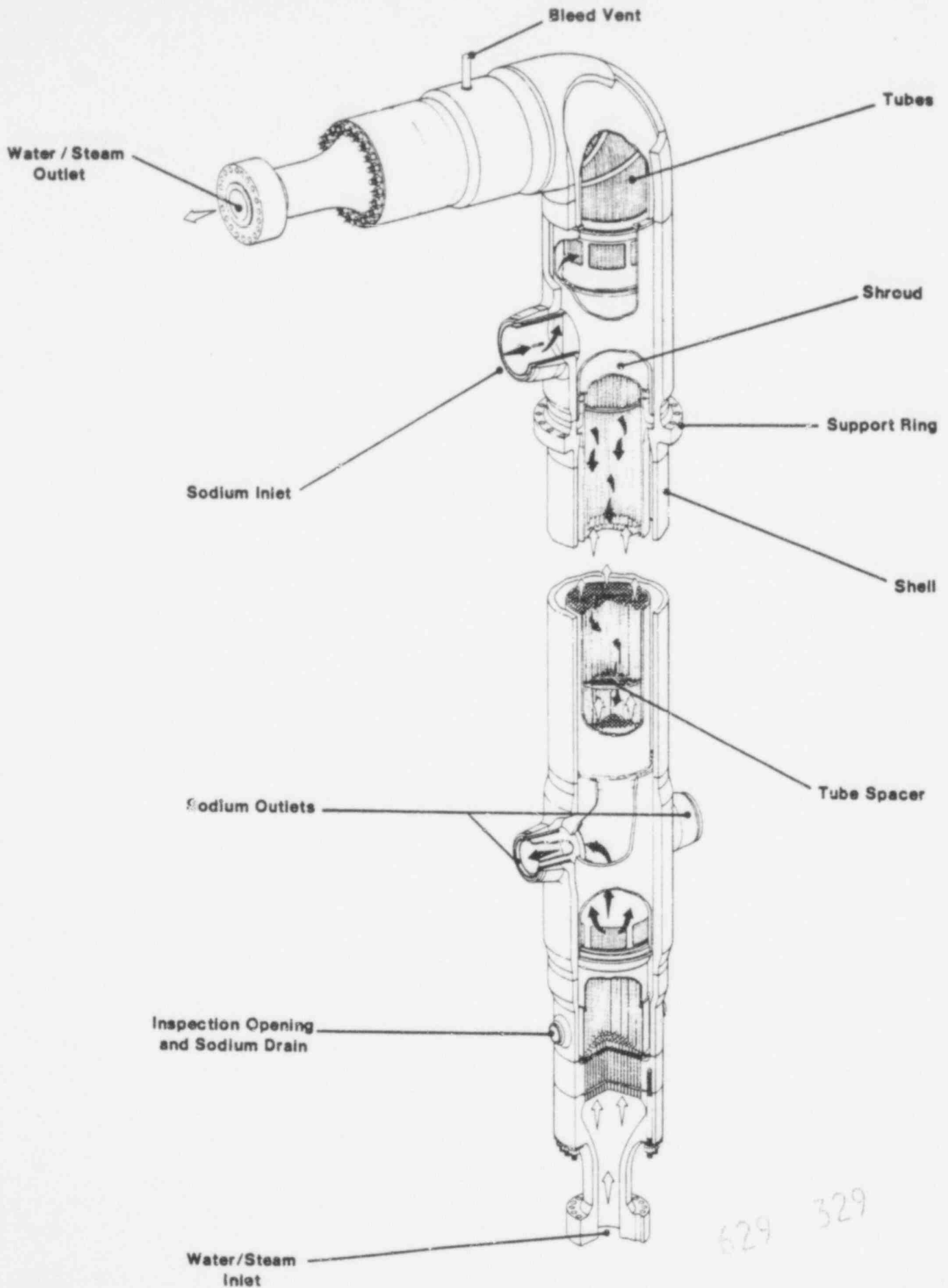
629-521

AGRAWAL/KHATIB-RAHBAR  
Fig. 6.2

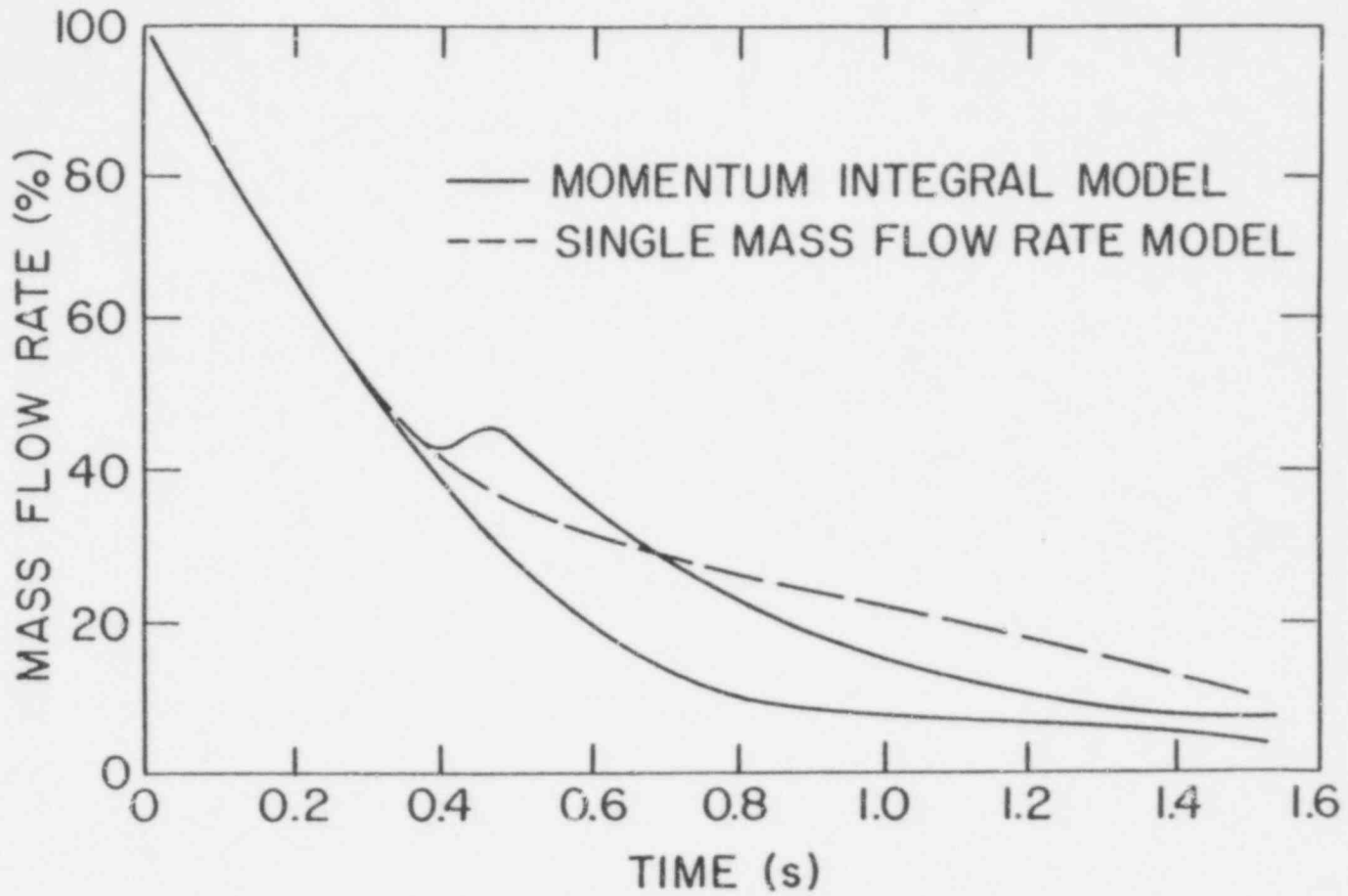


629 328

AGRAWAL/KHATIB-RAHBAR  
Fig. 6.3

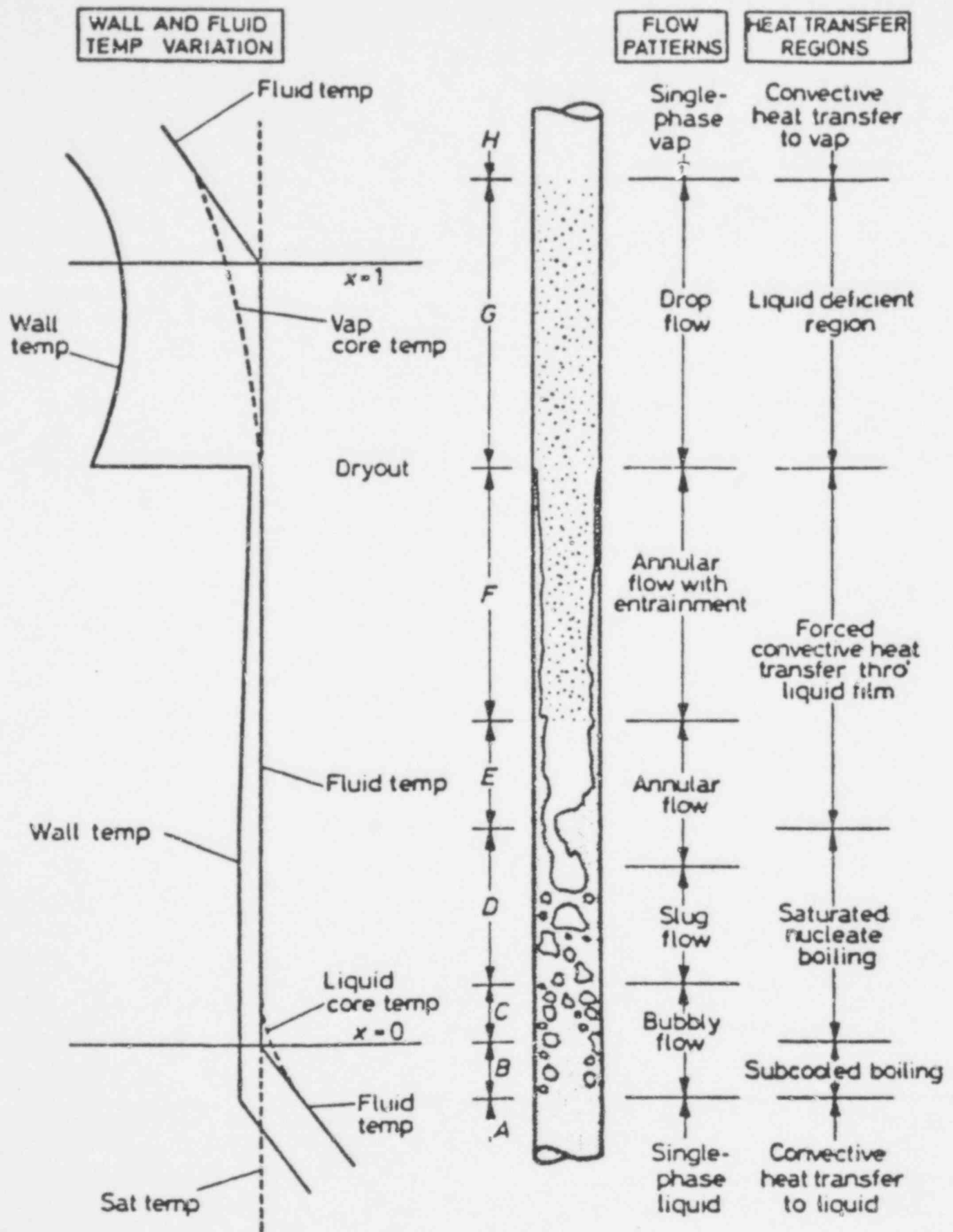


629 329

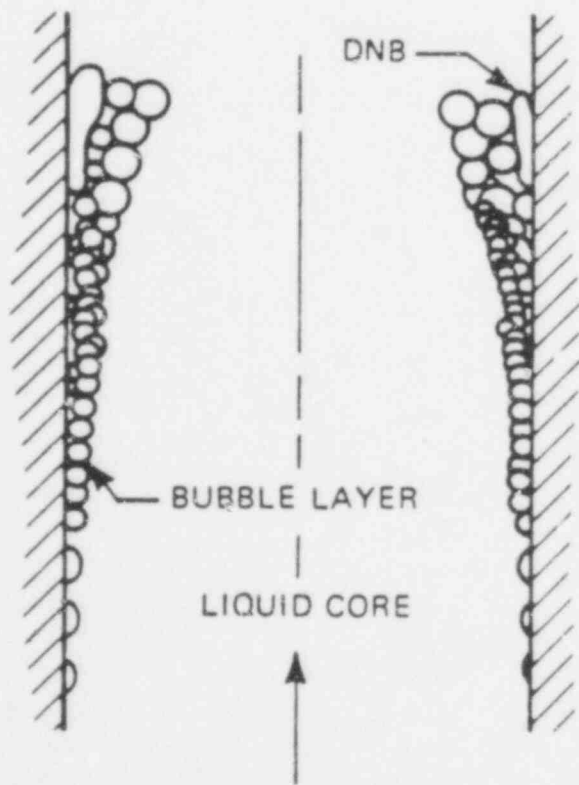
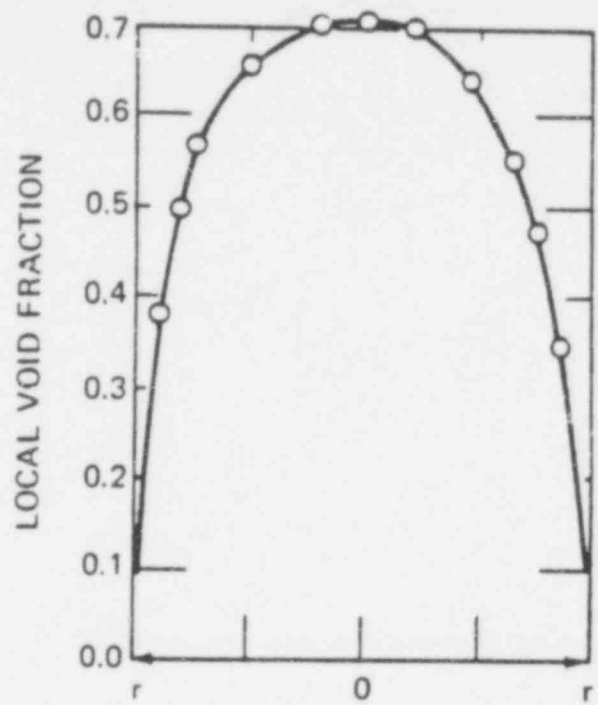
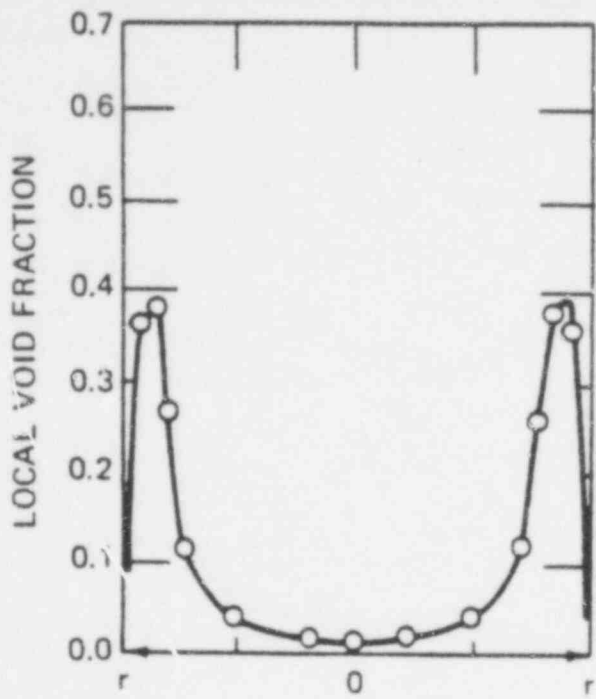


629 350

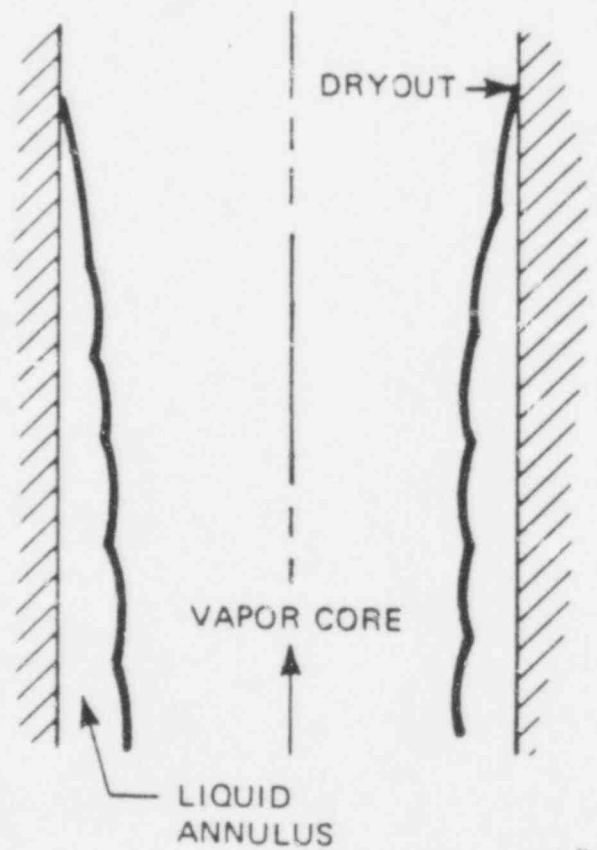




629 331

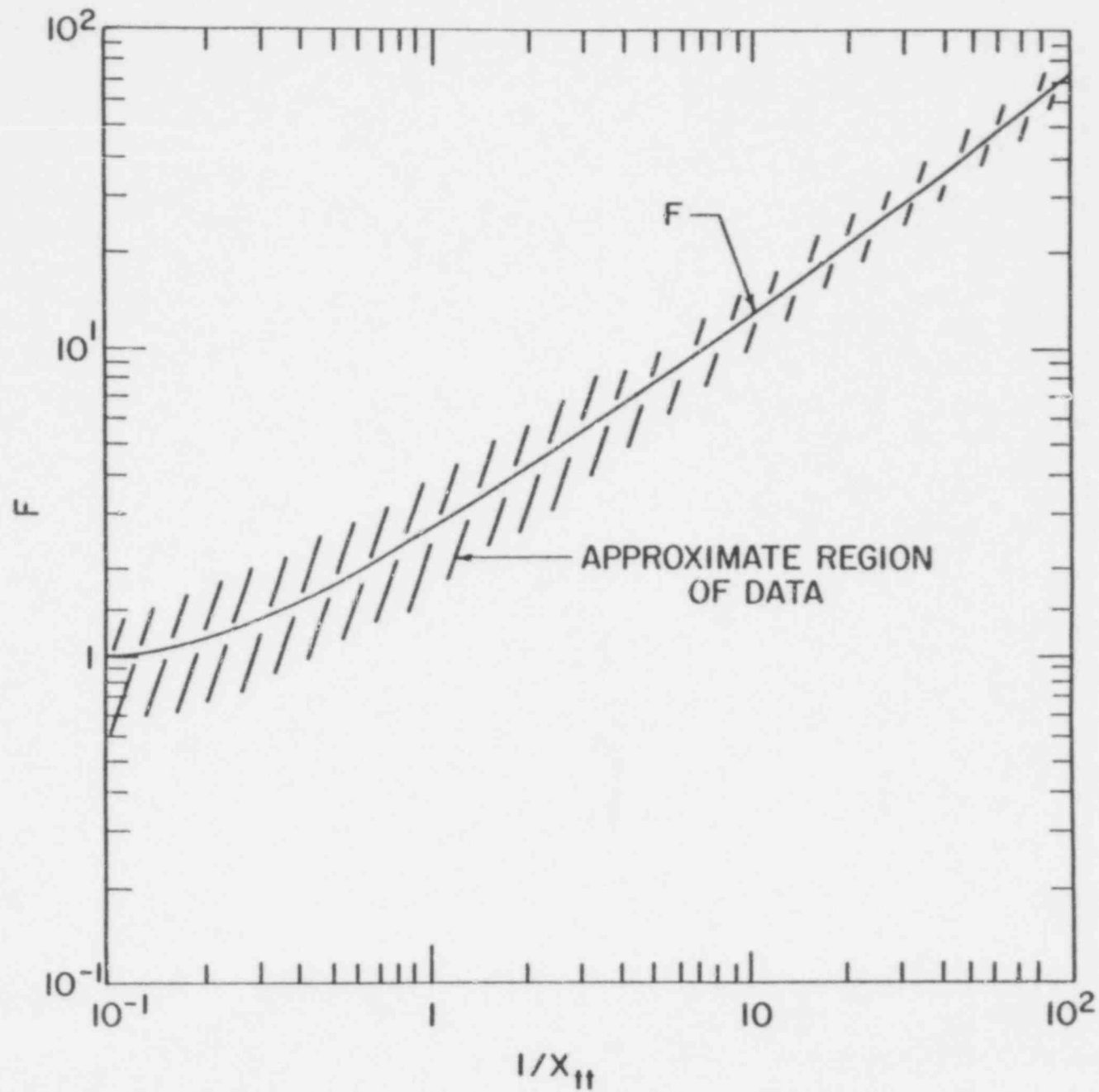


(a)

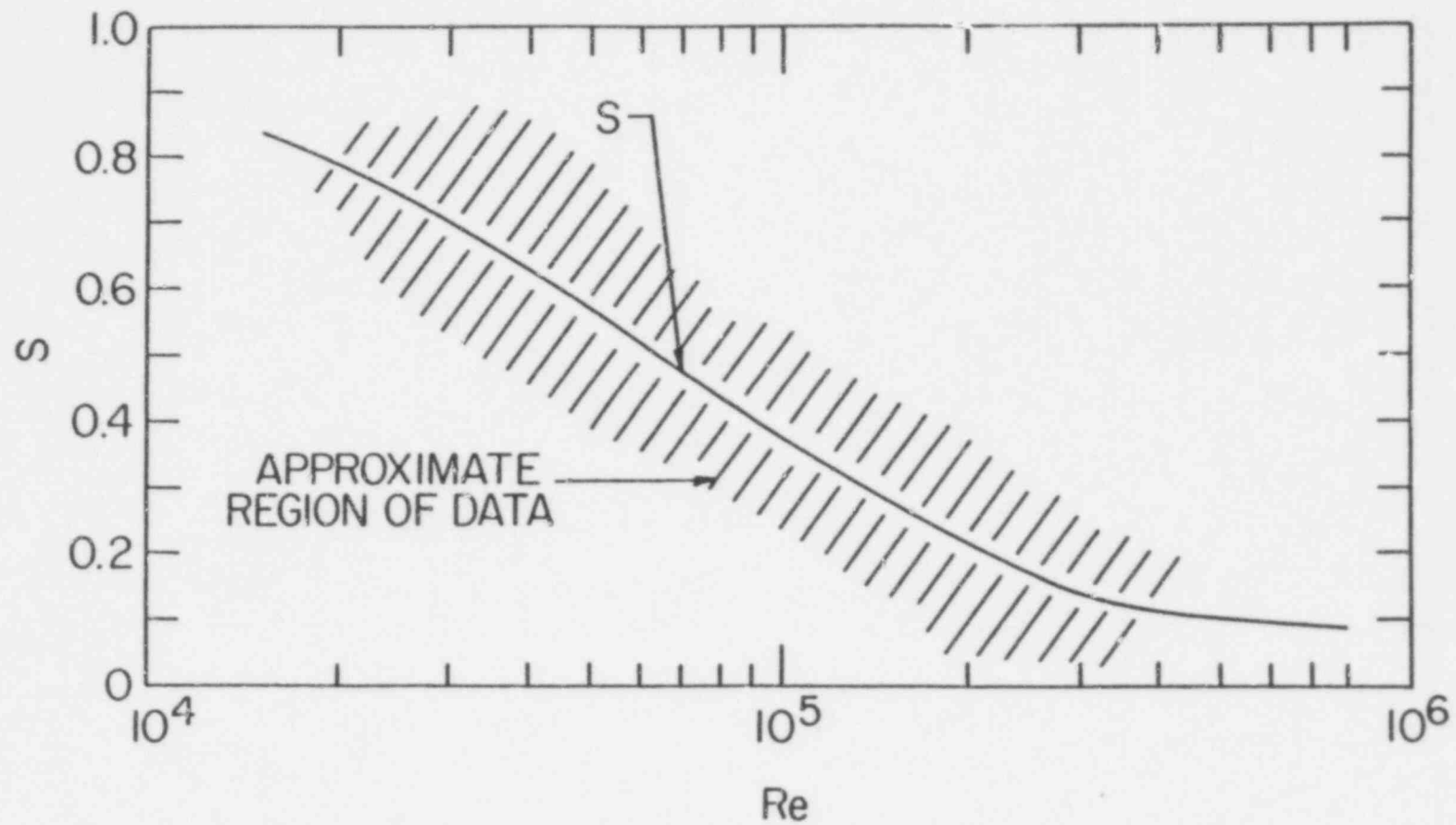


(b)

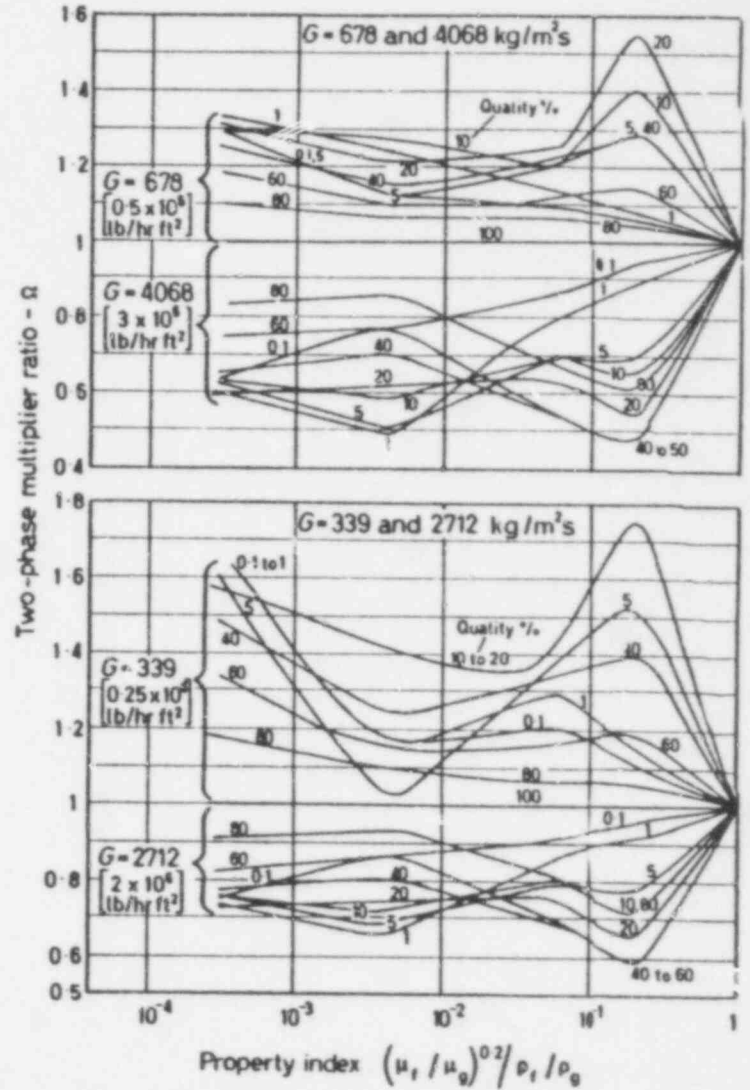
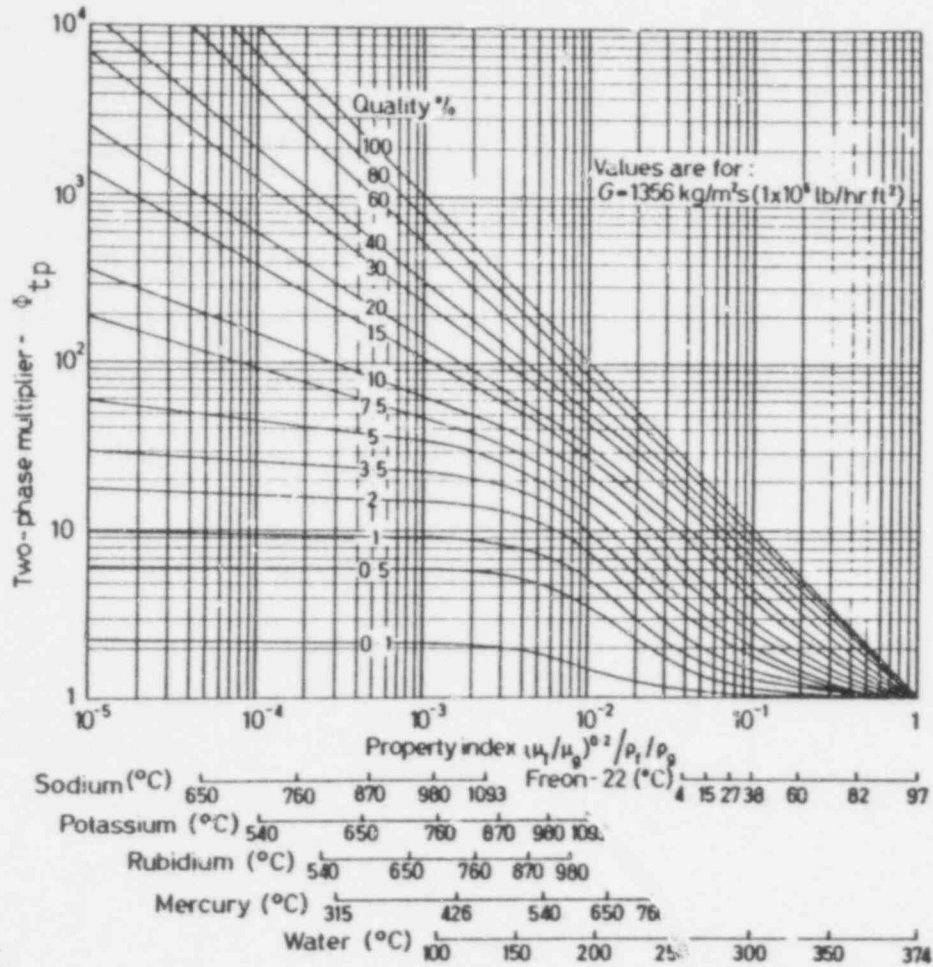
629 332



629 333



629  
334



AGRAWAL/KHATIB-RAHBAR  
 fig. 6.9

629  
 335

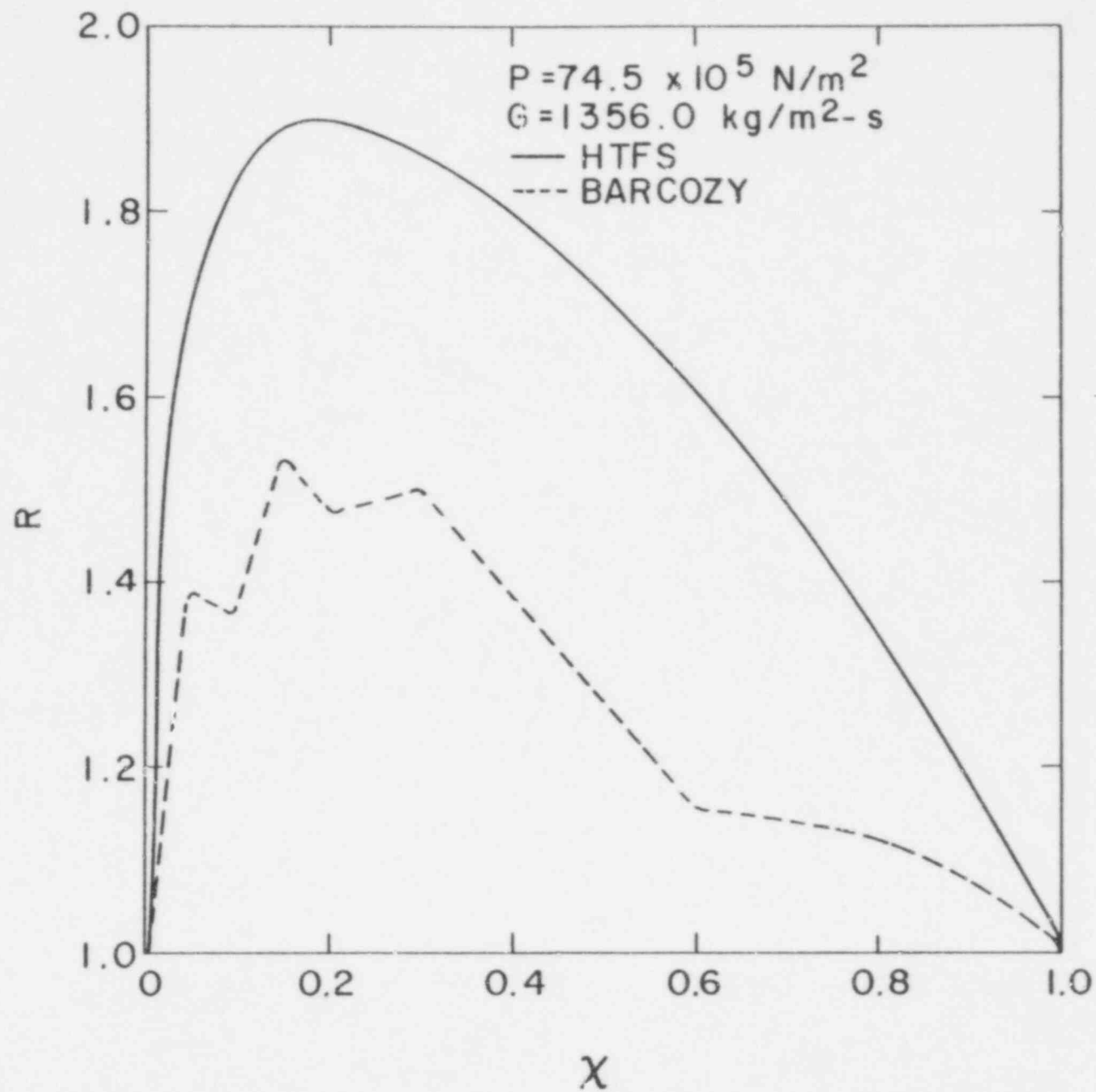
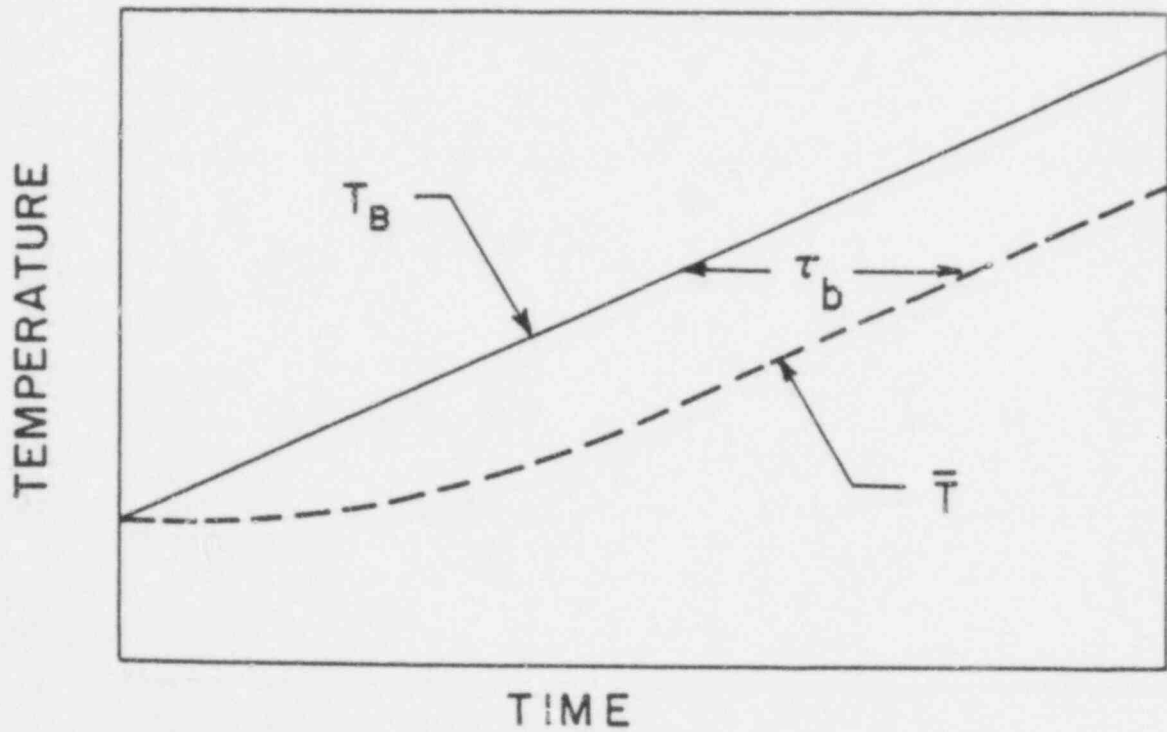
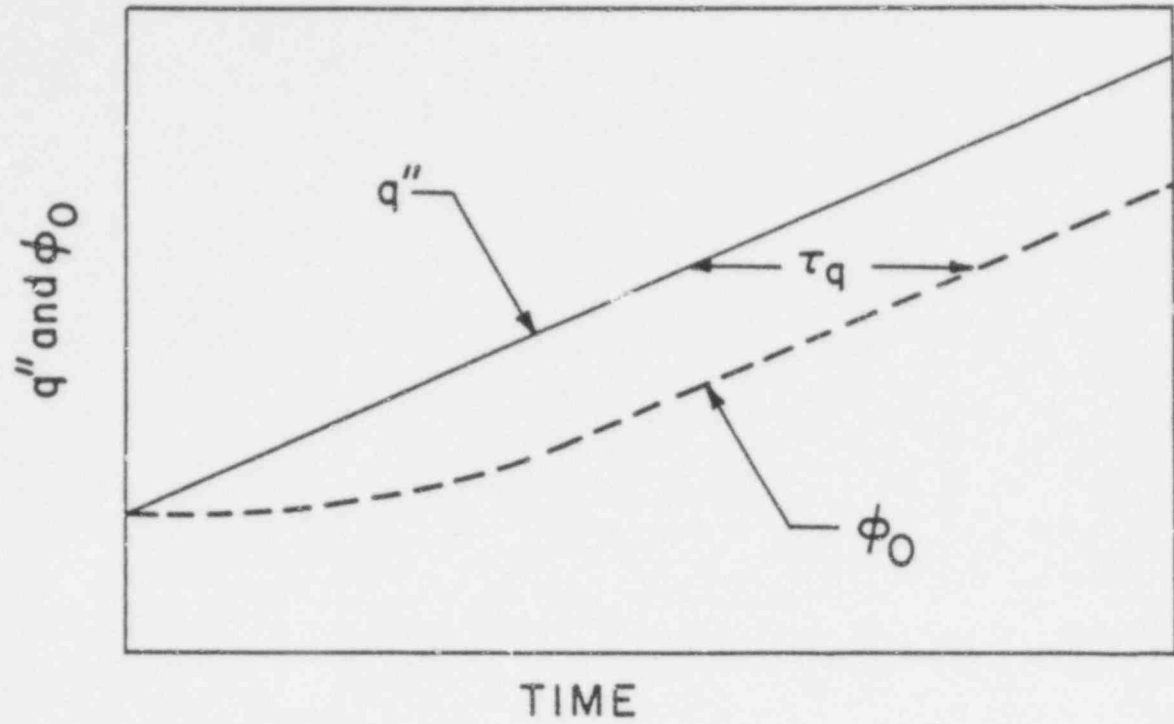


FIGURE CAPTIONS

Figure No.

- 7.1 Illustration of the Heat Flux and the Bulk Coolant Time Constants
- 7.2 Illustration of a Two-Component System

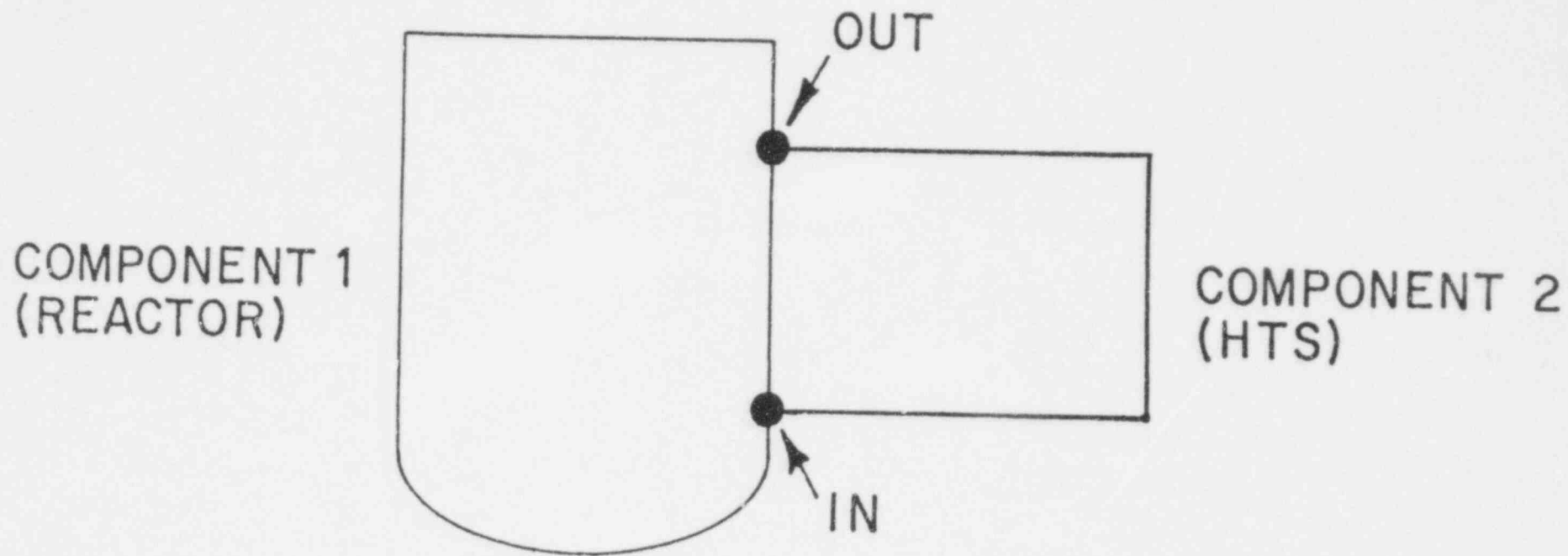
629 337



NOTE: OFFSET DUE TO  $q''$  HAS BEEN SUBTRACTED FROM THE  $\bar{T}$  BAR CURVE

629 338





629  
359

Fig 7.2  
AGRAWAL/KHATIB-RAHBAR

## FIGURE CAPTIONS

### Figure No.

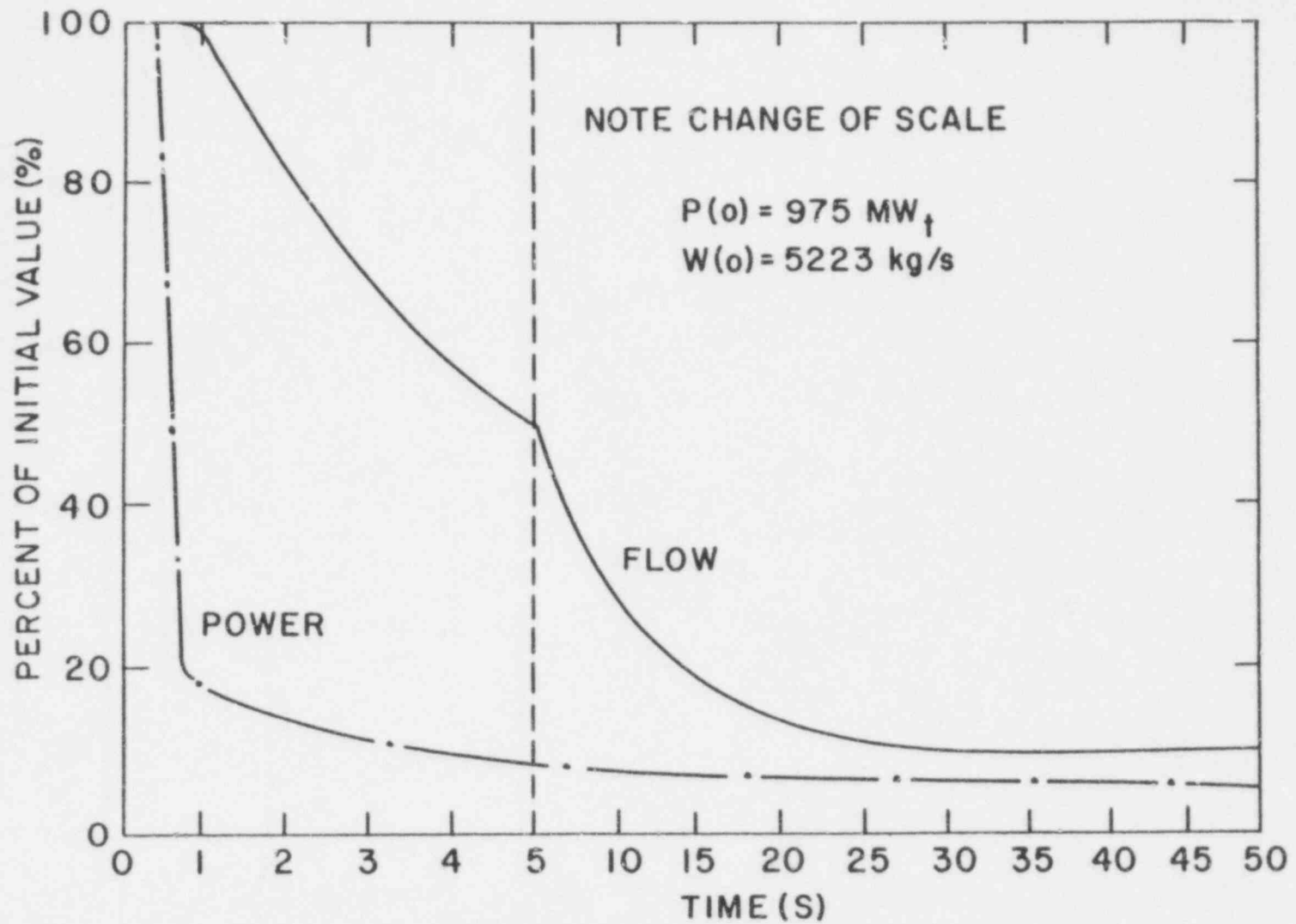
- 8.1a Power and Flow Decay for CRBRP Normal Reactor Scram Transient
- 8.1b Variation in Exit Coolant Temperature for CRBRP Fuel and Radial-Blanket Assemblies During Normal Reactor Scram Transient
- 8.2 Variation in CRBRP Core Parameters for Small Ramp Reactivity Insertions
- 8.3 Orificing Scheme and SSC-L Channels for the CRBRP Core
- 8.4 Axial Coolant Temperature Profiles in a Fuel Assembly (Channel 2)
- 8.5 Axial Coolant Temperature Profiles in a Blanket Assembly (Channel 8)
- 8.6 Coolant Temperatures in a Hot Blanket Channel
- 8.7 Normalized Primary and Secondary Loop Sodium Flow Rates
- 8.8 Primary Sodium Temperature Profiles in the IHX
- 8.9 Secondary Sodium Temperature Profiles in the IHX
- 8.10 Hot-Leg Sodium Temperatures
- 8.11 Cold-Leg Sodium Temperatures
- 8.12 Maximum Sodium Temperature in the Radial Blanket Hot Channel
- 8.13 Minimum Core Flow
- 8.14 Minimum Core Flow to Power Ratio
- 8.15 Maximum Sodium Temperature in the Hot Fuel Channel
- 8.16 Effect of Long Coastdown Time on PFR Core Outlet Temperature
- 8.17 Effect of Short Coastdown Time on PFR Core Outlet Temperature.

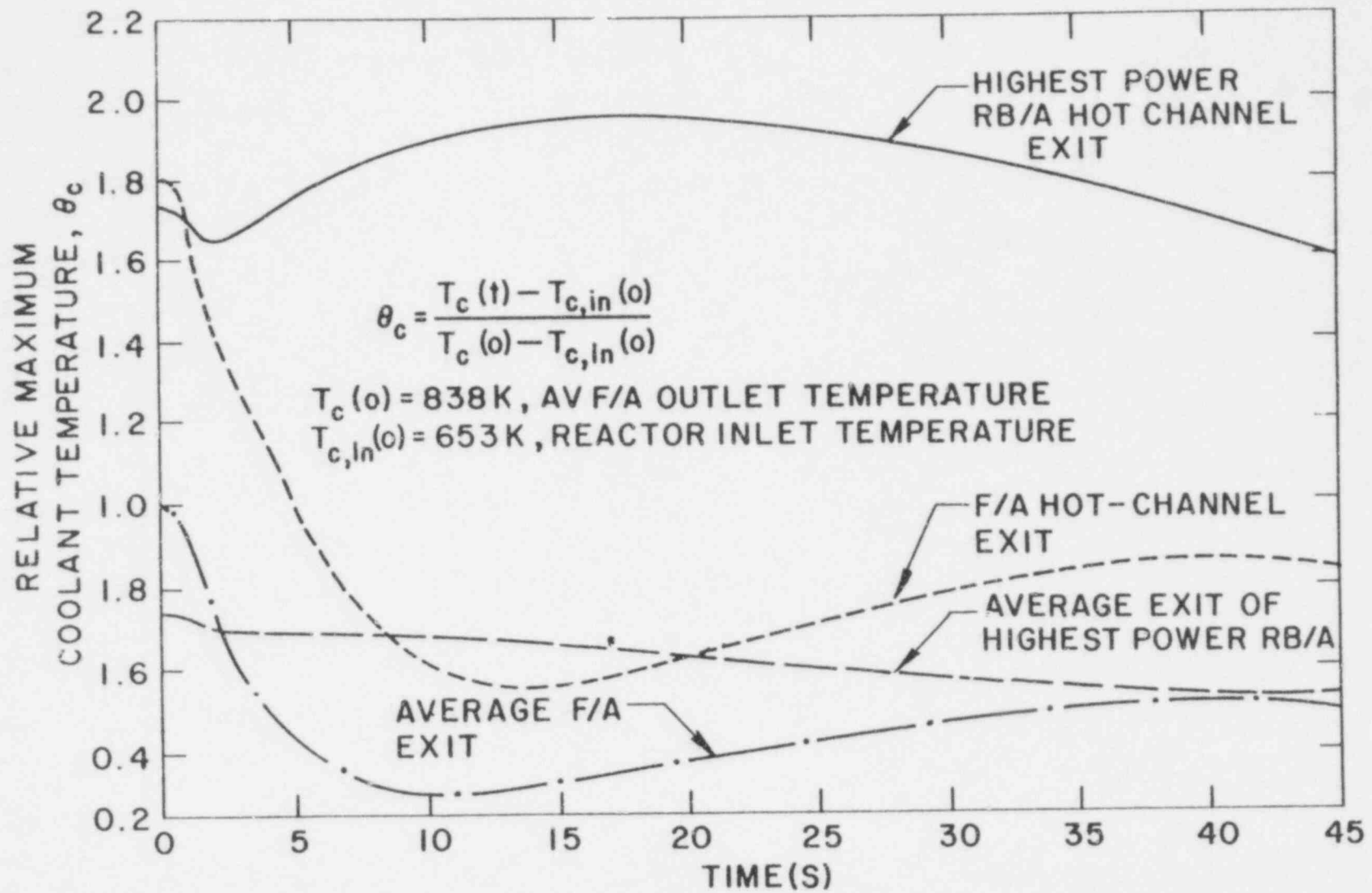
FIGURE CAPTIONS (Cont.)

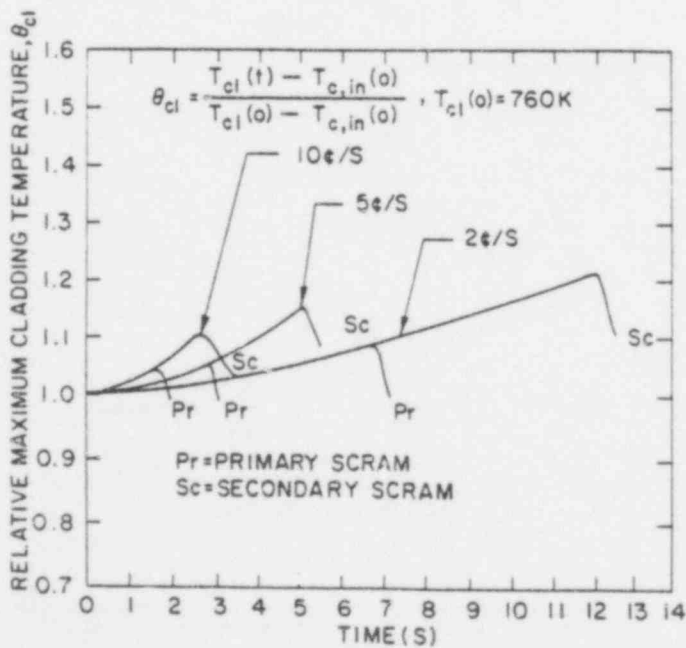
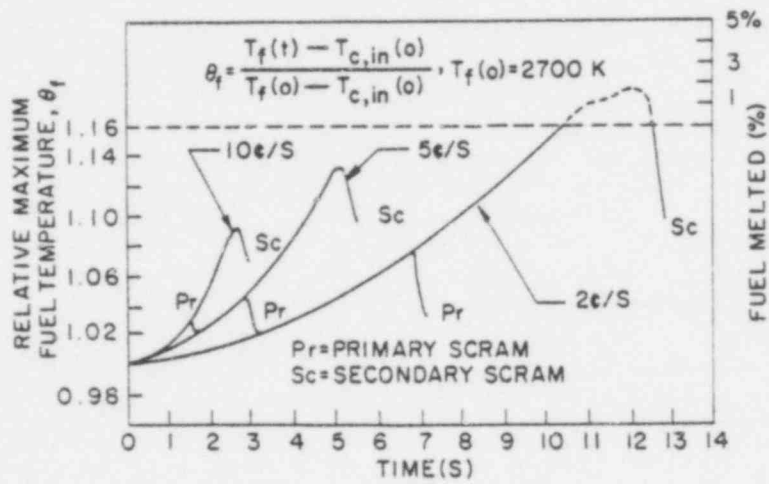
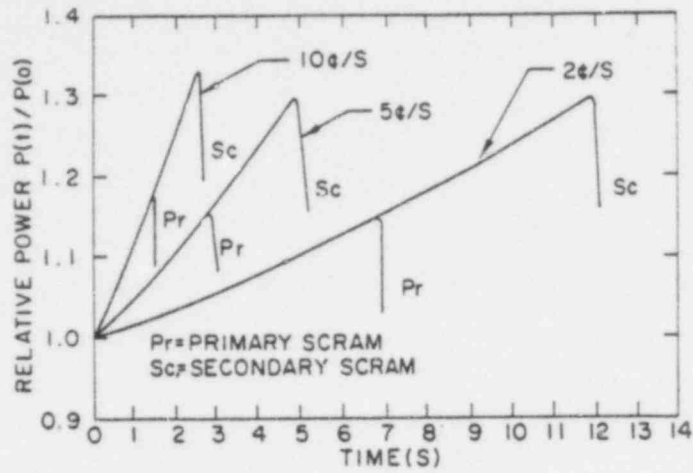
Figure No.

- 8.18 EBR-II Primary Heat Transport System
- 8.19 Schematic of the EBR-II Reactor
- 8.20 Schematic of the EBR-II Experimental Assembly XX07
- 8.21 Schematic of the EBR-II Experimental Assembly XX08
- 8.22 Cross-Sectional View of the XX08 Instrumented Subassembly
- 8.23 Typical Subassembly Temperature Rise in EBR-II Under Forced Flow Conditions
- 8.24 Typical Subassembly Temperature Rise in EBR-II Under Natural Convection Conditions
- 8.25 XX08 Flow Response Comparisons for Tests 1A and 1E
- 8.26 XX08 Coolant Temperature Rises for Tests 1A and 1E

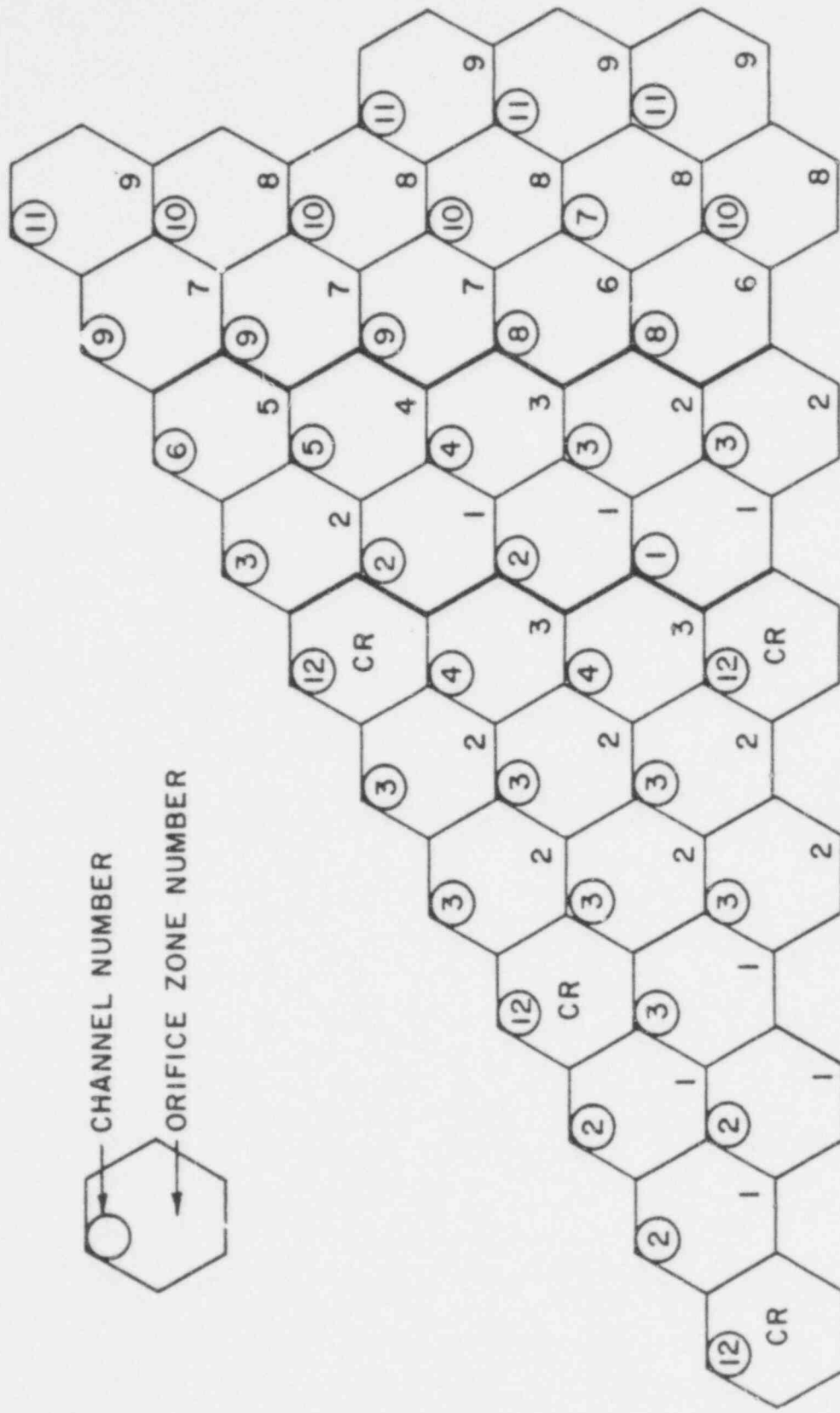
629 341



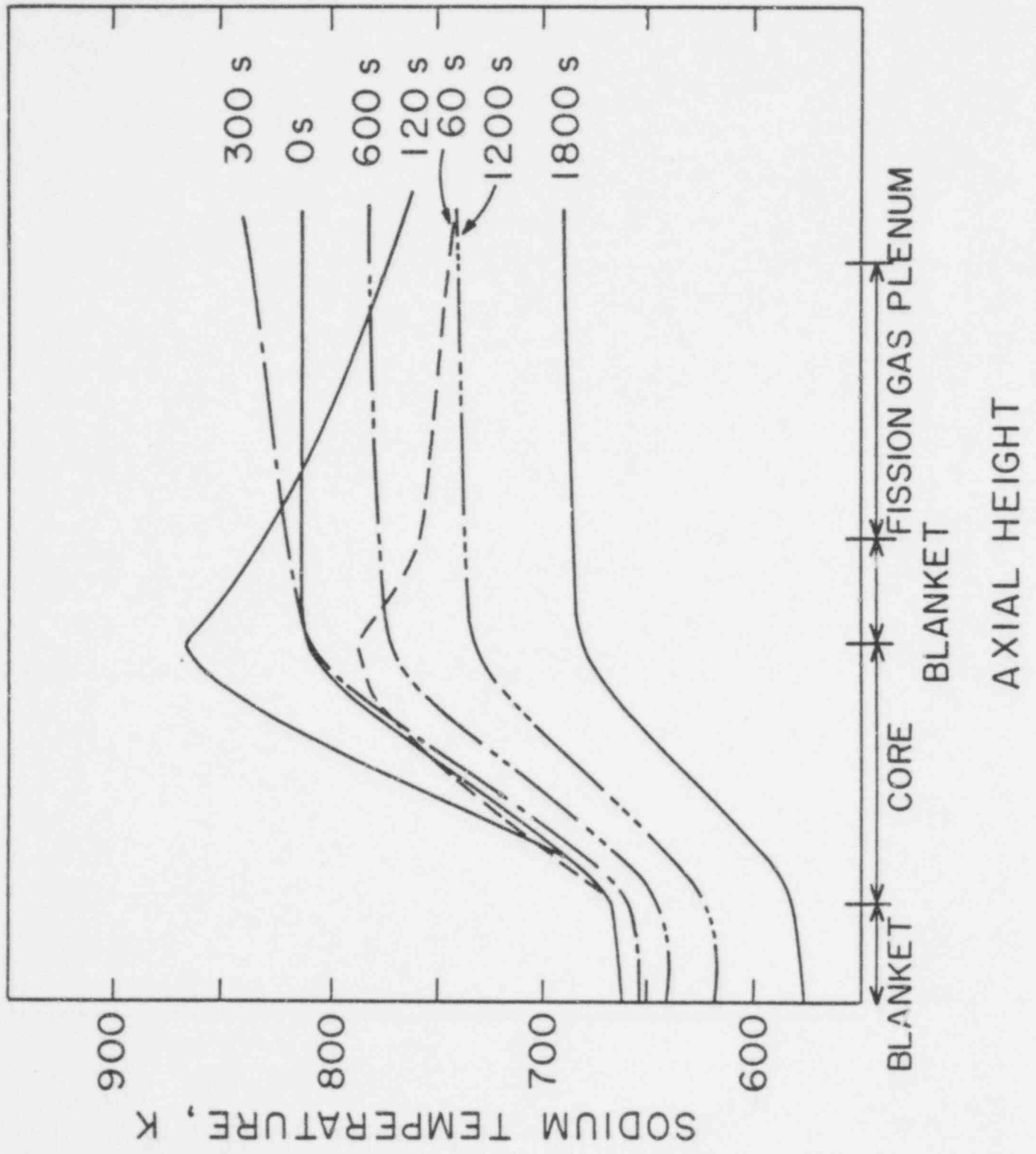




629 344

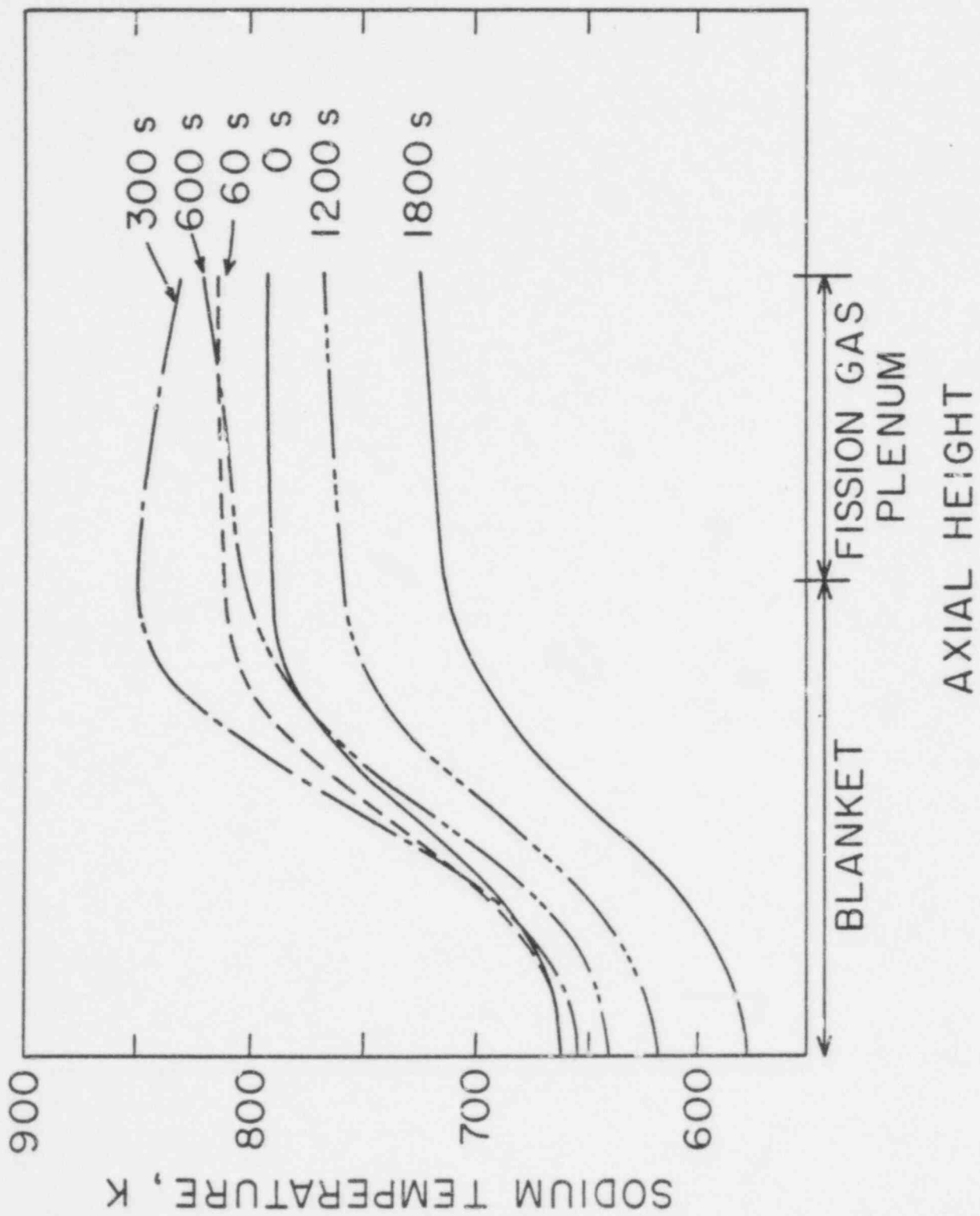


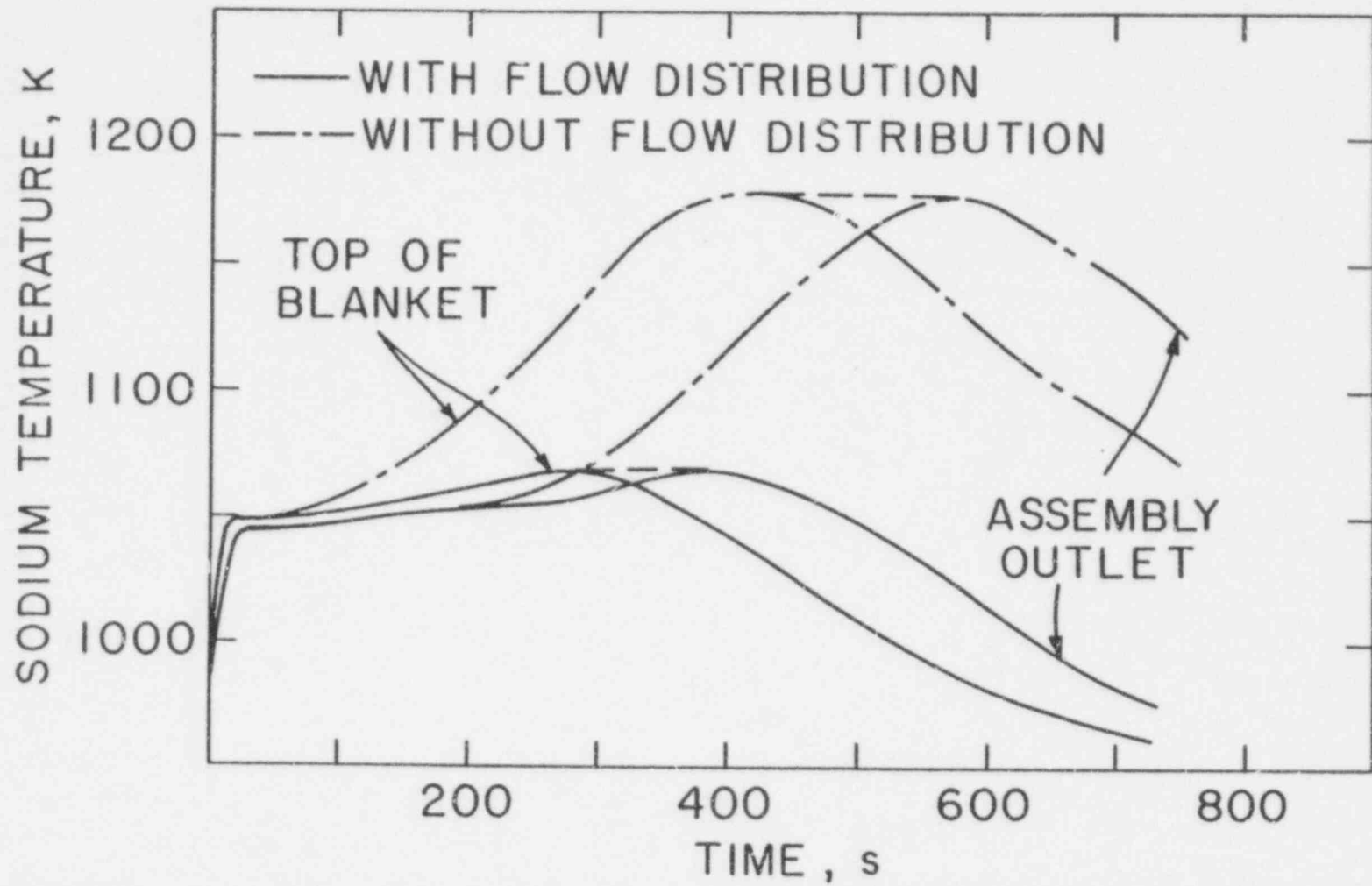
627 545



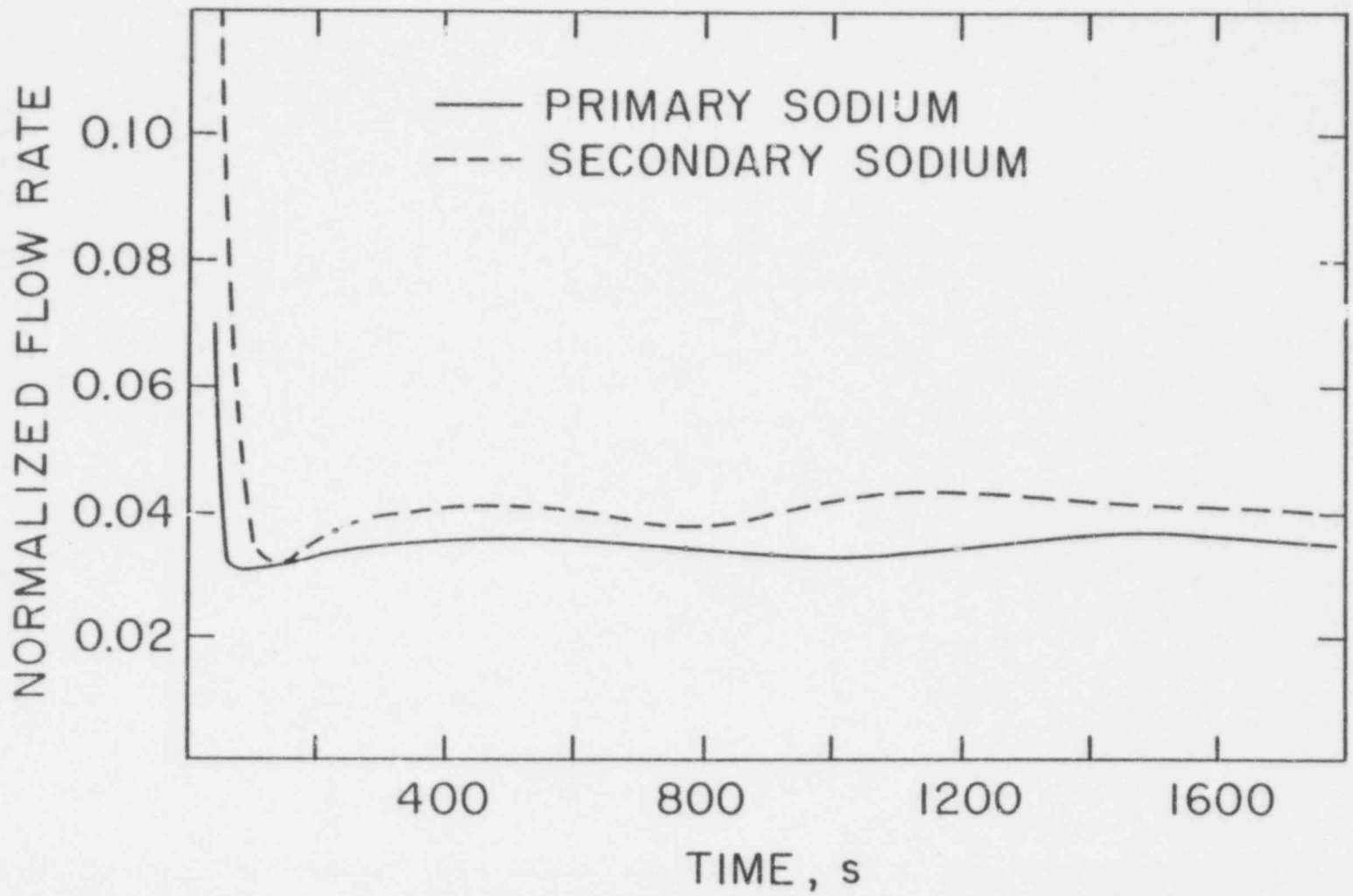
629 346



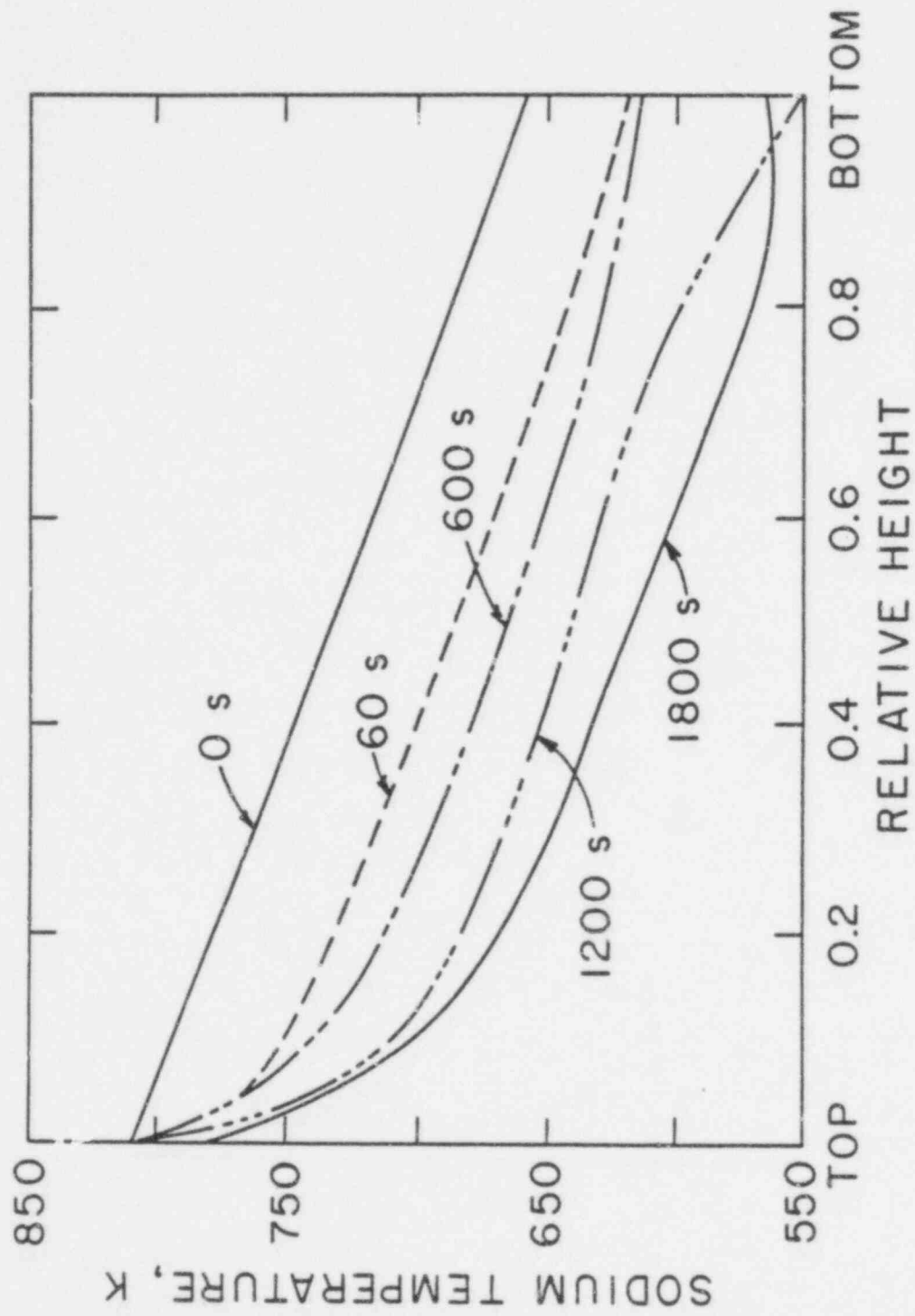




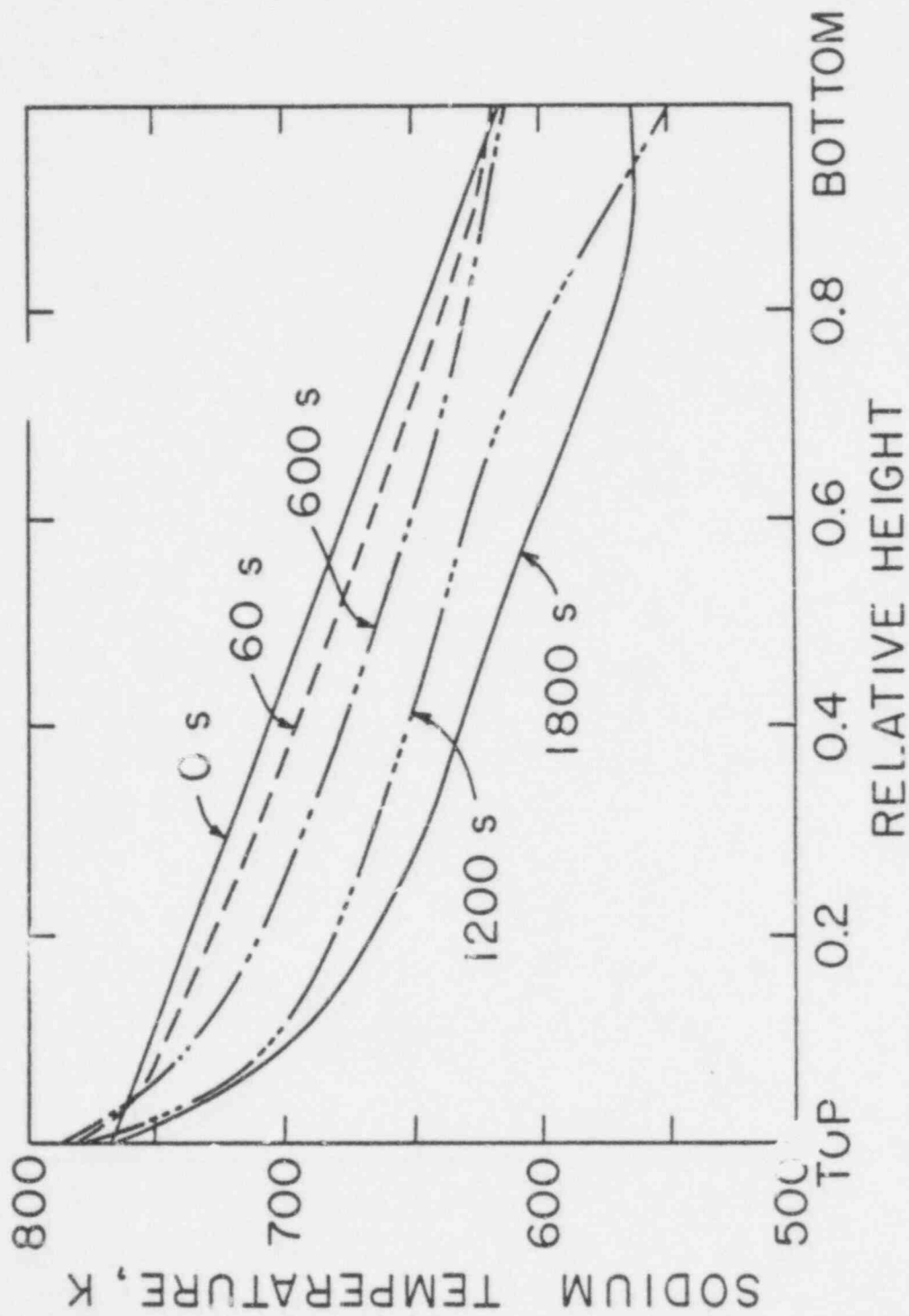
929  
348



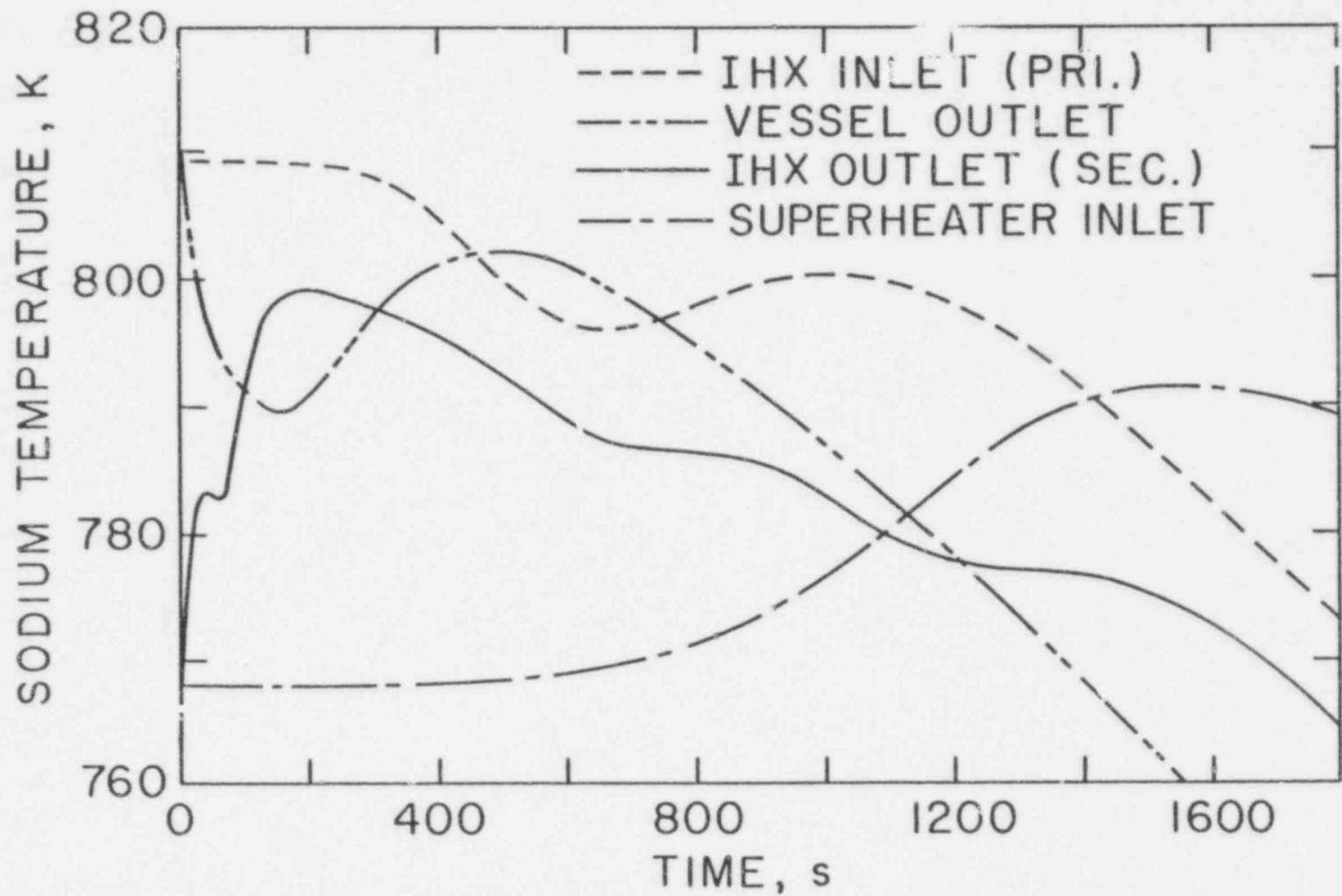
629  
349



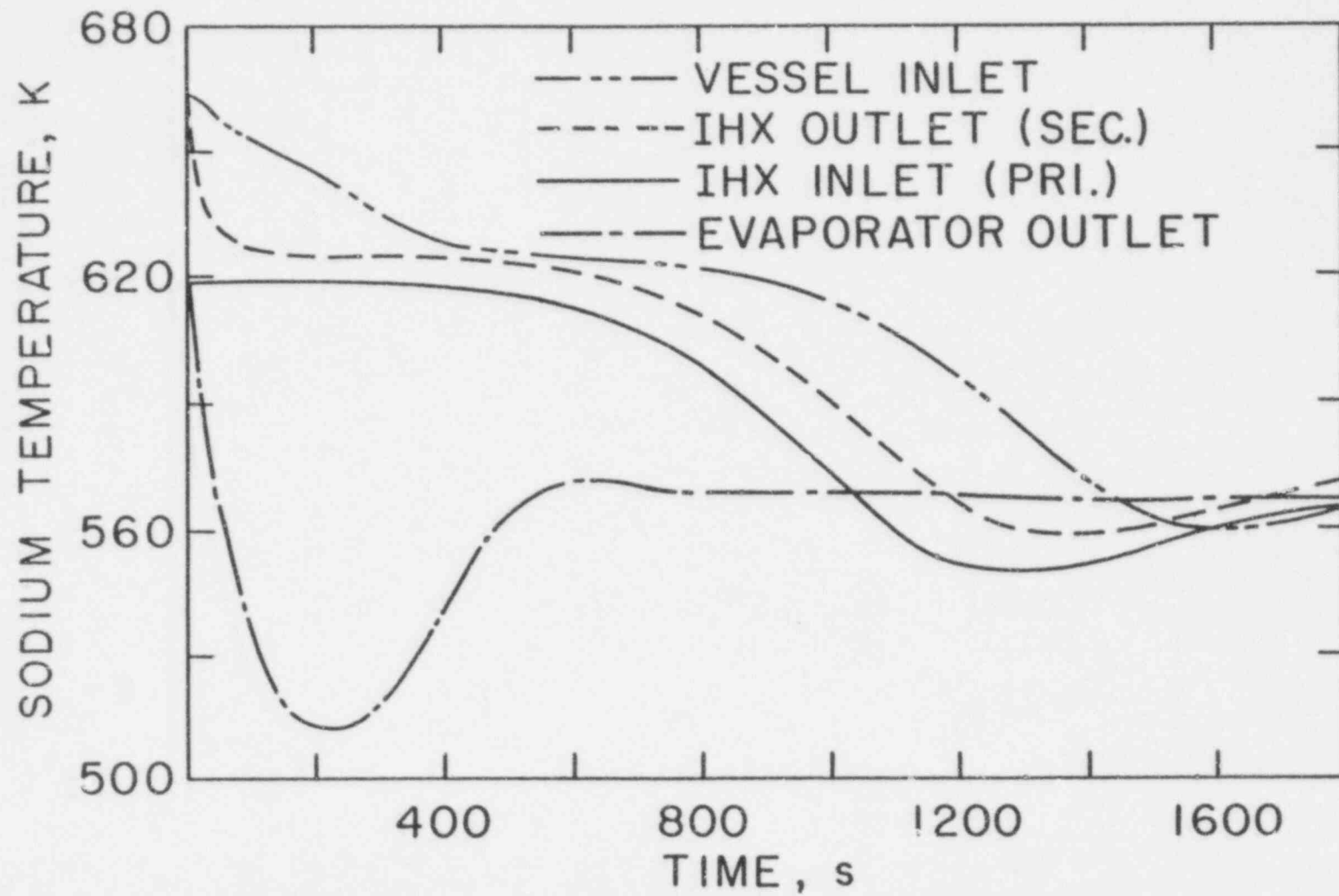
629 350

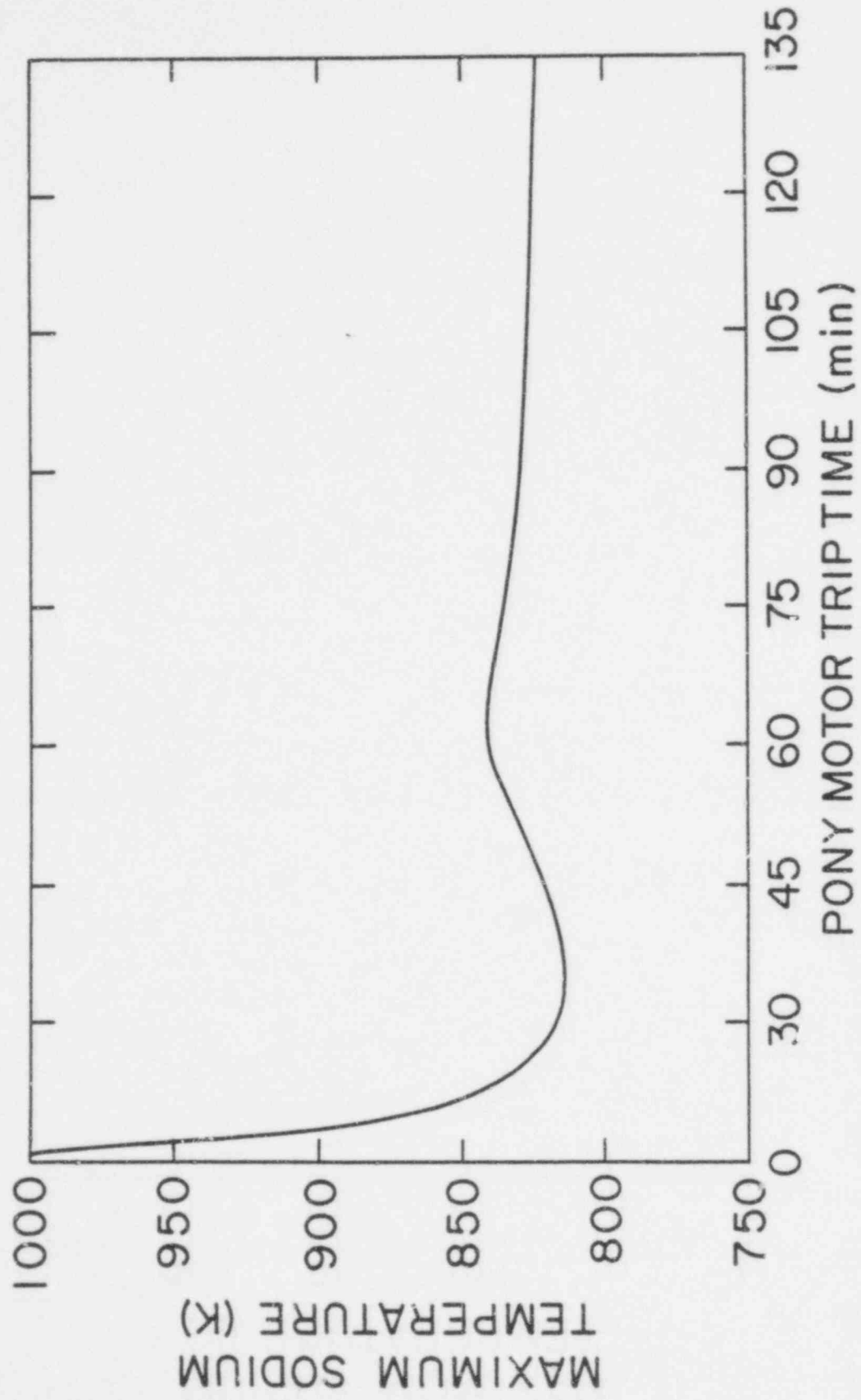


629 351



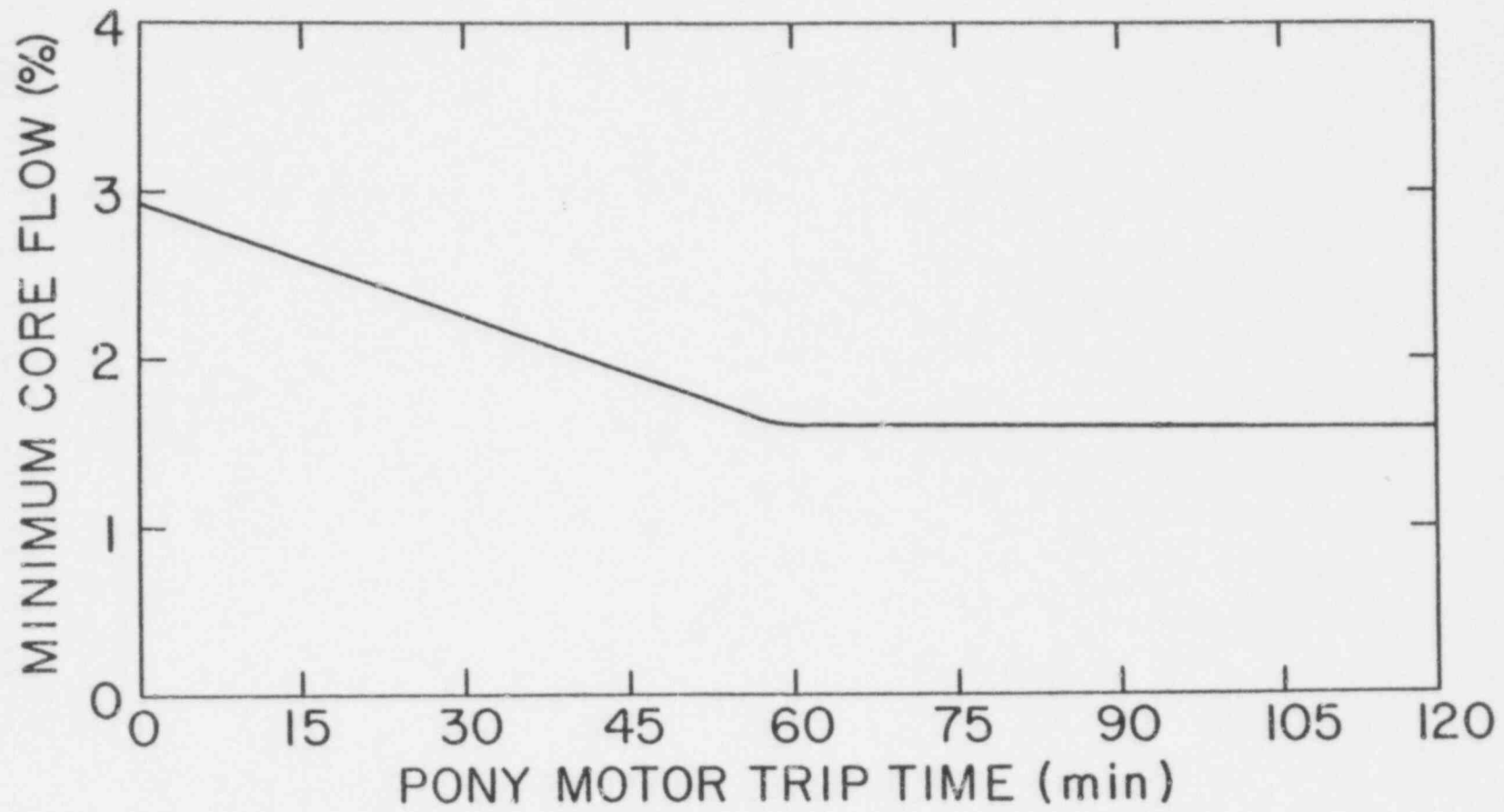
AGRAWAL/KHATIB-RAHBAR  
Fig. 8.10



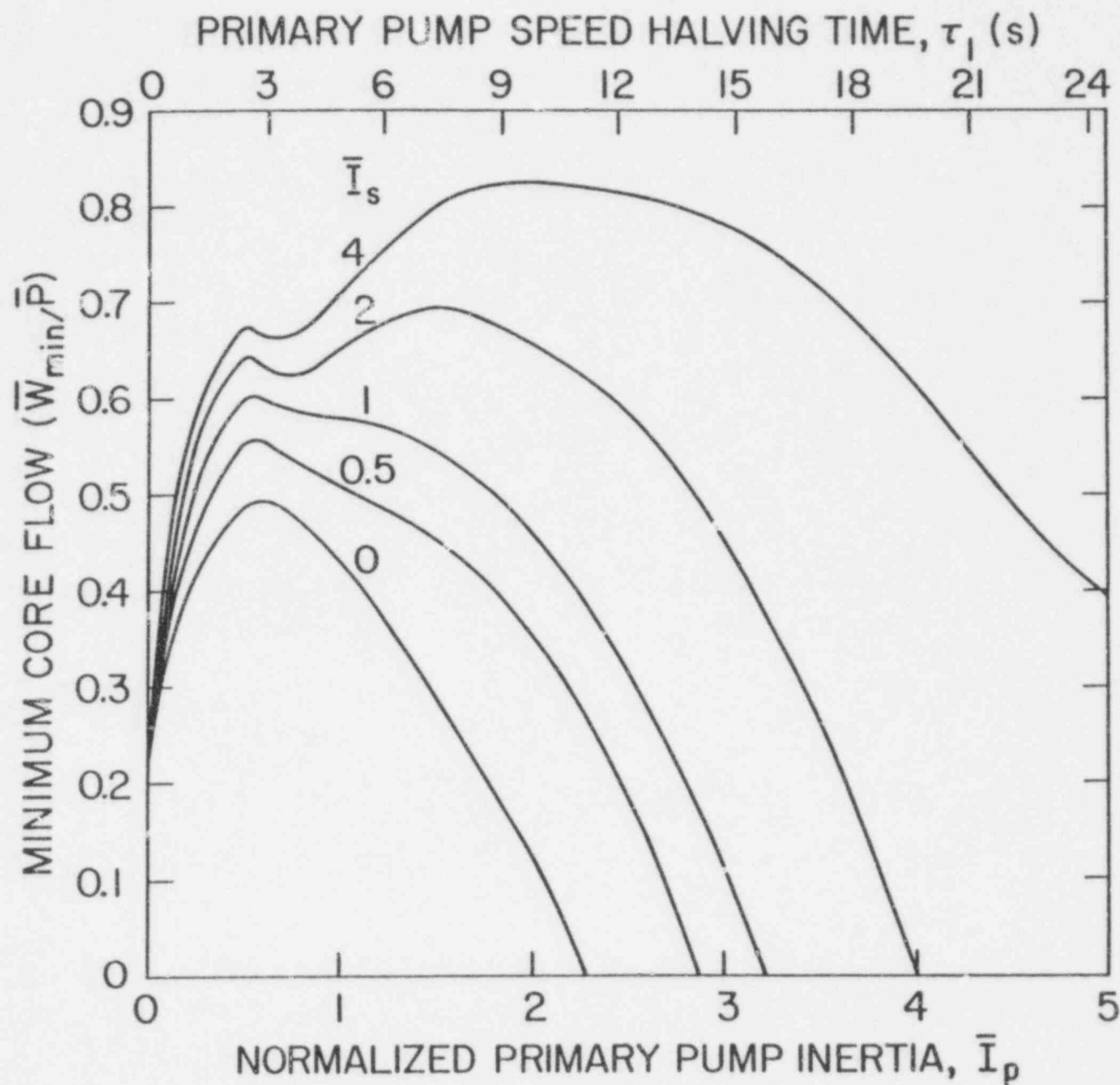


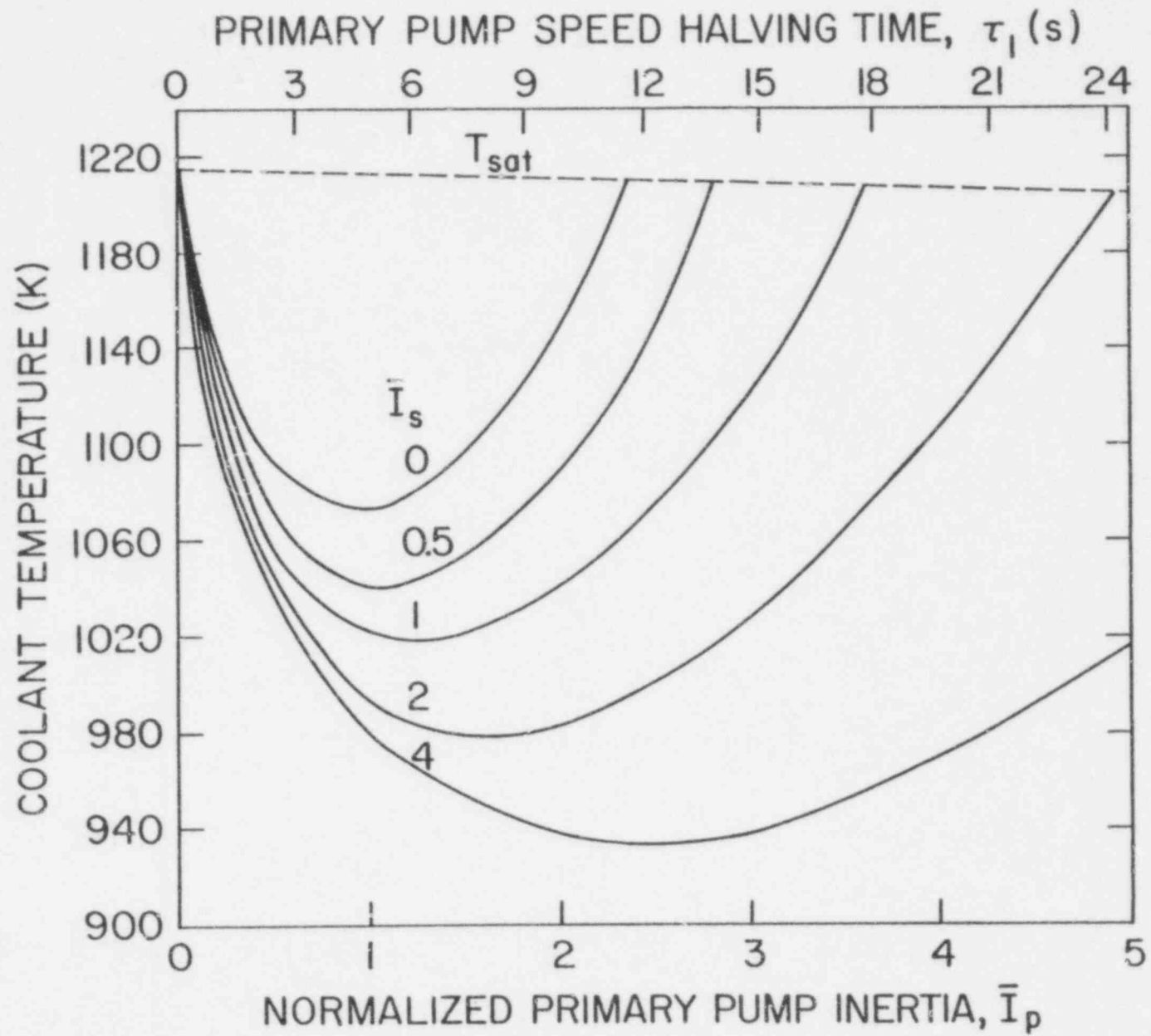
629 354

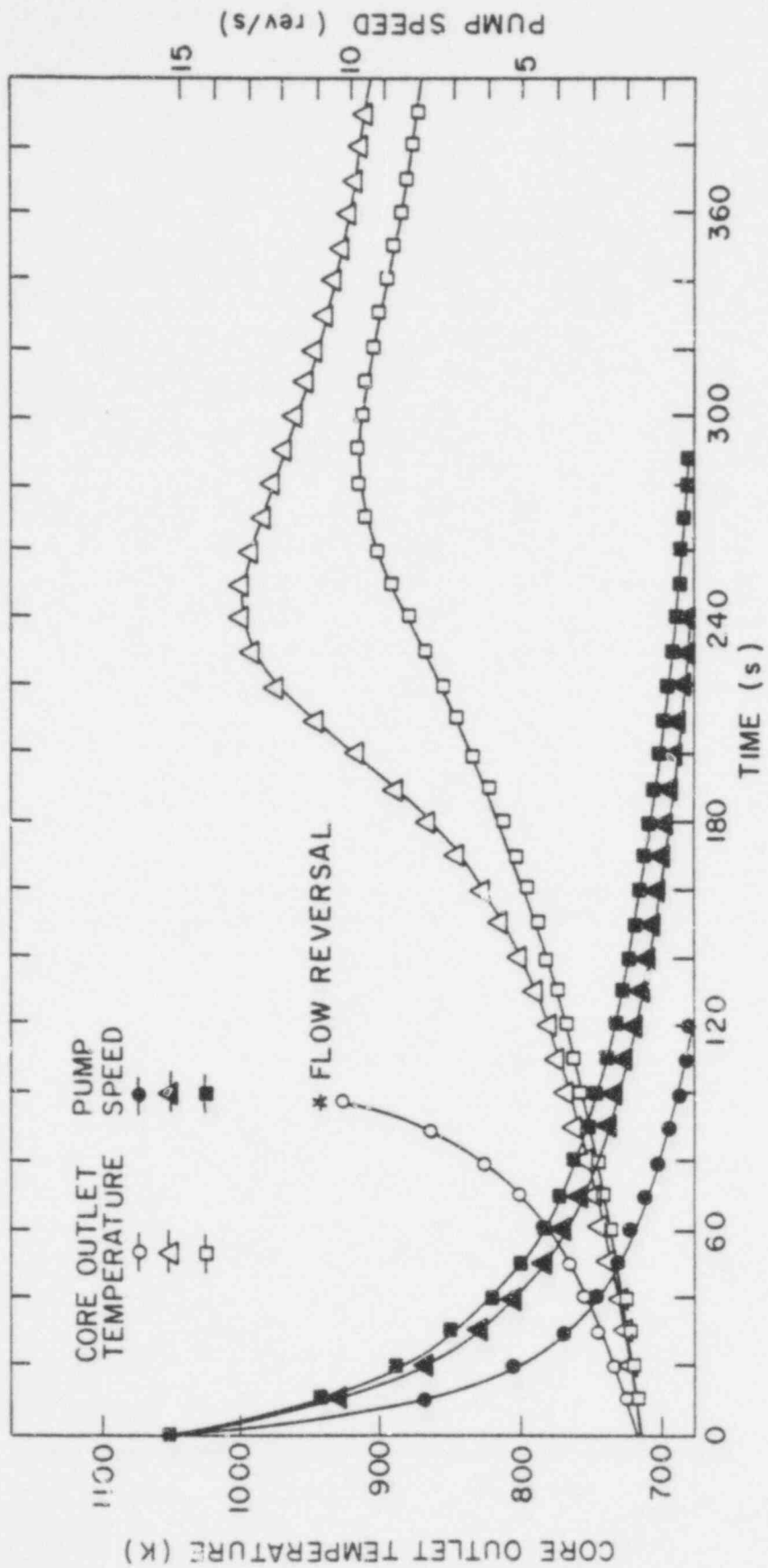




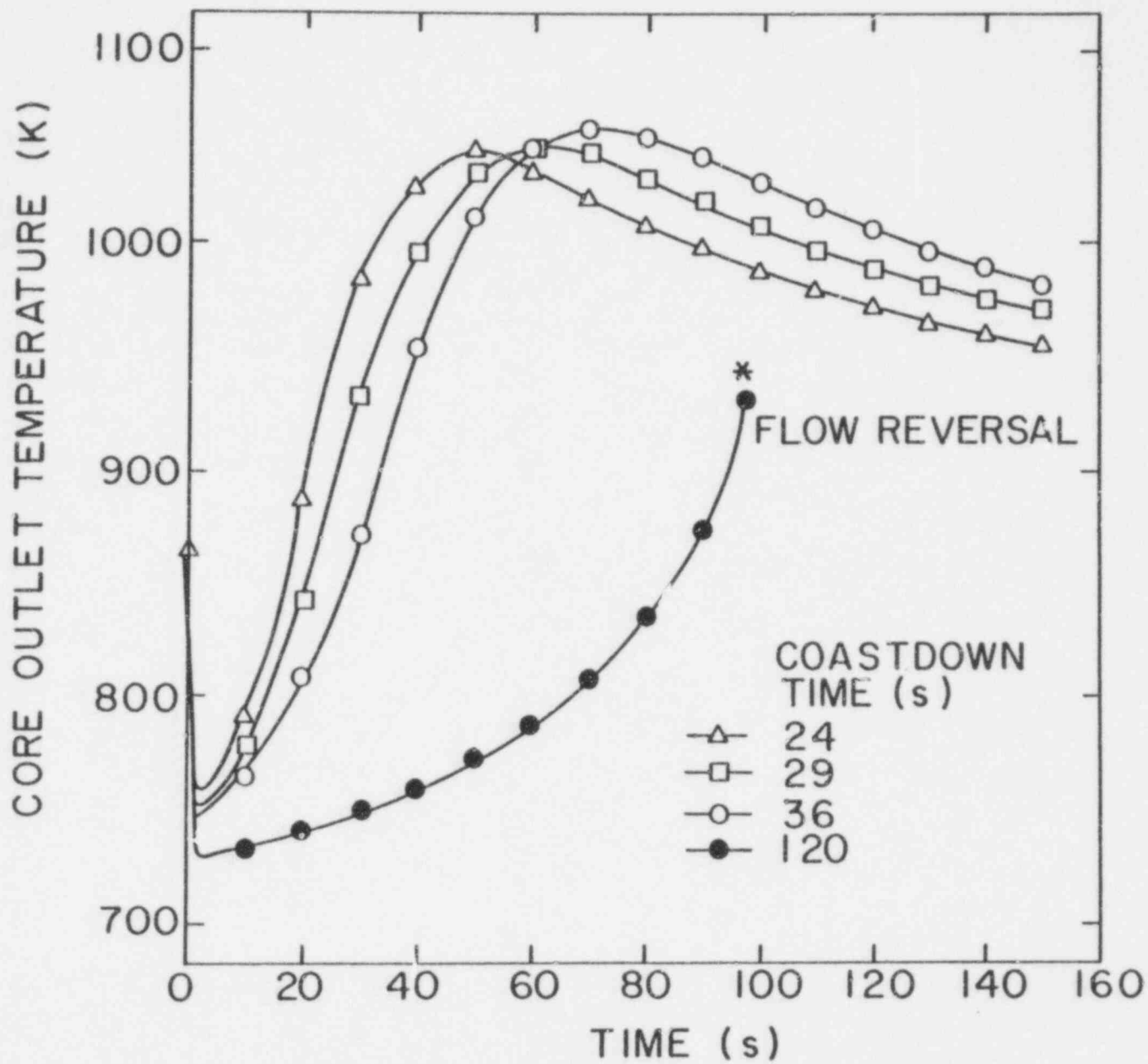
829  
355



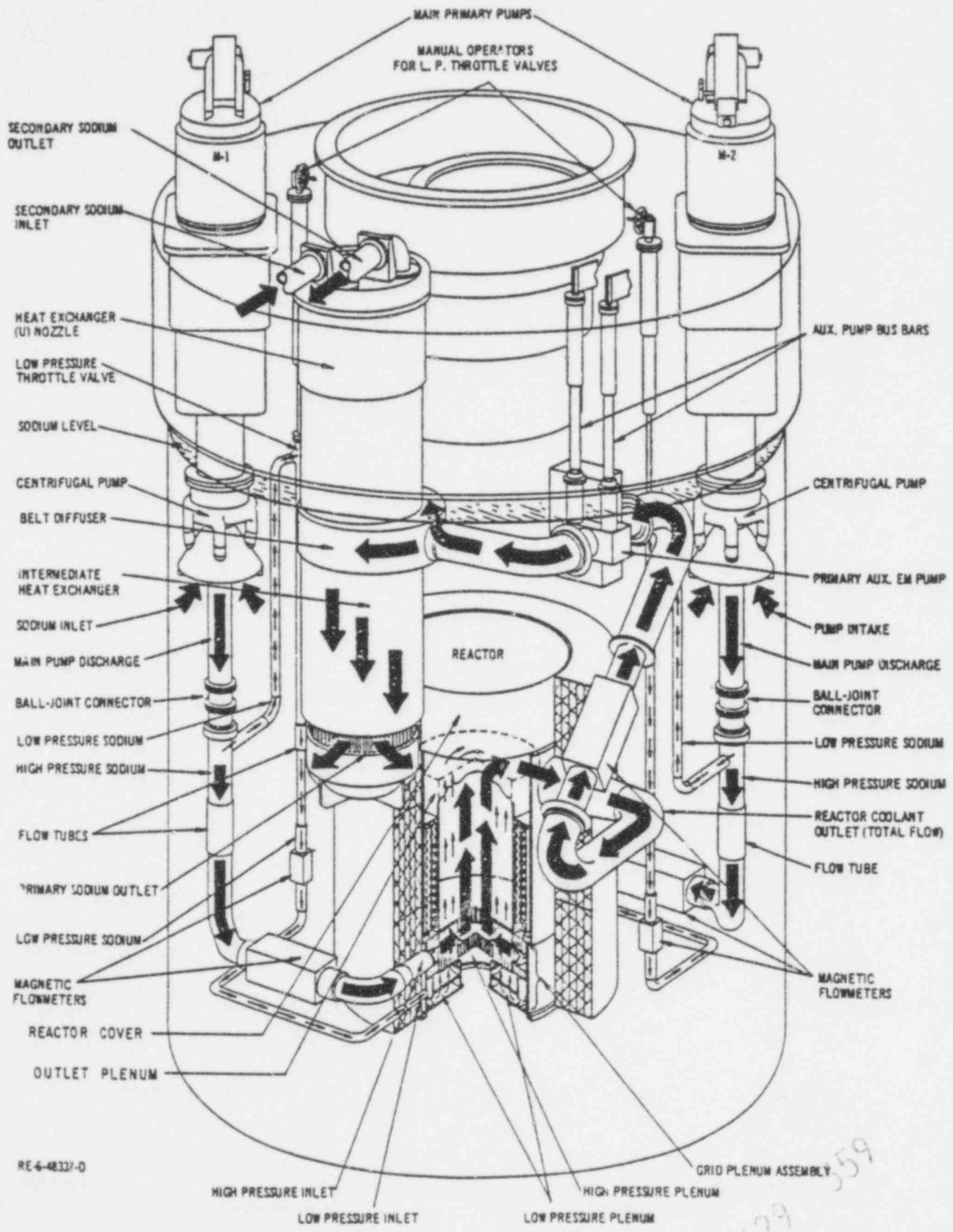




629 357

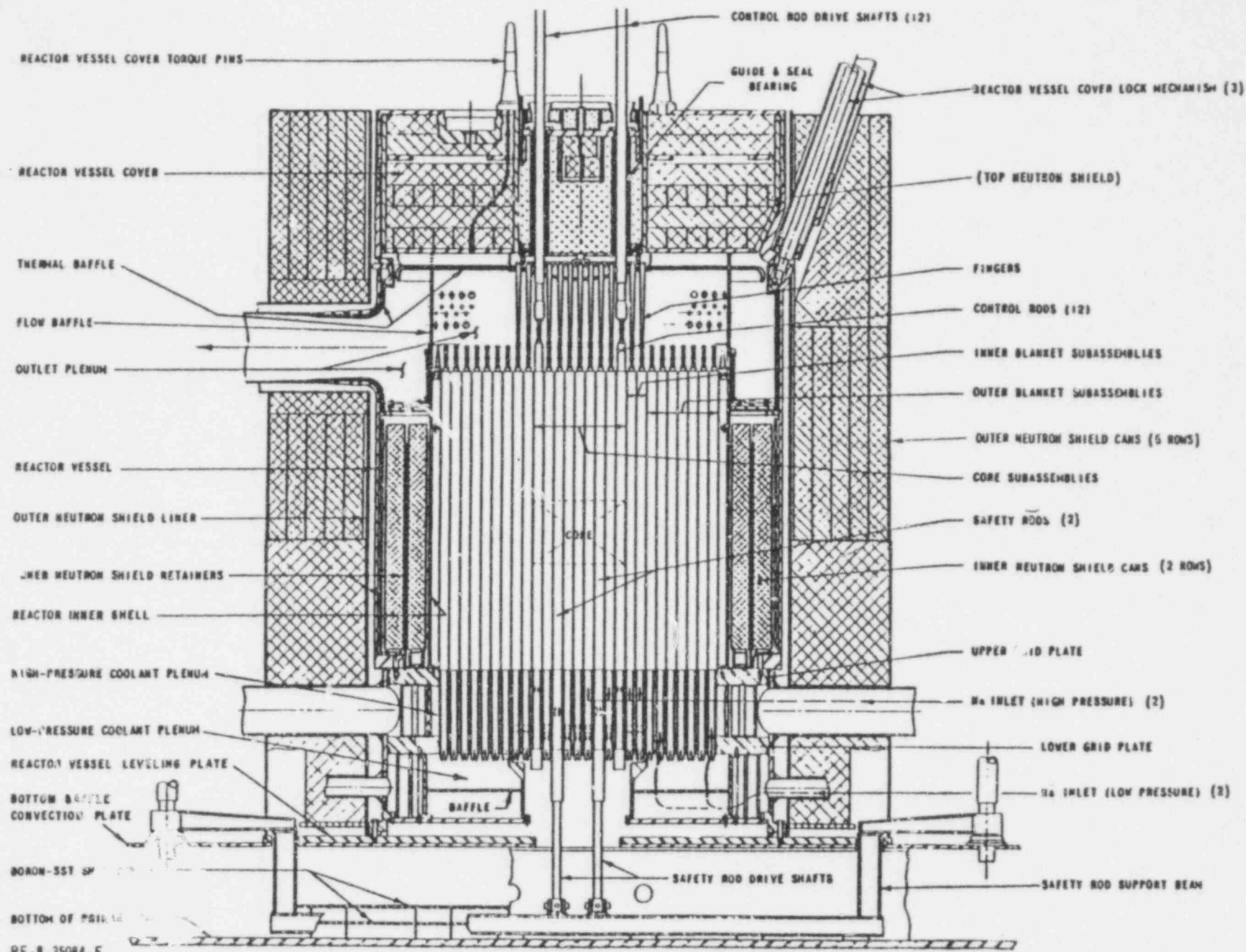


629  
358



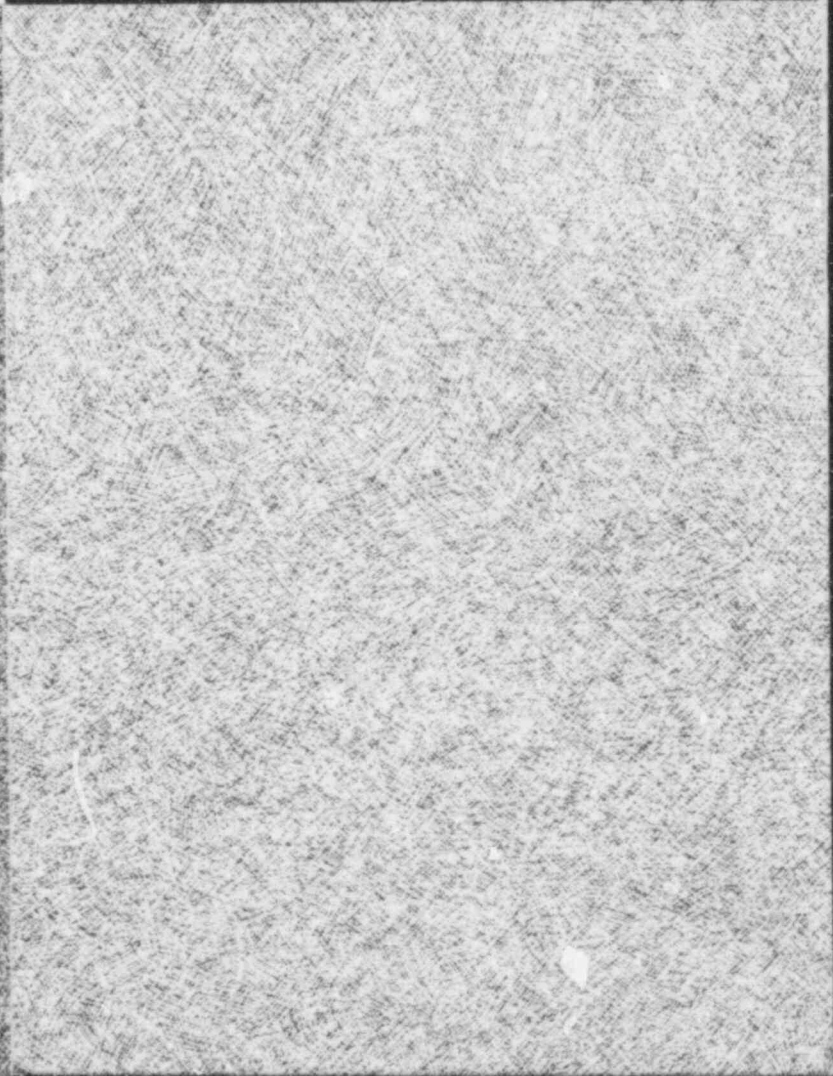
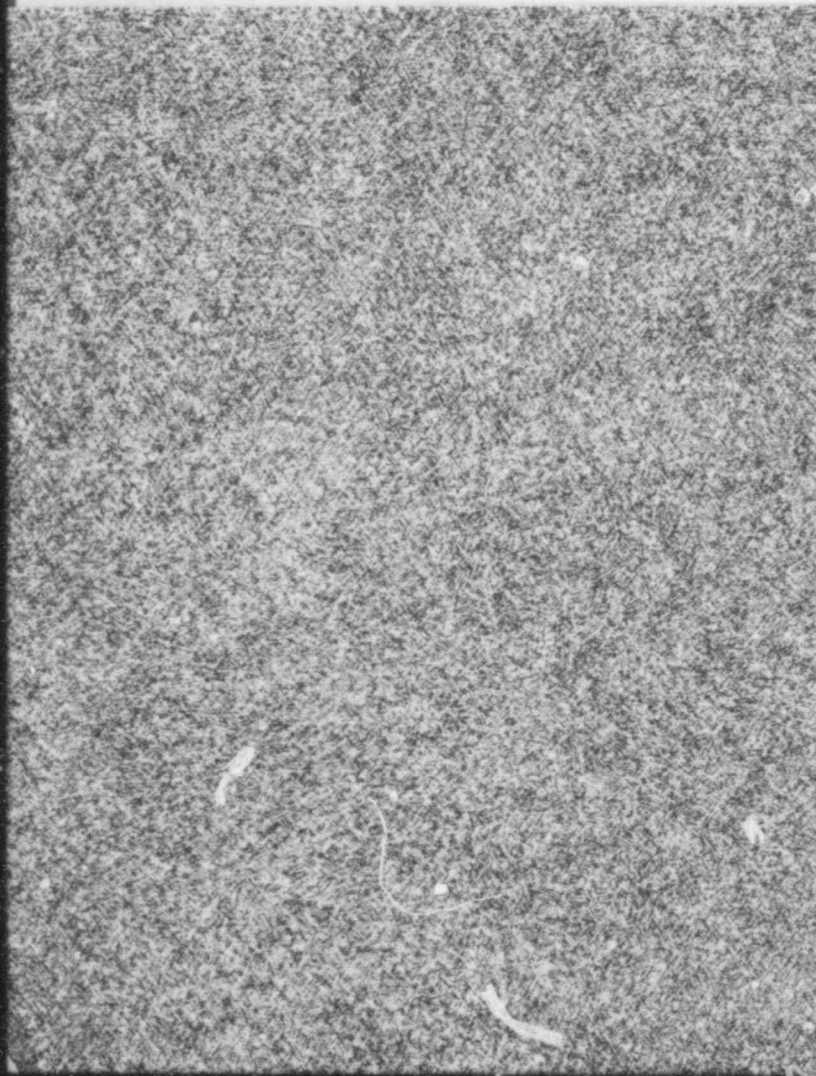
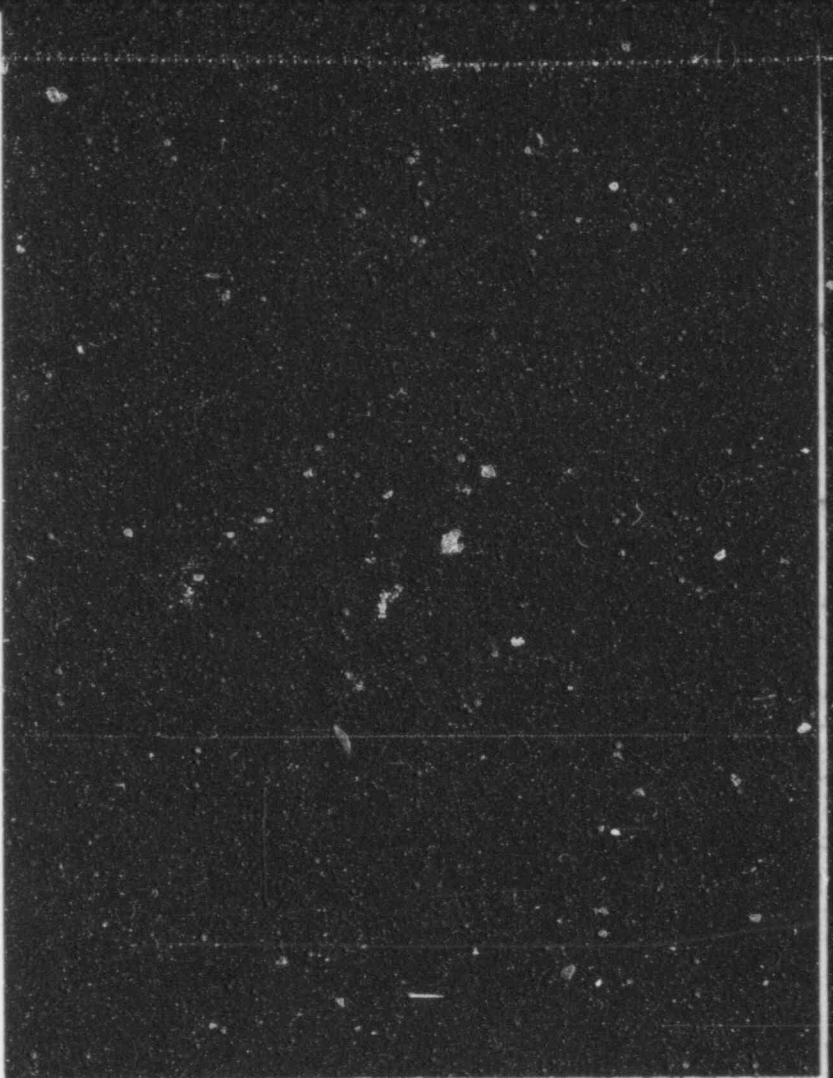
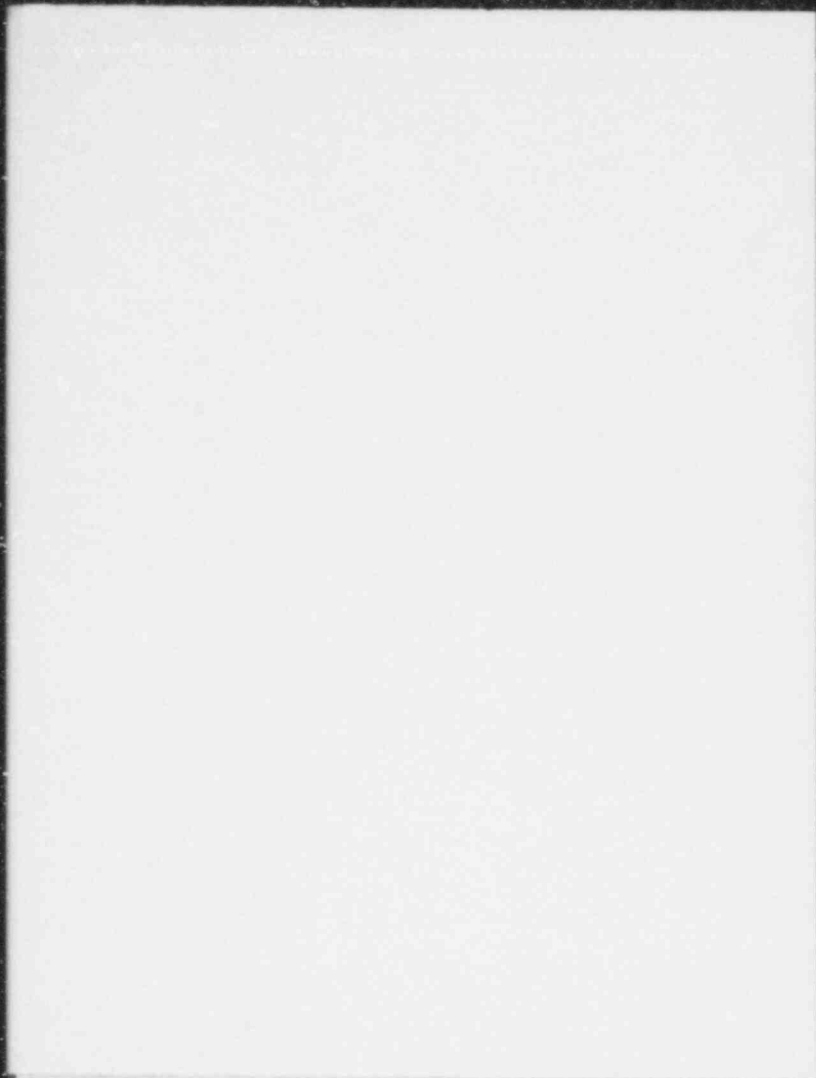
RE-4-48327-0

AGRAWAL/KHATIB-RAHBAR  
Fig. 8.18

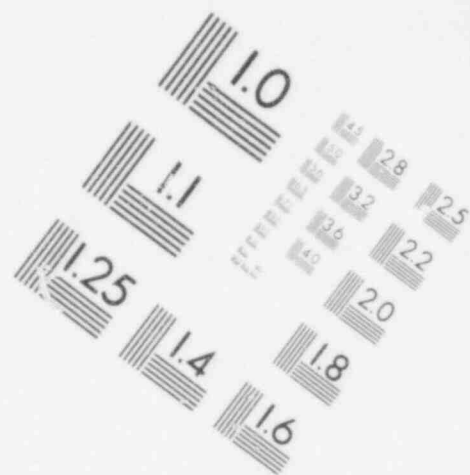
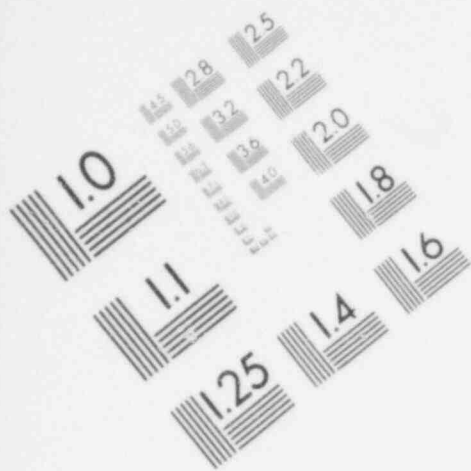


RE-8-35084-F

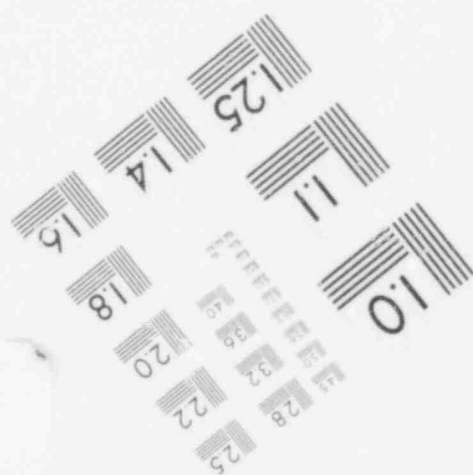
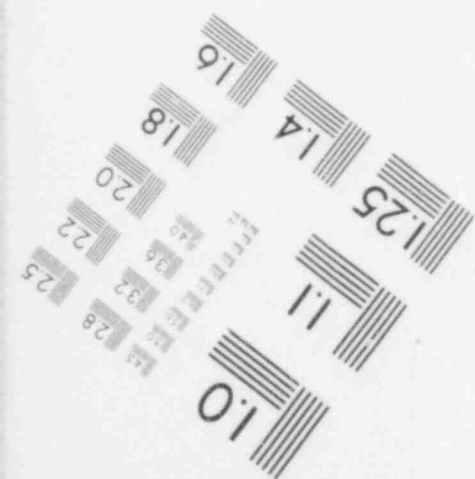
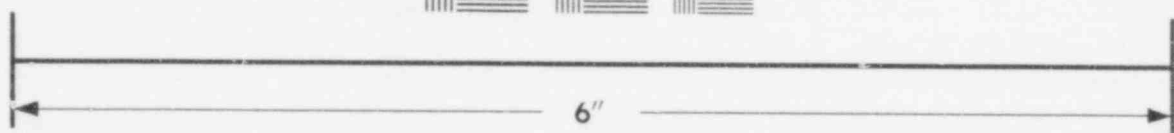
AGRAWAL/KHATIB-RAHBAR  
Fig. 8.19

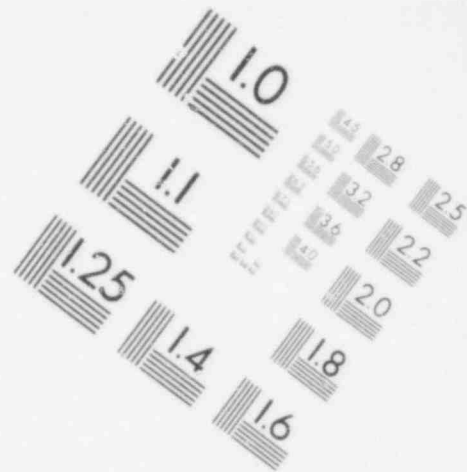
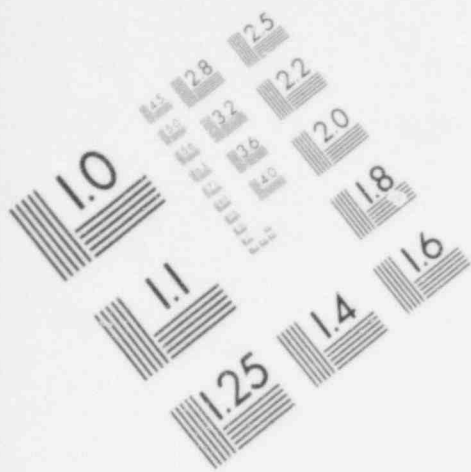




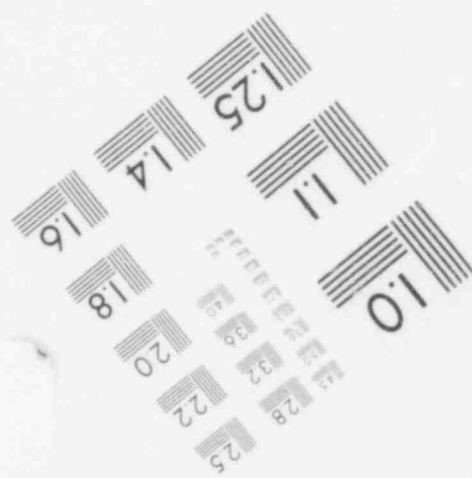
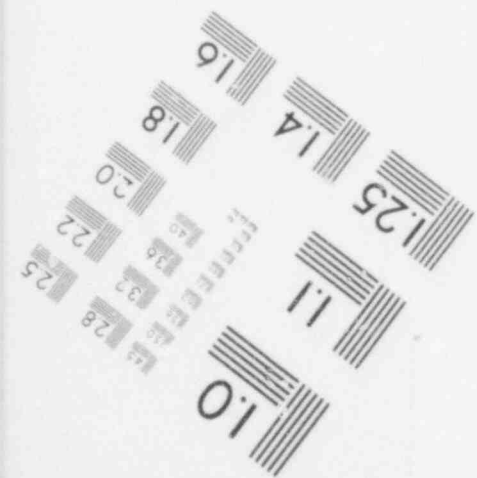
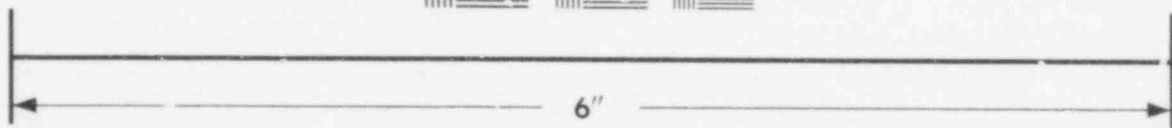
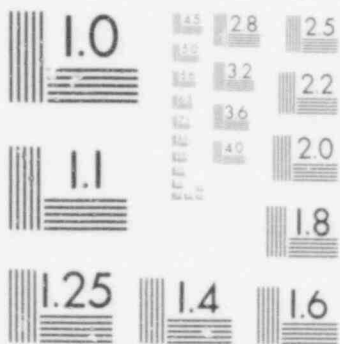


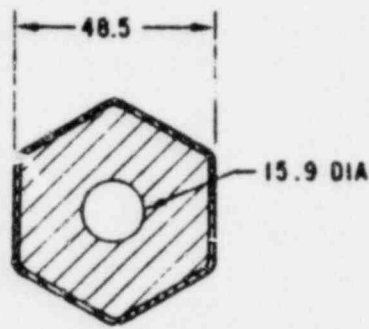
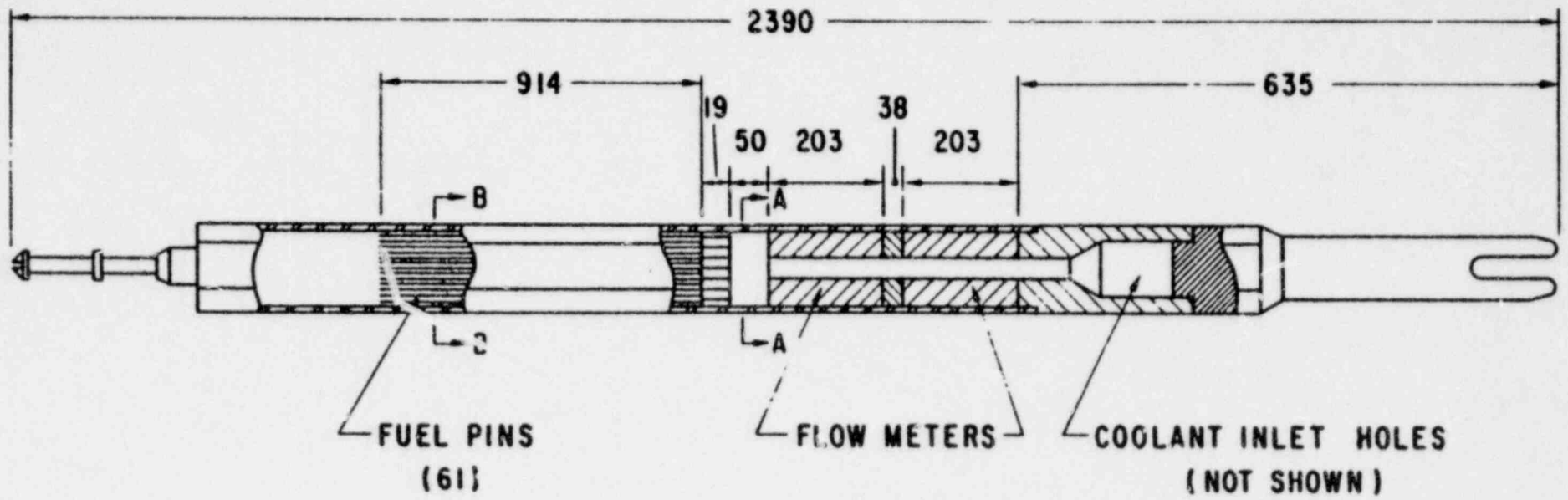
**IMAGE EVALUATION  
TEST TARGET (MT-3)**



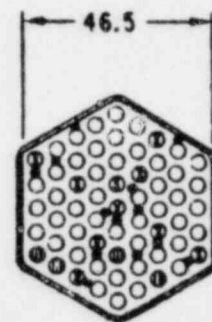


**IMAGE EVALUATION  
TEST TARGET (MT-3)**





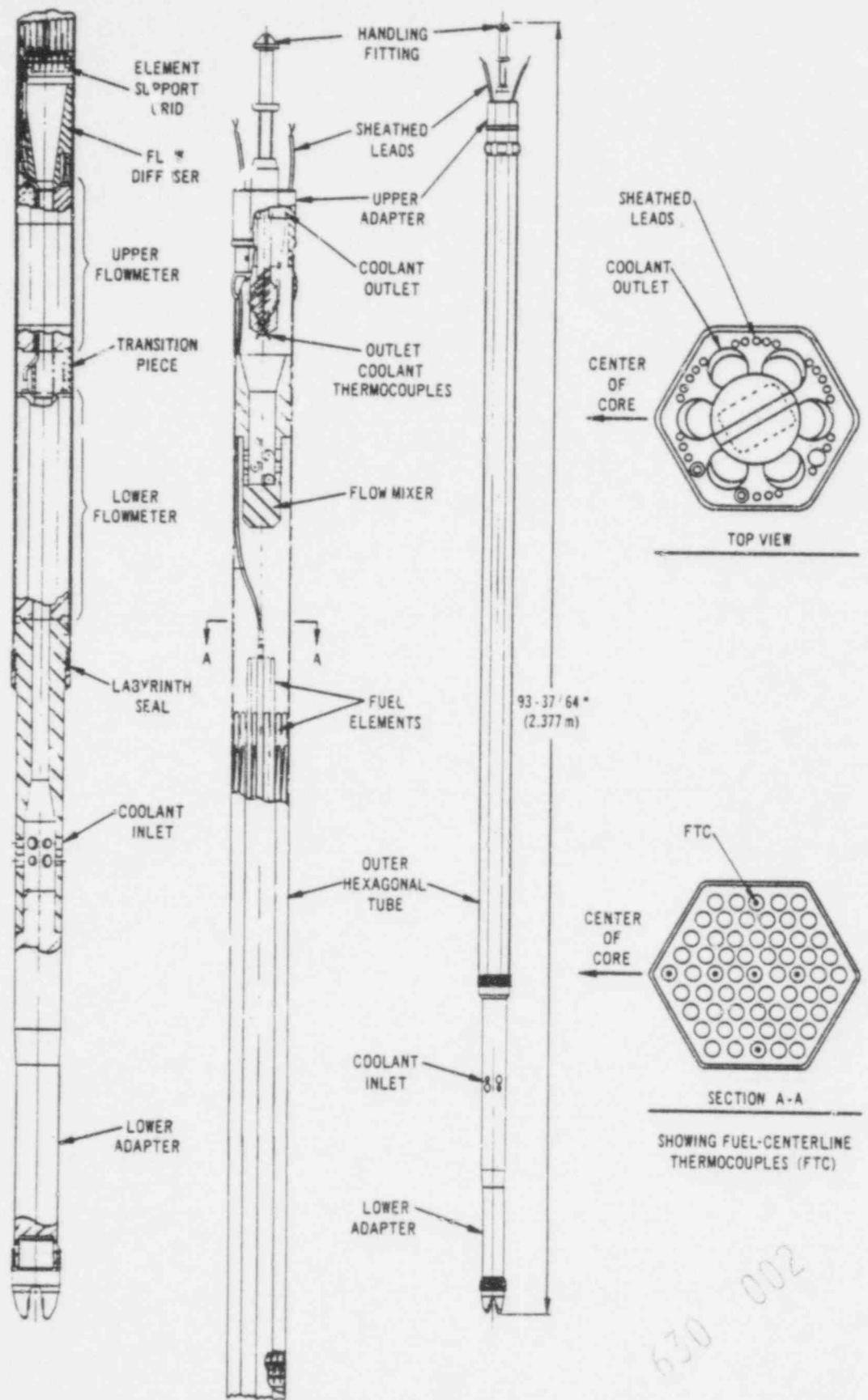
VIEW A-A



VIEW B-B

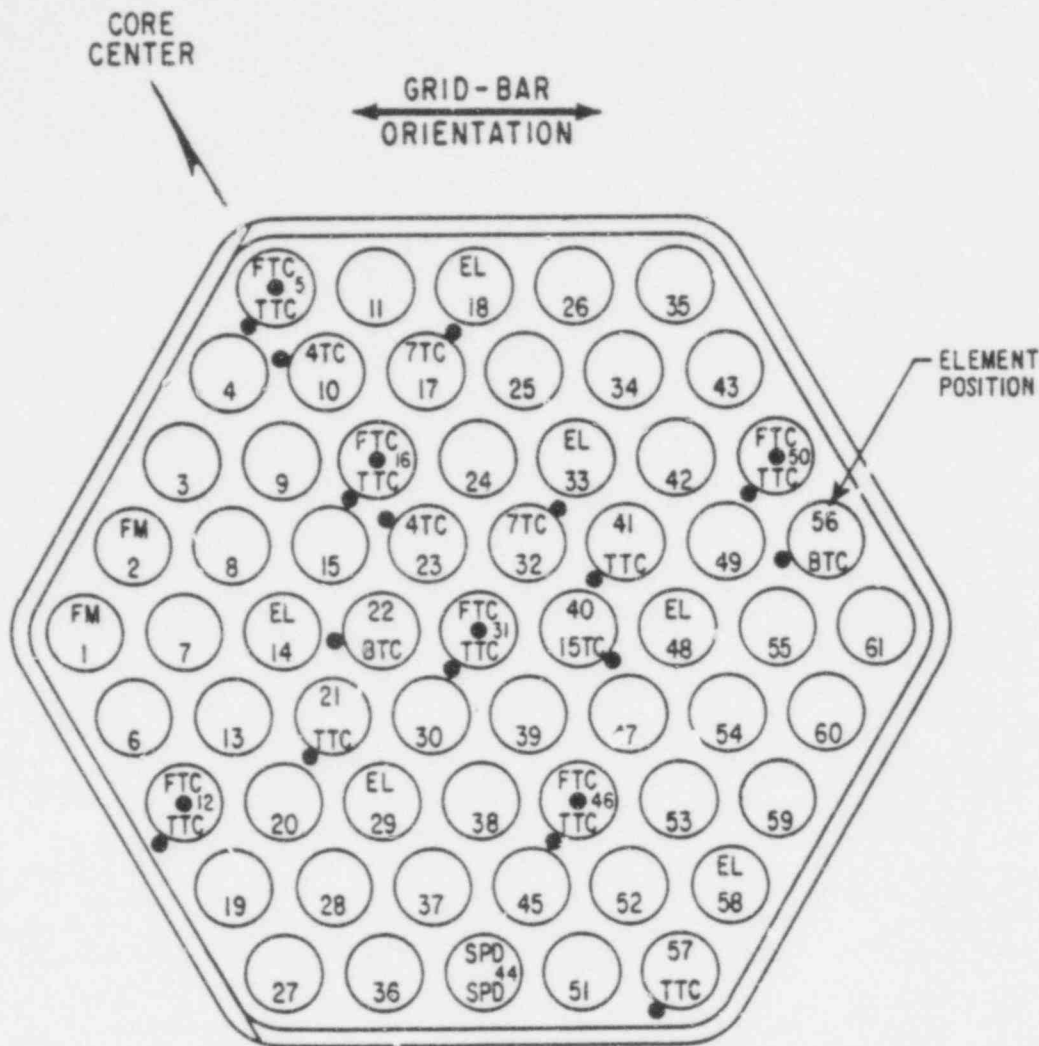
- x FUEL CENTERLINE THERMOCOUPLE
- COOLANT THERMOCOUPLE
- NON-FUELED PINS

630 001



630-002

AGRAWAL/KHATIB-RAHB.  
Fig. 8.21



LEGEND

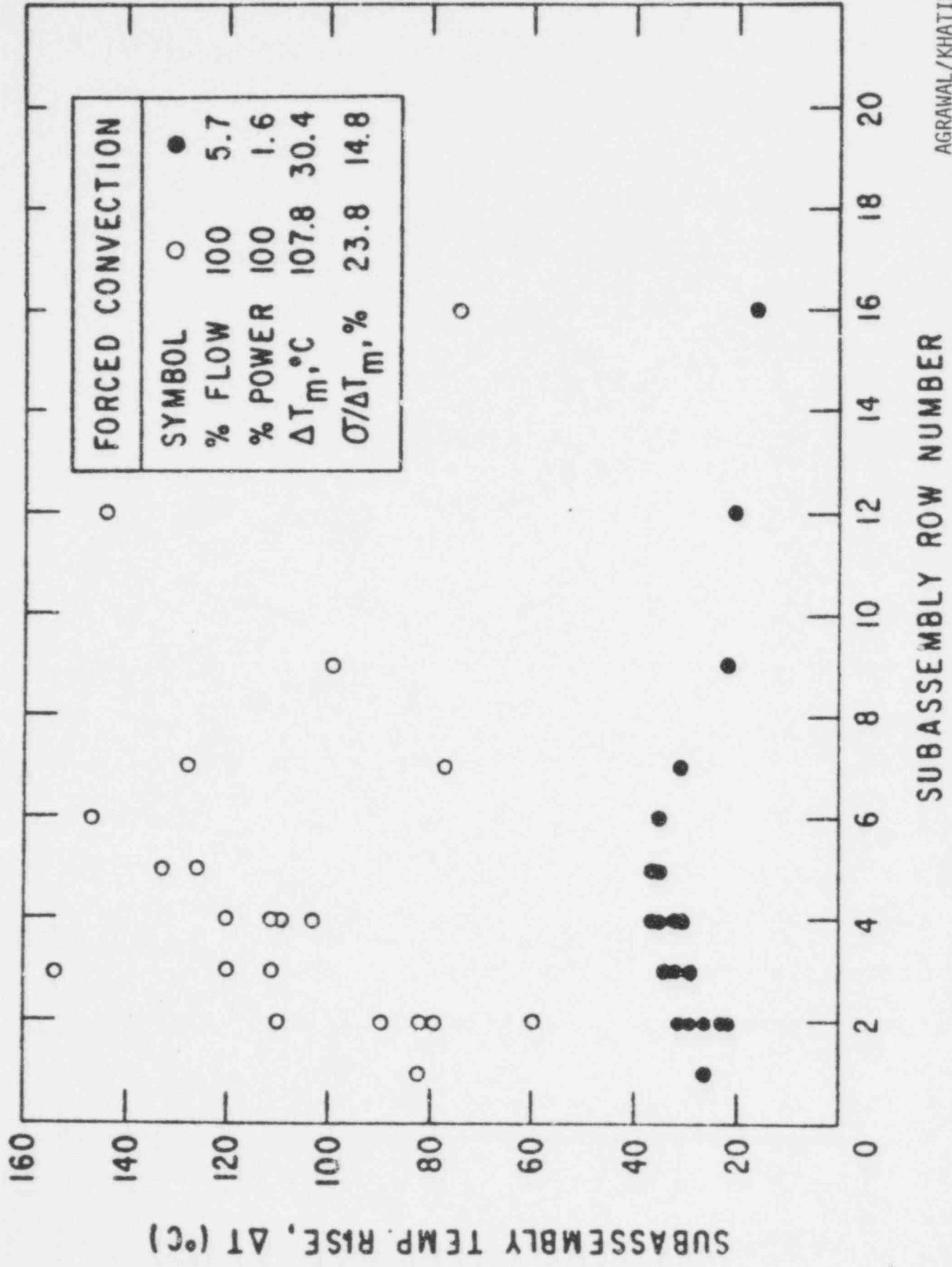
REQUIRED

FM - FLOWMETER LEAD .....	2
SPD - SELF POWERED DETECTOR .....	2
BTC - CORE-BOTTOM COOLANT TC .....	2
4TC - COOLANT TC 0.137m ABOVE CORE BOTTOM .....	2
7TC - COOLANT TC 0.240m ABOVE CORE BOTTOM .....	2
TTC - COOLANT TC TOP OF CORE .....	9
FTC - FUEL-CENTERLINE TC .....	6
15TC - COOLANT TC 0.514m ABOVE CORE BOTTOM .....	1
EL - EXTENDED-LENGTH (0.660m) MK-II ELEMENTS ...	6

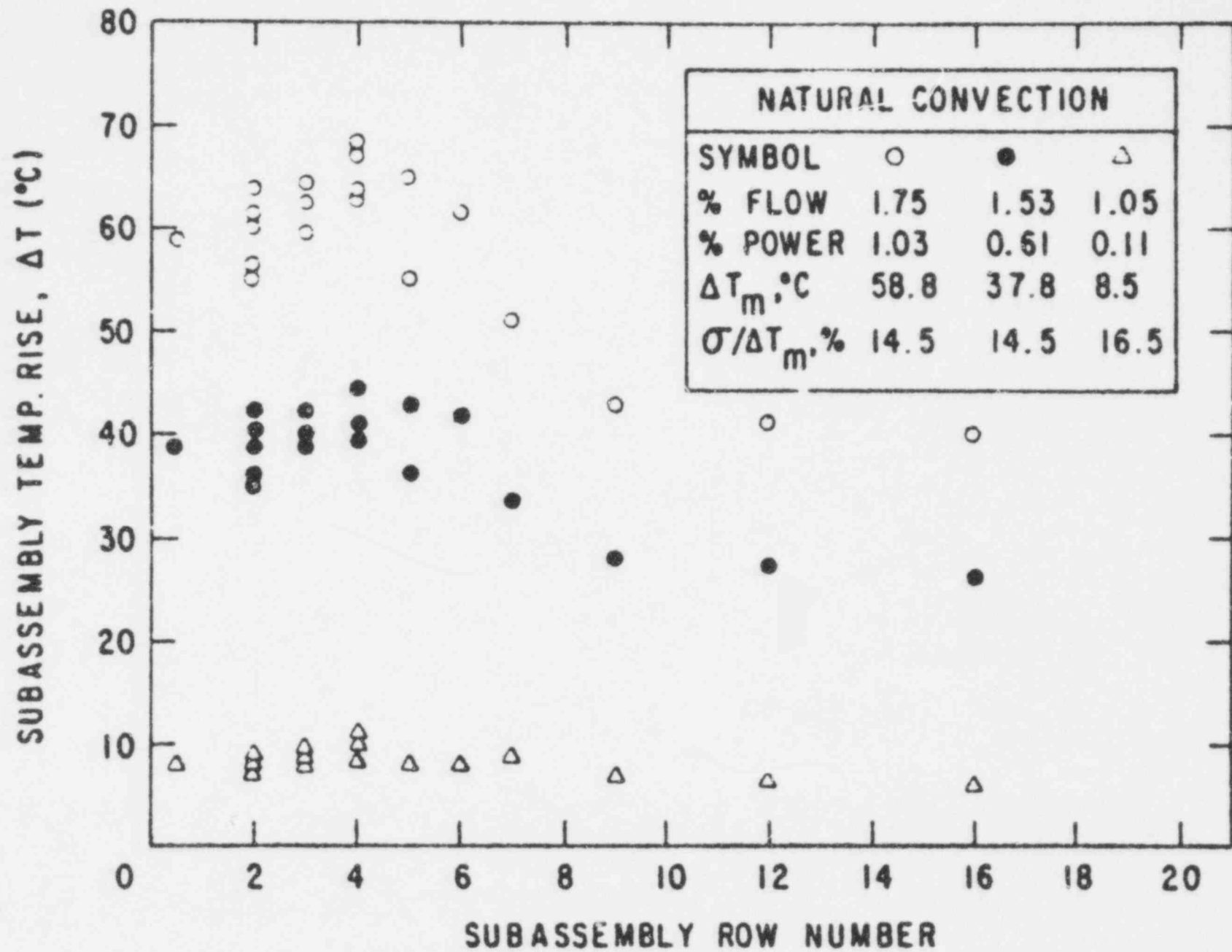
NOTES: a) DOTS REPRESENT LATERAL POSITION OF TC JUNCTIONS IRRESPECTIVE OF AXIAL LOCATION.

b) TWO OUTLET COOLANT TC's (NOT SHOWN) EXIST ABOVE THE FUEL ELEMENTS.

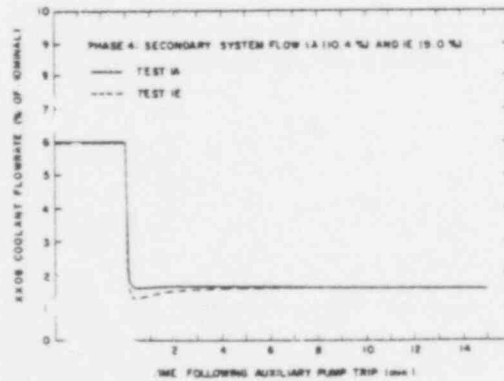
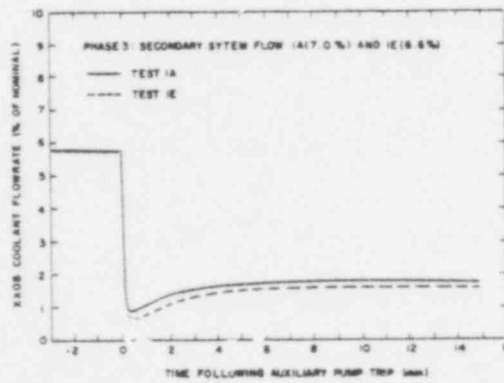
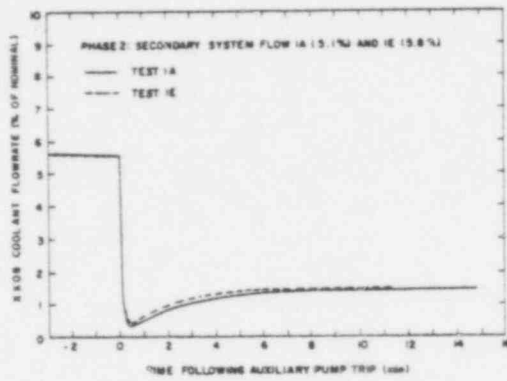
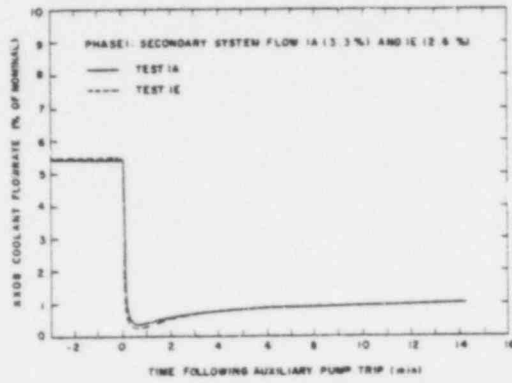
630 005



630 004



AGRAWAL/KHATIB-RAHBAR  
Fig. 8.24



630 006



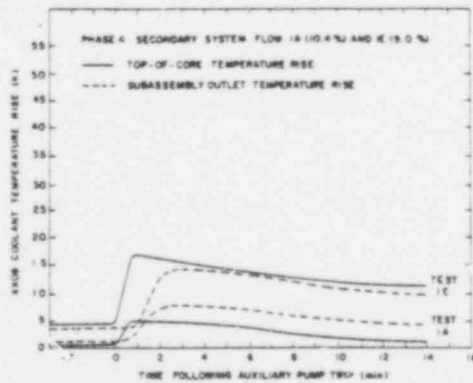
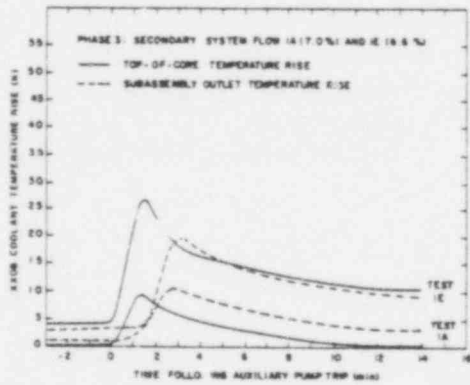
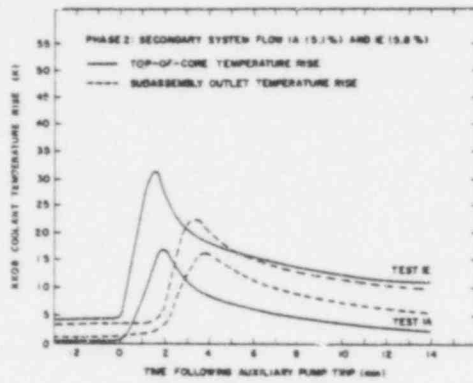
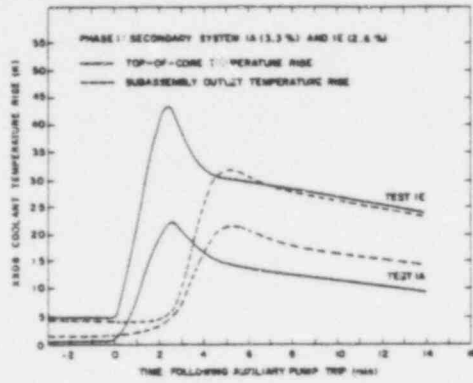
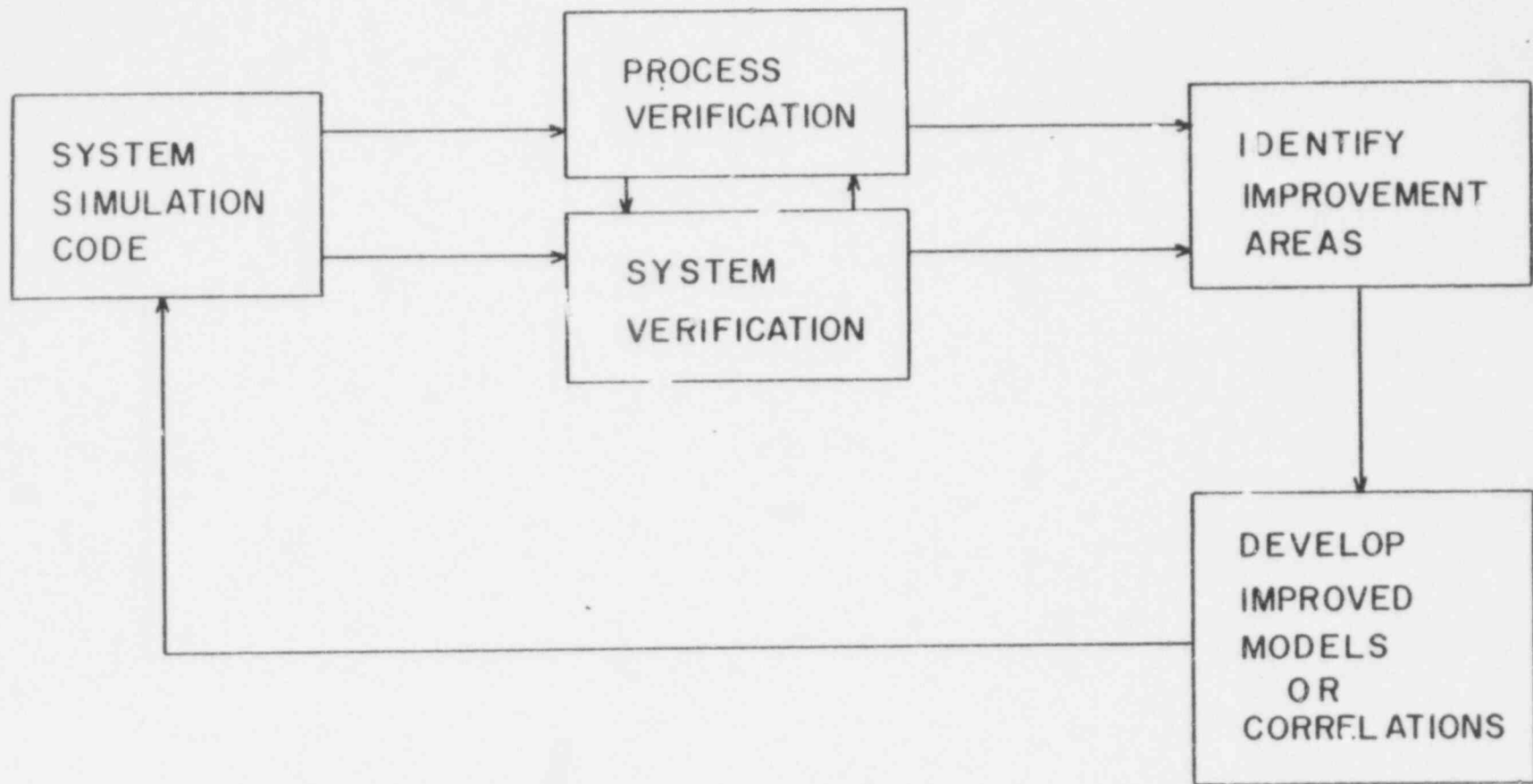


FIGURE CAPTIONS

Figure No.

- 9.1 Schematic Representation of the Relationship Between Model Development and Verification
- 9.2 Typical Variation of Consequence as a Function of Confidence Level

630 008



630 010

